Drops on Lubricated Polymer Brushes and Gels

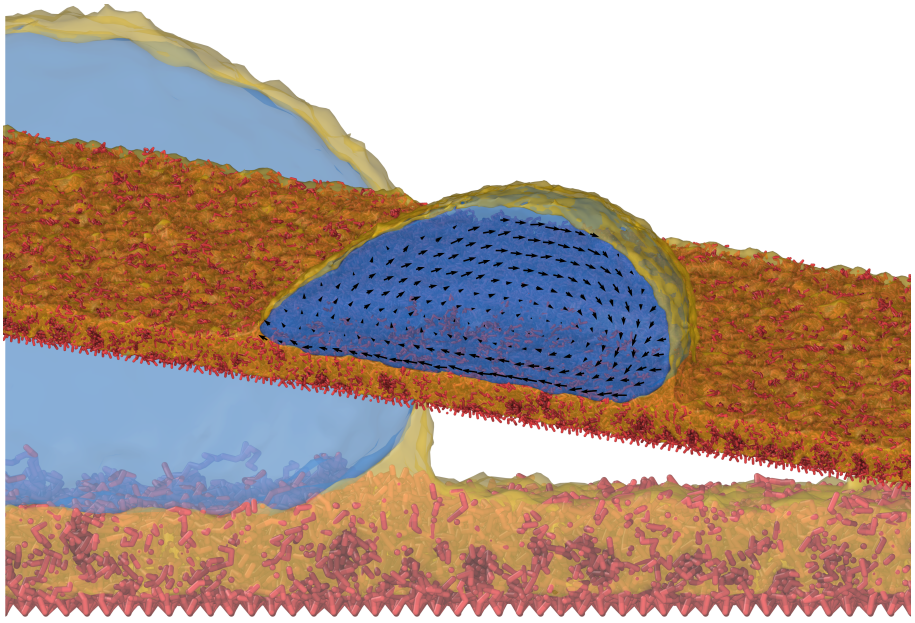

Rodrique G. M. Badr
geboren am: [redacted]

Dissertation for the award of the title
Doctor of Natural Science
submitted to the Institute of Physics
in the Faculty of Physics, Mathematics and Computer Sciences (FB 08)
of the Johannes Gutenberg-Universität Mainz
on 18.06.2025

I hereby assure that this work has been written independently and only with the help the specified sources and aids as well as the citations that have been indicated.

Some code snippets and proof reading were generated using various AI generative models.

Mainz, 18.06.2025
Rodrique G. M. Badr

Rodrique G. M. Badr
Drops on Lubricated Polymer Brushes and Gels
Oral examination: 20.11.2025
Supervisor: Prof. Dr. Friederike Schmid
Co-Supervisor: [redacted]

Condensed Matter Physics (KOMET)
Institut für Physik
Staudingerweg 7-9
Johannes Gutenberg-Universität
55128 Mainz

Acknowledgments

The journey leading to this dissertation has been a long one, and would not have been possible without certain people around me.

Starting at the academic level, the biggest gratitude goes to my supervisor Friederike Schmid. I think I was very lucky for having landed under her supervision, and am grateful for the freedom and understanding she provided me with during my research journey. Despite giving full freedom (and a lot of patience) to explore the research topic, it was not without providing me with very valuable insights and advice both at the scientific and career levels, and I appreciate her always trying to make time when I needed guidance and support. Many thanks also go to Doris Vollmer for being a spectacular scientist who also provided much support and guidance, and provided me with many opportunities to explore and learn methods at the experimental level. This section would not be complete without thanking my collaborator Lukas Hauer who was an invaluable presence due to his critical mind, creative ideas, and willingness to discuss any topic. Many ideas discussed in this dissertation originated through discussions with him. It was always a pleasure to learn from him and to meet, work, and even share presentations with him. Further thanks go to A[redacted] N[redacted], Lukas Stelzl, and L.K. for insightful discussions on various topics and valuable advice. I would also like to thank my committee members for their time reading my dissertation and examining my knowledge.

Having arrived to Germany during the global pandemic in 2020, the support and help of the wonderful Daniela was the only way I could survive, and her support continues until today, and is felt and appreciated by everyone who passes through our research group. Many thanks also go to Mariana for her role in the GRK 2516 as well as outside of it, for always making us feel welcome and supported as we navigated all the activities and responsibilities, and for always encouraging us to uphold our end of the bargain.

I want to thank the German research foundation (DFG) for funding through the project SPP 2171 (Grant No. 422796905, project Schm 985/22) and support through the GRK 2516 project.

At the personal level, I think it is important to first thank my father Georges, mother Mireille, and sister Monica, without whom I probably would not have even started on my journey of studying physics. Despite my parents originally expecting me to study medicine or engineering, as many parents expect their children to do, I am forever indebted to their support along with my sister when I decided to study physics. I am where I am now thanks to their crucial sacrifices both at the financial and emotional levels, and I hope to

give credit to that and pay homage to them by including their initials ‘G’ and ‘M’ in my publication name now and in the future.

I also want to thank my friends Wassim, Sara, Saly, and L.T. first for their amazing support and friendship before I arrived here. But I also want to thank them for the hours we spent on Discord and video chats during the pandemic working, eating, watching movies, basically spending whole days together. It made being stuck at home pleasurable and even worth the time sometimes. Mariam and Hana I thank for all the emotional support and being such wonderful and inspiring friends, who also made the lockdown bearable through hour long chats.

From the people I met in Mainz, I want to thank J.S., J.A., A.S., and Yannick for making me feel welcome upon my arrival in the city. I thank J[redacted], who started the journey with me, for all the long discussions trying to solve problems in our codes. Yashraj, Gaurav, Janka, and Emanuele for inspiration, support, long and engaging discussions, being there through thick and thin, and most importantly all the coffee breaks. For the wonderful times in the office and on and off campus I also thank Marios, Le, and Maurice, they are some of the most fun and interesting people to be around. Arya and Xiaofei for allowing me to engage in, learn from, and help with their research projects. Kyra and Lucia for the most interesting conversations on topics that I rarely get to discuss with other people. In addition, I thank all my friends from IMB who are unfortunately too many to list here, but who are all wonderful people nonetheless.

At the end go the most special thanks to Liza, who held a special place in my life since the moment we met, even though our meeting happened by showing up to dinner after a total stranger texted a friend group chat. Liza made and still makes my time here special and ever more meaningful. I thank her for her magnificent presence, her immense support, her valuable and grounding advice, and simply for being around.

Abstract

In this thesis, we engage with the physics of drops deposited on polymer brushes and gels that can also be swollen by a lubricant. We discuss results from simulation, theory, and experiment at three different levels: equilibrium, approach towards equilibrium, and steady state dynamics.

At the level of equilibrium, we use Molecular Dynamics (MD) simulations using the Many-body Dissipative Particle Dynamics (MDPD) model. We tune our model to emulate a water drop on a PDMS substrate. To characterize the brush, we find the point where it is saturated with lubricant and the corresponding brush height. In addition, we calculate the surface tension for different lubricant fractions. We show that the contact angle should theoretically be independent of the swelling of the brush. Afterwards, we show that drops deposited on lubricated polymer brushes undergo a cloaking transition, where the drop becomes covered by a film of lubricant. The transition sets in after a particular amount of lubricant is infused in the brush, a result which is supported by a theoretical thermodynamic analysis of the system. For spherical drops on dry brushes we reveal the presence in MDPD of a line tension that promotes the spreading of the drop. On lubricated brushes, the relation is not as transparent, though we do see a dependence of contact angles on the size of the drop. We also find that the brush in the area of the wetting ridge is swollen to a height that is close to the height at saturation, especially after the cloaking transition sets it. We complement our results for spherical drops with an analysis of cylindrical drops to eliminate the effect of line tension. In terms of the cloaking transition the results for both spherical and cylindrical drops are consistent. However, we see opposite behavior for the contact angle as a function of the lubricant fraction in the brush, which is indicative of a possible dependence of line tension on the swelling of the brush.

To study the approach towards equilibrium, our experimental collaborators ran experiments where a glycerol drop was deposited on PDMS gels swollen with high viscosity silicone oils. There, the lubricant separates from the gel so that the wetting ridge has a liquid component. We show that as the ridge grows, it does so in a geometrically similar fashion, maintaining the same shape. The separation height between the apex of the wetting ridge and the gel is followed through time and shown to depend on both the degree of swelling and the viscosity of the oil. We support the experimental findings with a theoretical model based on diffusion, and find that the results agree very well with the experiments for saturated gels, but not so much for undersaturated ones. To follow the approach towards equilibrium in terms of cloaking, we perform experiments where a drop is pending from a swollen gel, and follow the evolution of the shape with time. Unfortunately, few conclusions could be drawn from the experiments due to a lack of reproducibility. In addition, we perform numerical simulations using the MDPD model to follow the cloaking away from equilibrium. We find that the cloak front progresses on the drop linearly with time, with the rate increasing with the fraction of oil. Additionally, the cloak creeps onto the drop as it thickens simultaneously, and continues to get thicker after it covers the entire drop. We also find that the distribution of lubricant throughout the

brush is consistent with our assumption that the time scale is set through the diffusion of lubricant across the brush.

Finally, we address the steady state dynamics of drops moving on lubricated polymer brushes. The results of our experimental collaborators for water drops on PDMS brushes reveal an asymptotic power law relation between the dissipated power and the velocity of the drop. Our numerical simulations also show such a power law, albeit with different exponents. The exponent in the experiments is the same for two preparation methods of the brush. Meanwhile, in simulation, the exponent depends weakly on the swelling of the brush. To understand the discrepancy and the dissipation mechanisms that influence the exponent, we quantify the height of the wetting ridge and the flow field inside the drop. The analysis rules out slip as a major contributor to dissipation, but neither viscous dissipation in the drop nor viscoelastic dissipation in the brush can be ruled out at this stage. Instead, we find that the viscoelastic dissipation can remain relevant even at high velocities since the wetting ridge does not vanish at any velocity; in addition, the flow field inside the drop is complex with the possible presence of multiple vortices, and can possibly explain the observed exponents.

Preface

The largest struggle facing a person attempting a new project is filling gaps in their knowledge. The largest obstacle to of filling such gaps is having the right sources. As a young PhD student, my supervisor presented me with excellent review articles on the topic of wetting in general and wetting on soft substrates in particular. However, there is the problem that the articles in question are typically aimed at experienced researchers, as most review articles are. As such, certain concepts are presented in a matter-of-fact fashion, jargon is used freely without definition, and relations are presented without proper motivation. In many of these situations, references are not provided; however, even when provided, they tend to be overwhelmingly numerous and many times inappropriate, as they do not make the statements they are cited for.

Having gone through this struggle, my aim when writing the current work was to make it pedagogical. The goal I set for myself was:

> A student who is inexperienced in the field should be able to read this work and make further progress with the project, without the need to look for further references.

Whether I succeeded in my goal or not is yet to be revealed. Nevertheless, I made of effort into presenting a comprehensive overview of wetting phenomena and an introduction to polymer brushes with the utmost clarity and logical progression. When needed, I clarified the relevance of certain concepts. I chose references that I found to be the most transparent in the subtopic of interest. Where appropriate, I specified the particular section or chapter.

Part of the theory and the associated literature, especially in the section on dissipation, is not directly applied to the work presented in this thesis. The aim behind introducing them is to provide a well rounded overview of the topic, one that will allow a future student to have the necessary knowledge to pick up the project where it was left off. Additionally, the student should have enough knowledge to understand talks and discussions at conferences, even when the topic is not directly related to their main subject. This was a problem I struggled with significantly throughout the years working on this project, even late into my doctoral studies.

To differentiate particularly useful references, certain citations will be followed by the word ‘key’ as such: [00, key]. I view those references as key references. Any student working on a similar topic should go through the key references at least once. When the reference is a book, it provides a good introduction to a particular field. When the reference is an article, it is typically a foundational article, the results of which are used repeatedly in the

literature. For key articles, a person working on a similar topic is advised to be strongly familiar with the main results, and more importantly, with the range of applicability of the results, without necessarily being familiar with the details of the study. Key articles are not always the earliest or most influential publication on a particular topic, instead, I regard them as the most useful references for someone working on the topic.

The results are organized into three overarching themes. The corresponding chapters include both published and unpublished data. Chapters based on published work reproduce the original articles with some modifications, while those presenting unpublished material are written entirely from scratch. To distinguish between the two, we append the letter 'U' to the chapter numbers that contain unpublished results, while retaining the same numeral for chapters within the same thematic group. For instance, Chapters 4 and 4.U belong to the same theme, with the latter presenting unpublished data.

Table of Contents

List of Figures

List of Acronyms

List of Symbols

Below is a list of symbol that are repeatedly used in the document. Some symbols may refer to multiple quantities, but here is declared the most common usage.

- $\mathcal{F}_x$: free energy
- f_x: either free energy density or force per unit length
- F_x: force (magnitude)
- γ : surface energy, and unless stated otherwise also used for surface tension
- γ_{AB} : surface tension at the interface between phases A and B
- Υ: surface tension
- θ_Y: Young contact angle
- S: spreading parameter
- $\mathcal{T}$: line tension
- $\Pi(h)$: disjoining pressure at film thickness h
- σ_{ij}: stress tensor
- u_{ij}: strain tensor
- G: shear modulus
- l_{ec}: elastocapillary length
- v_{cl}: contact line velocity
- v_{cm}: center of mass velocity
- $G^*(\omega)$: complex modulus
- $G'(\omega)$: storage modulus
- $G''(\omega)$: loss modulus
- ρ: without a subscript, refers to the radial coordinate in cylindrical or 2D polar coordinates
- ρ_x: the bulk equilibrium density of species x

- $\varrho_x(\ldots)$: spacial density distribution of species x where $\ldots$ is replaced by the relevant coordinates.

1. Introduction

As we go on with our daily lives, it is near impossible not to encounter liquid drops, or items that were in contact with liquid drops. Drops play a relevant role in everyday life, such as condensation in refrigerators and on cold windows (Figure 1.1 a); in agriculture, with raindrops on leaves and in greenhouses; and in environmental solutions, such as passive water harvesting from moisture in the air and water drops on solar cells [1].

Due to their ubiquity, situations arise where the behavior of liquid drops can dramatically affect the functioning of equipment, or one's ability to perform certain tasks. A classic example is rain on a windshield as shown in Figure 1.1 (b). If the wipers are not in a good condition, the water will smear over the windshield, obstructing the driver's vision until it dewets and forms separate drops again. Another example comes from the renewable energy sector where solar panels continuously collect dust (Figure 1.1 c) which affects their efficiency. Problems like this can be avoided, or their severity reduced, if transparent and durable materials could be manufactured on which drops do not stick. This is where hydrophobic, slippery surfaces come into play. Examples of such surfaces already exist in nature, such as on the leaves of the lotus and taro plants [2] (Figure 1.1 d), which employ 'dry' patterned surfaces to induce hydrophobicity, or on the lip of carnivorous pitcher plants to trap their prey (Figure 1.1 e), where the surface is infused with water as a slippery liquid [3]. Inspired by nature, much research has been dedicated to designing slippery substrates as patterned surfaces [4]. However, despite their success in nature, interest is not limited to patterned surface as they show certain limitation. One possibility circumvent some limitations is to design slippery coatings [5].

Of available materials for such applications, silicones are very good candidates. The design of silicone-based slippery substrates relies heavily on the use of Polydimethylsiloxane (PDMS) as an integral material. PDMS is a polymer with a siloxane (Si-O-Si) backbone, and with methyl groups (CH3) attached to the silicon atoms, giving it the linear formula $[Si(CH_3)_2O]_n$. A PDMS monomer has a molecular mass of about 74 g/mol. The Si-O bond length is about 1.64, Å, and the Si-O-Si angle ranges from 130° to 150°, depending on the configuration of the molecule [6]. Owing to the large bond angle, PDMS chains experience low torsional barriers [7], resulting in a persistence length of only a few monomers, making them very flexible. When PDMS is in its free form at room temperature and atmospheric pressure, it forms a liquid polymer melt of density 965 kg/m^3, known as silicone oil. Silicone oil forms the foundation for the synthesis and fabrication of silicone-based substrates. Broadly speaking, silicone-based substrates can be split into three classes: Liquid/Lubricant Infused Surfaces (LIS), elastomeric surfaces

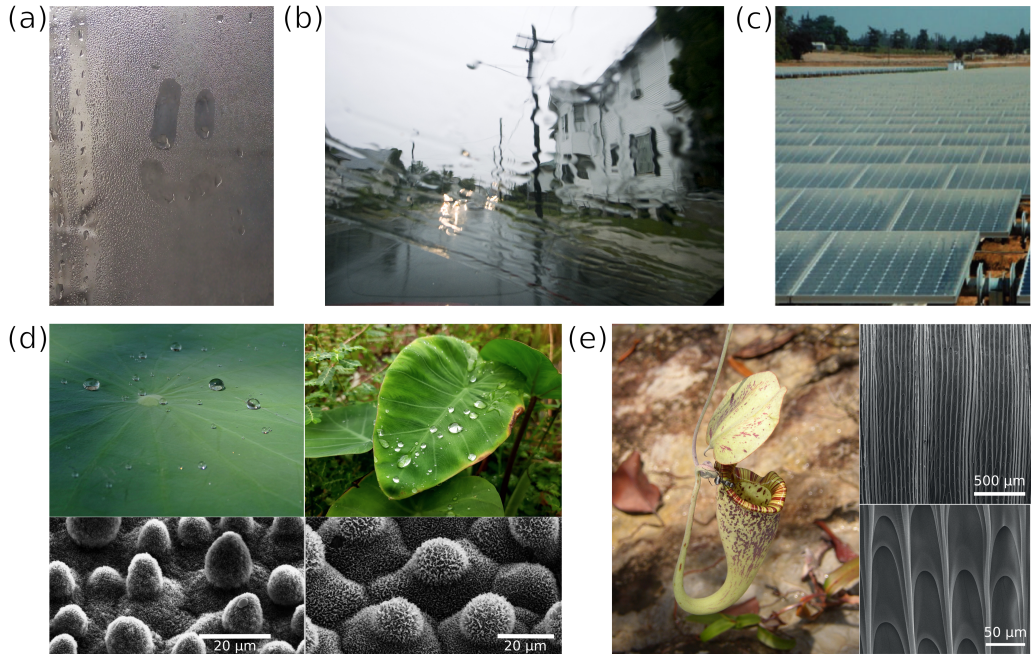

Figure 1.1.: (a) Condensation on a window with a smiley face drawn in. (b) Rainwater on a windshield obstructing the vision of the driver. (c) Dirty solar panels. (d) Water drops on lotus (left) and taro (right) leaves, with corresponding scanning electron microscopy (SEM) images of the corresponding microstructures below each image. (e) Carnivorous pitcher plant with an ant on it that is likely about to be devoured, and on the right are SEM images of the microstructure on the "lip" at two different magnifications. Adapted under public domain from [8], under CC BY 2.0 from [9], CC BY-SA 3.0 from [10], CC BY-SA 4.0 from [11], CC BY 2.5 from [12], and with permission from [2, 3, 13].

(elastomers), and brush-like surfaces, also known as Slippery Omniphobic Covalently Attached Liquid-like (SOCAL) surfaces.

LIS typically take the form of surfaces patterned with porous microstructures (Figure 1.2 a) and are later infused with a liquid that acts as a lubricant. In the absence of lubricant, drops on patterned surfaces can exist either in the Wenzel state or the Cassie-Baxter state (cf Figure 1.2 b). In the Wenzel state, the drop wets the substrate homogeneously [14], imbibes the microstructure, and is characterized by strong pinning [15]. In the Cassie-Baxter state, the drop wets the substrate heterogeneously, leaving air pockets within the microstructure, which dramatically reduces the friction experienced by the drop [16]. This forms the basis of so-called patterned superomniphobic surfaces [17, 18]. However, such superomniphobic surfaces suffer from low durability, due to vulnerability to mechanical stress [19], chemical reactions [20], and radiation damage [21], although sometimes the damage is reversible, for example, by heat treatment [20, 21]. Another challenge for superomniphobic patterned surfaces is the stability of air pockets. The collapse from the

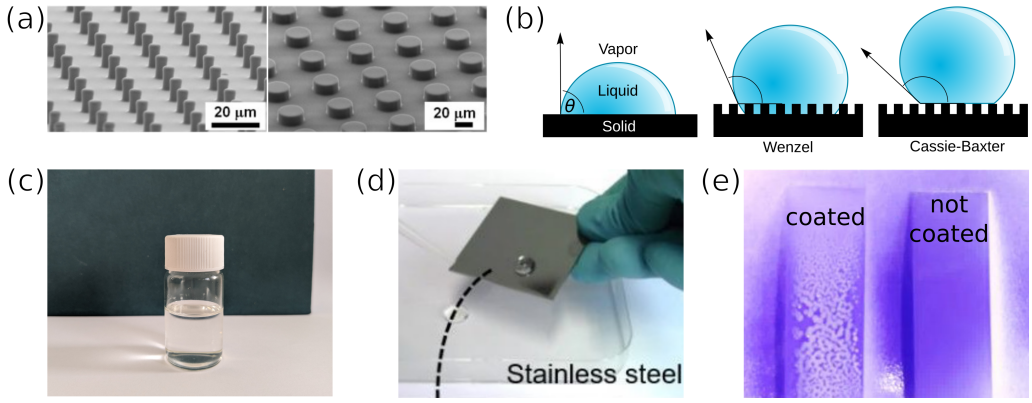

Figure 1.2.: (a) Two kinds of micro-pillar structures for LIS. (b) Possible states a drop can have on a solid surface. From left to right we have a drop on a smooth surface, on a rough surface in the Wenzel state, and on a rough surface in the Cassie-Baxter state. (c) A glass vial containing a PDMS gel. (d) A drop in the process of sliding off a stainless steel surface that was coated with grafted PDMS chains. (e) Left: Spray paint dewetting from a glass slide that was coated with grafted PDMS chains. Right: Spray paint sticking to a non-coated glass slide. Adapted under CC BY-SA 3.0 from [31], CC BY 4.0 from [32], and with permission from [30, 32].

---

slippery Cassie-Baxter state to the sticky Wenzel state can occur for various reasons [22–25]. One method to avoid this problem is to infuse the surface with a lubricating liquid. Silicone-based LIS typically consist of patterned surfaces infused with silicone oil as a lubricant [26]. LIS infused with silicone oil exhibit very low roll-off angles [27], i.e. the tilt angle at which drops roll off, and can perform well even with simple patterns that can be easily manufactured [28]. However, LIS generally lack durability due to lubricant depletion as drops roll off [27, 29], though strategies have been developed to replenish the lubricant [30].

The second class of silicone substrates is elastomers. Elastomers are crosslinked networks, or gels, of PDMS chains. PDMS gels are used as coatings on different materials to modify their wetting properties. The crosslinking is achieved by mixing PDMS chains with functionalized chain ends (vinyl- or hydroxyl-terminated) and a crosslinker, typically methylhydrogensiloxane, $(HCH_3)SiO$. The result is a transparent viscoelastic solid as shown in Figure 1.2 (c). The mechanical properties of PDMS gels are easily tunable, even with commercial kits, and the elastic modulus can range from 20 kPa to 1.6 MPa [33]. In most practical cases, the synthesis of PDMS gels leaves uncrosslinked chains within the gel [34, 35], which we will refer to as free chains. The presence of free PDMS chains within the gel can affect the wetting behavior in several ways. First, free chains can enhance the slippery nature of the gel, thereby acting as a lubricant. Second, free chains swell the gel, altering its elasticity [33], and ultimately its response to the wetting liquid. Additionally, free chains sometimes accumulate on the surface, even when the gel is not fully saturated

[36], which may reduce the adhesion of liquids onto the surface. When a drop sits on the gel, free chains can gather at the three phase contact line, further swell the gel locally [37], separate from the gel [38], or even cover the surface of the drop, fully cloaking it [35]. The properties of leftover free chains are generally not known. However, they can be washed out with a solvent and replaced with silicone oil of known properties [38], in order to tune the material for a specific application. Drops moving on PDMS gels experience little adhesion, and can roll off at relatively small tilt angles [39], making them excellent candidates for self-cleaning coatings. However, they also suffer from lubricant depletion. Nevertheless, one advantage PDMS gels have over LIS is better oil retention, as the oil swells the gel, making them more durable against lubricant loss.

The final class is SOCAL surfaces, such as PDMS brushes. PDMS brushes are layers of PDMS where the chains are anchored or grafted by one end to the substrate [40]. The typical thickness of PDMS brushes is on the order of nanometers. As opposed to crosslinked PDMS gels, which form solids, the PDMS chains in brushes retain their flexibility since one end is left free, and the free ends behave, more or less, as they would in liquid silicone oil, hence the term "liquid-like." Owing to the liquid-like properties of the resulting layer, drops deposited on PDMS brushes readily roll off even when the substrate is tilted by less than 5° [41]. The synthesis of polymer brushes can generally be achieved in one of two ways: grafting-from or grafting-to. In both methods, the substrate has chemically active sites that will bind to monomers at one of the free ends of the grafted chains. As the name suggests, grafting-from involves the growing of the brush chains from the substrate. For PDMS, this can be achieved by vapor deposition on plasma-treated glass [42]. In the grafting-to method, pre-polymerized chains are grafted by one of their free ends onto grafting sites on the substrates [32]. The grafting densities achievable using the grafting-to method are lower than those using the grafting-from method, due to the screening of the grafting sites by the chains [43]. On the other hand, lower polydispersity indices can be achieved through the grafting-to method if one starts the grafting procedure with monodisperse chains. As with the synthesis of crosslinked PDMS gels, at the end of the process, free, non-grafted chains will remain. Free chains can either be washed out with a solvent or removed by wiping with a cloth or tissue [32]. Grafted PDMS layers were shown to work as coatings on a variety of materials, such as glass, metals, and certain fabrics [32, 44] (see Figure 1.2 d). The synthesis can sometimes be carried out at room temperature, and the resulting film is very durable against strong mechanical stresses, such as scouring with a metallic sponge [32]. In addition, since the grafted chains already behave like a liquid at the interface, the slipperiness can be maintained even at low or zero lubrication, while crosslinked PDMS gels were shown to lose slipperiness after a certain number of drops roll off within a given period [32]. This is further confirmed by the fact that the low roll-off angles were maintained even after washing the coatings with toluene, ethanol, and water for as long as 120 s [32]. With water as the wetting liquid, the wetting properties of the coatings are also resilient to heating up to temperatures of 250° C for several days [41]. Finally, the ability of such coatings to repel liquids is not limited to water. Grafted PDMS layers can repel a multitude of liquids, from low surface tension liquids like ethanol, to super glue, permanent markers, and spray paint [32, 41]

(see Figure 1.2 e), making them truly omniphobic. PDMS brushes have very promising characteristics as durable, slippery coatings for self-cleaning and anti-fouling purposes [44].

Following this, the current thesis aims to investigate the static and dynamic wetting of polymer brushes for the ost part, but also of gels. Our main focus is on the numerical and theoretical aspects, but we couple our studies with experimental findings. We focus in particular on coatings that are swollen with lubricant, and quantify the effect and relevance of the lubricant, as well as the response of the coatings to drops, and vice versa.

We begin by introducing the fundamental theoretical concepts of wetting in Chapter 2. First, we cover the basics of static wetting on idealized and "real" rigid surfaces, and slowly make our way towards more involved situations, such as wetting on elastic and lubricated surfaces. We afterwards introduce the main concepts for dynamic wetting. As one of the motivations for this investigation is the design of slippery surfaces, the ultimate goal is to improve our understanding of the dynamics of drops moving on such surfaces. In this dynamic situation, energy dissipation is one of the most relevant physical processes that affect the efficacy of the slippery surfaces. We spend some time, therefore, discussing the possible sources of dissipation, and the resulting behavior of the moving drops. As will become apparent, many sources can result in similar macroscopic trends, making it hard to isolate the culprits without resolving the microscopic details. The discussion on wetting is followed by an introduction to polymer physics and polymer brushes.

Afterwards, we discuss the methods we applied for our study, followed by the main results to come out. The results are thematically divided into three parts. In Chapters 4 and 4.U we discuss the equilibrium properties of droplets on lubricated polymer brushes in simulation. In Chapters 5 and 5.U we describe the kinetic evolution of wetting ridges and cloaks for stationary drops deposited on swollen PDMS gels and brushes through experiment, simulation, and theory. Finally, in Chapters 6 and 6.U we investigate the dynamics of droplets moving on lubricated polymer brushes through simulation and experiment; the published results are supplemented with further interpretation based on the expected behavior of dissipative forces following the discussion in section 2.4.

2. Theoretical Background

2.1. Wetting fundamentals

2.1.1. Surface tension

Before talking about wetting, we need to introduce the concept of interfacial or surface energy. When a liquid forms, the driving force behind its formation is the cohesive interactions between the molecules that constitute it. Liquids generally exist in contact with other phases, either a gas, a solid, or another liquid that does not mix with it (immiscible liquids), leading to the formation of an interface that separates the two phases. If we consider a liquid molecule in the liquid, when it is in the bulk it is on average surrounded by a certain number of interaction partners, and its total interaction energy is at a particular value. If we instead consider a molecule at the interface with the other phase, the number of cohesive interaction partners decreases, raising the energy (see Figure 2.1 a). The total free energy of the system can be written as

$$\mathcal{F} = \mathcal{F}_0 + \mathcal{F}_{int} \tag{2.1}$$

where $\mathcal{F}$ is the total free energy, $\mathcal{F}_0$ is the free energy in the absence of interfaces, and $\mathcal{F}_{int}$ is the contribution of the interface. Since nature tends to minimize energies, the liquid therefore would like to reduce the number of molecules at the interface; in other words, it likes to reduce the interfacial area. From this intuitive view, one can then define the surface energy γ as the contribution per unit area to the interfacial free energy $\mathcal{F}_{int}$

$$\mathcal{F}_{int} = \gamma\, A \tag{2.2}$$

where A is the total interfacial area. From the above equation, we can see that the units of γ are [Energy]/[Area]. This unit, however, is equivalent to that of [Force]/[Length]. This suggests that γ can also be interpreted as a surface stress, or as it is more commonly called, interfacial or surface tension Υ. Indeed, for most simple liquids, where the surface energy does not depend on the strain, the surface tension Υ and surface energy γ are equivalent. This can be seen by following the change in interfacial energy upon a change in area

$$\delta\mathcal{F}_{int} = \gamma\, \delta A \tag{2.3}$$

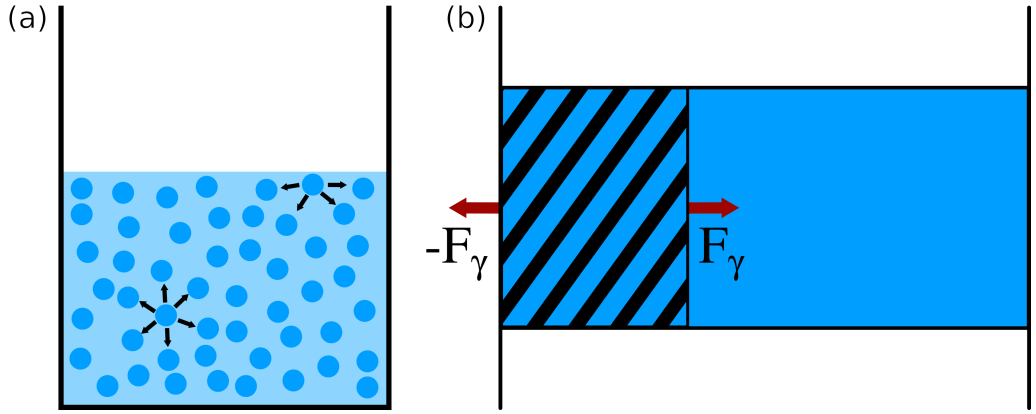

Figure 2.1.: (a) Cartoon of a liquid-vapor system showing a representation of the liquid molecules. The molecule in the bulk has more interaction partners than the one near the interface. (b) Cartoon of a liquid film caught in a rectangular frame. Considering a rectangular section of this film (dashed area), it is subject to horizontal external forces from two sources. The fluid to the right of this area exerts a force $\mathbf{F}_\gamma$ due to surface tension of magnitude $F_\gamma = \gamma L$ (right pointing arrow). This force is balanced by an equal and opposite force $-\mathbf{F}_\gamma$ from the left due to the adhesion to the frame.

---

and equating that to the work done during that change

$$\delta \mathcal{F}_{int} \equiv \Upsilon \, \delta A. \tag{2.4}$$

Therefore, we see that the surface tension is equal to the surface energy $\Upsilon = \gamma$. This equality may not always be valid, however (see section 2.1.1.2 below).

The surface energy is the reason why drops and bubbles take spherical shapes when immersed in another fluid, since at fixed volume, the sphere has the smallest area compared to other shapes, which minimizes the total interfacial energy $\mathcal{F}_{int} = \gamma A$. The surface tension is then the manifestation, in the form of stress, of the tendency to minimize the interfacial energy. This can be understood by making an analogy to how pressure is a bulk stress, that acts in the direction normal to surfaces cutting through the bulk. The surface tension is a form surface stress in the sense that it acts normal to lines on the interface, but still tangent to the interface.[1] Figure 2.1 (b) shows a flat liquid film in a rigid frame. Considering the dashed region alone, the surface tension aims to reduce its area, i.e. the dashed region is subjected to internal forces directed such that the area shrinks. To maintain equilibrium, considering only the horizontal direction, these internal forces are balanced by two external force: (1) a force $\mathbf{F}_\gamma$ exerted on the boundary to the

[1] This is not be confused with a two dimensional version of pressure. Pressure in a 2D system will act to increase the size of the system in a completely similar fashion to its 3D equivalent. The surface tension we are considering is defined for 2D interfaces in 3D systems, and always aims to reduce interfaces.

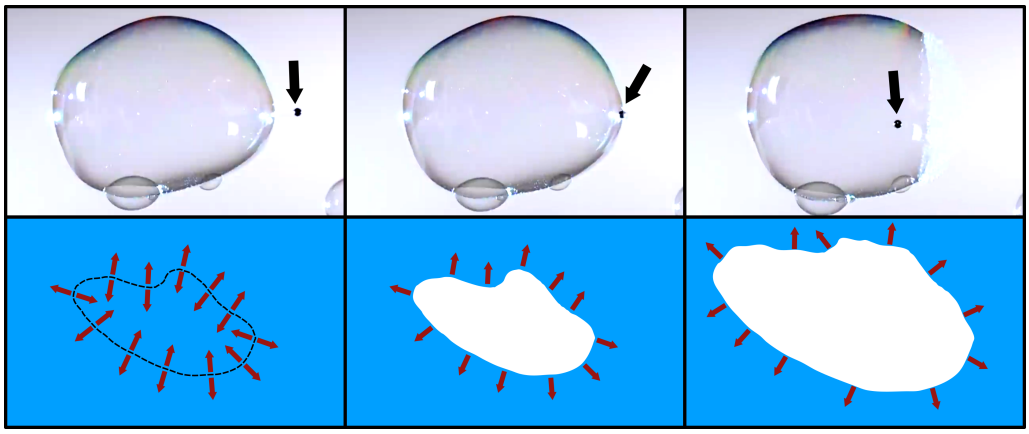

Figure 2.2.: Three stages of a bubble bursting: before, immediately after, and some time after puncture from a small black pellet. Black arrows indicate the position of a pellet causing the burst. Under each stage is a cartoon illustrating the forces due to surface tension in red arrows. Blue represents the soap film, the dashed line represents the shape of the puncture, and the white area represents air. Bubble screenshots obtained from [45]

right by the rest of the fluid, and directed outwards from the dashed region, and (2) a force $-\mathbf{F}_\gamma$ exerted on the other boundary in the opposite direction by the rigid frame.

The area reducing property of surface tension is well illustrated in the bursting of a soap film, where the puncture results in an imbalance in the tension, causing the total area of the film to decrease in the direction away from the puncture. Figure 2.2 (b) shows three stages of a soap bubble burst: before, immediately after, and some time after a puncture is made. Under each stage is a cartoon illustrating the forces due to surface tension. Considering a closed contour on the interface, before the puncture the tension takes the form of equal and opposite forces acting perpendicular to the contour at every point. When the interface is punctured, the tension is unbalanced, and the force acting on a length element $\mathrm{d}l$ on the line of the puncture is $dF_\gamma = \gamma\,\mathrm{d}l$ leading to the growth of the puncture and the decrease of the interfacial area of the film.

2.1.1.1. Laplace pressure

In the absence of surface tension, hydrostatic equilibrium dictates equality of pressure throughout the system. However, in the presence of curved interfaces, this is no longer true. If we consider two immiscible fluids as shown in Figure 2.3, the condition for equilibrium is given by

$$P_2 - P_1 = \gamma\,(\nabla \cdot \mathbf{n}) \tag{2.5}$$

where P_1 and P_2 are the hydrostatic pressures in the the bulk of each fluid, γ is the surface

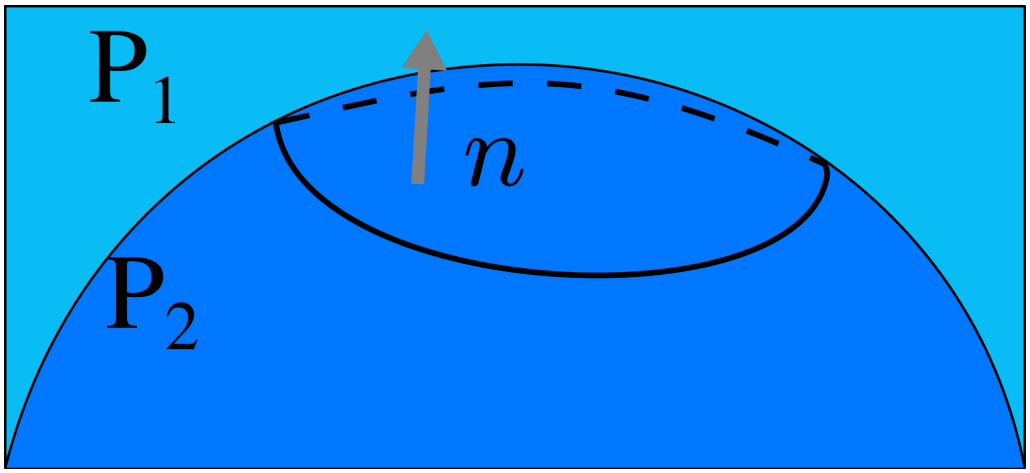

Figure 2.3.: Sketch of an arbitrary interface between two fluids. P_1 and P_2 are the hydrostatic pressures in the bulk of each fluid and **n** is a unit normal to the interface.

---

tension, and **n** is a unit vector that is normal to the interface, the divergence of which $\nabla \cdot \mathbf{n}$ measures the local curvature of the interface. Eq. (2.5) is called the Young-Laplace equation. The jump in pressure across the interface $\Delta P \equiv P_2 - P_1$ is known as the Laplace pressure. The solution of Eq. (2.5) for constant γ and in the absence of other forces is a surface of constant curvature. The Laplace pressure may affect the system in question in several ways, such as modifying the wetting configuration (see section 2.1.5) or locally compressing soft substrates. Derivations of Eq. (2.5) are presented in sections A.2 and A.3 based on two different approaches. The derivation in section A.3 accounts also for the case of inhomogeneous surface tension.

2.1.1.2. Shuttleworth effect

Comparing eqs. (2.3) and (2.4) above led to the result that the surface tension Υ is equal to the surface energy γ. Exceptions to this arise when the surface energy depends on the strain in a material. The result is known as the Shuttleworth effect [46] and in that case the change in interfacial free energy is

$$\begin{aligned} \delta\mathcal{F}_{int} &= \delta\left(\gamma A\right) \\ &= \gamma\,\delta A + A\delta\gamma \\ &= \left(\gamma + A\frac{\mathrm{d}\gamma}{\mathrm{d}A}\right)\,\delta A. \end{aligned} \tag{2.6}$$

We then see that the surface tension is not equivalent to the surface energy anymore. Instead we have the Shuttleworth relation [46]

$$\Upsilon = \gamma + A\frac{\mathrm{d}\gamma}{\mathrm{d}A}. \tag{2.7}$$

In our theoretical and computational work we either focus on systems where the surface energy is independent of the strain, or we assume that the dependence is weak so that the Shuttleworth effect can be neglected. We therefore use the symbol γ to refer to both the surface energy and the the surface tension.

2.1.2. Equilibrium contact angle

Equipped with our knowledge about surface tension, let us begin with the most basic wetting scenario: a simple liquid deposited on a rigid solid in an ambient gas or vapor phase. From this very simple statement of the setting we infer the presence of three phases: liquid (l), solid (s), and vapor (v); by extension we have three interfaces: liquid-vapor (lv), solid-liquid (sl), and solid-vapor(sv) with surface tensions γ_{lv}, γ_{sl}, and γ_{sv} respectively. The equilibrium configuration is eventually decided through a competition of the surface tensions of all three interface. The typical setting is illustrated in 2.4 (a). As mentioned above, the surface tension results in unbalanced forces at lines cutting through interfaces. Here, the relevant line is the so-called three phase contact line (cl): the boundary of the contact area between the drop and the solid, and the meeting point of the three phases (red line in Figure 2.4 a). Assuming the solid is perfectly rigid, we only need to balance forces in the horizontal direction. The force per unit length f_{cl} acting on the three phase contact line is (see Figure 2.4 b)

$$f_{cl} = \gamma_{sv} - \gamma_{sl} - \gamma_{lv}\cos\theta. \tag{2.8}$$

At equilibrium the local force should be zero at every point and we get

$$\cos\theta_Y = \frac{\gamma_{sv} - \gamma_{sl}}{\gamma_{lv}}. \tag{2.9}$$

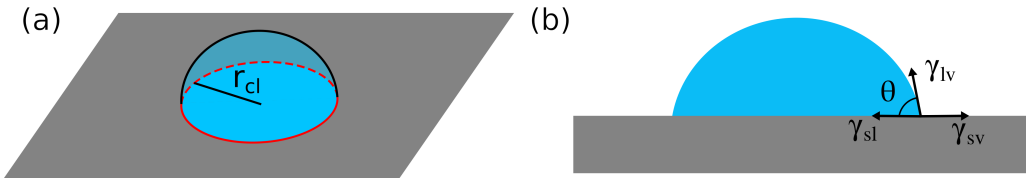

Figure 2.4.: (a) Cartoon of a drop on a rigid surface. Shown in red is the three phase contact line (b) Side view of the drop, showing the direction of the forces due to each surface tension. θ is the contact angle which is dictated by the balance of forces.

Eq. (2.9) is know as the Young-Dupré equation [47, 48], and θ_Y is known as the Young contact angle. The contact angle is the most fundamental measure which characterizes

the wetting state of a system. As can be seen from Eq. (2.9), not all combinations of surface tensions will result in allowed values for $\cos\theta$. One limit is $\cos\theta \leq 1$ leading to $\gamma_{sv} - \gamma_{sl} - \gamma_{lv} \leq 0$. When this is not satisfied the liquid will spread on the solid, wetting it completely. We therefore can define a spreading parameter S as

$$S = \gamma_{sv} - \gamma_{sl} - \gamma_{lv} \tag{2.10}$$

where if $S \geq 0$ the liquid wets or spreads on the surface, and if $S < 0$ the liquid will dewet from the surface and form puddles and drops.

2.1.3. Line tension

Line tension is a hypothesized tension of the three phase contact line, originally suggested by Gibbs [49]. The relevance of line tension in real life applications is heavily debated in literature, to the point where it is sometimes referred to as a myth [50], despite having a basis in thermodynamics [51, §8.6]. In addition, measurements of line tension yield different results regarding its effect: whether it promotes dewetting (positive line tension) [52] or promotes spreading (negative line tension) [53]. The line tension is allowed to have either sign since there is no thermodynamic ground for one sign or the other [54]. Measurements of the magnitude of line tension also vary majorly, with values between $10^{-11}\,N$ [55] and $10^{-5}\,N$ [56]. In the presence of line tension $\mathcal{T}$, the contact angle θ deviates from the Young contact angle θ_Y from Eq. (2.9) and becomes (see section A.1 for a derivation)

$$\cos\theta = \cos\theta_Y - \frac{\mathcal{T}/\gamma_{lv}}{r_{cl}} \tag{2.11}$$

where r_{cl} is the radius of the contact line (see Figure 2.4 a). $\mathcal{T}/\gamma_{lv}$ sets a length scale below which the effects of line tension become significant.

2.1.4. Contact angle hysteresis

So far we considered drops on idealized homogeneous surfaces where the contact angle can take its equilibrium value. However, in reality surfaces are rough or chemically heterogeneous, and the heterogeneity provides locations on the surface where the drop will want to stick. Such locations are known as pinning sites and result in real contact angles that deviate from the value predicted by the Young-Dupré equation. The extent by which pinning affects the wetting of a solid can be investigated experimentally with multiple methods. One such method is to inflate and deflate a drop that is sitting on a solid, and measure the contact angle during that process, shown schematically in Figure 2.5 (a). During inflation, it is observed that the contact line will remain stationary, and the contact angle increases until a particular angle is reached, then it starts moving. This angle is called the advancing contact angle θ_{adv}. During deflation, the contact line also

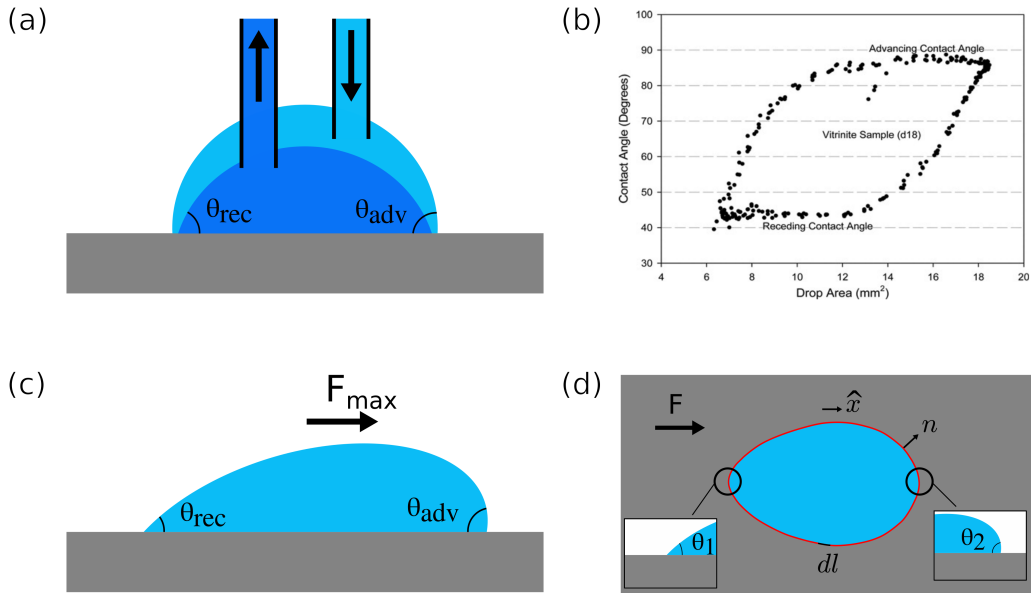

Figure 2.5.: (a) Cartoon of a drop being inflated (light blue), with the corresponding advancing contact angle θ_{adv} shown on the right hand side, and deflated (dark blue) with the corresponding receding contact angle θ_{rec} shown on the left hand side. (b) An example of a result from an inflation deflation experiment on a sample of vitrinite. Over multiple (clockwise) cycles the advancing contact angle averages at $\theta_{adv} = 88.5°$ and the receding contact angle at $\theta_{rec} = 42.9°$. Reproduced with permission from [57]. (c) Illustration of a drop under the effect of an external body force with magnitude equal to the maximum adhesion force F_{max}. Shown are the advancing and receding contact angles at the right and the left hand ends of the drop respectively. (d) Top view illustration of a drop under an external force $\mathbf{F}$ showing the deformation of the three phase contact line, along with the unit vector normal to the contact line $\mathbf{n}$, an infinitesimal length element dl, the unit vector $\hat{x}$, and the contact angles at the front and the back of the drop.

---

remains stationary and the contact angle decreases until a particular angle, the receding contact angle θ_{rec}, is reached [58]. When a drop is deposited on a heterogeneous surface, the contact angle will then take a value $\theta \in [\theta_{rec}, \theta_{adv}]$, and the hysteresis is quantified through the difference between the two limits: $\theta_{adv} - \theta_{rec}$. The value of the contact angle then depends on the manner by which the drop was deposited, and it can be said that we have "contact angle hysteresis". An example of a result from an inflation-deflation experiment is shown in Figure 2.5 (b). The measurements of the contact angle at the different stages of the experiment lie on a hysteresis curve, where we have two regions of constant values which correspond to the advancing and receding contact angles.

Contact angle hysteresis is a symptom of the lateral adhesion forces that a drop experiences on a heterogeneous substrate. If an external body force F_{ext} is applied to a

drop in the direction lateral to the surface, the drop will stay stationary until the force exceeds the maximum adhesion force F_{max} holding the drop in place. As the magnitude of the external force increases, the drop will deform while remaining stationary and the local contact angles around the contact line will change, until the angles at the front and the back of the drop reach the limiting values θ_{adv} and θ_{rec} respectively (see Figure 2.5 c) and the drop starts moving. For an external force of magnitude F the capillary adhesion force F_a can be related to contact angles through [59]

$$F_a = \oint \mathrm{d}l\, \gamma_{lv} \cos\theta_l\, \mathbf{n} \cdot \hat{x} \tag{2.12}$$

where the integral is carried out around the three phase contact line, $\mathbf{n}$ is a unit normal vector to the contact line, $\hat{x}$ is a unit vector pointing in the direction of the lateral force, and θ_l is the local contact angle. The integral can be approximated as [59–61]

$$F_a = \gamma_{lv}\, w\kappa\, (\cos\theta_1 - \cos\theta_2) \tag{2.13}$$

where w is the width of the drop, κ is a geometric factor that depends on the shape of the contact line with $\kappa = 1$ if the contact line is rectangular, and θ_1 and θ_2 are the contact angles at the back and the front of the drop respectively (see Figure 2.5 d). The maximum value for the adhesion force F_{max} is achieved for $\theta_1 = \theta_{rec}$ and $\theta_2 = \theta_{adv}$, and it is at this moment that the contact line depins and the drop starts moving.

2.1.5. Disjoining pressure

If a system is prepared by spreading a liquid thin film over a solid substrate, either the film is stable, or it is unstable, breaks, and dewets from the surface. What controls this is a physical quantity named disjoining pressure. Disjoining pressure is a pressure $\Pi(h)$ that appears between the two interfaces of a thin film, and depends on the distance h between those interfaces (see Figure 2.6 a). It may results from multiple physical origins [62, 63], such as dispersion (van der Waals) forces [64], electrostatic forces [65], or structural forces [66, 67]. For dispersion interactions, the disjoining pressure takes the form [64]

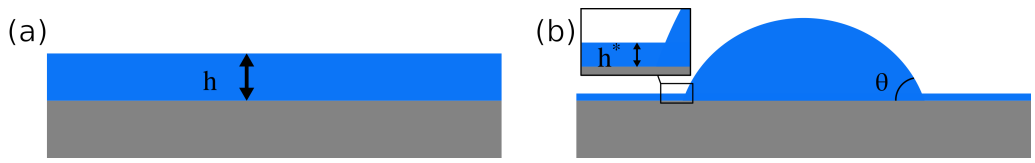

Figure 2.6.: (a) Cartoon of a thin film of thickness h. The value of the disjoining pressure depends on h and will control the stability of the film. (b) Cartoon of a configuration where a thin film of constant thickness is unstable. The system settles in a configuration with a drop forming a contact angle θ and a precursor film of thickness h^*, satisfying $\Pi(h^*) = 0$.

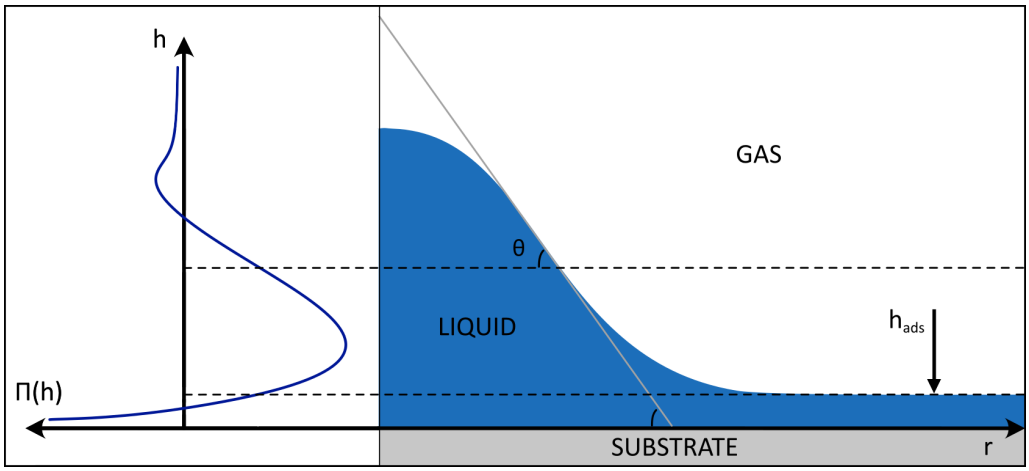

Figure 2.7.: Typical disjoining pressure curve for a nanodroplet with sketch of the resulting configuration. The thickness of the precursor film is at $h_{ads} \neq h^*$ due to the effect of the Laplace pressure. The contact angle is measured through the tangent at the inflection point of the shape. Adapted with permission from [68], copyrighted by the American Physical Society.

$$\Pi_d(h) = \frac{A_H}{6\pi h^3} \tag{2.14}$$

where A_H is known as the Hamaker constant whose value depends on the optical properties of the materials in the system. The contribution of electrostatic forces obtained from DLVO theory takes the form [65]

$$\Pi_e(h) = -A_e \exp\left(-h/\kappa\right) \tag{2.15}$$

where A_e depends on the dielectric properties of the liquid in the thin film and the surface potentials at the two interfaces, and κ is the Debye length. Finally, the structural forces originating for example from polar interactions [69, 70] are of the form [66, 67]

$$\Pi_s(h) = A_s \exp\left(-h/\lambda\right). \tag{2.16}$$

The sign of A_s depends on whether the structural forces are hydrophobic or hydrophilic, and λ is on the same order as the correlation length in the liquid.

The stability of a thin film depends on the total disjoining pressure $\Pi(h)$. The contribution from dispersion forces Eq. (2.14) is omnipresent and constitutes the main contribution to long range forces; however, it diverges when the thickness of the film vanishes. This is problematic when transitioning theoretically between macroscopic films and films of zero

thickness. It is typical to use a combination of Eq. (2.14) and Eq. (2.15) [68] or Eq. (2.16) [69, 70] which results in a disjoining pressure curve passing through 0 as shown in Figure 2.7. In such treatments only films of non-zero thickness can exist, and at a given uniform thickness, the film may be unstable. When the film is unstable, the system will end up in a configuration similar to that illustrated in Figure 2.6 (b). There, we have drop forming a contact angle θ and coexisting with a film of thickness h^* called the precursor film. The contact angle can be obtained through the Frumkin-Derjaguin equation [62]

$$\cos\theta = 1 + \frac{1}{\gamma_{lv}} \int_{h^*}^{\infty} \Pi(h')\mathrm{d}h' \tag{2.17}$$

where the thickness of the precursor film h^* is the thickness corresponding to $\Pi(h^*) = 0$. For very small nanodroplets, the Laplace pressure becomes significant and affects both the contact angle and the thickness of the precursor film [68]. A typical disjoining pressure curve with the resulting equilibrium configuration accounting for Laplace pressure is shown in Figure 2.7. Here, the thickness h_{ads} of the precursor film deviates from the thickness h^* at which $\Pi(h^*) = 0$ due to the effect of the Laplace pressure. The contact angle in this sketch is defined through the tangent at the inflection point of the shape of the drop.

The disjoining pressure, in addition, modifies the surface energy of a system. If we consider a solid with no film ($h \to 0$), the surface energy is γ_{sv}, while if the solid is covered with a film of macroscopic thickness ($h \to \infty$) the surface energy is the sum of the two available interfaces $\gamma_{lv} + \gamma_{sl}$. As the film thickness h varies between macroscopic $h \to \infty$ and microscopic $h \to 0$, the effective surface energy $\gamma_{eff}(h)$ varies like [65]

$$\gamma_{eff}(h) = \gamma_{sl} + \gamma_{lv} + \int_{h}^{\infty} \Pi(h')\mathrm{d}h' + \Pi(h)h. \tag{2.18}$$

From Eq. (2.18), it is evident that the disjoining pressure is related to the spreading parameter through

$$S = \gamma_{sv} - (\gamma_{sl} + \gamma_{lv}) = \int_{0}^{\infty} \Pi(h')\mathrm{d}h' \tag{2.19}$$

since we should recover $\gamma_{eff}(0) = \gamma_{sv}$. As mentioned above, the contribution of dispersion forces from Eq. (2.14) is present in most real-life treatments of the disjoining pressure. Therefore, the last term in Eq. (2.18) and the integral in Eq. (2.19) will diverge as the disjoining pressure itself diverges strongly for $h \to 0$. The divergence can be circumvented by integrating from a cut-off thickness h_c on the order of the range of hard-core repulsion between molecules [71]; the cut-off thickness h_c typically corresponds to the thickness of the precursor film $h_c = h^*$ with $\Pi(h^*) = 0$ [71]. In the case where the film dewets and a drop is formed the divergence can also be resolved by accounting for the dependence of the disjoining pressure on the gradients in thickness [72]. To the best of our knowledge, a full

treatment of disjoining pressure without a divergence for a flat film is absent. A qualitative description of the possible finite disjoining pressure curves and the corresponding wetting configurations can be found in Ref. 50 §4.1.4.

2.2. Static wetting on deformable surfaces

In the previous section we focused on wetting phenomena on rigid surfaces, both ideal and heterogeneous. In this section, we turn our attention to deformable surfaces. We start with drops on pure liquid surfaces, and make our way to wetting phenomena on elastic substrates.

2.2.1. Liquid lenses and the Neumann construction

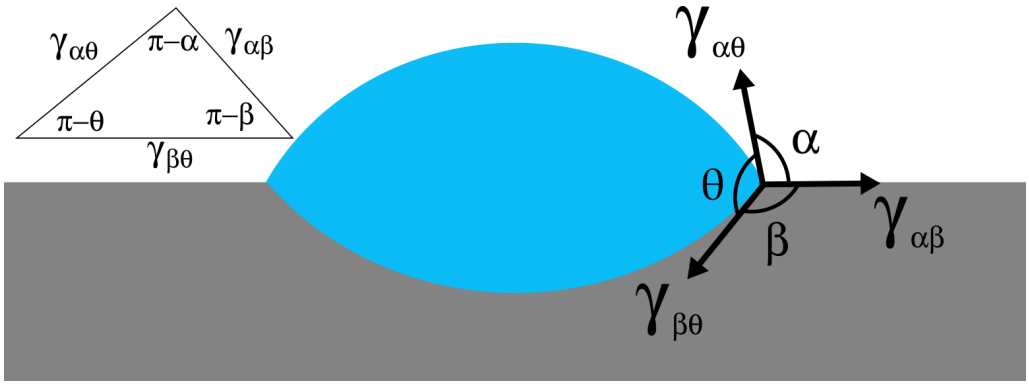

Figure 2.8.: Cartoon of a drop on a liquid surface. The configuration is that of a liquid lens, with three angle α, β, and θ at the three phase contact line. The angles are set by the balance of the three surface tensions between the three phases. Also shown is the corresponding Neumann triangle for this configuration.

When a drop is placed on the surface of an immiscible liquid on which it does not spread, the equilibrium configuration is that of a liquid lens illustrated in Figure 2.8. At the three phase contact line, the equilibrium is again dictated by the balance of forces. Now, however, the balance in the vertical direction is not possible without deforming the surface. We label the three fluid phases as α, β, and θ, which also corresponds to the angle in each phase. The surface tensions are labeled γ_{XY} for the tension at the interface between phases X and Y, with X, $Y \in \{\alpha, \beta, \theta\}$. The liquid surface is fully deformable and the equilibrium configuration is that of a liquid lens. Balancing forces (per unit length) in both the vertical and horizontal directions yields

$$\begin{aligned}\gamma_{\alpha\theta} + \gamma_{\beta\theta}\cos\theta + \gamma_{\alpha\beta}\cos\alpha &= 0\\ \gamma_{\alpha\theta}\cos\theta + \gamma_{\beta\theta} + \gamma_{\alpha\beta}\cos\beta &= 0\\ \gamma_{\alpha\theta}\cos\alpha + \gamma_{\beta\theta}\cos\beta + \gamma_{\alpha\beta} &= 0.\end{aligned} \tag{2.20}$$

The configuration satisfying the equations above is known as a Neumann configuration. Another way of identifying the angles in a Neumann configuration is through what is known as a Neumann triangle. One can construct a triangle whose side lengths are proportional to the surface tensions between the three phases as shown on the left side of Figure 2.8. The angles in the triangle can be mapped to the contact angles in the wetting configuration. We can see from this analogy that a Neumann configuration is only possible if the surface tensions satisfy a triangle inequality

$$\gamma_{XY} + \gamma_{YZ} \geq \gamma_{XZ} \tag{2.21}$$

with $X, Y, Z \in \{\alpha, \beta, \theta\}$. The inequality needs to be satisfied for all permutations of α, β, and θ. If the triangle inequality is broken, the equilibrium configuration is either one where the deposited liquid spreads on the surface, is engulfed by it, or fully detaches from it, depending on the spreading parameters.

In the case where a Neumann configuration is possible and in the absence of external forces, a liquid lens forms and the shapes of the interfaces are dictated by the Young-Laplace equation Eq. (2.5), with Eqs. (2.20) providing the boundary condition at the contact line. This means that the equilibrium configuration is one where every interface has a constant curvature, and the $\alpha - \beta$ interface remains flat all the way towards the contact line [73].

2.2.2. Elastic solids and wetting ridges

So far, we addressed the question of static wetting on either rigid surfaces or on liquids. Elastic solids fall somewhere in between the two extremes. When subjected to external forces or stresses, elastic solids, without flowing, react with a non-zero yet finite deformation. In reality, rigid solids are also elastic; however, the resulting deformation is so small that it can be neglected, and in the case of idealized solids it is assumed that there is no deformation.

The reaction of solids to different stresses is captured through constitutive relations. Constitutive relations relate the stress to the resulting deformation as quantified by the strain. In the linear deformation regime and for an isotropic body[2] the relation is [74, key]

[2]For non-isotropic bodies the moduli will depend on the direction of the strain, not only on whether it is a bulk or shear strain

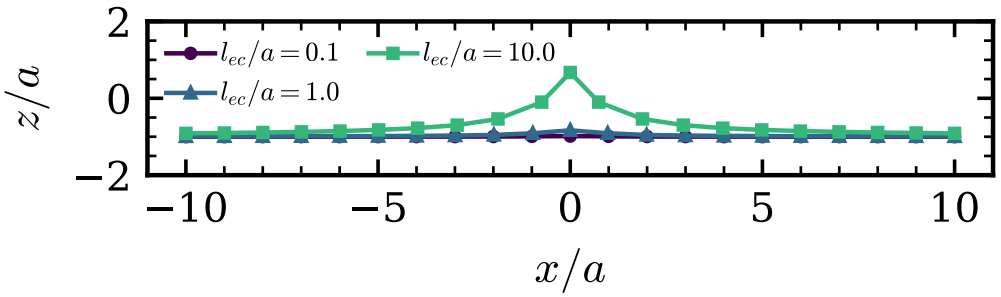

Figure 2.9.: The deformation of an elastic solid resulting from the application of a surface tension-like force at the origin $\mathbf{x} = \mathbf{0}$. The force is proportional to the liquid surface tension γ_{lv}, the contact angle is assumed to be $\theta_{eq} = 90°$, and the solid's shear modulus is G, resulting in an elastocapillary length $l_{ec} \equiv \gamma_{lv}/G$. a is a molecular length scale.

$$\sigma_{ij} = K u_{kk}\delta_{ij} + 2G\left(u_{ij} - \frac{1}{3}u_{kk}\delta_{ij}\right) \tag{2.22}$$

where K and G are the bulk modulus and shear modulus respectively, σ_{ij} is the stress tensor, and u_{ij} is the strain tensor (see Ref. 74 for definitions). The Einstein summation convention is applied in Eq. (2.22).[3] The diagonal elements of each tensor correspond to compressive stresses/strains, while the off diagonal elements correspond to shear stresses/strains.

When a drop is deposited on a solid, it exerts a stress on the surface of the substrate localized at the three phase contact line. For an equilibrium contact angle θ_{eq} from the horizontal, and a liquid vapor surface tension γ_{lv} the vertical force per unit length f_γ exerted on the solid at the three phase contact line is

$$f_\gamma = \gamma_{lv} \sin\theta_{eq}. \tag{2.23}$$

This force is equilibrated by the elastic force from the solid, resulting in its deformation. The extent of the deformation depends on the surface tension of the liquid, as well as the elastic properties of the solid. Considering the force to be concentrated on a point or a line, the deformation of the solid can be obtained as [74, 75]

$$u_i(\mathbf{x}) = \frac{\gamma_{lv}}{G} g_i(\mathbf{x}|\theta_{eq}) \tag{2.24}$$

where $i \in \{x, y, z\}$, and g_i is a function of position $\mathbf{x}$ that, given the contact angle θ_{eq}, sets the shape of the deformation in direction i. It is clear that the size of the deformation is set

[3] In the Einstein summation convention repeated indices are summed over: $u_{kk} \equiv \sum_k u_{kk}$

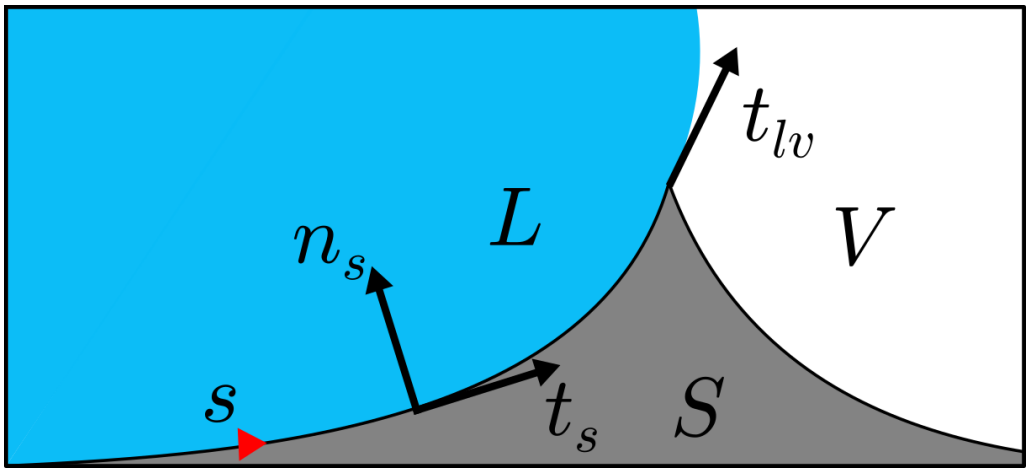

Figure 2.10.: Illustration of an elastic solid deformed by a drop.

by the length scale $l_{ec} \equiv \gamma_{lv}/G$, known as the elastocapillary length. The functions g_i are singular as one approaches the point where the force is applied, resulting in non-physical deformations.[4] If r is the distance from the point or line of force, the divergence is at least as strong as r^{-3} for a point force [74] and is logarithmic ($\sim \ln r$) for a line force [75]. In practice, the force is not applied to a mathematical point or line, but to a finite region that can be characterized by a molecular length scale a. Accounting for this molecular length scale both softens the singularity [76] and defines the regimes for the deformation of the solid. For $l_{ec} \ll a$ the solid is too rigid or the tension too small, and the deformation is negligible. For $l_{ec} \gg a$ the deformation is significant and a noticeable wetting ridge appears. Figure 2.9 shows the deformation of an elastic solid for a surface tension-like force applied at a point at the origin, with a contact angle $\theta_{eq} = 90°$, as calculated from the solution in §8 of Ref. 74. To avoid the singularity, the deformation is plotted for a layer originally a distance a below the surface of the solid, and it is shown for different values of the elastocapillary length l_{ec}.

A natural question that arises in the case of a liquid drop on an elastic solid is whether the Neumann balance (Eqs. 2.20) still applies at the contact line. Consider an elastic solid with a drop deposited on its surface. For simplicity we take a 2-dimensional slice of the solid along the x-z plane (see Figure 2.10). The positions of points on the surface can be traced with the parameterization $(x(s), z(s))$ where s is a curvilinear coordinate. The position of the contact line is at $s = s_{cl}$. The tangent to the solid surface is $\mathbf{t}_s$ and the tangent to the drop at the contact line is $\mathbf{t}_{lv}$. The surface stresses due to surface tension are directed along the aforementioned tangents. The normal to the solid is labeled $\mathbf{n_s}$. It can be shown that at the surface of the solid, the local stress balance takes the form [77]

[4] This appears in the linear elasticity treatment. Accounting for non-linear terms may remove the singularity

$$\sigma_{ij} n_{s,j} = \frac{\partial}{\partial s} \left[\gamma_s t_{s,i} \right] + \gamma_{lv} t_{\{lv\},i} \delta(s - s_{cl}) \tag{2.25}$$

where the left-hand side represents the contribution of bulk stresses to the surface, the first term on the right-hand side is a Laplace-pressure term, and the second term on the right-hand side is the stress caused by the drop, localized at the contact line through the Dirac delta function $\delta(s - s_{cl})$. Eq. (2.25) can be integrated over a small distance around the contact line (cl) $s \in [s_{cl}^-, s_{cl}^+]$

$$\begin{aligned} \int_{s_{cl}^-}^{s_{cl}^+} \mathrm{d}s \left[\sigma_{ij} n_{s,j} \right] &= \int_{s_{cl}^-}^{s_{cl}^+} \mathrm{d}s \left[\frac{\partial}{\partial s} \left[\gamma_s t_{s,i} \right] + \gamma_{lv} t_{\{lv\},i} \delta(s - s_{cl}) \right] \\ &= \gamma_s t_{s,i} \big|_{s=s_{cl}^+} - \gamma_s t_{s,i} \big|_{s=s_{cl}^-} + \gamma_{lv} t_{\{lv\},i} \\ &= \gamma_{sv} t_{\{sv\},i} + \gamma_{sl} t_{\{sl\},i} + \gamma_{lv} t_{\{lv\},i} \end{aligned} \tag{2.26}$$

where $\mathbf{t}_{sl}$ and $\mathbf{t}_{sv}$ are tangent to the solid surface at the contact line, directed towards the solid-liquid and the solid-vapor interfaces respectively. The right-hand side of Eq. (2.26) is the net force due to interfacial tensions at the three phase contact line. It is clear then that the Neumann balance is recovered if the left-hand side vanishes when we take the limit $|s_{cl}^- - s_{cl}^+| \to 0$. It can be shown that if the elastic solid at the contact line forms a sharp corner, $\sigma_{ij} n_{s,j}$ is only logarithmically singular [73] and the integral vanishes, recovering the Neumann balance of forces from Eq. (2.20).

2.2.2.1. Polymer gels as elastic coatings

Polymer gels are one type of material that exhibit elasticity. Polymer gels typically consist of polymer chains that are crosslinked, forming a network. When crosslinked and so that percolated gel forms, a flexible polymer like PDMS that is liquid at room temperature, will behave like a solid [78]. The elastic properties of the resulting solid can be controlled by varying the density of crosslinks, the length of the intermediate chains, the degree of swelling, as well as other means [79].

Though the elastic response of gels can take complicated forms, for wetting problems the deformations are small and the linear elasticity regime is valid. Then the energy of the gel is a quadratic function of the strain. The interest in PDMS gels for the context of wetting is typically as coatings on other materials [80]. When applied as a coating, the resulting layer is quite thin ($\mu\mathrm{m} - \mathrm{mm}$), such that one can assume uniform vertical strain. In such situations one can write the local elastic energy density f_{el} of the gel as a quadratic function of its thickness H (see Chapter 5 below)

$$f_{el} = \frac{1}{2} K \left(\frac{H}{H_0} \right)^2 \tag{2.27}$$

where H_0 is the reference thickness and K the bulk modulus.

2.2.2.2. Polymer brushes as elastic coatings

As mentioned in the introduction, another possible coating, and the main focus of this thesis, is polymer brushes. Polymer brushes consist of polymer chains that are grafted by one end to a substrate. As such, polymer brushes that are synthesized from flexible polymers retain their flexibility and in certain regards behave like a liquid. Following similar arguments as with polymer gels, one can write the elastic energy density of a polymer brush as a function of its thickness. For a brush in good solvent one can specialize to what is known as the Alexander-de Gennes brush [81, 82], where all the chains are assumed to extend to the same height H. The elastic energy per brush chain $f_{el,\mathrm{brush}}$ is in this case

$$f_{el,\mathrm{brush}} = \frac{3}{2} k_B T \left(\frac{H}{R_0} \right)^2 \tag{2.28}$$

where k_B is the Boltzmann constant, T is the temperature, and $R_0 = \sqrt{Nb^2}$ is the size of an ideal chain with N monomers of size b. This energy is nothing but the cost of stretching an ideal chain to an end-to-end distance H, which is a valid assumption since in the brush regime the chains are in a semi-dilute solution [81]. Even when the brush is in poor solvent, one can assume a quadratic dependence of $f_{el,\mathrm{brush}}$ on the thickness H, albeit with a different elastic constant than the one in Eq. (2.28) (see Chapter 4 below). If the brush occupies an area A at a grafting density σ, the total elastic energy within the brush is

$$\mathcal{F}_{el,\mathrm{brush}} = \sigma A f_{el,\mathrm{brush}}. \tag{2.29}$$

2.3. Static wetting on lubricated surfaces

While our descriptions above focused on substrates with only one type of material, it is possible to combine a solid or a polymer brush with a compatible liquid to create a hybrid surface with desirable properties. What is typically sought after is a surface with reduced friction, namely a lubricated surface. The equilibrium shape of drops on lubricated surfaces is dictated through the interplay of interactions between the drop, the lubricant, and the underlying substrate, be it a patterned surface, gel, or polymer brush. The lubricant typically is an oil with surface tension γ_o at the oil-vapor interface, and in the case of a gel or polymer brush, the oil is absorbed by the coating and swells it. An advantage of lubricated surfaces is that they reduce contact angle hysteresis (see section 2.1.4) [27] and dynamic friction forces experienced by moving drops [83].

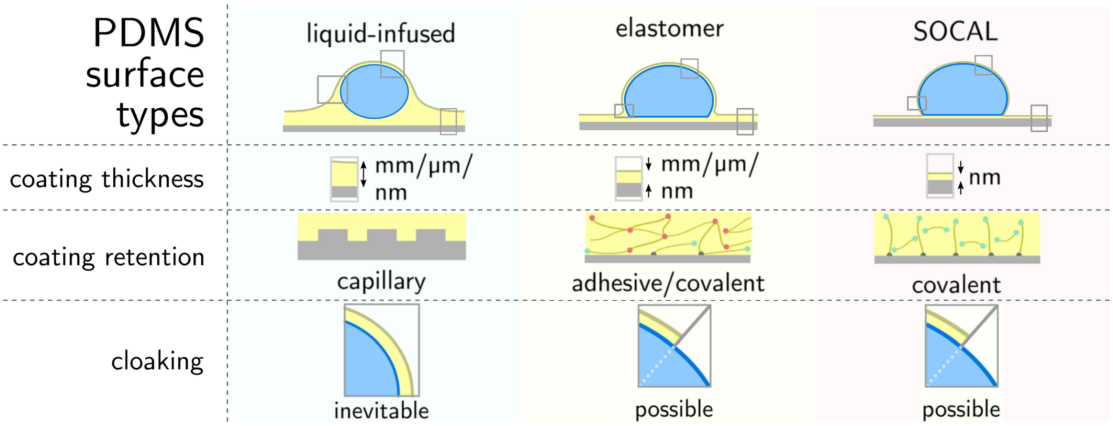

Figure 2.11.: Comparison of different PDMS surfaces. Designed by Lukas Hauer, adapted from [80] under CC BY 3.0.

2.3.1. Liquid wetting ridges

On LIS the lubricant layer is typically not thick enough for the drop to sink into it. Instead, the drop exercises the same kind of stress as described in section 2.2.2, leading to the formation of a purely liquid wetting ridge [83–85]. The contact angle at the three phase contact line is still expected to obey the Neumann configuration, except in the cases where the lubricant spreads on the drop, in which case the result is the cloaking of the drop.

2.3.2. Cloaking

In Eq. (2.10) we introduced the spreading parameter S for a liquid on a solid. One can introduce a similar parameter, $S_{o/w}$ for the spreading of oil on the liquid drop, which we will assume to be a water drop (w)

$$S_{o/w} = \gamma_w - \gamma_{ow} - \gamma_o. \tag{2.30}$$

where γ_w is the water-vapor surface tension, γ_o is the oil-vapor surface tension, and γ_{ow} is the oil-liquid surface tension. If the spreading parameter $S_{o/w}$ is positive, that means the oil likes to spread on the liquid of the drop. When dealing with an LIS this will always lead to the formation of an oil cloak on the surface of the drop [80]. For gels and polymer brushes with a positive $S_{o/w}$, the condition for cloak formation depends on the fraction of oil in the substrate and is the subject of study in Chapter 4. Such a cloaking layer can play a role in the durability of lubricated surfaces by contributing to the depletion of lubricant. In addition, the cloak might affects the static wetting properties as it changes the effective interfacial tension of the drop (see Eq. 2.18).

Cloaking on swollen gels and polymer brushes leads to the formation of a phase separated wetting ridge. The ridge consists then of a pure liquid part that coexists with the swollen gel/polymer brush. The size of the liquid phase in the ridge is another important factor when it comes to lubricant depletion, and the growth and size of this phase is the subject of Chapter 5.

Figure 2.11 summarizes the main differences between PDMS surface types as described so far.

2.4. Dynamics of moving drops

Wetting is not only relevant in the static situations. Often, in nature and applications, situations arise where the liquids are moving, such as in dip coating [86, 87], spin coating [88, 89], dewetting of films [90, 91], spreading of drops [92, 93] , and our particular topic of moving drops [94, 95]. One of the most relevant questions regarding moving drops is about the sources of dissipation and their contributions to the total friction experienced by a drop. Below we will present different predictions for the power dissipated as drops move. The dissipated power P_{diss} is presented as a function of velocity, either of the contact line v_{cl} or of the center of mass of the drop v_{cm}, as both are experimentally accessible.[5] We will attempt to give power law relations

$$P_{diss} \propto v^{\beta} \tag{2.31}$$

although as we will see below, this will not always be valid. We will replace the proportionality symbol $\propto$ with a similarity symbol $\sim$ when the relation is only valid asymptotically for large velocities. When possible, we aim to determine the exponent in Eq. (2.31) based on physical considerations.[6] The concepts discussed in this section will be most relevant for the interpretation of some results presented in Chapter 6.

2.4.1. Contact Line Dissipation

The majority of wetting dynamics will involve a moving three phase contact line. The topic has been studied extensively in the literature, and here we present the two dominant views for the dissipation at the contact line, and their contribution to friction. It is customary to quantify the forces acting on the three phase contact line through a dynamic contact angle θ_D which deviates from the equilibrium contact angle θ_E [100–102].[7] The motivation

[5] In most situations $v_{cl} = v_{cm}$ as the drop moves with constant shape. However, there are situations when this is not true, see for example stick-slip motion [96–99].

[6] In some of the cited references such relations are not given explicitly, but can be inferred for example from velocity versus force relations, or the dependence of dynamic contact angles on velocity.

[7] Some theories allow, during motion, for the coexistence of the "macroscopic" dynamic contact angle with a different "microscopic" contact angle by including a precursor film. It is common to assign the microscopic contact angle the same value as the equilibrium contact angle. See [101, 103] and section 2.4.1.1.

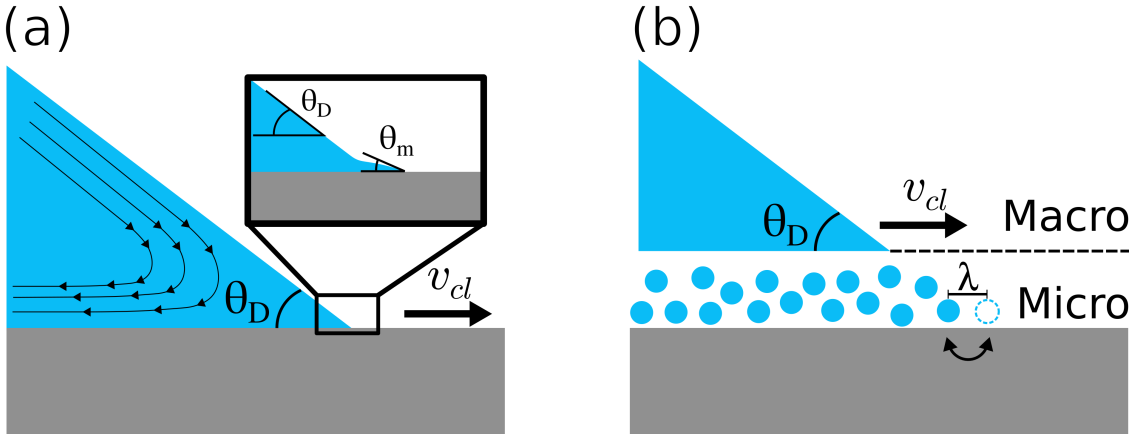

Figure 2.12.: Cartoons illustrating the two prevalent views for contact line dissipation. The contact line moves at a velocity v_{cl} and the macroscopic dynamic contact angle is θ_D. (a) Wedge dissipation where the source of dissipation is the viscous dissipation from the hydrodynamic flow in the contact line region. The inset is a close up of the contact line showing the microscopic contact angle θ_m (b) Molecular Kinetic Theory (MKT) view where the dissipation originates from the transition rates of molecules between the solid-liquid and solid-vapor interfaces, which occurs over a length scale λ.

---

behind this finds its origins in spreading dynamics, where the contact line is subject to a spreading force (per unit length) [100, 101, 104, 105]

$$f_s = \gamma\,(\cos\theta_E - \cos\theta_D) \tag{2.32}$$

where γ is the surface tension of the spreading liquid. If the contact line is moving at constant velocity and in the absence of other interactions, the friction force f_d acting on the contact line is then exactly equal to the spreading force [101]. Though the relation between f_d and θ_D originates in spreading dynamics, a similar relation applies to rolling drops [106]. Hence, one can quantify contact line dissipation by measuring the experimentally accessible dynamic contact angle. From that, one can then calculate the power dissipated in the motion of the contact line (cl) as

$$P^{cl}_{diss} = f_d \cdot v_{cl} \tag{2.33}$$

where v_{cl} is the contact line velocity. For brevity, in what follows we will refer to the results directly in terms of the power dissipated P^{cl}_{diss} not the dynamic contact angles. We give brief descriptions of the predicted relation between dissipation and contact line velocity in the following sections.

There are two prevalent views on the origin of contact line dissipation. The first is a hydrodynamic view which regards viscous dissipation as the dominant source. The viscous

dissipation takes place in a "wedge" adjacent to the actual contact line, this view is therefore referred to as wedge dissipation [101]. The other view ascribes the dissipation to dynamical processes and exchange rates related to the exchange of particles between phases as the contact line moves, and has been labeled Molecular Kinetic Theory (MKT) [105]. The two views are illustrated in Figure 2.12. Each of the two views was applied with varying success to explain various experimental results [105, 107]. There are other sources of dissipation that can be attributed to the motion of the three phase contact line such as viscous and viscoelastic dissipation in wetting ridges. However, we reserve the discussion of dissipation in wetting ridges for sections 2.4.4 and 2.4.5.

2.4.1.1. Wedge dissipation

For early researchers considering the hydrodynamic view, moving contact lines presented a paradox. The problem was to make sense of moving contact lines while maintaining the hydrodynamic no-slip boundary condition[8] at the solid-liquid interface [106]. Indeed, under simple considerations and maintaining the no-slip condition, the dissipative forces diverge logarithmically at the contact line [106, key]. As mentioned above, a lot of interest in contact line dissipation stems from the study of spreading liquids. During spreading, the dynamic contact angles are typically small. This leads to small variations in the height as one moves away from the contact line into the spreading liquid. Under such conditions, the power dissipated in the wedge can be approximated by [101, 108]

$$P_{diss}^{cl} = \frac{\eta}{\theta_D} v_{cl}^2 \ln\left(\frac{L_{max}}{L_{min}}\right) \tag{2.34}$$

where η is the viscosity of the liquid, θ_D is the dynamic contact angle, v_{cl} is the contact line velocity, and L_{max} and L_{min} are upper and lower cut-off lengths respectively. L_{max} can be taken to be related to the size of the drop. The divergence originates from taking the limit $L_{min} \to 0$. This can be circumvented by taking a finite non-zero value for L_{min}, dictated by for example a molecular slip length [101] or accounting for a precursor film of characteristic size L_{min} [109]. Another way to deal with the singularity is to solve the hydrodynamic problem allowing for slip from the start [110–112]. Allowing for slip, however, results in a flow profile where the contact line region is always composed of the same 'material' that is slipping on the solid. In addition, the dependence of the contact angle on velocity could not be recovered from such models, making them unattractive, although more recently progress was made to resolve this issue [112].

Assuming that the dynamic contact angle θ_D does not depend on the contact line velocity, Eq. (2.34) predicts

$$P_{diss}^{cl} \propto v_{cl}^2 \quad (\theta_D = cst). \tag{2.35}$$

[8] The no-slip boundary condition states that the velocity of the fluid and the solid at the interface are equal, so that the liquid does not slip on the solid.

Although Eq. (2.34) was derived under small angle considerations, the quadratic dependence of the power dissipated on velocity relation should still be valid for an arbitrary fixed angle $\theta_D < \frac{\pi}{2}$ [106]. However, following the Cox-Voinov theory [103, 109, key], the dynamic contact angle is expected to vary with velocity as

$$\theta_D \sim v_{cl}^{1/3} \tag{2.36}$$

which agrees well with experimental results [105, 113].Considering Eqs. (2.36) and (2.34), the relation for small dynamic contact angles is

$$P_{diss}^{cl} \sim v_{cl}^{5/3} \quad (\theta_D \sim v_{cl}^{1/3}). \tag{2.37}$$

For large dynamic contact angles, the power law dependence will be completely lost, although the Cox-Voinov relation $\theta_D \sim v_{cl}^{1/3}$ remains valid for $\theta_D \leq 3\pi/2$ [103]. One, therefore, needs to exercise caution when attempting to make predictions for the dissipation based on hydrodynamic considerations. For the types of systems we are interested in, namely drops rolling on surfaces with Young contact angles $\theta_Y > 90$, the small angle approximation is not valid. The relation is then not necessarily expected to follow a simple power law.

In the theories mentioned above, the introduction of the the small length scale L_{min} implies the existence of a "microscopic" contact angle θ_m that appears at those scales (see Figure 2.12). In some approaches the value of this angle is taken to be independent of velocity [103]. A more involved theory is by Shikhmurzaev [102, key]. There, the microscopic contact angle θ_m is allowed to vary through the implementation of interfacial thermodynamic considerations near the contact line. These considerations, in addition, eliminate the contact line singularity by effectively resulting in an apparent slip only in the contact line region, while away from the contact line the no-slip condition still applies. An (implicit) expression for the friction force is given, which takes a complicated form of the velocity, and does not resemble a power law.

2.4.1.2. Molecular kinetic theory (MKT)

The main idea in MKT is to view the phenomenon of moving contact lines as a molecular kinetic process, governed by transition rates that depend on energy barriers [100, key]. The transitions will correspond to displacements of gas molecules by liquid ones (spreading) or vice versa (dewetting). At equilibrium, the transition rates in either direction are equal, the contact line is stationary, and molecules transition back and forth at a characteristic rate κ^0. In out of equilibrium situations, the motion of the contact line is considered to be driven by an imbalance of interfacial forces, and subject to the force per unit length in Eq. (2.32). This force modifies the energy barriers, lowering one and raising the other. This in turn leads to an imbalance in the transition rates and then directional motion of

the contact line. the velocity of the contact line v can be related to the driving force per unit length f_s as [100, 105, 114]

$$v_{cl} = 2\kappa_0 \lambda \sinh\left(\frac{\lambda^2}{2k_B T} f_s\right) \tag{2.38}$$

where λ is a characteristic length for molecular motion in the vicinity of the contact line (see Figure 2.12). For a system at room temperature, $\lambda \approx 10^{-10}\,\mathrm{m}$, $k_B T \approx 10^{-21}\,\mathrm{Kg\,m^2\,s^{-2}}$, and assuming the liquid is water with a surface tension $\gamma \approx 72 \times 10^{-3}\,\mathrm{Kg\,s^{-2}}$ the force is $f_s \approx 10^{-3}$. This makes the argument of sinh in Eq. (2.38) very small, warranting the approximation

$$v_{cl} \approx \frac{\kappa_0 \lambda^3}{k_B T} f_s \quad \left(\frac{\lambda^2}{2k_B T} f_s \ll 1\right). \tag{2.39}$$

Eq. (2.39) takes the form of a drift velocity resulting from a force f_s and mobility $\mu = \frac{\kappa_0 \lambda^3}{k_B T}$. The friction force is, therefore, proportional to the contact line velocity, and the resulting dissipation from MKT is

$$P_{diss}^{cl} \propto v_{cl}^2 \tag{2.40}$$

2.4.2. Viscous dissipation in the bulk of the drop

For a viscous fluid with viscosity η, the energy dissipated in a volume $\mathrm{d}V$ due to shear dissipation is [116]

$$dP_{diss} = -\frac{1}{2}\eta \sum_{i,k} \left(\frac{\partial v_i}{\partial x_k} + \frac{\partial v_k}{\partial x_i}\right)^2 \mathrm{d}V \tag{2.41}$$

where $\mathbf{v}(\mathbf{x})$ is the velocity field in the fluid and $i, k \in \{x, y, z\}$. In particular situations it is safe to assume a constant shear rate within the drop as illustrated in Figure 2.13 (a). In this case, the power dissipated due to shear is found to be quadratic in the velocity v_{cm} of the center of mass

$$P_{diss}^{dr} \propto v_{cm}^2. \tag{2.42}$$

The assumption of constant shear rate is valid for drops at low velocities and in situations where one dimension is significantly smaller that the others [117]. However, for drops at larger velocities it may no longer be valid. Experiments of drops rolling on inclined surfaces [115] as well as numerical simulations [118, 119] show complex flow patterns that may invalidate the assumption of constant shear (See Figure 2.13 b). Despite this, it is

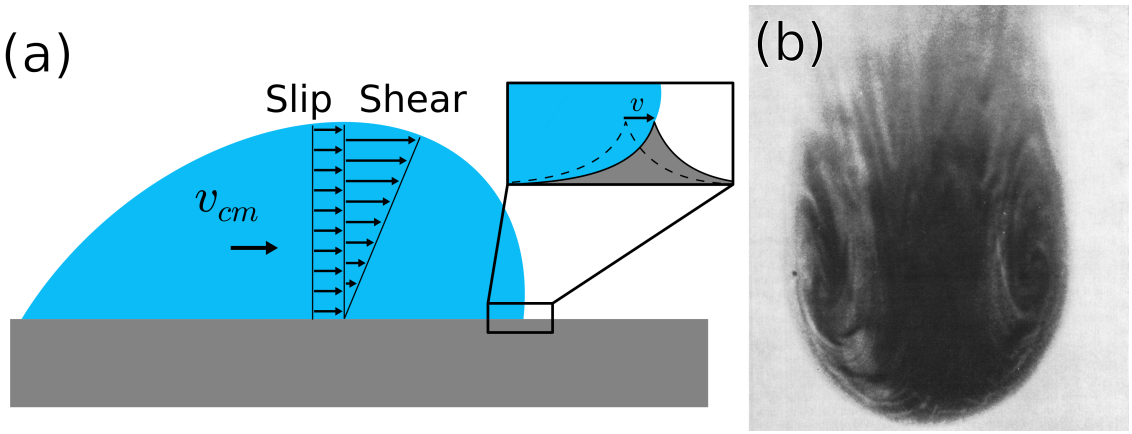

Figure 2.13.: (a) Cartoon illustrating a possible velocity profile for a drop with center-of-mass velocity v_{cm}. The profile can be divided into two components, a slip component and a shear component. The earlier contributes to dissipation through friction with the substrate, while the latter contributes through viscous dissipation. Inset shows a close up near the advancing contact line where the motion of the wetting ridge is shown. (b) Experimental picture showing a top view of a drop moving down an incline. The darker spots indicate the presence of dye which shows clear vortex formation, indicative of rolling motion. Reproduced with permission from [115].

found experimentally that when the dissipation in the drop dominates, the scaling in Eq. (2.42) is preserved [84, 85] (see section 2.4.4 below).

2.4.3. Dissipation due to slip at the interface

As mentioned above, it is customary when dealing with fluids to consider a no-slip boundary condition at solid-liquid interfaces (see footnote 8 on page 26). Although wildly successful, the no-slip boundary condition both leads to paradoxes in certain situations (see section 2.4.1.1) and is not always satisfied [117] (see Figure 2.13 a).

We consider a two-dimensional system consisting of a fluid in contact with a flat rigid solid and assign to it an orthogonal x-z coordinate system.[9] We define the z-direction to be normal to the interface, and place the solid interface at the $z = 0$ plane. The simplest way to account for slip at the interface, sometimes called Navier slip, is [120, 121]

$$\left.\frac{\partial v_x}{\partial z}\right|_{z=0} = \frac{1}{\delta_{slip}} v_x|_{z=0} \tag{2.43}$$

where δ_{slip} is called the slip length and v_x is the fluid velocity in the x-direction. $\delta_{slip} = 0$

[9] The results can be easily generalized to three dimensions by treating the y-direction in a similar fashion to how the x-direction is treated here.

corresponds to no slip, while $\delta_{slip} \to \infty$ corresponds to perfect slip. Now considering the rigid solid as stationary, we can use hydrodynamic considerations and linear-response theory to obtain the friction force dF_{slip} acting on an area $\mathrm{d}A$ at the interface [122]

$$dF_{slip} = \frac{\eta}{\delta_{slip}} v_{slip} \, \mathrm{d}A \tag{2.44}$$

where η is the viscosity of the fluid and $v_{slip} \equiv v_x|_{z=0}$ is the slip velocity. Assuming the contact area between the drop and substrate does not depend on velocity, the power dissipated due to slip is [117]

$$P_{diss}^{slip} \propto v_{slip}^2. \tag{2.45}$$

Comparing Eqs. (2.41) and (2.44) for the case of a finite drop, we see that the shear dissipation scales with the volume of the drop while the dissipation due to slip scales with the contact area. Therefore, as was pointed out by Servantie and Müller [117], when the slip velocity is proportional to the drop velocity, the contribution from slip will dominate for small drops, while the shear dissipation will dominate for large ones.

2.4.4. Viscous dissipation in liquid wetting ridges

Moving away from single component substrates, we consider lubricated surfaces. As mentioned above, drops deposited on lubricated substrates such as LIS are typically surrounded by a liquid wetting ridge. As the drop moves on the surface, the wetting ridge moves with the drop (see inset in Figure 2.13 a). This induces flow in the lubricant layer and ridge, which adds to the dissipation.

In typical situations, whether the dissipation in the liquid ridge is relevant depends on the ratio of viscosity between the drop and the lubricant. It was shown in experiment that for drops that are much more viscous than the lubricant, the dissipation in the drop dominates and the dissipated power follows [85]

$$P_{diss} \sim v_{cm}^2 \quad \text{(drop dominance)}. \tag{2.46}$$

However, if the lubricant is much more viscous than the drop, then the dissipation in the ridge dominates. To the best of our knowledge, there is no detailed model for the flow within liquid ridges. However, estimates can be made which fit experimental results reasonably well [83–85, 123]. As pointed out by Keiser et al. [85], the ridge at the advancing front can be regarded as a liquid spreading on the same liquid, and although a contact angle cannot be uniquely defined, the Cox-Voinov relation should be valid for a particular choice of the dynamic contact angle. The estimate is then based on similar arguments to those presented in section 2.4.1.1, and the dissipated power is expected to vary in a similar fashion to Eq. (2.34). At the receding end, the ridge is analogous to

a Landau-Levich-Derjaguin film pulled by the drop [124, 125, key] [126]. The height h_r and width l_r of the ridge are then related to the velocity through Landau-Levich scaling $h_r \propto v_{cl}^{2/3}$ and $l_r \propto v_{cl}^{1/3}$. Assuming constant shear rate in the small ridge, the the friction force per unit length in the receding ridge is then estimated to be $\sim v_{cl}^{2/3}$. At both the advancing front and the receding end we end up with the same dependence on velocity, and we have

$$P_{diss} \sim v_{cl}^{5/3} \quad \text{(ridge dominance)} \tag{2.47}$$

which was observed in both experiments [83, 84] and simulations [127] for drops on LIS. Simulations in addition reveal an equal contribution from both the advancing and receding sides. A transition from the above scaling was observed in experiments for drops traveling at faster velocities [85, 128].

2.4.5. Viscoelastic dissipation

For certain materials, the response to an applied stress or strain depends on the manner in which they are applied. A classic example is a mixture of starch and water. If the mixture is perturbed slowly it flows like a liquid, but under rapidly applied stresses it behaves as a solid. Such materials that under external perturbation respond partly as an elastic solid and partly as a viscous fluid are called viscoelastic materials [129, key, experimental][130, key, theoretical]. The materials we are interested in such as the PDMS gels and high viscosity silicone oils also exhibit viscoelastic behavior, and may contribute significantly to the dissipation.

2.4.5.1. Introduction to linear viscoelasticity

Viscoelastic materials are characterized by their response to varying types of stresses or strains. Similarly to the case of a purely elastic solid (see section 2.2.2), the relation between stress and strain in a viscoelastic material is captured through constitutive relations. However, differently from the case of purely elastic solids, the bulk and shear moduli for viscoelastic materials depend on the rate at which the strain is applied, and are therefore dependent on the history of the system. For small deformations, known as the linear viscoelasticity regime, a reasonable approach is to view the net strain at time t as the sum of a sequence of infinitesimal strains

$$u_{ij}(t) = \int_{-\infty}^{t} \mathrm{d}u_{ij}(t') = \int_{-\infty}^{t} \frac{\partial u_{ij}(t')}{\partial t'} \mathrm{d}t'. \tag{2.48}$$

The stress at time t can then be regarded as originating from the added effect of the infinitesimal strains, weighted based on how long in the past each strain is applied. Under

this assumption, a relation analogous to eq. (2.22) for isotropic materials can be obtained [129–131][10]

$$\sigma_{ij}(t) = \int_{-\infty}^{t} \mathrm{d}t' \left\{ K(t-t')\dot{u}_{kk}(t')\delta_{ij} + 2G(t-t') \left[\dot{u}_{ij}(t') - \frac{1}{3}\dot{u}_{kk}(t')\delta_{ij} \right] \right\} \tag{2.49}$$

where a dot signifies a time derivative, $\dot{u}_{ij}(t)$ are strain rates, and again we use the Einstein summation convention (see footnote 3 on page 19). $K(t)$ and $G(t)$ are known as the stress relaxation moduli for bulk and shear respectively; when determined $K(t)$ and $G(t)$ fully capture the viscoelastic properties of a material. As linear response functions, causality imposes that $K(t) = 0$ and $G(t) = 0$ for $t < 0$ [132]. Since most materials we are interested in are incompressible, the trace of the strain tensor vanishes $u_{kk} = 0$, and the viscoelastic properties are fully captured through the shear relaxation modulus $G(t)$. For the rest of the discussion we will focus on the incompressible material constitutive relation, along with its Fourier transform[11]

$$\sigma_{ij}(t) = 2\int_{-\infty}^{t} \mathrm{d}t'\, G(t-t')\, \dot{u}_{ij}(t') \tag{2.50}$$

$$\sigma_{ij}(\omega) = 2i\,\omega\, G(\omega)\, u_{ij}(\omega) \quad \text{(Fourier transform)} \tag{2.51}$$

where ω is a frequency, and to obtain the second relation the upper limit of integration in Eq. (2.50) was extended to ∞ and the convolution theorem was applied. The Fourier transform $G(\omega)$ of $G(t)$ is a complex function of frequency, and it is used to define the function $G^*(\omega)$

$$G^*(\omega) \equiv i\,\omega\, G(\omega) = G'(\omega) + iG''(\omega). \tag{2.52}$$

$G^*(\omega)$ is called the complex shear modulus, while $G'(\omega)$ and $G''(\omega)$ are named the storage modulus and loss modulus respectively. As a corollary of the causality condition stated above $G^*(\omega)$ obeys the Kramers-Kronig relations, which means that $G'(\omega)$ and $G''(\omega)$ form a Hilbert transform pair (see section 8.3.1 in Ref. 130). For a viscoelastic material that is periodically deformed at a frequency ω, the energy stored as elastic energy is proportional to $G'(\omega)$, while the dissipated energy is proportional to $G''(\omega)$ [130]. Typically, when $G'(\omega) < G''(\omega)$ the material behaves more like a liquid referred to as a viscoelastic liquid, while if the opposite is true it behaves more like a solid referred to as a viscoelastic solid.

[10] In some references the strain tensor is defined as larger by a factor of 2 than the convention we are following. This leads Eq. (2.49) to be defined with a factor of $\frac{1}{2}$ as in Ref. 129 for example.

[11] We will keep track of the Fourier transforms of functions $f(t)$ by explicitly showing that they are functions of the frequency $f(\omega)$

2.4.5.2. Viscoelastic braking

Experiments on the rheology of PDMS gels [98, 133, 134] reveal that the loss modulus $G''(\omega)$ obeys a power law for a wide range of frequencies ω

$$G''(\omega) \sim \omega^n \tag{2.53}$$

where n is an exponent that depends on the viscoelastic properties of the material, but is found to take values between 1/2 and 2/3 [135]. In fact, the power law is expected to be exact and valid at all frequencies for gels at the gel point [133–136].

For drops moving on a viscoelastic solid such as a PDMS gel, the solid will be pulled up at the three phase contact line as described in section 2.2.2. In dynamic situations, however, the ridge will be carried by the contact line, deforming material ahead of it, and allowing material behind to relax (see inset in Figure 2.13 a). This time dependent deformation leads to energy losses through the dissipative channels of the material. This ultimately slows the motion of the drop, a phenomenon known as viscoelastic braking. The total power injected into the material in a volume $\mathrm{d}V$ is [130, ch. 9]

$$\mathrm{d}P = \sigma_{ij}\, \dot{u}_{ij} \mathrm{d}V. \tag{2.54}$$

The total power injected has contributions from both elasticity and dissipation, proportional to $G'(\omega)$ and $G''(\omega)$ respectively. Therefore, we can write for the dissipated power

$$\mathrm{d}P_{diss} \sim G''(\omega_r)\, \dot{u}_{ij} \mathrm{d}V \tag{2.55}$$

where ω_r is the typical excitation frequency of the ridge as the contact line moves. If the ridge has a characteristic length l and is moving with velocity v, the excitation frequency ω_r can be estimated as

$$\omega_r \approx \frac{v}{l} \tag{2.56}$$

while strain rate can be approximated as

$$\dot{u}_{ij} \sim \omega_r. \tag{2.57}$$

Using these approximations in Eq. (2.55) and using Eq. (2.53) we get

$$P_{diss} \sim \omega_r^{n+1} \sim v^{n+1}. \tag{2.58}$$

2.4.6. Summary of dynamics

As drops move over surfaces, their dynamics can be affected by a multitude of dissipative forces. Since the velocity of the drop is a quantity that is relatively easily obtainable in experiments, it is valuable to find relations between the dissipated power and velocity. Such relations can offer insights into the dominant sources of friction, and guide the design of surfaces with desirable properties.

Going over the prevalent theories for dissipation, we attempted to write the relation between the power dissipated P_{diss} and the velocity v

$$P_{diss} \sim v^{\beta}. \tag{2.59}$$

Depending on the situation, v is either the velocity of the contact line or of the center of mass of the drop. We list here the different theoretical considerations along with the prediction for the exponent β:

- Hydrodynamic wedge dissipation with constant dynamic contact angle $\theta_D < \frac{\pi}{2}$ [106] (see section 2.4.1.1 Eq. 2.35):

$$\beta = 2$$

- Hydrodynamic wedge dissipation with variable and small dynamic contact angle $\theta_D \propto v^{1/3}$ [103, 109] (see section 2.4.1.1 Eq. 2.37):

$$\beta = 5/3$$

- Hydrodynamic wedge dissipation with variable and large dynamic contact angle [103, 109] (see section 2.4.1.1):

no power law

- Hydrodynamic wedge dissipation with variable dynamic and microscopic contact angles [102] (see section 2.4.1.1):

no power law

- Molecular Kinetic Theory (MKT) [100] (see section 2.4.1.2 Eq. 2.40):

$$\beta = 2$$

- Bulk viscosity in the drop with constant shear [117] (see section 2.4.2 Eq. 2.42):

$$\beta = 2$$

- Dissipation due to slip at the contact area [117] (see section 2.4.3 Eq. 2.45):

$$\beta = 2$$

- Dissipation in liquid wetting ridges [85] (see section 2.4.4 Eq. 2.47):

$$\beta = 5/3$$

- Viscoelastic braking on a medium with $G''(w) \sim w^n$ (see section 2.4.5.2 Eq. 2.58):

$$\beta = n.$$

As the list shows, caution is required when making conclusions on the sources of dissipation in dynamic wetting. A power law is not always present, and when it is, multiple sources could result with the same exponent, making it difficult to single out the dominant source of dissipation.

2.5. Polymer physics

2.5.1. Polymer science basics

Polymers are (macro)molecules composed of multiple sub-units covalently attached to each other, with the sub-units referred to as monomers. Based on composition we can differentiate between homopolymers where the sub-units are all the same, and heteropolymers where at least one sub-unit differs from the rest. Our material of interest PDMS where the monomer is dimethylsiloxane with the chemical formula $Si(CH_3)_2O$ is an example of a homopolymer, while proteins for example are heteropolymers. The number of monomers in a polymer is called the degree of polymerization N. In our work we are mainly interested in linear homopolymers and will focus on their properties. For an overview of the classes of polymers see Ref. 137 Ch. 1.

At the theoretical level, it is common to treat polymers as chains of connected units, and to deal with the chemical details of the underlying polymers implicitly. The state of a linear polymer chain can be quantified through its size. A measure of the size of a polymer chain is the mean end-to-end distance R_{ee} defined as

$$\left\langle R_{ee}^2 \right\rangle = \sum_{i=1}^{N-1} \left\langle \left(\mathbf{r}_{i+1} - \mathbf{r}_i\right)^2 \right\rangle \tag{2.60}$$

where $\mathbf{r}_i$ is the coordinate of the i-th monomer, N is the degree of polymerization and the angle brackets denote an average over the conformations of the chain at thermal equilibrium. Another quantity that quantifies the size of a chain is the gyration radius R_g defined as

$$\left\langle R_g^2 \right\rangle = \frac{1}{N} \sum_{i=1}^{N} \left\langle (\mathbf{r}_i - \mathbf{r}_{cm})^2 \right\rangle \tag{2.61}$$

where r_{cm} is the position of the center of mass of the chain. The radius of gyration is sometimes a more suitable measure of the size of a polymer, in particular when the polymer is not linear. The size of a polymer chain is dictated by the interaction between the monomers themselves and between the monomers and the surrounding medium which is named the solvent. One can distinguish many types of interactions, of which we summarize a select few.

We begin with bond interactions, which occur between pairs of consecutive monomers on the chain. The bonds between consecutive monomers are typically covalent bonds, and they keep the chain together and dictate its topology [137, Ch. 1].

Furthermore, one can consider interactions that contribute to the stiffness of the chain. The most common interactions of this type are bending stiffness which sets the average bond angle between three consecutive monomers (3-body interactions), and dihedral (torsion) interactions which control the dihedral (torsion) angle formed by four consecutive monomers (4-body interactions).[12] Stiffness interactions introduce correlations between the orientations of bonds along the chain, generally leading to larger sizes for a stiff chain than for a chain with no correlations. The characteristic length scale over which the correlations decay is called the persistence length l_p. A chain where all stiffness interactions are absent is called a freely jointed chain.

Additionally, monomer can interact through non-bonded interactions that depend on the energetic cost of bringing two monomers close to each other in the average background of other monomers and solvent; they therefore capture the specifics of monomer-monomer, solvent-solvent, and monomer-solvent interactions into one effective interaction. The combined effect is quantified through a parameter v. Despite situation where the parameter v can be negative, it is colloquially referred to as excluded volume; therefore, we will call such interactions "excluded volume interactions". Certain interaction, such as electrostatic interactions, are usually dealt with separately and not included in the contribution to excluded volume interactions. The interactions contributing to excluded volume effects are typically short-ranged and include, for example, London dispersion forces and steric repulsion, among others. The steric repulsion between monomers sets the hard core diameter of the monomers. Other contributions to v lead to an excluded volume different from the hard core volume of a monomer. In the case of a poor solvent the monomers prefer to interact among one another leading to attractive excluded volume interactions ($v < 0$) and the collapse of the chain; in the case of a good solvent the monomers prefer to interact with the solvent molecules leading to repulsive excluded volume interactions

[12] Every three consecutive monomers (two bonds) that are not co-linear define a plane that includes all three. The dihedral (torsion) angle is the angle between the two planes defined by consecutive sets of three monomers. The two sets share two monomers for a total of four consecutive monomers per dihedral angle.

($v > 0$) and the swelling of the chain. The excluded volume parameter v can be related to the mean-field parameter χ commonly known as the Flory-Huggins interaction parameter (see section 4.2 in Ref. 137). The value of the Flory-Huggins interaction parameter typically depends on the temperature T; a solvent where χ is independent of temperature is said to be an athermal solvent, and the excluded volume for an athermal solvent coincides with the hard core volume of a monomer [137, §3.1.1]. In addition to excluded volume interactions, which are 2-body interactions, there may be many-body interactions. Many-body interactions are crucial to stabilize chains against unphysical collapse in poor solvents [137, §3.3.2.2]. If excluded volume and many-body interactions are absent, we say the chain is an ideal chain, while we call it a real chain when they are present.

While interactions we describe do not exhaust all the possible interactions that can be present, such as electrostatic and depletion interactions, we do not discuss further types of interactions here as they are not relevant for our system.

2.5.2. Self-similarity and scaling

A key property of long polymer chains is their self-similarity, the observation that the chain looks similar at small and large length scales, or that smaller segments of the chain look similar to the entire chain if magnified.[13] Here, similar refers to the average statistical properties such as the size, as the smaller segment will not look exactly the same as the entire chain. Another way of stating the self-similarity property of polymer chains is by saying that the sizes of different segments of a chain, composed of different numbers of monomers, can be mapped to one another by appropriate rescaling, i.e. the size of segments of a chain are scale invariant. Therefore, the self-similarity of polymer chains suggests that the size obeys a scaling law

$$R_{ee} \equiv \sqrt{\langle R_{ee}^2 \rangle} \propto aN^{\nu} \tag{2.62}$$

where N is the degree of polymerization and a is a statistical segment length. Though presented in terms of the end-to-end distance, the same scaling is obeyed by the radius of gyration R_g. The exponent ν can take different values depending on the interactions between monomers. For a freely jointed ideal chain ($v = 0$), the chain conformations correspond to a random walk with step size a and the exponent takes the value [137, §2.2]

$$\nu = 1/2 \quad \text{(ideal chain)}. \tag{2.63}$$

For real chains, the solvent quality is related to the value of the interaction parameter χ as follows[14]:

1. Poor solvent: $\chi > \frac{1}{2}$

[13] This is only true at scales larger much larger than the size of a monomer, and smaller than the size of the entire chain.

[14] For an overview of solvent quality and phase behavior see Ch. 5 in in Ref. 137, in particular Figure 5.1.

2. θ solvent: $\chi = \frac{1}{2}$
3. Good solvent: $\chi < \frac{1}{2}$

For a real chain in a good solvent, the conformations correspond to a self-avoiding walk with the (mean-field) exponent [137, §3.1.2]

$$\nu = 3/5 \quad \text{(real chain, good solvent)}. \tag{2.64}$$

Numerical calculations of the exponent in a good solvent give $\nu \approx 0.588$ [138]. For a real chain in a poor solvent, the chain is collapsed and the exponent can be found to be [137, §3.3.2]

$$\nu = 1/3 \quad \text{(real chain, poor solvent)}. \tag{2.65}$$

One can transition between the above scaling exponents by changing the solvent quality. It is common that at low temperatures solvents are poor, and they are good solvents at higher temperatures. As one transitions between the poor and an good solvent regimes for real chains, there is a temperature where the chains have the same scaling as ideal chains

$$\nu = 1/2 \quad \text{(real chain, } \theta \text{ solvent)}. \tag{2.66}$$

The temperature where this scaling is valid is called the θ temperature, and the solvent is called a θ solvent and the excluded volume $v = 0$.

2.5.2.1. Scaling in polymer solutions and blends

While above we were focusing on the properties of single chains, we rarely deal with single chains in practice. It is more common to encounter mixtures where multiple polymer chains co-exist with other polymer species or a non-polymer solvent. For polymers in a non-polymer solvent, we call the mixture a polymer solution. The type of solution varies depending on the solvent quality as well as the concentration of polymers c_p or the corresponding volume fraction φ_p. The polymer volume fraction is defined as the ratio of the volume occupied by the polymers V_p to the total volume occupied by the solution

$$\varphi_p = \frac{V_p}{V_s + V_p} \tag{2.67}$$

where V_s is the volume occupied by the solvent. The fraction of solvent φ can be defined as the complement of φ_p such that $\varphi_p = 1 - \varphi$. In a good solvent we distinguish three regimes depending on the fraction of polymers φ_p [137, §5.3.1]:

1. The dilute regime $\varphi_p < \varphi_p^*$ where the chains behave as single chains in solution and obey the scaling of real chains in a good solvent.

2. The semidilute regime achieved when $\varphi_p^* \leq \varphi_p < \varphi_p^{**}$ where at large scales the inter-chain interactions screen the intra-chain interactions resulting in ideal chain-like scaling for long chains (see Figure 5.5 in Ref. 137).

3. The concentrated or melt regime achieved when $\varphi_p \geq \varphi_p^{**}$ where the chains have ideal chain-like scaling at all length scales [139, §II.1].

The lower limit for semidilute solution φ_p^* depends on the excluded volume interactions as well as the length of the polymer chain [137, §5.3.1]

$$\varphi_p^* \approx \left(\frac{a^3}{v}\right)^{6\nu-3} N^{1-3\nu} \tag{2.68}$$

while the upper limit for semidilute solution φ_p^{**} is independent of the chain length

$$\varphi_p^{**} \approx \frac{v}{a^3}. \tag{2.69}$$

Despite certain studies showing that in the melt regime ($\varphi_p \geq \varphi_p^{**}$) the behavior deviates from ideal behavior [140, 141], it remains a good first approximation for most applications. When the polymers are in a poor solvent, and if the interaction parameter is above a critical value χ_c (temperature is below a critical temperature T_c), we also distinguish three regimes depending on the polymer fraction φ_p:

1. The dilute regime $\varphi_p < \varphi_p^{'}$ where the chains behave as single chains in solution and obey the scaling of real chains in a poor solvent.

2. The phase separated regime $\varphi_p^{'} \leq \varphi_p < \varphi_p^{''}$ where the solution is demixed into a polymer rich phase and a polymer poor phase. The polymer rich phase, sometimes called the dense phase, has a polymer fraction equal to $\varphi_p^{''}$. The chains in the dense phase behave like chains in a melt and obey an ideal chain-like scaling due to the screening of the self-interaction of the chains [139, §II.1]. The polymer poor phase, sometimes called the dilute phase, has a polymer fraction equal to $\varphi_p^{'}$. The chains in the dilute phase behave like chains in a dilute solution and obey the scaling of real chains in a poor solvent.

3. The concentrated or melt regime $\varphi_p \geq \varphi_p^{''}$ where the chains obey an ideal chain-like scaling due to the screening of the self-interaction of the chains [139, §II.1].

The phase separated regime does not always exist for a poor solvent. For phase separation to be possible for a polymer in a simple (non-polymer) solvent, the interaction parameter χ needs to be larger than a critical value

$$\chi_c = (\frac{1}{2} + \frac{1}{\sqrt{N}} + \frac{1}{2N}) \tag{2.70}$$

where N is the degree of polymerization of the polymer chains. For very long chains $N \to \infty$, the critical interaction parameter χ_c coincides with the θ parameter χ_θ

$$\chi_c \approx \chi_\theta = \frac{1}{2} \quad \text{for } N \to \infty. \tag{2.71}$$

When multiple polymer species are mixed, the mixture is called a polymer blend. A binary blend is a polymer blend with only two species of polymers. A special type of binary blend is one where the two species A and B differ in the degree of polymerization $N_A \neq N_B$, but are otherwise the same. Since the species are the same the Flory-Huggins interaction parameter vanishes $\chi = 0$. In such a blend the scaling laws depend on the degrees of polymerization of each species. Considering the A chains, we have for the scaling of the end-to-end distance $R_{ee}^A \sim N^{\nu_A}$ [137, §4.5.2]

$$\nu_A = 1/2 \quad \text{for } N_A < N_B^2 \tag{2.72}$$

$$\nu_A = 3/5 \quad \text{for } N_A > N_B^2. \tag{2.73}$$

The second equation indicates that a melt of short chains acts as a good (athermal) solvent when mixed with much longer chains of the same species.

2.5.3. Polymer brushes

A polymer brush consists of polymer chains grafted by one end to a surface. In particular, a collection of grafted chains is said to form a brush when the typical distance between the grafting sites d is smaller than the size of a chain R_g [142]. When all the grafted chains have the same degree of polymerization N the brush is said to be monodisperse, while if the degree of polymerization varies between chains it is called a polydisperse brush. Instead of the distance between grafting sites d, it is customary to describe a polymer brush through the grafting density σ

$$\sigma = \frac{1}{d^2}. \tag{2.74}$$

For small grafting densities, the chains are far apart and do not interact with each other, and they are said to be in the mushroom regime. For large grafting densities the chains do interact and they are said to be in the brush regime. The crossover between the two regimes occurs when the typical distance between the chains in on the order of the radius of gyration of a single chain R_g, which for a monodisperse brush occurs at a grafting density [142]

$$\sigma^* \sim N^{-2\nu}. \tag{2.75}$$

However, for a brush in a poor solvent at intermediate grafting densities $\sigma > \sigma^*$, the grafted chains will aggregate into localized clusters leading to a rough polymer brush (see Figure 3.2 a) [143, 144]. For larger grafting densities $\sigma > \sigma^{**}$ the brush will be smooth again [144], though will remain in a collapsed state. In this collapsed state the fraction of grafted chains is uniform in the brush and the brush is similar to a polymer melt at the coexistence concentration φ''.

If we assume the solvent is uniformly distributed across the brush, known as the Alexander-de Gennes brush picture [81, 82], the free energy per particle for the polymer brush and solvent can be written as [145]

$$\mathcal{F}_B = \frac{\varphi}{N_s} \ln \varphi + \chi\varphi(1-\varphi) + \frac{(1-\varphi)}{N_B} \frac{K}{2} \frac{H^2}{N_B a^2} \tag{2.76}$$

where φ is the fraction of solvent, N_s is the degree of polymerization of the solvent, χ is the Flory-Huggins interaction parameter, K is a prefactor that captures the elasticity of the brush, H is the thickness of the brush, N_B is the degree of polymerization of the grafted chains, and a is the size of a monomer of a grafted chain. The first term is the contribution of the translational entropy of the solvent molecules. The grafted chains do not contribute any translational entropy, as they are grafted. The second term is the contribution of the interaction between the solvent and the grafted chains. Finally, the last term is the energy associated with the stretching elasticity of the brush; it takes the form of the (ideal chain) entropic contribution of stretching a grafted chain to a height H, with the prefactor K accounting for any deviations from the exact results for ideal chains. The thickness of the brush H is constrained by the solvent fraction as

$$H = \frac{N_B a^3 \sigma}{1-\varphi}. \tag{2.77}$$

In the following we will assume that $N_B \gg N_s$. In the presence of an excess of solvent, the equilibrium condition is the equality of chemical potentials of the solvent in the reservoir μ_s and the chemical potential in the brush μ_B, which in turn sets the fraction of solvent in the brush. For good and θ solvents, one can use virial expansions for $1-\varphi \ll 1$ to find the a relation of the thickness of the brush H with the grafting density σ, the degree of polymerization of the grafted chains N_B, and the interaction parameter χ

$$H \sim N_B \sigma^{1/3} \left(\frac{1}{2} - \chi\right)^{1/3} \qquad \left(\text{good solvent } \chi < \frac{1}{2}\right) \tag{2.78}$$

$$H \sim N_B \sigma^{1/2} \qquad \left(\theta \text{ solvent } \chi = \frac{1}{2}\right). \tag{2.79}$$

For the case of a poor solvent with $\sigma > \sigma^{**}$, the brush collapses into a melt-like state with uniform fraction φ_B'' [144]; the fraction φ_B'' corresponds to the coexistence value in

the polymer rich phase. The solvent fraction in the brush is set through $\varphi = 1 - \varphi_B''$ and we have by Eq. (2.77)

$$H = \frac{N_B \sigma}{\varphi_B''}. \tag{2.80}$$

Far from the critical point, the fraction φ_B'' is related to the interaction parameter through $\varphi_B'' \sim \chi - 1/2$ [137, §5.2] which allows us to write

$$H \sim N_B \sigma \left(\chi - \frac{1}{2}\right)^{-1} \left(\text{poor solvent } \chi > \frac{1}{2}\right). \tag{2.81}$$

2.5.3.1. The parabolic profile for a brush

When writing the brush free energy in Eq. (2.76) we assumed that the density distribution of both grafted chains and solvent is uniform. A more accurate approach based on Strong Stretching Theory (SST) [146][147, key] reveals that this is not the case [148, key]. The partition function Q of a polymer chain can be written as

$$Q \propto \sum_{\{\mathbf{r}_\alpha\}} \exp\left(\frac{-E[\mathbf{r}_\alpha]}{k_B T}\right) \tag{2.82}$$

where $\mathbf{r}_\alpha$ is the configuration of the chain describing the positions of its monomers, $E[\mathbf{r}_\alpha]$ is the energy of a particular configuration of the chain, and the sum is executed over all possible configurations $\{\mathbf{r}_\alpha\}$. The subscript α will be used to refer to different chains when multiple are present. The energy typically includes a term due to the elasticity of the chain, as well as a contribution from a field $w(\mathbf{r}_\alpha)$ external to the chain

$$\frac{E[\mathbf{r}_\alpha]}{k_B T} = \int_0^{N_\alpha} \mathrm{d}n \, \left\{ \frac{3}{2a^2 N_\alpha} \left| \frac{\mathrm{d}\mathbf{r}_\alpha(n)}{\mathrm{d}n} \right|^2 + w(\mathbf{r}_\alpha(n)) \right\} \tag{2.83}$$

where a is the size of a monomer, N_α is the number of monomers of the chain, $\mathbf{r}_\alpha(n)$ is the position of the n^{th} monomer of the chain, and the sum over monomers was replaced by an integral since we assume $N_\alpha \gg 1$. The first term in the integrand is the contribution of the chain elasticity. When the strength of the external field is much larger than the thermal energy $k_B T$, only configurations with low energy will contribute significantly to the partition function since the contribution of higher energy states is exponentially smaller [147]. SST corresponds to the situation where the partition function is dominated by configurations with the lowest energy

$$Q = \sum_{\{\mathbf{r}_\alpha\}} \exp\left(\frac{-E[\mathbf{r}_\alpha]}{k_B T}\right) \approx \exp\left(\frac{-E_{\min}[\mathbf{r}_\alpha]}{k_B T}\right) \tag{2.84}$$

where $E_{\min}[\{\mathbf{r}_\alpha\}]$ is the minimum of the energy. Therefore, under the assumptions of SST one needs to find the configurations that minimize the energy. Since $E[\mathbf{r}_\alpha]$ is a functional of the configuration, this is equivalent to solving the Euler-Lagrange equations which leads to the following equations for the configuration $\mathbf{r}_\alpha$

$$\frac{3}{a^2 N_\alpha}\mathbf{r}''_\alpha(n) - \nabla w(\mathbf{r}_\alpha) = 0 \tag{2.85}$$

where $\mathbf{r}''_\alpha(n)$ is the second derivative of $\mathbf{r}_\alpha(n)$ with respect to n. The equation is analogous to the equations of motion of a particle in a potential $U(\mathbf{r}) = -w(\mathbf{r})$, with time replaced by the monomer index n. In the case of monodisperse grafted chains in the brush regime, the brush exhibits lateral symmetry which means that the potential depends only on the coordinate perpendicular to the brush, which we choose to be the z-direction

$$w(\mathbf{r}) = w(z). \tag{2.86}$$

Since the potential is independent of the x and y coordinates, the positions of the monomers in those directions will correspond to random walks. As for the z-direction, the fact that the chains are grafted at one end can be captured by requiring that the z-coordinate of the last monomer in each chain lies on the grafting surface at $z = 0$

$$z_\alpha(N) = 0 \tag{2.87}$$

where N is the length of the chain. This condition is satisfied regardless of the initial position of the other end $z_\alpha(0)$. In addition, the free ends of the chains must be free of tension

$$z'_\alpha(0) = 0. \tag{2.88}$$

One can make sense of this condition by making the analogy with the tension in a massive rope in a gravitational field [147]. The conditions in Eqs. (2.87) and (2.88) indicate that starting with no initial 'velocity' and independent of the initial position $z_\alpha(0)$, the chains reach the same end position $z_\alpha(N) = 0$ in equal 'time' N. From classical mechanics, we know that this condition is satisfied by the simple harmonic oscillator potential, which is quadratic in position. The parabolic potential $w(z_\alpha)$ that satisfies these conditions is

$$w(z) = A - \frac{3\pi^2 z^2}{8a^2 N} \tag{2.89}$$

where A is a constant shift in the potential that depends on the thickness of the brush [148]. This potential is the solution to the SST of a brush when there are no positions within the brush where the free ends are excluded [148]. For grafted chains in a good solvent,

the brush regime corresponds to a situation similar to a semi-dilute solution, where the self interaction of a chain is screened by interactions with other chains. This means that the monomers interact through a mean field proportional to the average concentration at a position z [148]

$$w(z) = B \langle \varphi(z) \rangle \tag{2.90}$$

where B is a constant that is proportional to the excluded volume. Combining Eqs. (2.89) and (2.90) yields a parabolic concentration profile for a brush in a good solvent

$$\langle \varphi(z) \rangle = \frac{1}{B} \left(A - \frac{3\pi^2 z^2}{8a^2 N} \right). \tag{2.91}$$

For a brush in poor solvent, the situation corresponds to a phase separated system and we have a constraint on the concentration

$$\varphi(z) = \varphi''. \tag{2.92}$$

where φ'' is the concentration of polymers at phase coexistence. This constraint in addition to the potential in Eq. (2.89) dictate properties of the brush within SST (see section 1.6.1 in Ref. 147 for a discussion in the case of a dry brush).

2.5.3.2. Undersaturated brushes in a chemically identical solvent

In our work, the solvent is composed of polymer chains that are chemically identical to the grafted chains. Therefore, the interaction parameter between the solvent and the brush vanishes $\chi = 0$. However, we do not always have an excess of solvent. In this case, the system is better perceived as a ternary mixture, with the vacuum or air acting as a poor solvent for the solvent and grafted polymers. The polymers in the vacuum separate into two phases with coexistence number densities ρ_p and ρ_v in the polymer rich and the polymer poor (vapor) phase respectively. We can classify the state of the brush as undersaturated or oversaturated. When oversaturated, the solvent is in excess, and the brush will behave like a brush in good (athermal) solvent, since the grafted chains are much longer than the solvent chains (see Eq. 2.73). The chemical potential in all components of the system (vapor phase, polymer film, brush) is the same and corresponds to the chemical potential of solvent chains in vacuum at a concentration equal to ρ_v. However, when the brush is undersaturated, the thickness is set through Eq. (2.77) with the constraint that the combined number density of grafted and solvent chains in the brush is equal to the coexistence value ρ_p. The thickness varies as

$$H = \frac{\sigma N_B}{(1 - \varphi_{in})\rho_p} \tag{2.93}$$

where φ_{in} is the fraction of solvent inside the brush. At the theoretical level, the value of φ_{in} is preset. This is equivalent to setting the chemical potential potential in the system, which can be obtained from the free energy in Eq. (2.76) with $\varphi = \varphi_{in}$. Choosing the chemical potential in turn sets the concentration of solvent in the vapor phase by equality of chemical potentials between the brush and vapor. The concentration in the vapor phase for an undersaturated brush will be lower than the value at coexistence ρ_v.

3. Model and Methods

Our main method of investigation is through Molecular Dynamics (MD) simulations. In MD simulations one aims to obtain the trajectories of particles, i.e. the position of each particle as a function of time, given a set of initial positions and velocities of the particles. The trajectories of the particles can be influenced by their interactions among each other, external forces, constraints etc... Each particle, therefore, experiences a force $\mathbf{F}_i(\{\mathbf{x}_i\}, \{\dot{\mathbf{x}}_i\}, t)$ that depends on time t and the positions and velocities of all the particles within the system, where $\{\mathbf{x}_i\}$ is the set of the positions of N particles labeled $i \in \{1, \ldots, N\}$, and $\{\dot{\mathbf{x}}_i\}$ is the set of velocities. The trajectories of the particles can then be obtained by solving Newton's second law of motion

$$m_i \ddot{\mathbf{x}}_i(t) = \mathbf{F}_i(\{\mathbf{x}_i\}, \{\dot{\mathbf{x}}_i\}, t) \tag{3.1}$$

where m_i and $\ddot{\mathbf{x}}_i(t) \equiv \frac{\mathrm{d}^2\mathbf{x}_i}{\mathrm{d}t^2}$ are the mass and the acceleration of particle i respectively. The methods for solving the equations are numerous; however, since this thesis is not concerned with the development of simulation methods, we shall not list the methods here. Instead, we refer the reader to the vast and excellent literature on the topic [149, 150, key], and focus on introducing our model of choice along with the setup of our simulated system.

3.1. Simulation model

The first step in setting up MD simulations is to choose a model— namely, making a choice for the forces experienced by the particles in the system. For the interaction between particles, we use the Many-body Dissipative Particle Dynamics (MDPD) coarse-grained model which is an extension of the original Dissipative Particle Dynamics (DPD) model. In DPD-like models, the total force acting on particle i due to particle j is

$$\mathbf{F}_{ij} = \mathbf{F}_{ij}^C + \mathbf{F}_{ij}^D + \mathbf{F}_{ij}^R \tag{3.2}$$

where $\mathbf{F}_{ij}^C$ is the conservative contribution to the force, $\mathbf{F}_{ij}^D$ is the dissipative contribution, and $\mathbf{F}_{ij}^R$ is the random force contribution. The latter two forces act to maintain the system at a fixed temperature, therefore acting as a thermostat. As such, they are not completely independent, but are related through the fluctuation-dissipation theorem [150, ch 12]. The original DPD model [151, key] considers soft (non-singular) conservative forces between the particles

$$\mathbf{F}_{ij}^{C} = A_{ij} w^{C}(r_{ij}) \hat{r}_{ij} \tag{3.3}$$

where $\mathbf{r}_{ij} = \mathbf{r}_i - \mathbf{r}_j$, and $\hat{r}_{ij} = \mathbf{r}_{ij}/r_{ij}$ are vectors that point from particle j towards particle i. $w^{C}(r_{ij})$ is a positive non-singular weight function that decreases monotonically with the distance between the particles. When simulating a single species using DPD the conservative force has to be repulsive in order for the system to be stable. This eliminates the possibility of simulating a system with liquid-vapor coexistence. To circumvent this limitation, the MDPD model expands on the original DPD simulation model by including a density dependent term in addition to the original DPD interaction. The addition of the many-body force allows for the coexistence of liquid and vapor phases when the original force is chosen to be attractive and the many-body force is repulsive [152–154]. In the MDPD model the conservative force is

$$\mathbf{F}_{ij}^{C} = A_{ij} w^{C}(r_{ij}) \hat{r}_{ij} + B(\bar{\rho}_i + \bar{\rho}_j) \tilde{w}^{C}(r_{ij}) \hat{r}_{ij} \tag{3.4}$$

where $A_{ij} < 0$ is the strength of the attractive part, and $B > 0$ is the strength of the density dependent repulsion. To ensure that the force is conservative, B must have the same value for all pairs of particles as shown by the no-go theorem of MDPD [155, key]. $\tilde{w}^{C}(r_{ij})$ is an additional weight function with similar properties to $w^{C}(r_{ij})$, and $\bar{\rho}_i$ is a measure of the local density around particle i

$$\bar{\rho}_i = \sum_{j \neq i} \frac{15}{2\pi r_d^3} \left[\tilde{w}^{C}(r_{ij})\right]^2 . \tag{3.5}$$

In a system with multiple species, only particles of the same species as particle i contribute to $\bar{\rho}_i$ [153, key]. The weight functions are chosen as

$$w^{C}(r_{ij}) = \begin{cases} \left(1 - \frac{r_{ij}}{r_c}\right) & r_{ij} \leq r_c \\ 0 & r_{ij} > r_c \end{cases} \tag{3.6}$$

$$\tilde{w}^{C}(r_{ij}) = \begin{cases} \left(1 - \frac{r_{ij}}{r_d}\right) & r_{ij} \leq r_d \\ 0 & r_{ij} > r_d \end{cases} \tag{3.7}$$

where r_c and r_d are cutoff radii which set the ranges of the forces. Two cut-off radii are needed since the range of the density-dependent repulsion must be smaller than that of the attraction ($r_d < r_c$) in order to have liquid-vapor coexistence with $A_{ij} < 0$ and $B > 0$ [154].

As for the dissipative and random forces, they take the form

$$\mathbf{F}_{ij}^{D} = -\zeta w^{D}(r_{ij})(\hat{r}_{ij}.\mathbf{v}_{ij})\hat{r}_{ij} \tag{3.8}$$
$$\mathbf{F}_{ij}^{R} = \sigma^{R} w^{R}(r_{ij})\theta_{ij}\hat{r}_{ij} \tag{3.9}$$

where $\mathbf{v}_{ij} = \mathbf{v}_i - \mathbf{v}_j$, ζ is the drag coefficient, σ^R is the amplitude of the random forces, and θ_{ij} is an uncorrelated Gaussian distributed random variable with zero mean and unit variance. $w^D(r_{ij})$ and $w^R(r_{ij})$ are additional weight functions. As can be seen from Eqs. (3.8) and (3.9), the DPD thermostat functions through pairwise dissipative and random forces that are momentum conserving, allowing for the emergence of hydrodynamic phenomena [156, key][157, 158]. As mentioned above, the dissipative and random forces are related through the fluctuation dissipation theorem, which leads to the following relations [151]

$$w^{D}(r_{ij}) = \left[w^{R}(r_{ij})\right]^{2} \;;\; \sigma^{R} = \sqrt{2\zeta k_B T} \tag{3.10}$$

where k_B and T are Boltzmann's constant and the temperature respectively. Except for the condition in Eq. (3.10), the choice of weight function is more or less arbitrary. Therefore, for simplicity, it is typically chosen that $w^R = w^C$. With this choice, the final form of the dissipative and random forces is

$$\mathbf{F}_{ij}^{D} = -\zeta \left[w^{C}(r_{ij})\right]^{2} (\hat{r}_{ij}.\mathbf{v}_{ij})\hat{r}_{ij} \tag{3.11}$$
$$\mathbf{F}_{ij}^{R} = \sqrt{2\zeta k_B T} w^{C}(r_{ij})\theta_{ij}\hat{r}_{ij} \tag{3.12}$$

Some constituents of our systems of interest are polymer chains. To model the chains we adopt a bead-spring model, where the monomers of a particular polymer chain are point particles that interact with the forces described above, and the bonded monomers have an additional spring force keeping them bound to each other. We choose a simple quadratic spring potential U_{bond}

$$U_{bond}(r_{ij}) = k(r_{ij} - r_0)^2 \tag{3.13}$$

where k is the spring constant and r_0 is the equilibrium extension of the spring.

In addition to the forces mentioned above, we include a short-ranged purely repulsive force originating from a flat surface. This surface acts as the substrate to which the polymer brush is grafted (see section 3.2.3). For the potential of this force we choose the Weeks-Chandler-Anderson (WCA) potential [159]

$$V_{WCA}(r) = \begin{cases} 4\varepsilon \left[\left(\frac{\sigma_{WCA}}{r}\right)^{12} - \left(\frac{\sigma_{WCA}}{r}\right)^{6} \right] + \varepsilon & r \leq 2^{1/6}\sigma_{WCA} \\ 0 & r > 2^{1/6}\sigma_{WCA} \end{cases} \tag{3.14}$$

$$\tag{3.15}$$

where ε sets the strength of repulsion, σ_{WCA} sets the length scale and range, and r is the distance from the surface.

All simulations are run in the NVT (canonical) ensemble in the absence of gravitational forces and with periodic boundary conditions in all directions.

3.2. Simulation setup

We set up our simulations to model lubricated SOCAL surfaces. As such, our system consists of a polymer brush composed of grafted polymer chains, oil lubricant composed of free chains, and a droplet composed of individual particles forming a simple liquid. All our constituents coexist with a dilute vapor phase sparsely populated by the liquid particles and a few of the free chains. Quantities related to the liquid are denoted by a subscript 'l' (or 'w' for 'water'), those related to the polymer chains collectively are denoted by 'p', while for the brush chains alone we use the subscript 'B', and finally for the oil chains alone we use 'o'.

3.2.1. Choice of model parameters

To produce a system mimicking water on PDMS, we choose the interaction parameters such that the surface tensions between the different phases reproduce the relevant contact angles, i.e. contact angle of water on bulk PDMS materials under ambient conditions. This motivates in particular our choices of the DPD attraction strength for the polymer-polymer cohesion A_{pp}, the liquid-liquid cohesion A_{ll}, and the polymer-liquid adhesion A_{pl}.

Our simulation units are set through

$$k_B T = 1 \ ; \ r_c = 1 \ ; \ m = 1$$

where the unit of energy is set by the thermal energy $k_B T$, the unit of length by the cutoff distance of the DPD attraction r_c, and the mass unit by the mass particle m for all species. The unit of time can then be defined as

$$\tau = \sqrt{\frac{m r_c^2}{k_B T}} = 1.$$

All quantities are given in these units, represented between square brackets. The time step of the simulation is $\Delta t = 10^{-3}\,[\tau]$.

Unless otherwise specified, the strength of attraction between the different species is set as (see sections 4.U.1 and 4.U.2 for motivation)

$$A_{pp} = -28\,[k_BT/r_c]\ ;\ A_{ll} = -50\,[k_BT/r_c]\ ;\ A_{pl} = -21\,[k_BT/r_c].$$

The remaining MDPD parameters are

$$r_d = 0.8\,[r_c]\ ;\ \zeta = 4.5\,[k_BT \cdot \tau \cdot r_c^{-2}]\ ;\ B = 40\,[k_BT \cdot r_c^2].$$

The bond potential parameters are chosen as

$$k = 20\,[k_BT \cdot r_c^{-2}]\ ;\ r_0 = 1\,[r_c].$$

Bonded monomers are not excluded from the MDPD pair interaction. The resulting bond length is $a \approx 1.09\,[r_c]$ with a standard deviation of $\sigma_a = 0.22\,[r_c]$ based on an average over 10^6 bonds.

For the grafting surface WCA potential we choose

$$\sigma_{WCA} = 1\,[r_c]\ ;\ \varepsilon = 1\,[k_BT].$$

The surface is chosen to be normal to the z-axis.

With our model parameters, we obtain values

$$\gamma_w = 3.14 \pm 0.04\,[k_BT/r_c^2]\ ;\ \gamma_o = 0.841 \pm 0.020\,[k_BT/r_c^2]\ ;\ \gamma_{ow} = 1.41 \pm 0.03\,[k_BT/r_c^2]$$

for the liquid-vapor surface tension, the oil-vapor surface tension, and the the oil-liquid surface tension respectively.

This results in a predicted Young contact angle (Eq. 2.9) of $\theta_Y \approx 100°$ for a droplet on a planar polymer surface. The spreading parameter of the oil on the liquid is positive, $S_{ow} = \gamma_w - \gamma_{ow} - \gamma_o = 0.89 \pm 0.06\,[k_BT/r_c^2]$. Therefore, a Neumann triangle construction (Eq. 2.20) does not exist.

The simulations are conducted using the HOOMD-Blue simulation package [160, 161] versions 2.9.7 and 4.5.0. All snapshot visualizations are made with the OVITO visualization package [162].

3.2.2. Liquid slab preparation

Many of our systems of interest require the preparation of a liquid coexisting with a vapor phase in a slab geometry. The slab can consist of either a simple liquid or a polymeric liquid. We refer to the latter as a melt. The slab is prepared in two stages.

In the first stage, chains or individual particles are equilibrated in a box with periodic boundary conditions. The size of the box in the $x - y$ direction is chosen manually. The size in the z-direction is chosen so that the number density of monomers has a specific

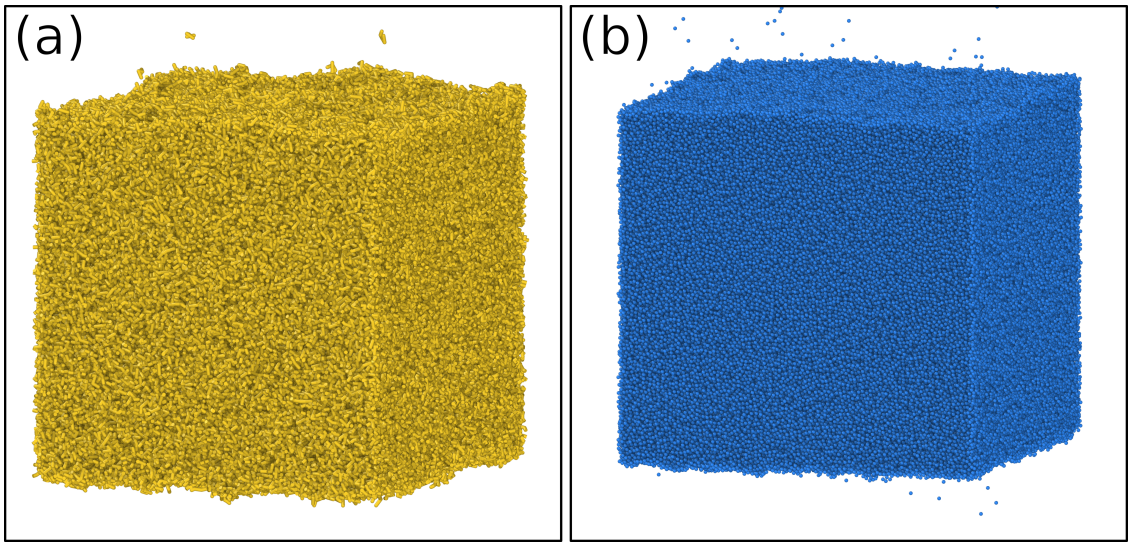

Figure 3.1.: Simulation snapshots of slabs of (a) a polymer liquid and (b) a simple liquid each coexisting with a dilute phase. The interaction parameters are described in section 3.2.1.

value. If the density of the liquid phase at coexistence is known, the starting density is chosen close to that. From experience, it is better to choose the starting density as slightly smaller than the coexistence value.

In the second stage the size of the simulation box in the z-direction is doubled. When simulating a polymeric liquid, chains that cross the boundary in the original box are properly unwrapped. The system is then left to equilibrate until a single liquid slab is coexisting with a dilute vapor phase as shown in Figure 3.1.

3.2.3. Dry brush preparation

The polymer brush consists of chains of length N_B grafted by one end by fixing the end monomer to one position. The position of the grafted monomer coincides with the purely repulsive flat surface (Eq. 3.14). The brush has $n_B = N_x \times N_y$ chains, with N_x and N_y the number of grafting sites in the x and y directions respectively. The grafting sites are distributed on a square lattice with a lattice constant (distance between nearest sites) equal to d; this results in a grafting density

$$\sigma = \frac{1}{d^2}. \tag{3.16}$$

The polymer brush is initialized with the chains fully elongated along the z-direction, then left to relax until equilibrium is reached.

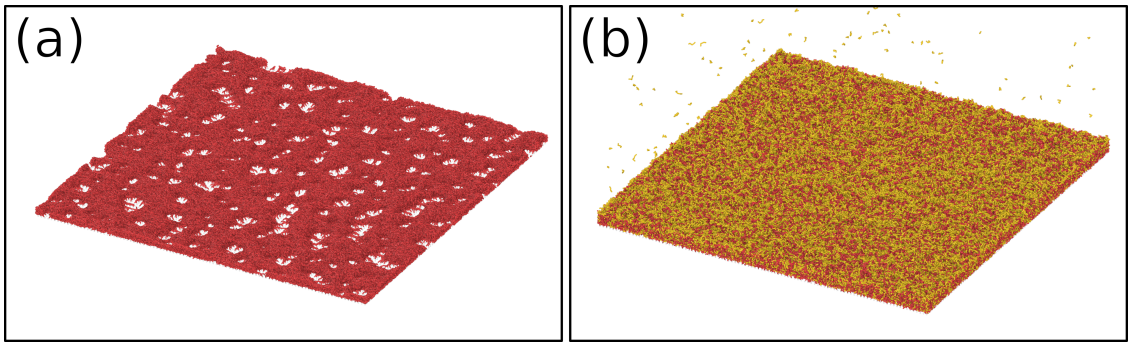

Figure 3.2.: (a) Simulation snapshot of a dry brush composed of 100×100 chains and showing the rough topography of the collapsed brush. (b) Same brush as in (a) but swollen with oil at a number fraction $\Phi = 0.44$. The interaction parameters are described in section 3.2.1. Grafted chains are shown in red, free chains in yellow.

Unless stated otherwise we choose $N_B = 50$ and $d = 2\,[r_c]$ resulting in a grafting density $\sigma = 0.25\,[r_c^{-2}]$. With the choice of parameters described in section 3.2.1, the brush is in bad solvent and the equilibrium corresponds to a collapsed state with a rough topography as shown in Figure 3.2 (a).

3.2.4. Swollen brush preparation

To swell the brush, it is placed in contact with a melt of oil chains prepared as described in section 3.2.2. The number of chains in the melt is n_o and each chain has length N_o. The size of the melt in the $x - y$ direction is equal to that of the brush, which results in faster equilibration as the diffusion of free chains is quite slow.

The next step is to place the melt in the vicinity of the brush, and run the simulation until the brush absorbs the oil and swells to its equilibrium thickness. The degree of lubrication is characterized through the number fraction Φ of oil monomers to the total number of monomers

$$\Phi = \frac{\text{number of oil monomers}}{\text{total number of monomers}} = \frac{n_o N_o}{n_o N_o + n_B N_B}. \tag{3.17}$$

In our simulations we choose $N_o = 5$ and vary the degree of lubrication. For the choice of parameters described in section 3.2.1, the equilibrium monomer density of oil in coexistence with vapor is $\rho_o \approx 2.95\,[r_c^{-3}]$. With a grafting density $\sigma = 0.25\,[r_c^{-2}]\sigma = 0.25\,[r_c^{-2}]$, the brush is saturated with oil at a fraction $\Phi \approx 0.77$, beyond which the brush stops swelling and additional oil will form a film on top of the brush. A snapshot of a swollen brush at is shown in Figure 3.2 (b).

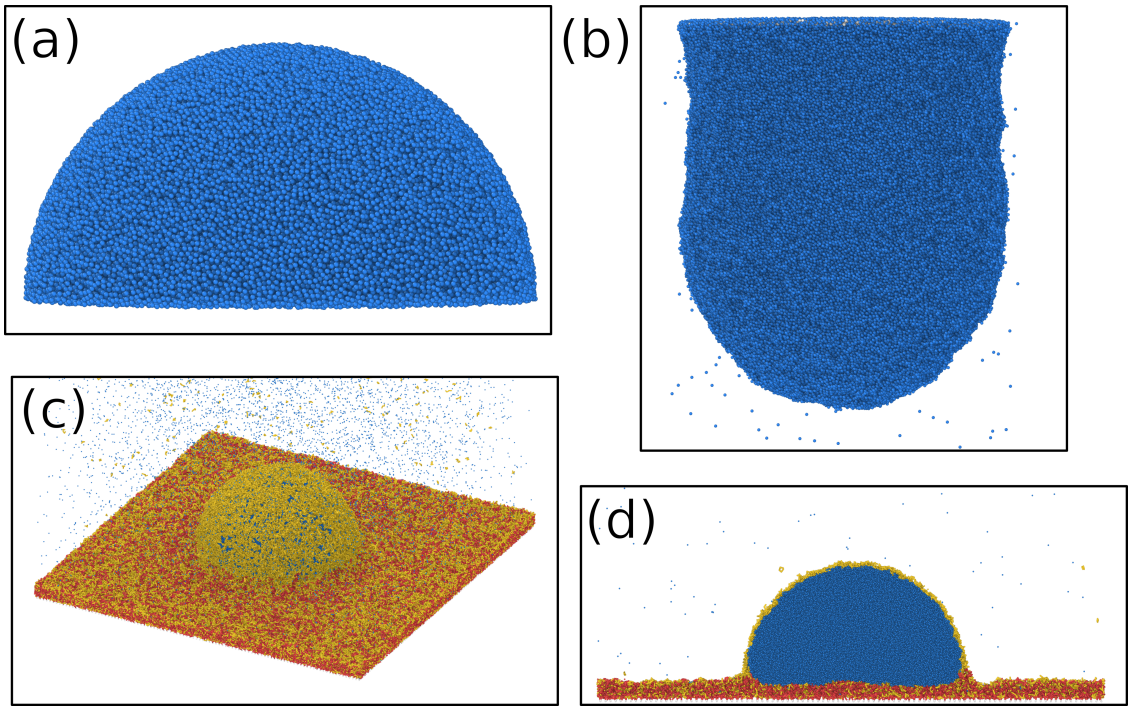

Figure 3.3.: (a) The first method of a extracting a drop resulting in a hemispherical drop. (b) The second method of extracting a drop resulting in a pendant drop. (c) Equilibrium configuration of a swollen brush with a drop. The number fraction of oil is $\Phi = 0.44$. The drop is clearly cloaked. (d) Cross section of the system shown in (c). The interaction parameters are described in section 3.2.1. Grafted chains are shown in red, free chains in yellow, and liquid particles in blue.

3.2.5. Liquid drop preparation and deposition

To prepare a drop to be deposited on the brush, the first step is to prepare a slab of simple liquid as described in section 3.2.2. The second step is to use this slab to deposit a droplet on the brush, which can be done in one of two methods.

The motivation behind the first method is to have better control over the contact radius and size of the droplet. Here, we extract a hemisphere of radius R_D from the slab (see Figure 3.3 a) and place it in contact with the brush. The first method was applied to obtain the results in section 5.U.2.

The motivation behind the second method is to emulate experiments. To achieve this we start by extracting a cylinder from the liquid slab with the axis along the z-direction. Afterwards, we fix the positions of particles in a layer at the top and apply a downward gravitational force until a pendant droplet is formed (see Figure 3.3 b). Finally, we place this pendant drop in contact with the brush. The second method was applied to obtain the results in the attached publications. Figure 3.3 (c) and (d) show the equilibrium

configuration of the drop on a swollen brush at an oil fraction $\Phi = 0.44$ with the choice of parameters described in section 3.2.1.

With the choice of parameters described in section 3.2.1, we have a liquid density of $\rho_l \approx 4\,[r_c^{-3}]$ and dynamic viscosity $\mu \approx 5.806 \pm 0.008\,[k_B T \cdot \tau \cdot r_c^{-3}]$.

3.3. Analysis Methods

Here follows a brief description of certain analysis methods that are used repeatedly throughout this work. A big role in our analysis is played by what we call density maps: multi-dimensional spatial histograms of particle positions. We create density maps in varying coordinate systems, and subsequently extract quantities of interest.

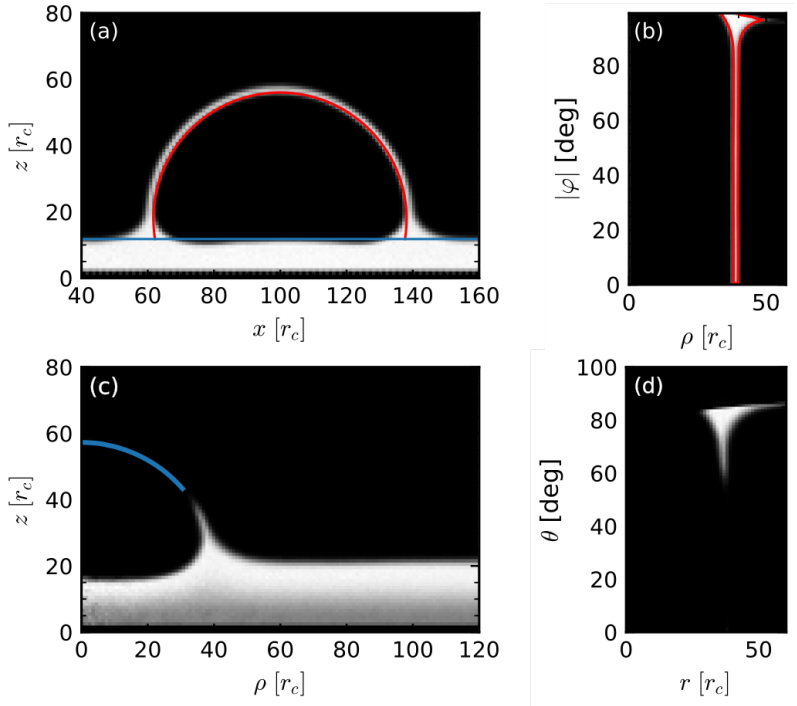

Figure 3.4.: (a) Cartesian density map $\varrho_o(x, z)$ of oil for a cylindrical droplet deposited on a lubricated polymer brush. The blue line shows the height of the unperturbed brush and the red line is a circular fit of the drop. (b) A cylindrical density map $\varrho_o(\rho, \varphi)$ of the same system as in (a) with the rotation axis oriented along the axis of the drop. The red line is a constant density contour $\varrho_o(\rho, \varphi) = \rho_o/2$. (c) Cylindrical density map $\varrho_o(\rho, z)$ of oil a spherical drop deposited on the brush. The blue line is a part of the best fitting circle for the drop. The chosen frame is away from equilibrium so that the cloak has not reached the top of the droplet. (d) Spherical density map $\varrho_o(r, \theta)$ for the same system and frame and in (c).

3.3.1. Density maps

For a particular simulation snapshot, the first step is to shift the coordinates of all particles so that the center of mass of the droplet coincides with the z-axis, while accounting for periodic boundary conditions. The density map ϱ is created by counting the number of particles belonging to each bin and dividing by the volume of the bin.

3.3.1.1. Cartesian coordinates

In Cartesian coordinates, the bin size in every direction is Δx, Δy, and Δz for x, y, and z-directions. All bins have equal volume

$$\Delta V = \Delta x \times \Delta y \times \Delta z. \tag{3.18}$$

A two-dimensional version of this map is employed in section 4.U.5 where Δy is chosen to be equal to the length of the box in the y-direction as we are dealing with a cylindrical droplet. An example of the resulting density map $\varrho_o(x, z)$ for the oil is shown in Figure 3.4 (a). The full three-dimensional version is used in Chapter 6 where the lack of symmetry does not allow us to average over an entire dimension (see for example Figure 6.5 which shows $\varrho(x, y, z)$ for all species at a particular choice of y).

3.3.1.2. Cylindrical coordinates

The density maps in cylindrical coordinates are used in Chapter 4 and section 5.U.2 where we are dealing with sessile droplets. There, the choice of cylindrical coordinates is motivated by the azimuthal symmetry of the drop. Therefore, the box is partitioned into bins in the z-direction and the radial direction, with respective sizes Δz and $\Delta\rho$. The bin edges are positioned at

$$\rho_i = i \times \Delta\rho \tag{3.19}$$

$$z_j = j \times \Delta z \tag{3.20}$$

with $i, j \in \mathbb{N}$ the indices of the radial bin and of axial bins respectively. In this case, bins have different volumes depending on the index of the radial bin (see section A.5.1 for a more general expression)

$$\Delta V_{ij} = \pi \Delta z \Delta\rho^2 (2i + 1). \tag{3.21}$$

An example of such a density map $\varrho_o(\rho, z)$ for the oil is shown in Figure 3.4 (c). Cylindrical coordinate density maps are also employed in section 4.U.5. In this case, the rotation axis of the coordinate system is along the y-direction and is chosen to pass through the center of curvature of the droplet (see section 3.3.2.1); in addition, we average over the length

of the box L_y in the y-direction. The box is partitioned into bins in the the radial and angular directions, with respective sizes $\Delta\rho$ and $\Delta\varphi$. The bin edges are positioned at and the volume is

$$\rho_i = i \times \Delta\rho \tag{3.22}$$

$$\varphi_j = j \times \Delta\varphi \tag{3.23}$$

$$\Delta V_{ij} = \frac{L_y}{2}\Delta\varphi\Delta\rho^2(2i+1) \tag{3.24}$$

with $i, j \in \mathbb{N}$ the indices of the radial bin and of angular bins respectively. An example of such a density map $\varrho_o(\rho, \varphi)$ for the oil is shown in Figure 3.4 (b).

3.3.1.3. Spherical coordinates

We use spherical coordinate density maps in Chapter 4 and section 5.U.2 where we are dealing with sessile droplets and have azimuthal symmetry. The origin of the coordinate system is placed at the center of curvature of the droplet (see section 3.3.2.1). The box is partitioned into bins in the radial and polar directions, with respective sizes Δr and $\Delta\theta$. The bin edges are positioned at

$$r_i = i \times \Delta r \tag{3.25}$$

$$\theta_j = j \times \Delta\theta \tag{3.26}$$

with $i, j \in \mathbb{N}$ the indices of the radial bin and of polar bins respectively. In this case, bins have different volumes depending on the index of the radial bin (see section A.5.2 for a more general expression)

$$\Delta V_{ij} = \frac{2\pi}{3}\Delta r^3(\cos\theta_j - \cos\theta_{j+1})[(i+1)^3 - i^3]. \tag{3.27}$$

An example of such a density map $\varrho_o(r, \theta)$ for the oil is shown in Figure 3.4 (d).

3.3.2. Equal density contours

Having the density maps, one key method for delineating the boundaries between the different phases is through equal density contour lines.[1] An example of such a contour is shown in Figure 3.4 (b), where the line is an equal density density contour $\varrho_o(\rho, \varphi) = \rho_o/2$, with ρ_o the bulk density of the bulk polymer phase. Density contours are used in various ways to extract information from the simulations as described in the following sections.

[1] In the case of a three-dimensional density map, this corresponds to equal density isosurfaces.

3.3.2.1. Droplet shape

One way of using the density contours is to characterize the shape of the droplet. In the case of a sessile cylindrical or spherical droplet, a density contour at $\varrho_l(\ldots) = \rho_l/2$ is extracted for the density map of the droplet; afterwards, the top half is fit to a circle, providing us with the coordinates of the center of curvature and the radius of curvature of the droplet. This information is then used to calculated other types of density maps if needed. An example of such a fit is shown in Figure 3.4 (a) and (c).

In the case of a moving drop, the shape deviates from a spherical cap. A reasonable approximation of the shape of a section of the moving droplet is an ellipse. In this case, we fit the top half of the contour to a rotated ellipse, which provides us with a quantification of the shape. An example of such a contour with the corresponding fit is shown in Figure 6.5.

3.3.2.2. Unperturbed brush height

To find the height of the brush far away from the droplet, we calculate density contours $\varrho_o(\ldots) = \rho_o/2$ from the density map of polymers, where ρ_o is the density of the bulk polymer phase. Having this contour, we then calculate the average height far away from the drop, and use that as the height of the unperturbed brush.

3.3.2.3. Apparent contact angle

Having the height of the brush away from the droplet, we can use it as a baseline for calculating apparent contact angles. In our work, the apparent contact angles are always defined as the angle the fit to the droplet shape makes with a horizontal line at the height of the unperturbed brush. In the case of moving droplets, we can differentiate between advancing and receding contact angles. Helpful relations for such calculations can be found in section A.5.3.

3.3.2.4. Cloak thickness

An example of an oil density contour $\varrho_o(\rho, \varphi) = \rho_o/2$ for a cylindrical droplet in cylindrical coordinates in shown in Figure 3.4 (b). It is clear that at equilibrium the distance between the contour lines is constant across the droplet before it starts increasing when we reach the wetting ridge. Therefore, we define the cloak thickness as the average distance between the contour lines for $\theta \in [0, \pi/6]$. In cases where the cloak is not thick enough to have clear contour lines, we set the cloak thickness to 0.

4. Cloaking Transition of Droplets on Lubricated Polymer Brushes

Note: This chapter reproduces the publication in Ref. 163. Additions and changes from the original publication are marked with a violet text color, while omissions are marked through the symbol [...].

Contributions to the publication:

- **Simulation setup:** R.G.M. Badr designed and wrote the simulation initialization and execution scripts which rely on the HOOMD-Blue version 2.9.7 [160, 161].
- **Analysis and figures:** R.G.M. Badr developed the analysis schemes with input from F. Schmid. R.G.M. Badr wrote and executed the analysis codes and visualized the data. Experiments were performed by L. Hauer and D. Vollmer.
- **Writing:** R.G.M. Badr in collaboration with F. Schmid wrote the bulk of the simulation results sections, the conclusion, and drafted the introduction of the original article which was then substantially revised by D. Vollmer. Experiment section was written by L. Hauer and D. Vollmer.

4.1. Introduction

Droplets are omnipresent. Important applications include self cleaning [164–166], spray coating, anti-icing, anti-fouling [167], anti-corrosion or more efficient application of pesticides [168, 169]. Understanding the interactions of droplets with surfaces is also of inherent interest for physicists due to the interplay of various forces and energies acting at different length and time scales. Here, we aim to understand the wetting of water droplets on dry and lubricated brushes. Applications of polymer brushes in regards to wetting include moisture harvesting using PNIPAAm brushes on cotton fabric [170], anti-fogging using stimuli-responsive brushes [171], and the manufacture of materials with modifiable and switchable adhesive, dissipative, and wettablity properties [172].

For a long time, wetting research focused on modelling the static and dynamic properties of droplets on smooth and rigid surfaces. Modelling wetting dates back to Thomas Young [47]. He showed that in thermodynamic equilibrium the contact angle of a droplet deposited on an ideally smooth, chemically homogeneous rigid surface is determined by the interplay of the interfacial tensions.

$$\cos\theta = \frac{\gamma_s - \gamma_{sw}}{\gamma_w} \tag{4.1}$$

γ_s, γ_w and γ_{sw}, are the solid-vapour, droplet-vapour and solid-droplet interfacial tension. While this equation holds for micrometer sized droplets and larger ones, for nanometer sized droplets line tension changes the contact angles, too. In contrast to Thomas Young's equation, in real life a droplet never has a unique well-defined contact angle. Surface roughness, chemical inhomogeneities, adaptation of the surface due to the presence of a drop [173] or droplet induced charging of the surface [174] cause pinning of the three phase contact line. The measured apparent contact angle can take any value between the apparent receding and apparent advancing contact angle. Contrary to experiments, in simulations the realization of the ideal condition is possible. Modelling idealized conditions has the advantage that the influence of different factors on wetting phenomena can be well separated. In particular if small length or time scales are involved this might be hard or even impossible to probe with currently available experimental techniques. Here, it should be kept in mind that the wetting properties are determined by the properties of the droplet and the surface close to the three-phase contact line.

Particularly challenging is the understanding of the wetting properties of sessile droplets on dry or lubricant infiltrated brushes. A brush is composed of chains grafted by one end to a surface. The resulting layer is elastic and of very small thickness (order of nm). Therefore, the length scales are too small and curvatures are too large to experimentally investigate the shape of the area close to the three-phase contact line. However, to a certain extent, information gained from droplets on rigid surfaces, gels, or lubricant infused surfaces can be used to understand the wetting properties of droplets on dry and lubricated brushes [26, 175–177]. For example it has been shown that sessile droplets on gels and lubricant infused surfaces are surrounded by an annular wetting ridge. The vertical component of the interfacial tension at the three phase contact line exerts a force on the surface, pulling

the gel or lubricant up. Depending on the elastic modulus of the gel or the thickness of the lubricant layer, now the contact angles can be modelled by a Neumann triangle [178]. For lubricant impregnated surfaces the droplet can be covered by a thin cloak. Whether it is possible to form a cloak or not depends on the balance of the interfacial tensions. A cloak forms for a positive spreading parameter S, $S = \gamma_w - \gamma_o - \gamma_{ow}$, where γ_o and γ_{ow} is the interfacial tension of lubricant-vapour and droplet-lubricant, respectively. Interference measurements allow an estimate of the thickness of the cloak but are insufficiently sensitive to quantify the variation of the thickness over the surface [29]. The reason is that the curvature of the droplet complicates data analysis. So far it is also unclear how the thickness of the cloak depends on the amount of lubricant available.

In the present paper, we aim to tackle these questions for sessile droplets on dry and lubricated brushes using coarse-grained molecular dynamic simulations. We use a simple rather generic model, however, with interactions parameters adjusted to polydimethylsiloxane (PDMS). Brushes made of PDMS recently have attracted a lot of attention because droplets experience particularly low contact line pinning [179]. Reported values [32, 180, 181] for the contact angle hysteresis of water on PDMS vary between $1 - 11°$. The differences may be caused by varying amounts of non-crosslinked chains in the brush. The reason for this low contact angle hysteresis is that PDMS chains are very flexible, having a persistence length of a few monomers. The large bond angle of approximately 150° between Si-O-Si atoms induces a very low torsional barriers [7]. The hydrophobic methyl side groups lead to the low interfacial tension of 0.02 N/m. They also shield the inorganic Si-O backbone [182]. As opposed to PDMS gels where the chains are crosslinked resulting in an elastic solid, PDMS brushes keep their high flexibility. Figure 4.1 shows an example of an experimental view of a droplet on a PDMS brush covered by a layer of silicone oil as a lubricant, obtained with confocal microscopy, where the yellow fluorescence signal indicates the presence of lubricant. Details on the experimental setup are given in the Appendix A. The confocal image shows two very important features. Near the three phase contact line there is an accumulation of lubricant, forming a wetting ridge. Especially clear in the cross sectional view is a visible fluorescent signal all over the droplet, showing that the droplet is indeed cloaked by the lubricant.

While a molecular understanding of wetting properties of sessile droplets on brushes cannot be achieved experimentally, molecular dynamics studies can give detailed insight at the molecular level. Previous molecular dynamics simulations of polymeric droplets on polymer brushes by Léonforte and Müller have provided insight into the dependence of the contact angle and height of the wetting ridge on the affinity between the droplet and the brush, in addition to the effect of line tension [183]. Later work by Mensink, de Beer, and Snoeijer investigated the transition between mixing, total wetting, and partial wetting, of polymeric droplets on polymer brushes [184], and studied the effects entropic contributions have on the transitions [185]. As for droplet on lubricated surfaces, molecular dynamics simulations on lubricant-infused patterned surfaces have reproduced the phenomenon of the cloaking of the droplet by the lubricant [186, 187]. Here, we use such simulations to study the shape of the wetting ridge, the onset and thickness of the cloak, and the influence of the amount of lubricant on the apparent contact angle.

[...]

4.2. Results and discussion

4.2.1. Experiment

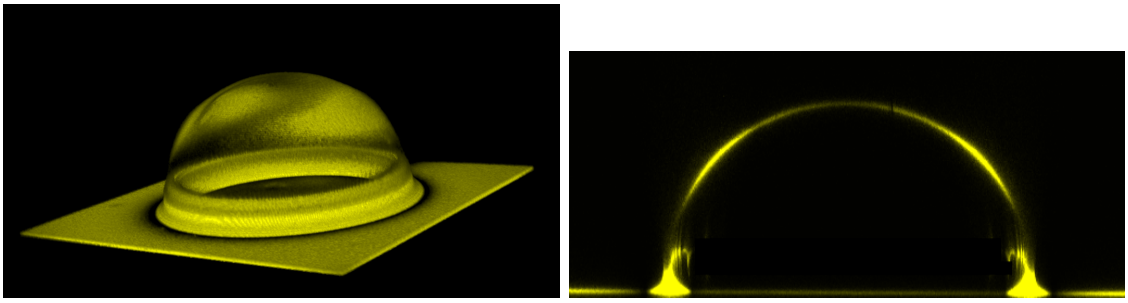

Figure 4.1.: Left: Experimental 3D view of the droplet on a PDMS brush infused with silicone oil, obtained through confocal microscopy. The image shows a clear wetting ridge at the three phase contact line, in addition to a cloaking layer on the surface of the droplet. Right: Cross sectional side view of the same droplet. A wetting ridge is clearly visible, in addition to a cloak indicated by the fine fluorescence signal all over the droplet.

Figure 4.1 shows an example of an experimental view of a droplet on a PDMS brush covered by a layer of silicone oil as a lubricant, obtained with confocal microscopy, where the yellow fluorescence signal indicates the presence of lubricant. Details on the experimental setup are given in section 4.5. The confocal image shows two very important features. Near the three phase contact line there is an accumulation of lubricant, forming a wetting ridge. Especially clear in the cross sectional view is a visible fluorescent signal all over the droplet, showing that the droplet is indeed cloaked by the lubricant.

4.2.2. The brush

To better understand the wetting behavior, we first investigate the characteristics of the brush. At grafting densities $\sigma \leq 0.25$ the dry brush has a rough topography, with the density in the saturated sections having a value similar to the melt density. Figure 4.2 shows the variation in the height of the brush as a function of the amount of lubricant present for grafting densities $\sigma = 0.17, 0.25, 0.31$. The x-axis is the fraction of lubricant in the system

$$\Phi = \frac{n_o N_o}{n_o N_o + n_B N_B}, \tag{4.2}$$

where n_o is the number of lubricant chains, N_o is the length of lubricant chains, n_B is the number of brush chains, and N_B is the length of brush chains. This fraction does not always coincide with the fraction of lubricant strictly inside the brush, to which we will

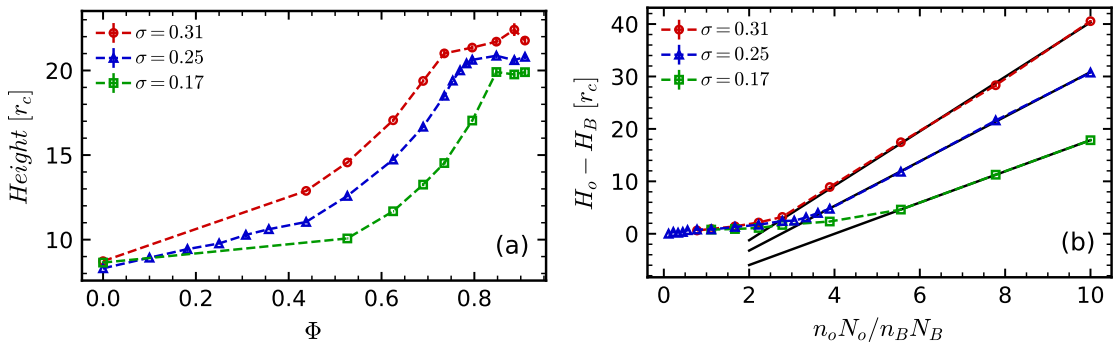

Figure 4.2.: (a) Height of the brush versus the total fraction of lubricant Φ for different grafting densities and (b) difference in height between the brush and the top of the lubricant layer versus the ratio of lubricant particles to grafted chain particles n_oN_o/n_BN_B, for different grafting densities. The solid lines illustrate the extrapolation procedure used to determine the saturation point (see text). For $\sigma = 0.25$, we obtain a saturation point $n_oN_o/n_BN_B \approx 3.33$ or $\Phi \approx 0.77$

---

refer as Φ_o^B, because a layer of lubricant forms on top of the brush if Φ exceeds a certain value (see below). With our choice of grafting density and length of the free chains, we are in the regime where the free chains are not expelled from the brush, and the film formed after the brush is saturated is stable against autophobic dewetting [188, 189].

We begin with examining the brush height, which we define as the point where the density distribution of brush particles drops below a cut-off value of 10^{-3}. Here and in the rest of this article, the error bars correspond to the standard error on the average value obtained from 5 independent simulations. Figure 4.2a shows that the brush height increases with the lubricant content as one might expect, but then reaches a constant value, indicating that the brush is saturated with lubricant. Once the brush is saturated, a film of lubricant forms on top of the brush, which is in coexistence with a vapor phase that has a very low lubricant density ($< 10^{-3}$). To identify the saturation point, we calculate the difference between the height of the brush (H_B) and the height of the lubricant (H_o), which are both defined as the height at which the respective densities drop below a value of 10^{-3}. We then plot the difference, $H_o - H_B$, versus the ratio of the number of lubricant particles to brush particles n_oN_o/n_BN_B. When the brush is saturated it stops swelling, which means $H_o - H_B$ should increase linearly with the overall fraction of lubricant chains. Fitting the last 3 points of each curve for $H_o - H_B$ to a line, we can clearly detect the saturation point as the point where the curve deviates from that line. For example, at grafting density $\sigma = 0.25$, the saturation point is at $\Phi \approx 0.77$. This value for the grafting density will be chosen below to study droplets on brushes. [...]

Figure 4.3 shows the variation of the brush height versus $\sigma^{1/3}$ for a saturated brush. The data points show linear behavior, which is consistent with a brush in good solvent [82]

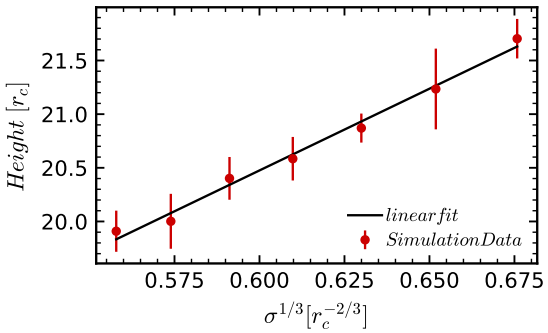

Figure 4.3.: Height of the brush versus $\sigma^{1/3}$ for a saturated brush $\Phi = 0.84$. The linear trend is consistent with the prediction for a brush in good solvent.

(see section 2.5.2.1).

For the cloaking and wetting properties, surface tension plays an important role. The surface tensions of the different components of the system are calculated through integration of the stress tensor anisotropy across flat interfaces [190, 191][192, §2.3]

$$\gamma_x = \int dz(P_\perp - P_\parallel) \tag{4.3}$$

Different configurations were simulated in order to determine separately the liquid-vapor interfacial tension γ_w, the lubricant-vapor tension γ_o, the lubricant-liquid tension γ_{ow}, the brush-vapor tension γ_b, and the brush-liquid tension γ_{bw}, A liquid or lubricant slab surrounded by vapor for γ_w and γ_o, a brush for γ_b, a brush covered by a slab of liquid for γ_{bw}, and a lubricant slab in contact with a liquid slab for γ_{ow}. Here and throughout, the subscripts o, w, and b refer to the oil (lubricant), water (liquid droplet), and brush respectively. A single subscript refers to the interface of the respective phase with the vapor phase, while a combination of two subscripts refers to the interface between the two respective phases. A distinction needs to be made between the oil-water interface and the brush-water interface since the surface tension of the latter depends on the degree of swelling of the brush as will be shown below.

Figure 4.4 shows the stress anisotropy profile for an undersaturated and a fully saturated brush in contact with vapor, and an undersaturated brush in contact with liquid. The three curves show similar features, i.e., strong oscillations of same magnitude near $z = 0$ characterizing the brush-substrate interactions ($z < 4$). This zone is followed by a zone where the stress anisotropy is slightly negative due to the mutual repulsion of the stretched polymers and decays to zero, and finally a positive peak at the position of the polymer interface away from the grafting surface. (In the case of the brush-liquid system, an additional peak appears around $z = 35$, which marks the position of the liquid-vapor interface).

[...] We note that the curve for the strongly oversaturated brush covered by a lubricant

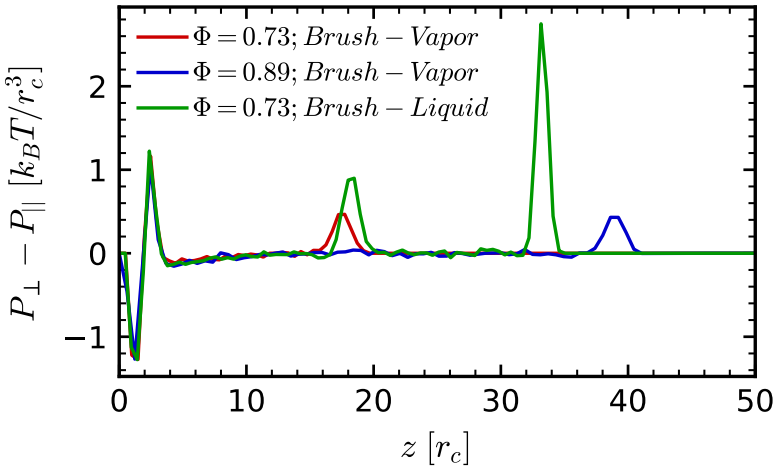

Figure 4.4.: Stress tensor anisotropy for a brush with different lubricant content. The integral over the peak gives the relevant surface tension for the wetting. Both profiles show similar properties near the grafting surface, due to the repulsion of the surface and the tension in the first (grafted) bond. The large peak near $z = 35$ is the liquid-vapor interface.

---

layer (blue line corresponding to $\Phi = 0.89$ in Figure 4.4) does not feature an additional peak which would mark the brush-lubricant interface. Hence we conclude that the interfacial tension between brush and lubricant film is zero. Furthermore, one can see that the behavior of the curves inside the brush is independent of the fraction of lubricant and of the type of the adjacent phase (vapor or liquid). Here we are mainly interested in the difference of γ_{bw} and γ_b, which is the quantity entering the expected value for the equilibrium contact angle of the droplet (the Young's angle). From the curves in Figure 4.4 it is apparent that when we calculate this difference the contribution from the bulk of the brush will cancel. This was later confirmed by Veldscholte et al. [193]. Therefore, to reduce statistical errors, we choose to evaluate only the integral over the peaks at the interfaces, which correspond to the pure polymer-vapor and polymer-liquid interfacial tension, omitting the contributions of the brush and brush-substrate interactions to the surface energy.

To be as close as possible to the experimental conditions of water on PDMS, we choose the interaction parameters such that the ratios of these surface tensions match the corresponding experimental values. Specifically, we choose $A_{ij} = A_{ww} = -50\,[k_BT/r_c]$ for the liquid-liquid cohesion which results in a liquid-vapor surface tension of $\gamma_w \approx 3.1\,[k_BT/r_c^2]$, we choose $A_{ij} = A_{pp} = -28\,[k_BT/r_c]$ for the polymer-polymer cohesion which gives $\gamma_o \approx 0.8\,[k_BT/r_c^2]$ for the pure lubricant-vapor interface, and finally $A_{ij} = A_{pw} = -21\,[k_BT/r_c]$ for the polymer-liquid cohesion which gives a lubricant-liquid surface tension of $\gamma_{ow} \approx 1.4\,[k_BT/r_c^2]$ (see section 4.U.2).

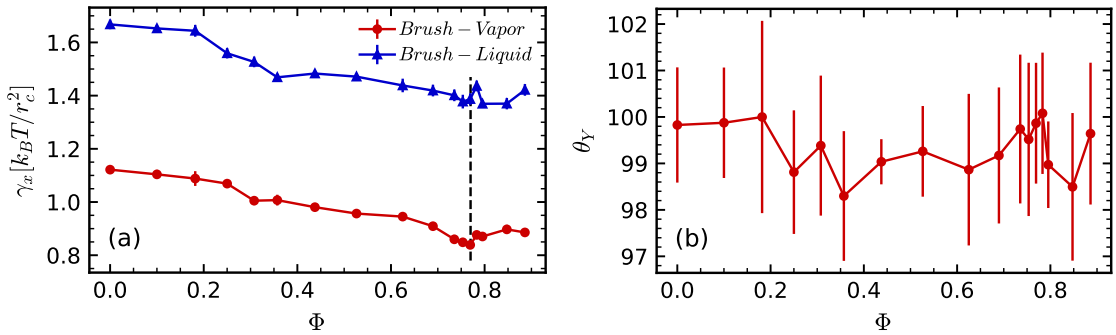

Figure 4.5.: (a) Surface tension versus lubricant content for both the brush-vapor and the brush-liquid interfaces. (b) Young angle versus lubricant content, as calculated using equation 2.9 with $\gamma_w = 3.2$

The brush-vapor and brush-liquid surface tensions are calculated as a function of the lubricant content of the brush at $\sigma = 0.25$. The results are shown in Figure 4.5a, while Figure 4.5b shows the predicted Young angles versus the lubricant content as calculated using equation (2.9). The surface tension starts at a higher value for dry brushes, possibly due to the roughness, and then decreases and eventually reaches the melt (lubricant) γ_o value after saturation.

4.2.3. Cloaking

When a water droplet is placed on a PDMS substrate, the residual silicone oil/lubricant accumulates on the droplet, resulting in a cloaking layer as shown in Figure 4.1 and [194]. The main driving force for this phenomenon is the positive spreading parameter of silicone oil (uncrosslinked PDMS) on water $S_{o/w} = \gamma_w - \gamma_{ow} - \gamma_o = 11$ mN/m, effectively lowering the droplet-vapor surface tension. With our choice of parameters we get a spreading parameter $S_{sim} = 0.9$, which results in cloaking as shown in Figure 4.6 (a). To investigate the cloaking, we study the cloak thickness as a function of the lubricant fraction in the system (see section 3.3.2.4 for details on the calculation method). We define a cloak as a layer of lubricant chains that is at the bulk density. Figure 4.6 (b) shows the cloak thickness versus lubricant content. The figure shows that cloaking is absent for low Φ and sets in at a certain transition point, beyond which the cloak thickness increases with the lubricant content. The graph seems to flatten as we approach the brush saturation point. No points beyond saturation were simulated here because of computational limitations.

To rationalize these findings, we develop a simple theoretical picture (see appendix 4.6 for the full derivation, and Figure 4.7 for a schematic representation). We consider a coupled system of a spherical droplet, which is possibly covered by lubricant, and a lubricant infused brush, which can exchange lubricant chains. Equilibrium is achieved when the

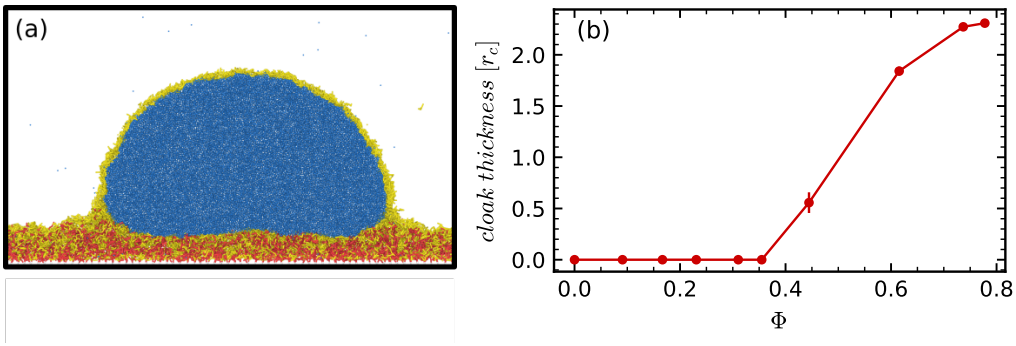

Figure 4.6.: (a) Side cross-sectional view of a spherical droplet on lubricated brush. Yellow particles represent the free chains, red the grafted chains, and blue the liquid particles. (b) Cloak thickness as a function of lubricant content. R in the legend is the radius of curvature of the droplet. We define a cloak as a layer of free chains that has the bulk density ρ_o of the lubricant melt. The thickness is at zero before a certain transition point is reached, after which the thickness increases before seeming to flatten near the brush saturation point $\Phi \approx 0.77$.

---

chemical potentials of both subsystems are equal. The free energy of the brush-lubricant subsystem is

$$\frac{F_B}{k_B T} = n_o \ln \Phi_o^B + \frac{k}{2}\, n_B\, H_B^2 - \mu_o^B n_o \tag{4.4}$$

where first term is the mixing free energy of the lubricant in the brush, the second term is the stretching elasticity cost of the brush with the spring constant $k/2 = K/N_B$ (K is an undetermined prefactor with units of inverse length squared), and the last term is the chemical potential contribution. Eq. (4.4) can be rewritten as the free energy per unit area and in terms of the fraction of lubricant in the brush as

$$\tilde{F}_B = \frac{N_B}{N_o}\sigma \frac{\Phi_o^B \ln \Phi_o^B}{1-\Phi_o^B} + K N_B \sigma^3 \frac{1}{(1-\Phi_o^B)^2} - \mu_o^B \frac{N_B}{N_o}\sigma \frac{\Phi_o^B}{1-\Phi_o^B} \tag{4.5}$$

where Φ_o^B is the volume fraction of lubricant in the brush, and μ_o^B the chemical potential of the lubricant in the brush. If we impose the equilibrium condition $\partial \tilde{F}_B / \partial \Phi_o^B = 0$, we can obtain a relation between the lubricant chemical potential and the lubricant content, Φ_o^B,

$$\mu_o^B = 1 - \Phi_o^B + \ln \Phi_o^B + 2K N_o \sigma^2 \frac{1}{1-\Phi_o^B} \tag{4.6}$$

Next we consider the droplet-lubricant subsystem. In our simulations we work with short ranged forces. This leads us to hypothesize a rapidly decaying disjoining pressure for the

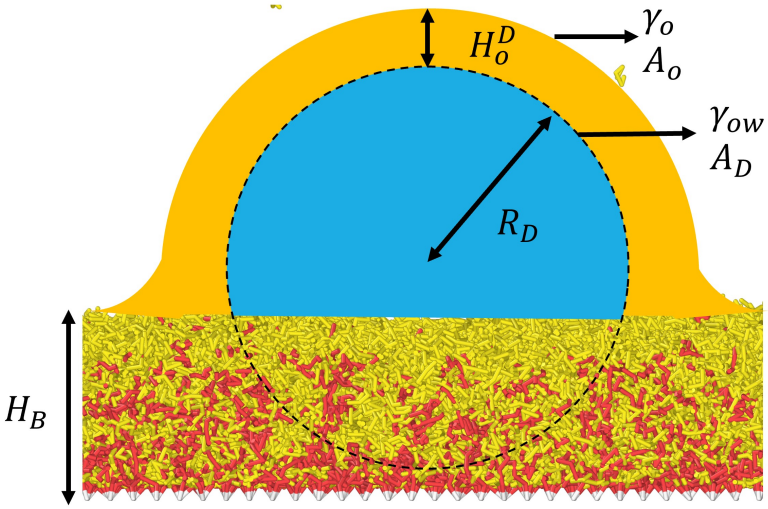

Figure 4.7.: Diagram representing the most relevant quantities involved in the theory.

cloaking layer, as opposed to the typical h^{-3} dependence associated with long range Van der Waals forces. This is also supported by the results in section 4.U.3. The driving mechanism for the cloaking phenomenon is the difference in surface tensions, captured by the spreading parameter $S = \gamma_w - \gamma_{ow} - \gamma_o$ (we use S instead of $S_{o/w}$ here for compactness). We then write our free energy contribution F_Π of the disjoining pressure as

$$F_\Pi = A_D \, S \, \exp\left(-H_o^D/\xi\right) \tag{4.7}$$

where A_D is the surface area of the droplet, H_o^D is the thickness of the cloaking layer, and ξ a length scale characterizing the range of the disjoining pressure. Therefore, we write the free energy of the cloaking layer as

$$\frac{F_D}{k_B T} = A_D S \exp\left(-H_o^D/\xi\right) + A_D \gamma_{ow} + A_o \gamma_o - \mu_o^D n_o^D \tag{4.8}$$

The first term is the contribution of the disjoining pressure, the following two terms are the interfacial energies, and the last term is the contribution of the chemical potential. In the above expression μ_o^d is the chemical potential of the lubricant on the droplet, n_o^D the number of lubricant chains in the cloaking layer, A_D and A_o are the areas of the droplet surface and the surface of the cloaking layer, respectively, given by

$$A_D = \kappa_D 4\pi R_D^2$$

$$A_o = \kappa_o 4\pi (R_D + H_o^D)^2,$$

and κ_D and κ_o are geometric factors that depend on the contact angle. For thin cloaking layers, we approximate $\kappa_D = \kappa_o \equiv \kappa$. Using this information we write the free energy of the cloaked droplet per unit area of the droplet A_D as

$$\tilde{F}_D = S\ \exp\left(-H_o^D/\xi\right) + \gamma_{ow} + \left(1 + \frac{H_o^D}{R_D}\right)^2 \gamma_o - \mu_o^D \frac{n_o^D}{\kappa 4\pi R_D^2} \tag{4.9}$$

Minimizing $\tilde{F}_D$ with respect to n_o^D, we obtain an expression for the relation between the chemical potential of the lubricant, μ_o^D, and the thickness of the cloaking layer, H_o^D:

$$\mu_o^D = \frac{N_o}{\rho_o} \frac{1}{\left(1 + \frac{H_o^D}{R_D}\right)^2} \left[\frac{-S}{\xi} \exp\left(-\frac{H_o^D}{\xi}\right) + 2\frac{\gamma_o}{R_D}\left(1 + \frac{H_o^D}{R_D}\right)\right]. \tag{4.10}$$

Equating equations (4.6) and (4.10) gives the equilibrium condition between the lubricated brush and the cloaked droplet $\mu_o^B(\Phi_o^B) = \mu_o^D(H_o^D)$. Setting $H_o^D = 0$ on the R.H.S implies the existence of a transition when the fraction of lubricant is equal to the value Φ_o^{B*}, which corresponds to a chemical potential value μ_o^{B*}

$$\mu_o^{B*} = \mu_o^B(\Phi_o^{B*}) = \frac{N_o}{\rho_o}\left[-\frac{S}{\xi} + 2\frac{\gamma_o}{R_D}\right] \tag{4.11}$$

The existence of a cloaking transition is a clear feature from the results of our simulations. When the brush is fully saturated, including the configurations where a film of pure lubricant is formed on top of the brush, we have $\mu_o^B = 0$. When this is the case the equilibrium condition is given by

$$\mu_o^D = 0 \implies \frac{-S}{\xi} \exp\left(-\frac{H_o^D}{\xi}\right) + 2\frac{\gamma_o}{R_D}\left(1 + \frac{H_o^D}{R_D}\right) = 0. \tag{4.12}$$

This means that the cloaking layer will reach a limiting thickness as the brush gets fully saturated, found by solving equation (4.12) for H_o^D. We were not able to simulate systems with an oversaturated brush and a droplet due to computational limitations, but the trend in Figure 4.6 (b) seems to be flattening near the saturation point $\Phi \approx 0.77$.

4.2.4. Cloaking and wetting: effect on contact angles and the wetting ridge

After having investigated the cloaking transition, we now turn to study the influence of cloaking on the wetting properties of droplets, in particular the contact angle and the properties of the wetting ridge.

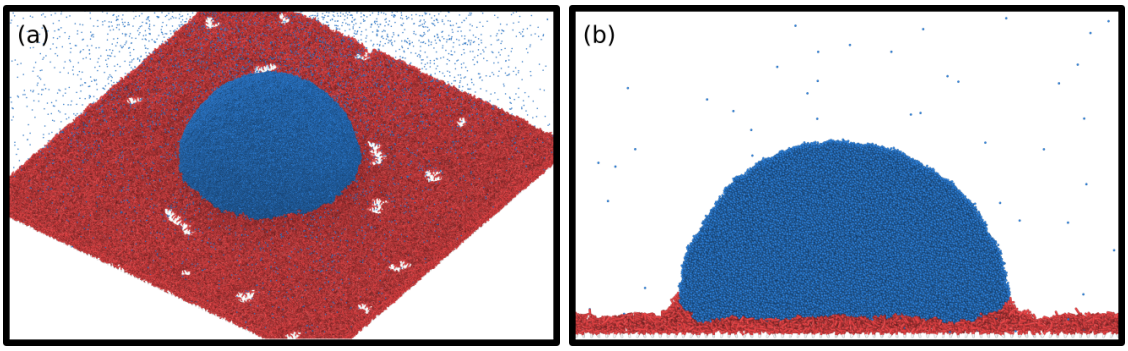

Figure 4.8.: (a) Spherical Droplet on a dry brush (b) cross-sectional side view of the same droplet on a dry brush.

4.2.4.1. Contact angles on a dry brush

We first investigate spherical droplets on dry brushes with a grafting density $\sigma = 0.25$. This results in systems as shown in Figure 4.8.

A key qualitative observation is the formation of a wetting ridge at the three phase contact line. Of particular interest is the contact angle between the droplet and the brush. Here we are specifically looking at the apparent contact angle, which can be compared to the angle calculated from the Young equation. The angle is calculated by fitting the top of the droplet to a circle and finding the angle it makes with a horizontal line at the level of the unperturbed brush. This procedure results in an apparent contact angle θ_{app}. For details on the calculation see section 3.3.2.3.

Figure 4.9 shows the variation of $\cos(\theta_{app})$ with the inverse radius of the contact line. The graph shows linear behavior, which is in agreement with the line tension hypothesis at the three phase contact line. The hypothesis suggests a contribution to the free energy that is proportional to the length of the three phase contact line. This results in a correction to the apparent contact angle of the form [195]

$$\cos(\theta_{app}) = \cos(\theta_\infty) - \frac{\tau/\gamma_w}{r_{contact}} \tag{4.13}$$

where θ_∞ is the limiting Young contact angle, achieved for infinitely large droplets, τ is the line tension, and $r_{contact}$ is the radius of the three phase contact line. Here the line tension is an effective parameter which possibly includes other corrections, most notably the correction due to the Tolman length. Fitting the data points to a line gives an effective line tension value $\tau/\gamma_w = -5.0$ and a Young angle $\theta_\infty = 101°$. The latter is in good agreement with the value calculated from the corresponding surface tensions, assuming the Shuttleworth effect (see section 2.1.1.2) is negligible due to the nature of the brush, where the stresses and strains are in the normal direction to the unperturbed brush interface [46].

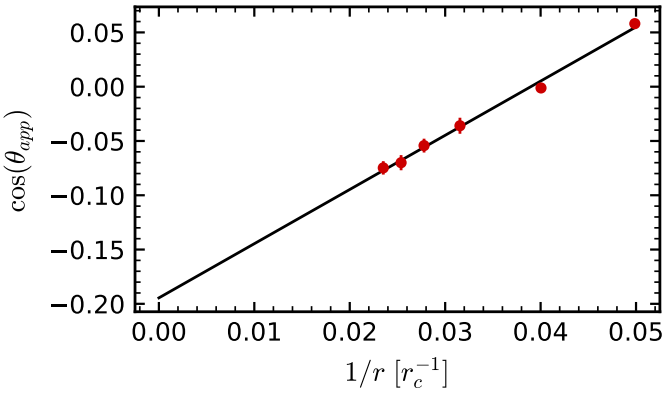

Figure 4.9.: Variation of $\cos(\theta_{app})$ with the inverse radius of the contact line. The variation is linear suggesting that the dominant correction to the Young equation is that due to an effective line tension $\cos(\theta_{app}) = \cos(\theta_\infty) - \frac{\tau/\gamma_w}{r_d}$. Our simulations suggest $\tau/\gamma_w = -5.0$ for a dry brush. The y-intercept has the value -0.19, which corresponds to a Young angle of 101°. This angle is in good agreement with the result calculated from surface tensions ($\approx 100°$)

The correction due to the Tolman length should result in a small variation of the contact angle; however, it is expected to be smaller than 1° based on the values obtained in section 4.U.4. This indicates that the correction due to curvature is not a major contributor to the apparent line tension in the system.

4.2.4.2. Contact angles on a lubricated brush

The next line of inquiry is to investigate the influence of lubricant on the contact angles. Figure 4.10 (a) shows the variation of the apparent contact angle on lubricated brushes. The graph shows a gradual decrease in the contact angle until about $\Phi = 0.44$. This suggests the hypothesis that the magnitude of the line tension increases when lubricant is added, and then again when the cloaking transition sets in, since in our case the line tension is negative and therefore promotes the spreading of the droplet.

To test this hypothesis we measure the contact angle versus the size of the droplet on a lubricated brush beyond the cloaking transition point. The results are shown in Figure 4.10 (b). The points do not clearly fall on a line, indicating that the interpretation of the apparent contact angle in terms of surface tensions and line tensions may be too oversimplified, at least for the nanodroplets considered in this work. If we nevertheless enforce a fit and try to extract the limiting angle and line tension, we get a value for the line tension $\tau/\gamma_w = -5.7$ and a limiting angle $\theta_\infty = 101°$. The line tension strength slightly increased, but more investigation is required to rule out other mechanisms that might be in play.

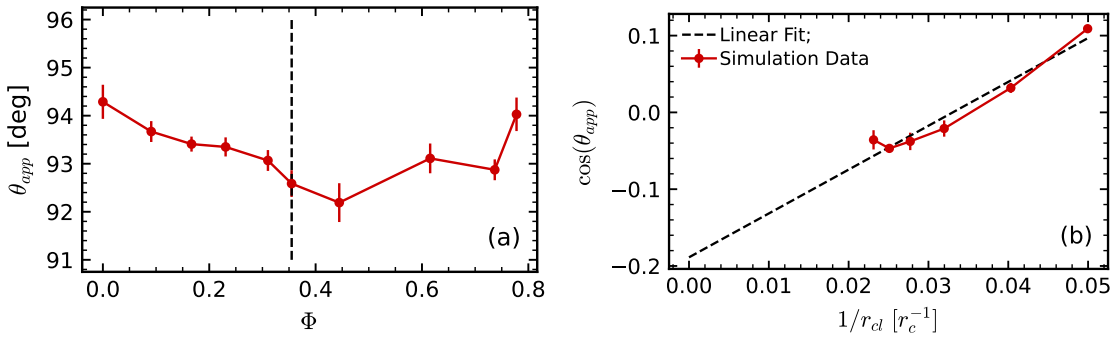

Figure 4.10.: (a) Variation of θ_{app} with the lubricant content. The contact angle decreases when lubricant is added and after the transition point (black dashed line), suggesting a possible increase in the magnitude of line tension. (b) Variation of $\cos(\theta_{app})$ with the inverse radius of the contact line for a lubricated brush with $\Phi = 0.44$. Here the behavior is not exactly linear, which is likely due to effects other than line tension. If we forcefully try to extract a line tension however, we get $\tau/\gamma_w = -5.7$ and the y-intercept has the value -0.19, which corresponds to a Young angle of 101°.

After $\Phi = 0.44$ we see a slight increase in the contact angle for the following two points. Since the droplet is cloaked for those points, the effective droplet-vapor surface tension is expected to be lower [194]. Lowering the droplet surface tension drives the contact angle away from 90°, which is what we observe. The final point suggests a jump in apparent contact angle. However, this jump is most likely an artifact of the large curvature of the droplet near the contact line at high lubrication.

4.2.4.3. Brush ridge reduction

The cloaking of the droplet can be seen as an example for fluid separation from the underlying substrate, which is observed in certain cases of soft wetting. We observe in our simulation that the fluid separation is accompanied by a reduction in the height of the grafted chains near the droplet, in the vicinity of the wetting ridge as seen in Figure 4.11. Such a phenomenon has also been observed experimentally for water droplets on swollen PDMS gels [38]. Figure 4.12 (a) shows the maximum height of the grafted chains near the droplet after subtracting the unperturbed height away from the droplet. The ridge height slightly increases after lubricant is added to the system. At some point it reaches a maximum then decreases. After cloaking sets in, the height decreases more rapidly as the the fraction of lubricant increases. The non-monotonic behavior before cloaking is qualitatively in agreement with the experimental results from [38].

In many experiments, the resolution is not high enough to allow for visualization of the cloaking layer, but one can still observe a wetting ridge where Neumann angles can be calculated. The confocal image in Figure 4.1 show an accumulation of lubricant close to

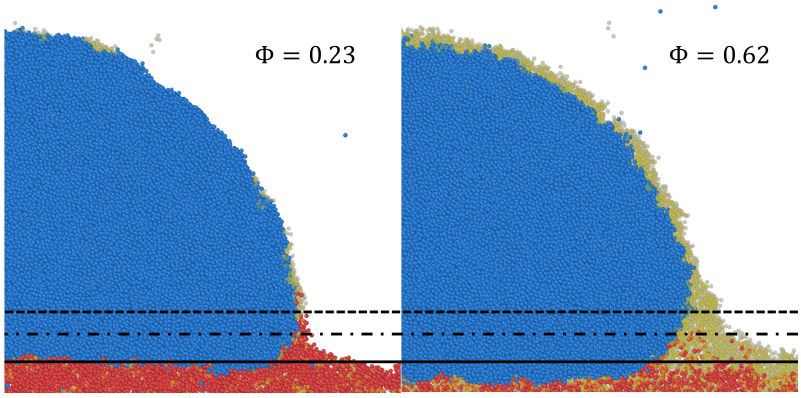

Figure 4.11.: Snapshots showing the reduction in the grafted ridge height (red particles) as lubricant is added. The solid line shows the height of the unperturbed brush, the dashed line the height of the grafted ridge at low lubrication, and the dash-dot line the height at higher lubrication.

---

the three phase contact line. This accumulation can be considered as an effective wetting ridge, so that if the resolution of the microscope were lower, the cloaking layer would not be visible, only the ridge. We observe a similar effect in our simulations, where the cloaking layer of constant thickness gets wider near the contact line (see section 3.3.2.4). From the simulation we can extract an effective ridge height, which we define as the position where the thickness of the cloaking layer increases by more than 10% above its mean value far from the contact region, in the region of constant thickness. In the absence of a cloaking layer, the ridge height can be calculated directly. Figure 4.12 (b) shows the change in the brush ridge height h_B, the lubricant ridge height h_R, and the lubricant-brush separation $h_{sep} = h_R - h_B$, as the amount of lubricant is increased. h_B and h_R are measured as the height above the unperturbed brush as illustrated in Figure 4.11. The trends are very similar to the ones observed by Cai et al in [38]. Notable is the rapid increase in the separation after the onset of cloaking. Also shown in Figure 4.12 (b) is the brush ridge height h_B^0 measured as the height above the grafting surface instead of the unperturbed brush. h_B^0 increases gradually until the cloaking transition, then remains constant at the value of the saturated height of the brush $\approx 22\,[r_c]$. This is an indication that the accumulation of lubricant in the wetting ridge results in a local swelling of the brush at the three phase contact line; when the cloaking transition sets in, the lubricant is in excess and the brush locally swells to its saturation value. This means that the height of brush part of the ridge does not decrease as originally suggested in Figure 4.12 (a) and Ref. 38 for PDMS gels. Instead, the more likely scenario is that, when there is enough lubricant, the elastic material near the three phase contact line is fully swollen to its maximum height; what is observed as a decrease in the height is due to the swelling of the surrounding material as more lubricant is added to the system.

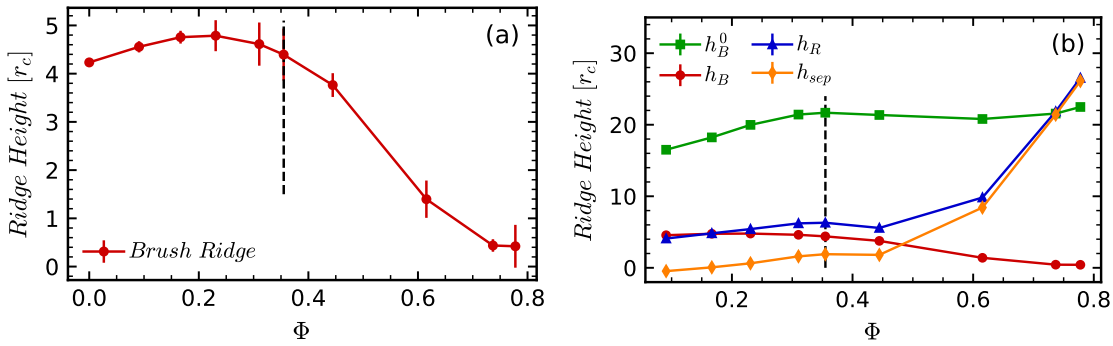

Figure 4.12.: (a) Height of the brush ridge versus the lubricant content, the dashed black line indicates the onset of the cloaking transition. The ridge height shows non-monotonic behavior. It first increases as lubricant is added, then decreases again, with the decrease being more steep after the onset of cloaking. [...] (b) Variation of the lubricant ridge height h_R, the brush ridge height h_B, and the separation between the two h_{sep} versus the lubricant fraction. In the absence of cloaking the ridge height is calculated directly. Shown as well is the brush ridge height h_B^0 measured from the grafting surface, which increases gradually until the cloaking transition, then remains constant at the value of the saturated height of the brush $\approx 22[r_c]$ (see Figure 4.2).

4.3. Conclusion

In this study we have examined the cloaking of liquid droplets on lubricant infused polymer brushes by simulations and supporting experiments and theoretical considerations.

The experiments clearly demonstrate the existence of such cloaking layers for droplets on brushes with a high lubricant content. This is accompanied by an accumulation of lubricant near the contact line between the droplet and the substrate. In experiments where the resolution does not allow for the observation of a cloaking layer, the accumulation near the contact line will appear as a Neumann type wetting ridge. The qualitative properties of the droplets in simulation are in very good agreement with the experiment.

In the simulations we characterized the swelling of the brush by the lubricant and found the saturation point for different grafting densities, which plays a role in the thickness of the cloaking layer. The surface tension of the brush surface with vapor and liquid as a function of swelling is found to gradually decrease as one goes from a dry brush to a saturated brush, where for the latter the value approaches the values corresponding to the lubricant with the relevant interface.

Furthermore, we characterized the cloaking of the droplet by the lubricant by calculating the variation of the cloak thickness versus the amount of lubricant present in the system. We find that a cloaking-transition takes place already for lubricant concentrations that are significantly lower than those where the brush saturates with lubricant. The cloak

thickness seems to flatten as one approaches the saturation point of the brush. We derive a thermodynamic theory that predicts the cloaking transition, the increase of the cloak thickness, and the limiting thickness at saturation. Given the approximate nature of the theory however we do not have quantitative agreement. An additional effect of the presence of lubricant is liquid-substrate separation at the three phase contact line. This is accompanied by a decrease in the height of the substrate in the wetting ridge as more lubricant is added, which is an effect that has also been observed experimentally for droplets on PDMS gels.

We [...] investigate the contact angles of the droplet on the brush. On a dry brush, we study the dependence of contact angles on the size of the droplet and find that line tension plays an important role for spherical droplets, where we find the value $\tau/\gamma_w = -5.0$. On lubricated brushes, we find that the angle is reduced, implying that the addition of lubricant increases the magnitude of line-tension (negative in our case). Overall, the effect of cloaking on the apparent contact angle is remarkably small, in the range of only a few degrees. It is strongly affected by the finite size of the droplet, but the extrapolated value for infinite droplet size is in good agreement with the Young's angle predicted from the surface tension, both for cloaked and uncloaked droplets. Thus we find that the cloaking transition has only a minor effect on the static equilibrium wetting properties of droplets.

Given that cloaking has a strong effect on the structure of the contact line, we do however expect that it will strongly influence the dynamic wetting properties, i.e., contact angle hysteresis and the friction of rolling droplets. This will be the subject of [...] Chapter 6. Another interesting subject for future investigation is the spreading and imbibition of the free chains into the brush and comparison with atomistic simulations [196].

4.4. Acknowledgments

This work was funded by the German Science Foundation within the priority program SPP 2171 (grants Schm 985/22 and VO 639/16). R.G.M.B. thanks Leonid Klushin for useful discussions.

4.5. Experimental details

4.5.1. PDMS brush substrate

Glass slides ($24 \times 60\ mm$, 170 μm thick) were rinsed with ethanol and acetone and dried under nitrogen gas. Thereafter, they were exposed to oxygen plasma (0.3 bar) for 10 minutes at 300 W (Femto, Diener Electronic, Germany). This treatment adds hydroxyl groups to the surface. Approximately 250 μl of methyl terminated PDMS oil (6000 Da) is cast on the surface and distributes homogeneously. Over time, PDMS chains condense on the hydroxyl (anchor) groups at the surface [32]. After 24h, we remove ungrafted PDMS

chains from the surface by immersing the substrate in a toluene-sonication bath for 15 minutes. A $5 - 10$ nm thick film of surface-grafted PDMS chains remains. Free PDMS oligomers (3500 Da) are distributed overnight (3 ± 2 $\mu l/mm^2$) into the grafted PDMS chains. The oligomers were fluorescently labeled (Lumogen Red, BASF, 0.1 mg/ml).

4.5.2. Experimental visualization of oligomer cloaking

We place the PDMS brush substrate on a laser scanning confocal microscope (Leica TCS SP8)). We place a droplet (approx. 500 nl) of glycerol (57 $\%wt$) water (43 $\%wt$) on the substrate. The glycerol-water mixture was chosen to suppress evaporation. The mixing ratio yields a refractive index match between drop and PDMS (i.e. $n = 1.4$) and a surface tension of around $\gamma_w \approx 67$ mN/m[197, 198]. Combining this with $\gamma_o \approx 21$ mN/m for silicone-oil-air, and $\gamma_{wl} \approx 40$ mN/m for silicone-oil-water, we expect an apparent contact angle (for uncloaked droplets) $\theta_Y = \cos^{-1}\left(\frac{\gamma_o - \gamma_{wl}}{\gamma_w}\right) \approx 106°$.

After 20 minutes, we capture 3D stacks of the droplet using a Leica HC PL APO CS 10x/0.40 objective lens. We observe stark silicone oil (yellow) accumulations in the vicinity of the three-phase contact line in Figure 4.1. Additionally, silicone oil distributes on the entire air-exposed interface of the drop, indicated by the fine fluorescence signal. This gives direct indication of a silicone oil cloak on the droplet.

[...]

4.6. Derivation of the thermodynamic theory for cloaking

4.6.1. Notation

- k_B: Boltzmann constant
- T: temperature
- n_o^B: number of lubricant chains
- N_o: length of a lubricant chain
- n_B: number of grafted chains
- N_B: length of a grafted chain
- a: size of a monomer
- Φ_o^B: fraction of lubricant in the brush
- H_B: height of the brush
- μ_o^B: chemical potential of the lubricant in the brush
- σ: grafting density of the brush

- γ_w: surface tension of the droplet-vapor interface
- γ_o: surface tension of the lubricant-vapor interface
- γ_{ow}: surface tension of the droplet-lubricant interface
- $S = \gamma_w - \gamma_{ow} - \gamma_o$: spreading parameter of the lubricant on the lubricant on the droplet
- H_o^D: thickness of the lubricant layer
- ξ: length scale of the decay of the disjoining pressure
- R_D: radius of curvature of the droplet
- μ_o^D: chemical potential of the cloaking layer (lubricant on the droplet)
- n_o^D: number of lubricant chains on the droplet
- ρ_o: density of pure lubricant melt

4.6.2. Free energy of the brush

We consider the lubricated brush and the cloaked droplet as coupled thermodynamic systems which can exchange energy and lubricant chains. The free energy of the brush subsystem is given by

$$\frac{F_B}{k_B T} = n_o \ln \Phi_o^B + K n_B \frac{H_B^2}{N_B} - \mu_o^B n_o \tag{4.14}$$

The first term is the mixing free energy of the lubricant in the brush, the second term is the stretching elasticity cost of the brush the spring constant $k/2 = K/N_B$ (K is an undetermined prefactor with units of inverse length squared), and the last term is the chemical potential contribution. Here $\mu_o^B \leq 0$ with $\mu_o^B = 0$ corresponding to a fully saturated brush. Rewriting n_o^B and n_B as

$$n_o^B = A_B H_B \frac{\Phi_o^B}{N_o a^3}$$

$$n_B = A_B \sigma$$

with A_B the surface area of the brush, we can rewrite the free energy as

$$\frac{F_B}{k_B T} = A_B H_B \frac{\Phi_o^B}{N_o a^3} \ln \Phi_o^B + A_B \sigma K \frac{H_B^2}{N_B} - \mu_o^B A_B H_B \frac{\Phi_o^B}{N_o a^3} \tag{4.15}$$

The fraction of grafted chains is given by

$$\Phi_B = 1 - \Phi_o^B = \frac{N_B \sigma a^3}{H_B} \tag{4.16}$$

which leads to an expression for the height of the brush

$$H_B = \frac{N_B \sigma a^3}{1 - \Phi_o^B} \tag{4.17}$$

making this final replacement and dividing by the area A_B to get the free energy per area we get the final form for our free energy

$$\tilde{F}_B \equiv \frac{F_B}{k_B T A_B} = \frac{N_B}{N_o}\sigma \frac{\Phi_o^B \ln \Phi_o^B}{1 - \Phi_o^B} + K N_B \sigma^3 \frac{1}{(1 - \Phi_o^B)^2} - \mu_o^B \frac{N_B}{N_o}\sigma \frac{\Phi_o^B}{1 - \Phi_o^B} \tag{4.18}$$

Where a factor of a^6 has been absorbed into the prefactor K. Now if we impose the equilibrium condition $\partial \tilde{F}_B / \partial \Phi_o^B = 0$, we can obtain the chemical potential as

$$\mu_o^B = 1 - \Phi_o^B + \ln \Phi_o^B + 2K N_o \sigma^2 \frac{1}{1 - \Phi_o^B} \tag{4.19}$$

4.6.3. Free energy of the cloak

In our simulations we work with short ranged forces. This leads us to hypothesize a rapidely decaying disjoining pressure for the cloaking layer, as opposed to the typical h^{-3} dependence associated with long range Van der Waals forces. Given that the driving mechanism for the cloaking phenomenon is the difference in surface tensions, captured by the spreading parameter $S = \gamma_w - \gamma_{ow} - \gamma_o$, we write our free energy contribution F_Π of the disjoining pressure as

$$F_\Pi = A_D \, S \, \exp\left(-H_o^D / \xi\right). \tag{4.20}$$

Therefore, we write the free energy of the cloaking layer as

$$\frac{F_D}{k_B T} = A_D \, S \, \exp\left(-H_o^D / \xi\right) + A_D \gamma_{ow} + A_o \gamma_o - \mu_o^D n_o^D \tag{4.21}$$

and dividing by the area of the droplet we get

$$\tilde{F}_D = \frac{F_D}{k_B T A_D} = S \, \exp\left(-H_o^D / \xi\right) + \gamma_{ow} + \frac{A_o}{A_D}\gamma_o - \mu_o^D \frac{n_o^D}{A_D} \tag{4.22}$$

where A_D and A_o are the areas of the droplet and the cloaking layer respectively, given by

$$A_D = \kappa_D 4\pi R_D^2$$
$$A_o = \kappa_o 4\pi (R_D + H_o^D)^2$$

where κ_D and κ_o are geometric factors that depend on the contact angle. For thin cloaking layers, we approximate $\kappa_D = \kappa_o \equiv \kappa$. Inserting this into the expression for $\tilde{F}_D$ we get

$$\tilde{F}_D = S \exp\left(-H_o^D/\xi\right) + \gamma_{ow} + \left(1 + \frac{H_o^D}{R_D}\right)^2 \gamma_o - \mu_o^D \frac{n_o^D}{\kappa 4\pi R_D^2} \tag{4.23}$$

To minimize $\tilde{F}_D$ with respect to n_o^D, we use

$$n_o^D = \frac{\rho_o}{N_o} V_o \implies dn_o^D = \frac{\rho_o}{N_o} dV_o \tag{4.24}$$

where V_o is the volume of the cloaking layer, whose differential dV_o is given by

$$dV_o = \kappa 4\pi (R_D + H_o^D)^2 dH_o^D \tag{4.25}$$

the above two equations give

$$\frac{\partial H_o^D}{\partial n_o^D} = \frac{N_o}{\rho_o}\left[\kappa 4\pi (R_D + H_o^D)^2\right]^{-1} \tag{4.26}$$

using the above equation to evaluate $\partial \tilde{F}_D / \partial n_o^D = 0$ we obtain the chemical potential of the cloaking layer as

$$\mu_o^D = \frac{N_o}{\rho_o} \frac{1}{\left(1 + \frac{H_o^D}{R_D}\right)^2}\left[\frac{-S}{\xi} \exp\left(-\frac{H_o^D}{\xi}\right) + 2\frac{\gamma_o}{R_D}\left(1 + \frac{H_o^D}{R_D}\right)\right] \tag{4.27}$$

4.6.4. Cloaking transition and limiting cloak thickness

Equilibrium between the brush and the cloaked droplet is achieved when the chemical potentials are equal $\mu_o^B(\Phi_o^B) = \mu_o^D(H_o^D)$. The transition from uncloaked to cloaked droplet is found by setting $H_o^D = 0$ on the R.H.S implying the existence of a transition when the fraction of lubricant is equal to the value Φ_o^{B*} which corresponds to a chemical potential value μ_o^{B*}

$$\mu_o^{B*} = \mu_o^B(\Phi_o^{B*}) = \frac{N_o}{\rho_o}\left[-\frac{S}{\xi} + 2\frac{\gamma_o}{R_D}\right] \tag{4.28}$$

when the brush is fully saturated, including the configurations where a film of pure lubricant is formed on top of the brush, we have $\mu_o^B = 0$. When this is the case the equilibrium condition is given by

$$\mu_o^D = 0 \implies \frac{-S}{\xi} \exp\left(-\frac{H_o^D}{\xi}\right) + 2\frac{\gamma_o}{R_D}\left(1 + \frac{H_o^D}{R_D}\right) = 0 \tag{4.29}$$

which means that the cloaking layer will reach a limiting thickness as the brush gets fully saturated.

4.U. Unpublished Results: Cloaking Transition of Droplets on Lubricated Polymer Brushes

The following sections include unpublished results obtained in preparation or after the conclusion of the published article in Chapter 4.

4.U.1. Phase diagrams

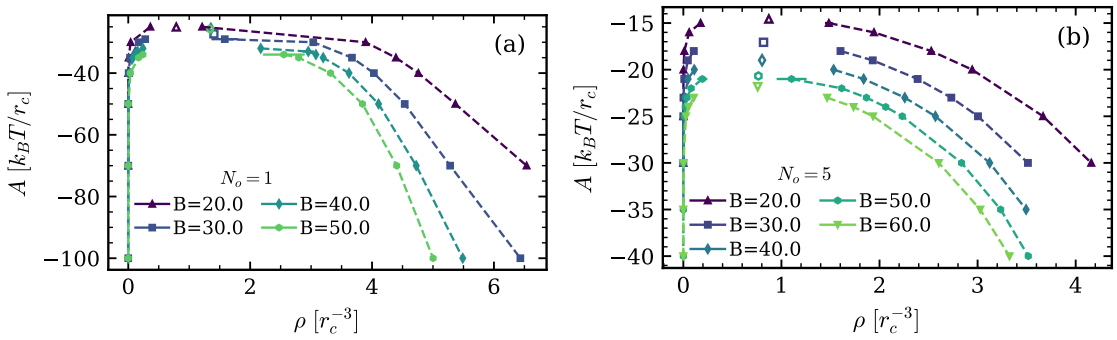

Figure 4.U.1.: Phase Diagrams for the MDPD model for (a) monomers $N_o = 1$ and (b) oligomers $N_o = 5$. A is the strength of monomer-monomer cohesion, ρ is the number density, and B is the strength of many-body repulsion. The dashed lines connect the data points to guide the eye. Open symbols are the critical points. The critical points in (a) overlap with each other and some of the data points.

In preparation for the wetting on polymer brush simulations, it was important to find out what choice of interaction parameters results in a phase separated state in the MDPD model. To that end, we run single species liquid slab simulations (see section 3.2.2) of liquids composed of molecules of different degrees of polymerization $N_o \in \{1, 5, 10, 20, 40, 80\}$. From the simulation we extract the densities of the dense and dilute phases by fitting the density profile of the liquid slab to a form derived from mean field theory [199][200, §6.3]

$$\rho(z) = \frac{1}{2}(\rho_h - \rho_l)\left[1 - \tanh\left(\frac{z - z_0}{w}\right)\right] + \rho_l \tag{4.U.1}$$

where ρ_h is the 'high' density in the dense phase, ρ_l is the 'low' density in the dilute phase, z_0 is the position of the interface, and w is the width of the interface.

We choose the same interaction parameters as described in section 3.2.1, except that the strengths of attraction and repulsion A and B are varied (see Eq. 3.4). Due to the volume of simulations needed, only one simulation was used for every data point. After equilibrium is reached each simulation was run for $t = 3200\,[\tau]$ from which we extract 50 frames for analysis. The results for $N_o = 1$ and $N_o = 5$ are shown in Figure 4.U.1 (a) and (b) respectively. The phase diagrams are represented as $A - \rho$ diagrams, with different lines corresponding to different values of B. Horizontal error bars on ρ correspond to the standard error on the fit parameters. Open symbols are placed at the critical point as calculated through least-squares fitting to

$$\rho_h - \rho_l \propto \left(1 - \frac{A}{A_c}\right)^{\beta} \tag{4.U.2}$$

$$\frac{\rho_h + \rho_l}{2} = \rho_c + C(A_c - A)^{1-\alpha} \tag{4.U.3}$$

where A_c and ρ_c are the critical attraction strength and critical density respectively, and $\beta \approx 0.326$ and $\alpha \approx 0.11$ are critical exponents corresponding to the 3D Ising model universality class [201]. For $N_o = 1$ the critical points overlap among each other and with some of the data points. Additional phase diagrams for the other values of N_o are shown in Figure B.1.

4.U.2. Surface tension

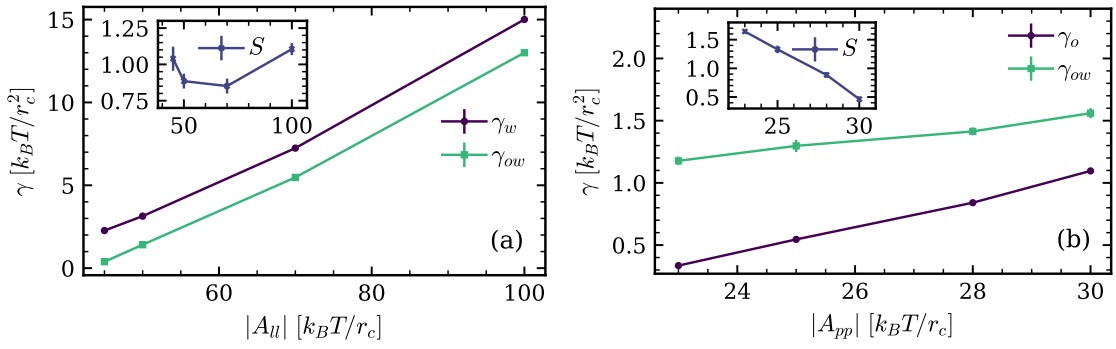

Figure 4.U.2.: Surface tension and spreading parameter of oil on water versus cohesion strength $|A_{ij}|$ for (a) a simple liquid and (b) a polymer liquid $N_o = 5$. The oil-liquid surface tension and spreading parameter of oil on water are calculated for adhesion strength $A_{pl} = -21$.

The next step in the set up was to find suitable values for interaction parameters that would reproduce the ratios of surface tensions in the experiments. We begin by varying the cohesion strength and calculating the liquid-vapor surface tension for a simple liquid and a polymer liquid ($N_o = 5$) which will be our oil. As the simple liquid represents water, we label the related physical quantities with a subscript 'w', while we use the subscript 'o' for the polymer liquid as it represents the oil. The results are shown in Figure 4.U.2. To be as close as possible to the experimental conditions of water on PDMS, we choose the interaction parameters such that the ratios of these surface tensions match the corresponding experimental values. Specifically, we choose $A_{ij} = A_{ll} = -50$ for the liquid-liquid cohesion which results in a liquid-vapor surface tension of

$$\gamma_w = 3.14 \pm 0.04\,[k_B T/r_c^2],$$

we choose $A_{ij} = A_{pp} = -28$ for the polymer-polymer cohesion which gives

$$\gamma_o = 0.841 \pm 0.020\,[k_B T/r_c^2]$$

for the pure oil-vapor interface. Finally, we need to match the ratio of oil-liquid surface tension to the other two. After some exploration of the parameter space, we settle on $A_{ij} = A_{pl} = -21$ for the polymer-liquid adhesion which gives an oil-liquid surface tension of

$$\gamma_{ow} = 1.41 \pm 0.03\,[k_B T/r_c^2].$$

With this choice the spreading parameter of the oil on the liquid is positive,

$$S_{o/w} = \gamma_w - \gamma_{ow} - \gamma_o = 0.89 \pm 0.06\,[k_B T/r_c^2].$$

Figure 4.U.2 also shows the variation of the oil-liquid surface tension and the spreading parameter of oil on the liquid as we vary the cohesion strengths A_{ll} and A_{pp} for a fixed adhesion $A_{pl} = -21$.

4.U.3. Disjoining pressure in simulations

As we are interested in droplets on lubricated brushes, there is the possibility that the drops will be cloaked by the oil. This is driven by the positive spreading parameter of the oil on the droplet Eq. (2.30). This driving force for the cloaking can also be captured through the disjoining pressure $\Pi_o(h)$ for a thin film of oil of thickness h on the surface of the droplet (see section 2.1.5). The disjoining pressure is related to the spreading parameter through Eq. (2.19). A way of determining the disjoining pressure is to measure the effective surface tension $\gamma_{eff}(h)$ for a thin film of thickness h and relate it to the disjoining pressure through Eq. (2.18), resulting in

$$\Pi_o(h) = -\frac{\mathrm{d}\gamma_{eff}}{\mathrm{d}h} \tag{4.U.4}$$

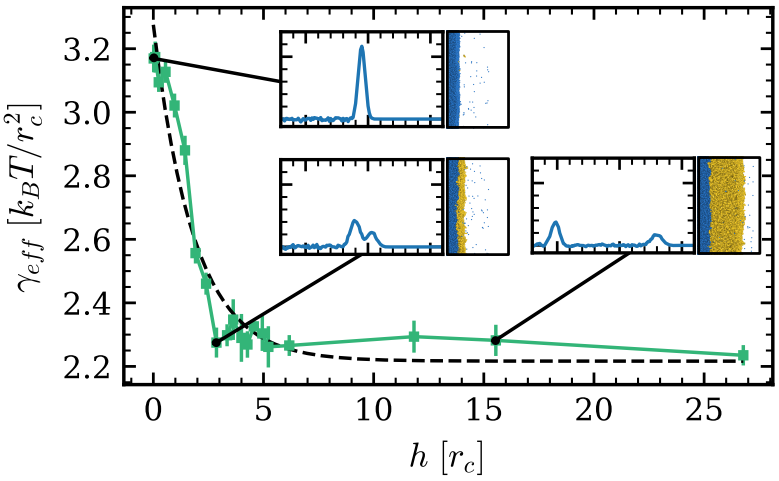

Figure 4.U.3.: Effective surface tension versus film thickness for free chains on liquid. The dashed line is a fit to $\gamma_{eff} = S_{o/w} \exp(-h/\xi) + \gamma_{eff,\infty}$ with $S_{o/w} = 1.06 \pm 0.06\,[k_BT/r_c^2]$, $\xi = 1.85 \pm 0.29\,[r_c]$, $\gamma_{eff,\infty} = 2.22 \pm 0.04\,[k_BT/r_c^2]$. Insets show the stress anisotropy at the interface for the different thicknesses with a single apparent interface, two overlapping interfaces, and two well separated interfaces. The corresponding simulation snapshots are also shown, where the simple liquid is shown in blue, while the polymers are shown in yellow.

To that end, we perform simulations of a thick slab of simple liquid placed in contact with polymeric liquid slabs of different thicknesses. We use the set of parameters described in section 3.2.1. The surface tension is calculated by integrating the stress tensor anisotropy across the interface. The results are shown in Figure 4.U.3. Each point corresponds to an average over 5 independent simulations, with the error bars corresponding to standard errors of the mean. The thickness is calculated as [65]

$$h = \frac{n_o N_o}{\rho_o \mathcal{A}} \tag{4.U.5}$$

where n_o is the number of polymer chains, $N_o = 5$ is the length of individual chains, $\rho_o \approx 2.95[r_c^{-3}]$ is the density of the polymer melt at equilibrium, and $\mathcal{A}$ is the surface area of the interface. The insets in Figure 4.U.3 show the shape of the stress tensor anisotropy at the interface for the different thicknesses. For low thickness we have a singular peak, for intermediate thickness two overlapping peaks, and for thick polymer films the two peaks are well separated. Finally, the dashed line corresponds to a fit to a function $\gamma_{eff}(h)$ and corresponding disjoining pressure $\Pi_o(h)$

$$\gamma_{eff}(h) = S_{o/w} \exp\left(-\frac{h}{\xi}\right) + \gamma_{eff,\infty} \tag{4.U.6}$$

$$\Pi_o(h) = -\frac{\mathrm{d}\gamma_{eff}}{\mathrm{d}h} = \frac{S_{o/w}}{\xi} \exp\left(-\frac{h}{\xi}\right) \tag{4.U.7}$$

where $\gamma_{eff,\infty} = \gamma_{ow} + \gamma_o$ and $S_{o/w}$ is the spreading parameter of oil on the droplet. Our choice is motivated by the fact that we have short range forces between the particles which leads to the assumption of a fast decaying disjoining pressure. The fit results in

$$S_{o/w} = 1.06 \pm 0.06\,[k_BT/r_c^2]\ ;\ \xi = 1.85 \pm 0.29\,[r_c]\ ;\ \gamma_{eff,\infty} = 2.22 \pm 0.04\,[k_BT/r_c^2]$$

where the errors are standard errors on the fitting parameters. The reasonable fit for the data supports the assumption made in the theory of sections 4.2.3 and 4.6 of an exponentially decaying disjoining pressure.

4.U.4. Curvature and surface tension: Tolman length

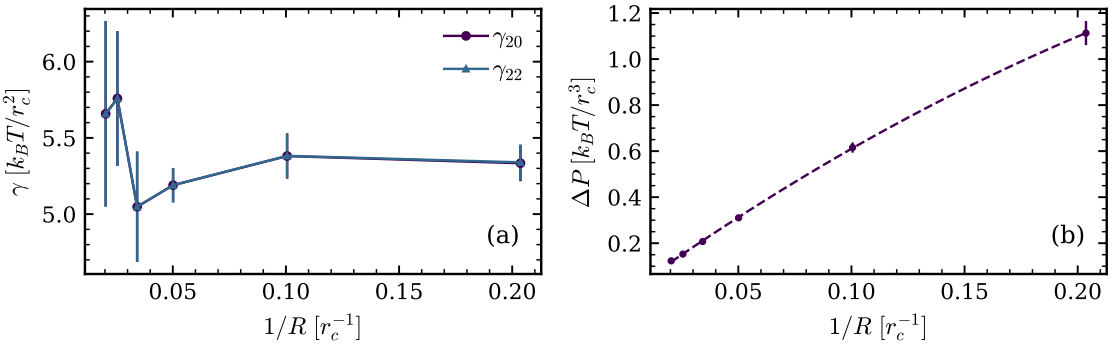

Figure 4.U.4.: (a) Surface tension versus the curvature of spherical drops based on capillary wave theory for spherical drops. The results for the '20' and '22' modes overlap. Even for the largest droplets, the results deviate from the surface tension of the flat interface $\gamma_w \approx 3.2\,k_BT/r_c^2$. (b) Laplace pressure versus the curvature of spherical drops. The dashed line is a fit accounting for the Tolman length correction $\Delta P = \frac{2\gamma_\infty}{R}\left(1 - \frac{\delta}{R}\right)$. The fit results in $\gamma_\infty = 3.5163 \pm 0.0023\,[k_BT/r_c^2]$, $\delta = 1.02 \pm 0.08\,[r_c]$ and y-intercept $\Delta P_\infty = -0.0214 \pm 0.005\,[k_BT/r_c^3]$.

It is common practice to treat the surface tension as a fixed quantity, and rely on measurements of the surface tension for flat interfaces to infer results for droplets. However, the surface tension may vary with the curvature of the interface. The dependence of the surface tension on the radius of curvature was first investigated for a single component system by Tolman [202]. Tolman considered the definition of surface tension based on the

Gibbs adsorption isotherm (a.k.a. Gibbs adsorption equation, see Ref. 54 §2.3 and §2.4) for a single species at liquid-vapor coexistence and followed the consequences for spherical interfaces to obtain

$$\gamma = \gamma_\infty \left(1 + \frac{2\delta}{R}\right)^{-1} \tag{4.U.8}$$

$$(\text{for } R \gg \delta) \approx \gamma_\infty \left(1 - \frac{2\delta}{R}\right) \tag{4.U.9}$$

where γ_∞ is the surface tension for a flat interface, R is the radius of curvature of the interface, and δ is known as the Tolman length. The last approximation corresponds to large drops $R \gg \delta$ which applies for most situations of interest. To investigate the effect of curvature on our system, in particular on the liquid droplet, we ran simulations for spherical droplets of different radii. The drops were initialized by extracting spheres from liquid slabs prepared as described in section 3.2.2.

As a first approach, we calculated the surface tension using an approach based on capillary wave theory, which relates the surface tension to thermally excited oscillation modes of the interface [203, key]. Considering a spherical coordinate system with the origin at the center of mass of the drop, the position of every point on the interface is $r(\theta, \varphi)$, where $\theta \in [0, \pi]$ is the polar angle and $\varphi \in [0, 2\pi]$ is the azimuthal angle. The shape of the interface at time t is expanded in spherical harmonics $Y_{lm}(\theta, \varphi)$

$$r(\theta, \varphi, t) = R + \sum_{l>0} \sum_{m} \zeta_{lm}(t) Y_{lm}(\theta, \varphi) \tag{4.U.10}$$

where $\zeta_{lm}(t)$ is the amplitude of the (l, m) mode, and $R \equiv \zeta_{00}$ is the unperturbed equilibrium radius of the drop. The surface tension is related to the fluctuation $\langle|\zeta_{lm}|^2\rangle$ in the amplitude of every (l, m) mode

$$\gamma_{lm} = \frac{k_B T}{(l-1)(l+2)\langle|\zeta_{lm}|^2\rangle} \tag{4.U.11}$$

where γ_{lm} is the surface tension obtained through a particular mode. The value of surface tension should be independent of the modes considered $\gamma_{lm} = \gamma$, but considering different modes provides independent measurements. To apply the theory we follow the approach described in the supporting information of Ref. 204. There, the drop at every measured frame is fit to an ellipsoid and the fluctuations in the axes of the ellipsoid are calculated. This is then related to the fluctuations of the $(l, m) = (2, 0)$ and the $(l, m) = (2, \pm 2)$ oscillation modes. From that two independent measurements γ_{20} and γ_{22} for the surface tension are obtained. The results for the surface tension versus the curvature of the droplet $1/R$ are shown in Figure 4.U.4 (a). At a first glance, it seems the curvature does not have

an effect on the value. However, the value obtained from both estimates at all curvatures deviates significantly from the value for a flat interface $\gamma \approx 3.2\,[k_BT/r_c^2]$.

As a second approach to quantify the Tolman length we calculate the Laplace pressure across the spherical interface (see section 2.1.1.1). Accounting for the Tolman correction, the Young-Laplace equation becomes [51]

$$\Delta P = \frac{2\gamma_\infty}{R}\left(1 - \frac{\delta}{R}\right). \tag{4.U.12}$$

Where ΔP is the Laplace pressure and $R \gg \delta$ is the equilibrium radius of the droplet. Having the Laplace pressure and the equilibrium radius of the droplet from simulation we fit ΔP vs $1/R$ to Eq. (4.U.12). The results are shown in Figure 4.U.4 (b). The data points fit the expectation nicely, and the fit parameters have reasonable values

$$\gamma_\infty = 3.5163 \pm 0.0023\,[k_BT/r_c^2]\,;\ \delta = 1.02 \pm 0.08\,[r_c]$$

where the errors are standard errors on the fitting parameters. In addition, the y-intercept (Laplace pressure for the flat interface) $\Delta P_\infty = -0.0214 \pm 0.005\,[k_BT/r_c^3] \approx 0$ as expected. The calculated value for γ_∞ is reasonably close to the value calculated for flat interfaces $\gamma \approx 3.2\,[k_BT/r_c^2]$, though it still falls outside the confidence interval. The value of the Tolman length is on the order of the size of a molecule, also as expected.

To conclude this section, we reiterate the discrepancy between the surface tension for flat interfaces and the results obtained through the application of capillary wave theory to the spherical drop, especially compared to the significantly better performance of the approach based on the measurement of the Laplace pressure. The discrepancy in the first approach can be explained by the fact that the theory that leads to Eq. (4.U.11) does not account for the possible variation of the surface tension with curvature and assumes a constant value. This is a valuable observation as it illustrates that applying capillary wave theory in a naïve manner may lead to strikingly misleading results.

4.U.5. Cylindrical droplets

In section 2.1.3 we described line tension, which, if present, can affect the wetting properties of the system. In section 4.2.4.1 we show that indeed our system does have some dependence on the curvature of the contact line (see Figures 4.9 and 4.9). In particular, we show that the line tension in our system is negative, i.e. it acts to decrease the contact angles. To avoid such effects, it is customary in MD simulation of droplets to use cylindrical droplets [117, 184]. Such simulations are set up such that the simulation box has a long dimension and short dimension, and periodic boundary conditions. If the droplet is large enough, it will form a rivulet across the periodic boundary of the short dimension and adopt a cylindrical equilibrium shape, as opposed to the typical spherical shape.

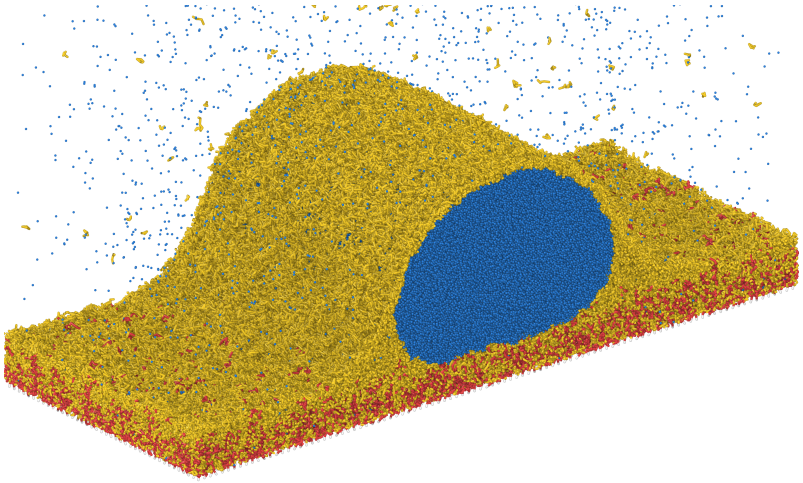

Figure 4.U.5.: Simulation snapshot from a cylindrical droplet simulation.

To investigate the differences between spherical and cylindrical droplets for our system, we run simulations of cylindrical droplets on lubricated brushes. We set up the lubricated brushes in a manner similar to that described in sections 3.2.4 and 3.2.3, the difference being that we choose a different number of grafting sites in the x and y-directions. Our short dimension will always be along the y-direction. We prepare systems with $N_x \times N_y \in \{100 \times 20,\ 120 \times 20,\ 120 \times 40,\ 120 \times 50\}$, at a grafting density $\sigma = 0.25\,[r_c^{-2}]$. The resulting box sizes are $L_x \times L_y \in \{200 \times 40,\ 240 \times 80,\ 240 \times 40,\ 240 \times 80\}\,[r_c^2]$. To place the droplets on the brush, we extract a half cylinder from a simple liquid slab and place it in contact with the brush. The axis of the cylinder is along the y-direction, and its length is equal to L_y. The radius of the cylinder is varied to study the effect of droplet curvature. We use radii $R \in [10, 50]\,[r_c]$. For the larger values of L_y, certain values of R result in a rivulet instability and the cylinder break into spherical droplets.[1] A snapshot from a simulation of a cylindrical droplet is shown in Figure 4.U.5.

We begin by investigating the cloaking of the droplet. In section 4.2.3 we show the existence of a cloaking transition which sets in at a particular oil fraction Φ^*. The transition fraction Φ^* depends on the radius of curvature of the drop as well as other factors (see Eq. (4.11)). For a valid comparison we use cylindrical drops with radii comparable to the spherical drop. Figure 4.U.6 shows the calculated cloak thickness versus the oil fraction Φ for cylindrical drops of different radii and box lengths, as well as the results for a spherical drop of radius $R \approx 45\,[r_c]$. For all of the simulated systems the transition occurs at $0.333 < \Phi^* \leq 0.444$. The inset shows the values of the thickness without averaging at $\Phi = 0.444$. We see that the spread is largest for the $R = 30\,[r_c]; L_y = 40[r_c]$ droplet, with one of the data points corresponding to a vanishing thickness. This could be an indication that the transition sets in later for this smaller drop, which is predicted by the thermodynamic considerations resulting in Eq. (4.11). The smallest spread corresponds

[1] The rivulet instability kicked in when $R < 15\,[r_c]$ for $L_y = 80\,[r_c]$, and when $R < 20\,[r_c]$ for $L_y = 100\,[r_c]$

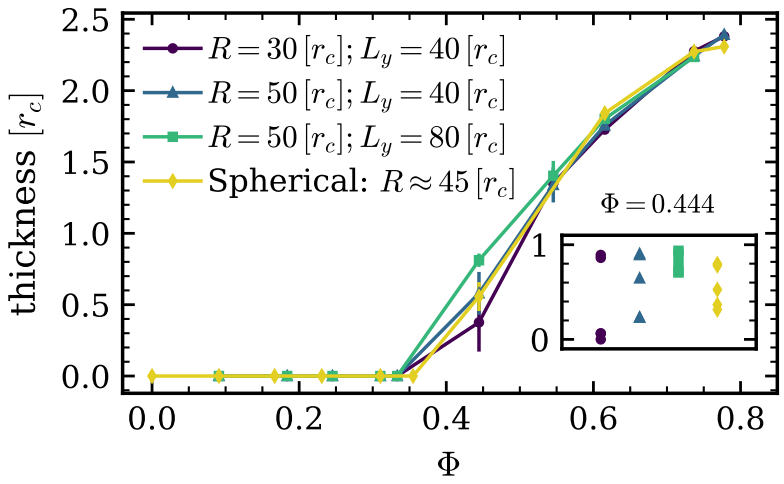

Figure 4.U.6.: Thickness of the cloak versus oil fraction Φ for cylindrical droplets. The different lines correspond to variations in the radius of the drop and the box length in the short dimension. Within the values of Φ we chose, no detectable change in the transition point is found. The thickness varies slightly for the three lines near the transition at $\Phi = 0.444$. Inset shows the individual data points at $\Phi = 0.444$. The larger spread for the smaller radius may indicate a delay in the onset of the transition as expected from Eq (4.11).

---

to the $R = 40\,[r_c]; L_y = 80[r_c]$ droplet, and that is likely due to the larger sample in the larger system, as all results are averaged over the y-direction.

Afterwards, we study the effect of the drop curvature on the equilibrium contact angle on dry brushes. We in addition vary the box dimensions to capture any finite size effects. The results are shown in Figure 4.U.7 (a). Except for the smallest droplets, the contact angle seems independent of the curvature of the cylindrical droplet. For very small radii we see some variation which is likely due to the drop "sinking" into the brush which results in smaller apparent contact angles. The correction due to the Tolman length should result in a small variation of the contact angle, but given the parameters from section 4.U.4 it is expected to be smaller than 1°. The dimensions of the box also do not seem to influence the results, although L_y is more than doubled.

Finally, we investigate the effect of lubrication on the contact angle. As described above, the cloaking of the drop is expected to affect the contact angles as it results in a smaller effective surface tension of the drop (see also section 4.U.3). As the equilibrium contact angle on dry brushes is larger than 90°, the decrease in droplet surface tension should lead to larger contact angles. To compare cylindrical and spherical droplets, we use similar oil fractions as those used for the spherical drop. We again vary the box length and the radius of the cylindrical droplet, and show the results for a spherical drop with a radius of curvature $R \approx 45\,[r_c]$. For the cylindrical droplets the contact angle is unaffected by the

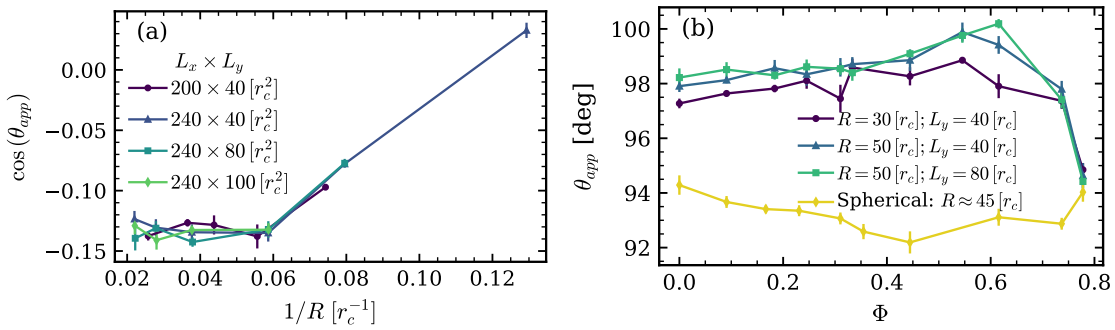

Figure 4.U.7.: (a) Cosine of the apparent contact angle versus the curvature of cylindrical drops on dry brushes. Boxes of different dimensions are shown. For larger droplets, neither curvature nor box size seem to affect the result. (b) Apparent contact angle versus oil fraction Φ. The droplet radius and the box length in the short dimension are varied. Also shown are the results for a spherical droplet with a radius of curvature $R \approx 45\,[r_c]$.

---

change in Φ until the cloaking transition sets in, where for the larger droplets the contact angle seems to increase slightly, before rapidly decreasing due to the drop "sinking" into the brush for very high oil fractions. This is to be contrasted with the spherical drop, where all values of the contact angle are smaller than those for cylindrical drops, but more importantly, the contact angle seems to be decreasing as the oil fraction increases, until the cloaking sets in and it increases slightly again. In section 4.2.4.2 we speculated that the decrease is likely due to changes in the magnitude of line tension. This speculation is partly validated by the behavior of the cylindrical droplets, as before the cloaking transition they are unaffected, and after the cloaking transition they exhibit a slight increase in contact angle.

4.U.6. Summary of unpublished results

We began by calculating liquid-vapor coexistence phase diagrams for the MDPD model for a simple liquid and polymeric liquid. Afterwards, we calculated the liquid vapor surface tension for each type of liquid with the aim of matching the ratios of surface tension in simulation to the values in the experiments. The results for the phase behavior and interfacial tension guided our choice of interaction parameters in the simulations.

Afterwards, we quantified the disjoining pressure of lubricant on the drop and found an exponentially decaying disjoining pressure, which is consistent with the short ranged forces in our simulations. In addition, as we are investigating small droplets, we studied the effect of curvature on surface tension as summarized through the Tolman length. Here we find that applying capillary wave theory blindly to small spherical droplets results in wrong values of the surface tension, and in our system showed no variation with curvature. We found that a better approach is to calculate the Laplace pressure across the interface of

spherical droplets and extract physical quantities through fitting to the Young-Laplace equation that includes the correction due to curvature.

Finally, to eliminate the effect of line tension and compare to the published results, we perform similar analysis on cylindrical droplets as we did for spherical droplets. The cloaking transition and cloak thickness coincide for the spherical and cylindrical drops suggesting that they are not strongly affected by line tension for the spherical droplet size we investigated; in addition, the are not affected by the length of the cylindrical droplet. As expected, the apparent contact angle for cylindrical droplets on dry brushes does not depend on the size of the droplet, except when it is small enough to sink into the brush. There also does not appear to be a finite size effect relating to the length of the cylindrical droplet, at least in the range of box sizes we studied. The apparent contact angles for cylindrical droplets are larger than the angles for spherical droplets. In addition, on lubricated brushes, the apparent contact angle for cylindrical droplets appears to increase with the fraction of lubricant, although the change is only a couple of degrees. This increase is expected with cloaking, as the contact angles are larger than 90° and cloaking reduces the droplet surface tension. This is in contrast to the case of a spherical drop where the apparent contact angle seems to gradually decrease for a certain range of lubrication, before increasing again. This is an indication of the effect of line tension, and possibly shows that the magnitude of line tension slightly increases with lubrication, as the negative line tension we found promotes spreading, resulting in smaller contact angles.

5. Wetting Ridge Growth Kinetics on Lubricated Gels

Note: This chapter reproduces the results from the publication in Ref. 205. Additions and changes from the original publication are marked with a violet text color, while omissions are marked through the symbol [...].

Contributions to publication:

- **Theoretical model setup:** the main model was formulated by F. Schmid. Modification, and extensions to the model were performed by R.G.M. Badr and F. Schmid.
- **Analysis and figures in original publication:** R.G.M. Badr generated and analyzed the theoretical data in the original publication. Experiments were performed by co-authors. Part of the analysis of experiments was performed by R.G.M. Badr. Interpretation of the results was performed by R.G.M. Badr in collaboration with the co-authors.
- **Writing:** R.G.M. Badr in collaboration with F. Schmid wrote the bulk of the theoretical results sections. The introduction was written by co-authors. Experimental results section written by R.G.M. Badr and co-authors. Conclusion to the original article was mainly written by J. T. Pham with minor contributions from R.G.M. Badr.

5.1. Introduction

Wetting on soft surfaces has gained significant attention for the wide range of potential applications, from soft robots [206] and biological processes [207] to adhesives and self-cleaning coatings [208, 209]. Drops on soft elastomers generate an out-of-plane deformation around the three-phase contact line, known as a wetting ridge, due to the drop surface tension pulling vertically on the surface [210–214]. Such behavior is more easily observed when the modulus of the polymer network is soft enough for the surface tension force to cause visible deformations. This ridge can play a role in drop spreading, drying, and sliding [77, 215–222]. Similarly, wetting ridges can also be found on slippery, lubricant-infused surfaces, although these ridges are comprised purely of liquid lubricant [163, 223–226]. Swollen elastomers, which are polymer networks infused with a liquid, can behave as an intermediate between these two cases; the swelling liquid can separate from the polymer network, making the wetting behavior even more complex [37, 80, 107, 227–239]. Specifically, when a drop is placed on a swollen elastomer, the imbibed liquid may phase separate at the contact line, affording a pure liquid phase at the wetting ridge tip [38, 219, 236, 240]. While wetting-induced phase separation on swollen elastomers has been investigated, the shape and growth dynamics of the phase separated region is not well understood, especially as a function of the swelling oil viscosity. Such information is critical for designing time-dependent processes for soft polymer coatings.

To study soft wetting, silicone elastomers (e.g., crosslinked polydimethylsiloxane, PDMS) are one of the most widely used substrates, [80] due to their commercial availability, easily tuned modulus, and simple preparation methods [38, 215, 228, 241–246]. However, many elastomers contain uncrosslinked molecules (i.e. extractable oils) that are left over after curing, which serve as a liquid swelling agent in the network [247–249]. Hence, these materials are two-component systems that include a crosslinked network and an uncrosslinked liquid; the liquid phase is effectively a high viscosity silicone oil. For example, the Sylgard 184 elastomer kit has a base liquid polymer with a viscosity of $\sim 5000\,\mathrm{cSt}$, which likely makes up most of the remaining extractable oil in the elastomer after curing [34, 35, 247]. This high viscosity imbibed oil can play an important role in dynamic surface properties, like drop sliding dynamics [250] and adhesive detachment dynamics [251]. However, prior studies have not investigated the phase separation shape and dynamics with varying oil viscosities.

In this work, we study the dynamics of wetting-induced oil phase separation of on lightly crosslinked elastomers near the contact line of a liquid drop (Figure 5.1a). We focus on how the oil viscosity (i.e., molecular weight) and the degree of swelling (i.e., amount of infused oil) affects the size and growth rate of the separated oil region (Figure 5.1b-c). For highly swollen networks, the oil separation size increases with time after a drop is placed on the surface. The separation occurs faster at early times and then slows at longer times. For intermediately swollen elastomers, the oil separation size reaches a maximum and remains constant with time. The separation rate is a function of the oil viscosity; lower viscosities separate more and faster at early stages, while the ridge growth is faster for higher viscosity during later stages. Interestingly, we observe that the growth of the

oil region grows with a consistent geometry that scales up during growth. Motivated by the slow time scales at the later stages of growth, we supplement the experiments with a theoretical model for the diffusion of oil from the gel into ridge. Our result suggests that phase separation size and rate are strongly affected by the viscosity and amount of oil in soft elastomers, which may provide insight into the design of soft polymer coatings.

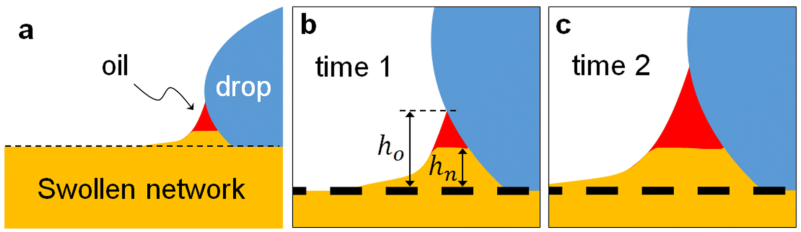

Figure 5.1.: Schematic diagram illustrating the experiment. (a) A drop is placed on swollen elastomer, creating a zone of oil separation near the contact line. (b) and (c) Zoomed-in regions of the contact line at two different time points. The oil (h_o) and network heights (h_n) are measured over time, with the separation height given by $\Delta h = h_o - h_n$. At an early time point (e.g. time 1), there is a small amount of oil separation. At a later time point (e.g. time 2), the h_n remains constant and h_0 increases. Note that the wetting ridge zone is not to scale and serves only to describe the process.

5.2. Growth of phase separated wetting ridges on lubricated gels

5.2.1. Surfaces with different viscosity oils

To prepare our surfaces, we use a commercially available polydimethylsiloxane (PDMS) elastomer kit (Sylgard 184, Dow) with a base to crosslinker ratio of 60:1 by weight; this leads to an as-prepared Young's modulus of the order ~ 5 [kPa] [233, 245, 252]. At this high base/crosslinker ratio (noting that the manufacturer recommended ratio is 10:1), the base is in excess relative to the crosslinker, resulting in uncrosslinked chains that remain in the as-prepared samples after curing. The properties of the uncrosslinked chains are generally unknown because they come from a commercial product and because there is limited control over the molecular weight distribution and architecture after curing. To control the number and molecular weight of free chains, we first remove these uncrosslinked chains by washing samples in hexane. In this procedure, the as-prepared samples are immersed in hexane for several days to allow the uncrosslinked chains to migrate from the elastomer into the surrounding solvent. The process is repeated three times. The washed elastomers are then dried to remove residual hexane; we consider these washed samples as dry polymer networks. Details of this washing process are described elsewhere [38, 247].

To study the effect of oil viscosity, the dry samples are swollen with different silicone oils. We use unreactive, trimethylsiloxy-terminated silicone oils with molecular weights of $14\,\mathrm{kg \cdot mol^{-1}}$, $28\,\mathrm{kg \cdot mol^{-1}}$, and $49\,\mathrm{kg \cdot mol^{-1}}$, which have viscosities of 350, 1000, and

5000 cSt, respectively. To measure the maximum degree of swelling for the different molecular weights, we prepare dry blocks of 60:1 PDMS (1.5 x 1 cm x 1 mm) and subsequently immerse them in oil. Upon immersion, the oil penetrates the network until it reaches a maximum degree of swelling (i.e., saturated). The degree of swelling is defined as $Q = V_d/V_s$, where V_d is the volume of the dry sample and V_s is the volume of the swollen elastomer. For all molecular weights, Q increases with immersion time, indicating that silicone oil expands the PDMS elastomer (Figure 5.2). The rate of increase in Q is fast initially and slows down in the range of 25-50 days, although Q continues to increase after 135 days ($\sim$ 4.5 months). As anticipated, the maximum degree of swelling and the rate of swelling decrease with increasing molecular weight. At 135 days, $Q \sim 4.0$ for $14\,\mathrm{kg \cdot mol^{-1}}$ oil, ~ 2.9 for $28\,\mathrm{kg \cdot mol^{-1}}$ oil, and ~ 2.0 for $49\,\mathrm{kg \cdot mol^{-1}}$. Q appears to be approaching a maximum at 135 days. The increase in swelling over these long times may be due to the slow reaching of equilibrium by swelling thick samples with high viscosity oil or possibly due to chains breaking (e.g. hydrolysis) and altering the equilibrium swelling ratio. Nevertheless, since these values are approaching a plateau, we assume these are around their saturated swelling states, and will be used as a baseline comparison for preparing swollen, micron-scale thick films for the following wetting experiments. It should be noted that due to challenges in high viscosity swelling and sample preparation of thin films of micron-scale thickness, some variations exist in the maximum measured Q in the following samples for wetting experiments.

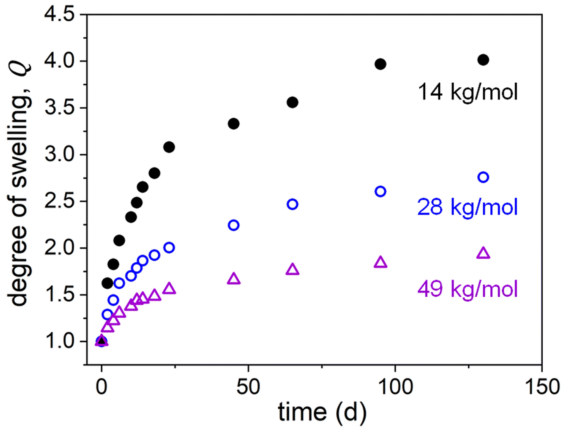

Figure 5.2.: The degree of swelling Q as a function of immersion time in days for macroscopic, bulk PDMS elastomers being swollen with silicone oil having molecular weights of $14\,\mathrm{kg \cdot mol^{-1}}$, $28\,\mathrm{kg \cdot mol^{-1}}$, and $49\,\mathrm{kg \cdot mol^{-1}}$.

5.2.2. Observing time-dependent phase separation

To investigate the wetting ridge at the periphery of a drop, a glycerol drop is placed onto the surface while imaging its contact line. Glycerol is used because it has a similar surface tension to water, low volatility, and does not swell or mix well with PDMS [34]

or silicone oil [253], which are important for long term wetting experiments. Moreover, we previously found that the spreading parameter S should be positive for oil separation to occur spontaneously [38, 80]; $S > 0$ for a glycerol and silicone oil system. In Figure 5.3a, confocal images are presented for a drop on a surface with $14\,\mathrm{kg \cdot mol^{-1}}$ oil and a measured swelling of $Q = 4.1$ ($\sim$ maximum swelling). At early stages (30 s), the swollen polymer network is pulled up and a small amount of oil separation is visible. This suggests that the emergence of the phase separated region is a fast process. One can hypothesize that at initial contact (t=0), the drop interfaces with both polymer network chains and oil molecules. Shortly after, the oil separates and the vertical interfacial stresses at the tip are mostly felt by the phase separated oil region. After 50 minutes (3000 s), more oil separated, while it appears that the polymer network relaxed in the vertical direction. After an even longer time of 5 hours (18000 s), the oil separation becomes more apparent. Additionally, it is observed that not only does the height of the distinct oil wetting ridge grow over time, but so does the width to the same extent; that is, the shape remains geometrically similar.

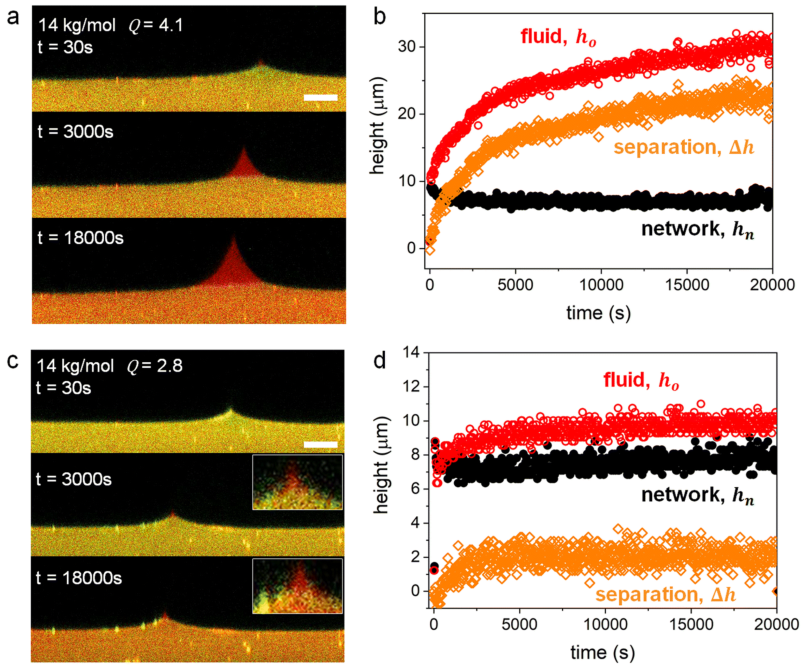

Figure 5.3.: (a) and (c) Confocal imaging of oil separation during wetting of a glycerol drop on PDMS elastomers swollen with $14\,\mathrm{kg \cdot mol^{-1}}$ silicone oil. The insets in (c) are to illustrate oil separation more clearly at these low separations. (b) and (d) The corresponding measured heights are plotted. The degrees of swelling Q are (a) and (b) 4.1 and (c) and (d) 2.8. Scale bar: $20\,\mu\mathrm{m}$

To gain more insight into this time-dependent process, we measured the maximum network height h_n and the oil tip height h_o relative to the original, unperturbed surface. The

separation size is calculated from these values, defined as $\Delta h = h_o - h_n$. These heights are presented in Figure 5.3b for the corresponding images in Figure 5.3a. Consistent with our confocal images, the oil separation size increases as a function of time. In the short time regime (e.g. 30 s), a quick formation of the network wetting ridge is observed when the drop is placed, while a very small Δh is observed. However, h_o increases with increasing time. After 3000 s, $\Delta h \approx 16\,\mu$m , and reaches $\approx 30\,\mu$m at 18000 s. This qualitative trend also holds for a polymer network swollen to a lower degree of $Q = 2.8$ (Figure 5.3c), but with smaller Δh. In this case, we find again that the network wetting ridge forms quickly, but without clear oil separation at $t = 30$ s. After 3000 s, a small amount of oil separation can be visualized, which appears to be maintained after 18000 s. This is evident in Figure 5.3d, which shows that the separation size Δh reaches $\sim 2\,\mu$m after about $\sim$ 2500s; thereafter it does not increase significantly with time (Figure 5.3c-d). This concept of a stable Δh is consistent with our prior work on low molecular weight oils ($770\,\mathrm{g \cdot mol^{-1}}$), which showed an apparently stable oil separation after a few minutes [38]. When the degree of swelling is decreased even more to $Q = 2.1$, effectively no oil separation is visible in our confocal images. The data becomes rather noisy, and the oil and network heights are difficult to discern. It is likely that a small amount of oil does separate, which is outside the resolution limit of our confocal microscope.

To investigate the idea of geometric similarity in the ridge, we trace the ridge shapes at different times and overlay them. Figure 5.4a shows the shapes of the ridge for $14\,\mathrm{kg \cdot mol^{-1}}$ oil at the highest swelling for all times. The lines are colored according to the measurement time, gradually changing from dark purple at early times to light yellow at the latest time. To show the similarity in the shape, we rescale the ridges at different times to have the same ridge height, as measured from the unperturbed surface of the network. Figure 5.4b shows the ridge at different times after rescaling. As it turns out, the ridge initially steepens with time (illustrated by the outlying purple lines), but soon assumes a invariant shape. Except for the outlying early times, we see a collapse of the shapes after rescaling. At equilibrium, a self-similar shape is expected to appear as the result of a point load on a viscoelastic medium [254], and we believe this manifests itself in the geometrically similar growth of the liquid ridge at steady state. To further characterize the shape during growth, we measure the opening angle at the tip of the separated ridge. To measure the angle, we take the 30 points closest to the tip of the ridge from either side, and fit each set to a line. This gives an approximation of the left and right tangents to the ridge. The opening angle is then calculated as the angle between those lines. The results for $14\,\mathrm{kg \cdot mol^{-1}}$ are shown in Figs. 4c and 4d at $Q = 2.8$ and $Q = 4.1$, respectively; the angles relax and take constant values after about 500 s and 1000 s, respectively. Both durations are shorter than the time needed to reach equilibrium, which is about 2500 s for $Q = 2.8$, and longer than 20000 s for $Q = 4.1$. The steady value for the measured angle further supports the similarity in the ridge shape during growth.

An interesting point is that the tip angle is relatively large (>40°). Due to the interfacial tensions at play in our system, vanishingly small angles are expected. The reason is because the spreading parameter of the oil on the glycerol is positive, meaning that at equilibrium, a Neumann configuration is not possible [80]. In addition, if the network is

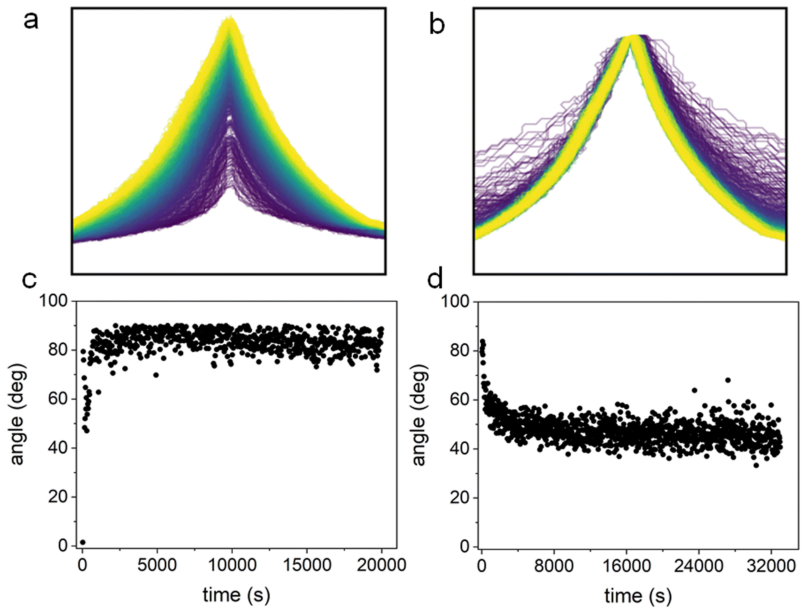

Figure 5.4.: Geometry of the wetting ridge for 14k and $Q = 4.1$. (a) Original ridge and (b) rescaled ridge at all times. The time span between two lines is about 30s, and the lines are colored according to the measurement time, gradually from dark purple at early times to light yellow at the latest time. Except for ridges at early times, the ridge shapes collapse to a common one after rescaling. (c) and (d) Opening angles of the oil ridge tip for 14k oil swollen surfaces for (c) $Q = 2.8$ and (d) $Q = 4.1$. The opening angle is measured using estimates of the tangents from both sides of the tip of the ridge

highly swollen, the oil likely cloaks the drop, leading to a vanishing angle at the tip of the ridge. Measuring angles from microscopy images suffers from inherent limitations, namely the imaging resolution and the inability of image analysis tools to find infinitely sharp corners in noisy images. This may lead to measured angles being larger than they are in reality. The reported angles should, therefore, not be taken as a sign of the existence of a stable Neumann state at equilibrium, but simply as an indication of the similarity of the shape of the ridge during growth.

To compare the oil separation for the different molecular weights, Δh for different Q are plotted for the 14, 28, and 49 $\mathrm{kg \cdot mol^{-1}}$ surfaces as a function of time (Figs. 5a-c). In the 14 $\mathrm{kg \cdot mol^{-1}}$ case, the sample with high swelling ($Q = 4.1$) displays a large separation size, which decreases with decreased swelling. Hence, the maximum separation size is a function of the degree of swelling. The same general trend is observed for the 28 $\mathrm{kg \cdot mol^{-1}}$ and 49 $\mathrm{kg \cdot mol^{-1}}$ oils (Figure 5.5b-c); when the networks are swollen to their maximum values, a large oil separation is observed ($Q_{\max} = 3.5$ for 28 $\mathrm{kg \cdot mol^{-1}}$ and $Q_{\max} = 2.3$ for the 49 $\mathrm{kg \cdot mol^{-1}}$), which decreases with decreased swelling. This can be conveniently observed in Figure 5.5b for the 28 $\mathrm{kg \cdot mol^{-1}}$ samples, where the long time Δh decreases

with decreasing Q. At a sufficiently low Q, the separation size Δh becomes too small to clearly image. For example, samples with $Q = 1.9$ for the $28\,\mathrm{kg \cdot mol^{-1}}$ and $Q = 1.4$ for the $49\,\mathrm{kg \cdot mol^{-1}}$ do not display clear separation, even after a long wetting time of ~ 5 hours; the values remain around $\sim 1\,\mu m$ with noisy data, close to our resolution limit. This little to no oil separation is consistent with our previous study suggesting that the fluid is held inside the polymer network for elastomers with a low Q, possibly due to osmotic pressure [38, 220, 227, 239].

To make a direct comparison between the different viscosity oils, we replot the highest swelling data from Figs. 5a-c in Figure 5.5d; during the duration of our experiments, the separation size clearly increases with decreasing oil molecular weight. However, we note that the lower molecular weight system has a larger absolute amount of oil within the network, since it has a higher maximum Q (Figure 5.2). Hence, it is not immediately obvious whether the molecular weight or the amount of oil in the network governs the oil separation size. One could also compare samples with similar degrees of swelling but different molecular weights (e.g. $Q = 2.3$ for $49\,\mathrm{kg \cdot mol^{-1}}$, $Q = 2.5$ for $28\,\mathrm{kg \cdot mol^{-1}}$, and $Q = 2.8$ for $14\,\mathrm{kg \cdot mol^{-1}}$, Figure 5.5a-c); however, $\Delta h_{\max}$ for these are not similar. For example, although the swelling ratio for $49\,\mathrm{kg \cdot mol^{-1}}$ is the lowest ($Q = 2.3$), the ridge height reaches higher values than for $28\,\mathrm{kg \cdot mol^{-1}}$ ($Q = 2.5$), followed by $14\,\mathrm{kg \cdot mol^{-1}}$, which has the highest swelling ratio of the three ($Q = 2.8$). These overall results indicate that even though the swelling ratio plays a role in $\Delta h_{\max}$, it is also strongly governed by the viscosity.

Figure 5. Separation height Δh as the function of wetting time with different degrees of swelling Q for PDMS elastomers swollen with silicone oil having molecular weights of (a) 14, (b) 28, and (c) $49\,\mathrm{kg \cdot mol^{-1}}$, respectively. (d) Separation height Δh as the function of wetting time for elastomers swollen with different molecular weight oils near their maximum; $Q_{\max} = 4.1$ (black, $14\,\mathrm{kg \cdot mol^{-1}}$), 3.5 (blue, $28\,\mathrm{kg \cdot mol^{-1}}$) and 2.3 (purple, $49\,\mathrm{kg \cdot mol^{-1}}$).

In addition to the separation size, we can make a comparison of the time-dependent, oil separation dynamics from Figure 55.5d for the different viscosities. For all samples, the oil separation occurs fastest in the early stages of wetting, which is then followed by a slower rate of oil separation. Qualitatively, one can observe that the early-stage oil separation occurs faster with lower viscosity oil. For example, the slope (separation height growth rate) of the curves in Figure 5.5d in the first 1500 s (25 minutes) increase with decreasing molecular weight. This is intuitive if we consider that the oil mobility will scale inversely with the molecular weight. On the other hand, the growth slows down after a certain point in time, suggesting two regimes.

5.2.3. Description of separation process

Based on our experimental findings, it is clear that the separation process is associated with both the molecular weight of the swelling oil and the swelling ratio. The timescale of the separation process is relatively long, suggesting that it is dominated by diffusion.

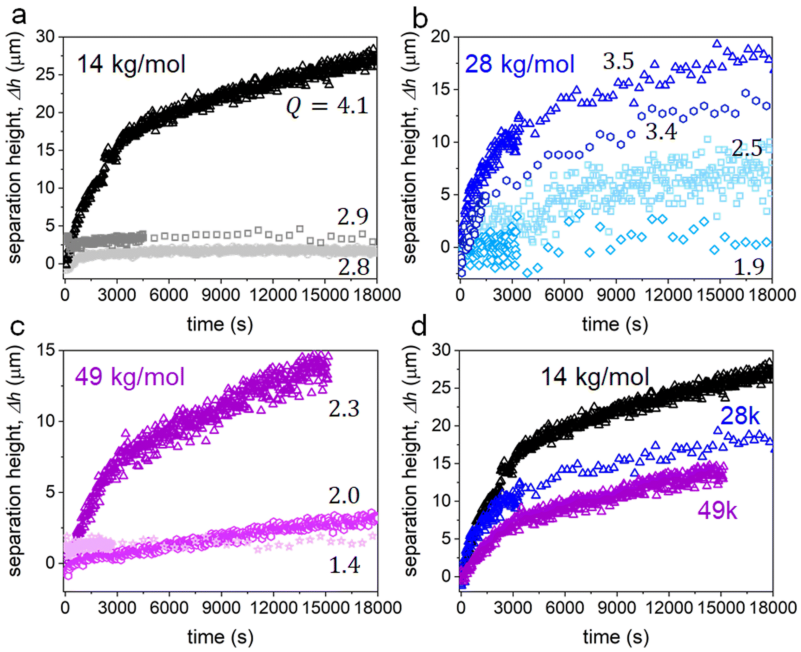

Figure 5.5.: Separation height Δh as the function of wetting time with different degrees of swelling Q for PDMS elastomers swollen with silicone oil having molecular weights of (a) 14, (b) 28, and (c) $49\,\mathrm{kg \cdot mol^{-1}}$, respectively. (d) Separation height Δh as the function of wetting time for elastomers swollen with different molecular weight oils near their maximum; $Q_{max} = 4.1$ (black, $14\,\mathrm{kg \cdot mol^{-1}}$), 3.5 (blue, $28\,\mathrm{kg \cdot mol^{-1}}$) and 2.3 (purple, $49\,\mathrm{kg \cdot mol^{-1}}$).

Given the time scales of our experiments, it is safe to consider that the system reaches the diffusion limit. To describe the phase separation growth dynamics, we consider that the ridge grows through the accumulation of oil near the three-phase contact line, and that the oil is supplied by a diffusive flow through the swollen network. To describe the process, we set up a simple diffusion model for the growth of the wetting ridge in the presence of a drop. A key part of a theoretical description of the process is the driving force for the accumulation of oil in the ridge. The accumulation of oil is driven by differences in chemical potential between the ridge and the network outside the three-phase contact line. The ridge chemical potential can be obtained from the free energy in the ridge. We consider the ridge to be composed of the elastic network and the phase separated fluid, located at the three-phase contact line. The ridge free energy F_r depends on the number of chains n_r in the ridge and will be a complicated expression with contributions from the elasticity of the network, interfacial tensions, and possibly other contributions. Developing a comprehensive theory for the ridge free energy goes beyond the scope of the present work. Instead, we approximate the free energy function by an expansion about its minimum, which corresponds to the saturated ridge with n_0 chains:

$$F_r \propto (n_r - n_0)^2 \tag{5.1}$$

where n_r is the number of chains in the ridge and n_0 is the number of chains at saturation, which is unknown. We consider the location of the ridge to be at the three-phase contact line radius R, and express the ridge free energy in terms of the line number density in the contact line

$$F_r = \int dl \frac{\kappa}{2} (\lambda - \lambda_0)^2 \tag{5.2}$$

where $\lambda \propto n_r/R$ and $\lambda_0 \propto n_0/R$ are the actual line density and the line density at saturation respectively, and κ is an unknown proportionality constant. The above-mentioned details of the physics in the ridge are captured implicitly within the two free parameters κ and λ_0. The details of the free energy in the ridge, however, should not play a major role, since the time evolution is dominated by slow diffusion.

For the free energy of the swollen polymer network, we include contributions from the translational entropy of the oil, in addition to a term relating to the elasticity of the network. The equilibrium free energy for the network is then chosen as

$$F_G = F_{id} + F_{el} \tag{5.3}$$

where F_{id} is the entropic contribution and $F_{el} \propto Q^2$ is the elastic contribution. To capture the local details in the network, the free energy can be expressed in functional form, which depends on the local fraction of oil at different positions within the network. Expressed in this way, the free energy takes the form

$$\mathcal{F}_G[\varphi] = \iiint_\Omega dV \left\{ \frac{\varphi}{N_o} (\ln \varphi - 1) + \frac{K}{2} \frac{1}{1-\varphi} \right\} \tag{5.4}$$

where the integral is evaluated over the volume of the network, N_o is the number of repeat units per oil chain, φ is the local fraction of oil, and K is the elasticity of the network. The first term in Eq. (5.4) is the entropic contribution of the oil, while the second term is the contribution from elasticity.

Equilibrium between the ridge and network is achieved when the chemical potentials in both are equal. The equilibrium line density $\lambda_e \leq \lambda_0$ is then given by

$$\lambda_e \equiv \lambda_0 + \frac{\mu_G^{eq}}{\kappa}. \tag{5.5}$$

Here μ_G^{eq} is the equilibrium chemical potential of the elastomer, which is negative and increases monotonously with φ and N_o. This means that when the swelling or the molecular

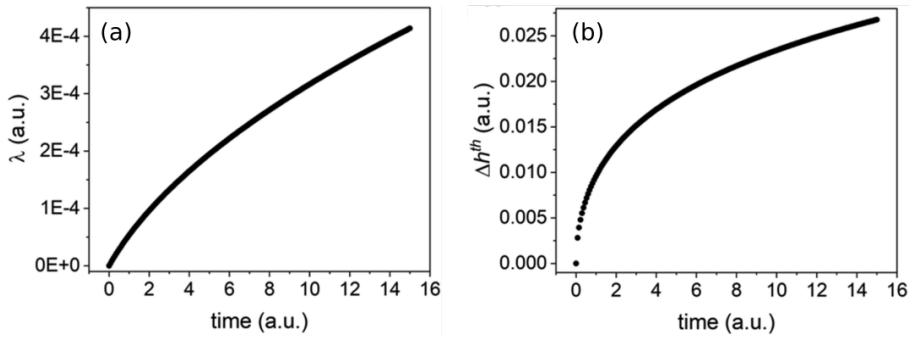

Figure 5.6.: (a) $\lambda(t)$ vs. time as the direct result of solving the dynamical equations. (b) The separation height as calculated using $\lambda(t)$ in eqn (9) and (10).

---

weight of the oil increases, more material will accumulate in the ridge at equilibrium. This provides theoretical support for the observations made earlier in Figure 5.5.

For the out of equilibrium situation, having the expressions for the free energies of the ridge and the network enables us to derive dynamic equations. At the ridge, the flux j_r into the ridge is driven by the difference in chemical potential between the ridge and the network

$$j_r \propto \mu_r - \mu_G. \tag{5.6}$$

Within the network, the local flux j_G is driven by local gradients in chemical potential. Using variational calculus, Eq. (5.4) can be varied to obtain the local flux j_G at every point within the network, in a fashion similar to Fick's first law. Combining the flux with a continuity equation results in a diffusion equation for the local fraction of oil within the network

$$\partial_t \varphi = M \nabla_r \left\{ \left[\frac{1}{N_o} + \frac{K\varphi}{(1-\varphi)^3} \right] \nabla_r \varphi \right\} . \tag{5.7}$$

Since our focus is on the separation rate, we assume that the liquid separates immediately from the network upon the formation of the ridge. With this assumption and since no material is lost during the growth of the ridge, any oil leaving the network must accumulate in the pure liquid ridge. With this we set up our diffusion equation with the appropriate boundary conditions, namely

$$j_G = -j_r. \tag{5.8}$$

The full details on the derivation of the theoretical model are included in the Appendix. The diffusion equation with the boundary condition does not admit analytical solutions; we use a simple spatial discretization and integrate it with a forward Euler scheme.

Solving the dynamical equations gives us the line density within the ridge as a function of time $\lambda(t)$. An example of a solution is shown in Figure 5.6a. To compare the results from the theory to the experiment, it is necessary to calculate the separation height from the line density. To accomplish this, we first calculate the volume of the phase-separated ridge from $\lambda(t)$ as

$$V(t) = \frac{2\pi R\lambda(t)N_o}{\rho} \tag{5.9}$$

where ρ is the density of the liquid, R is the radius of the three-phase contact line, and N_o is the number of repeat units per chain. As noted earlier in Figure 5.4, the shape of the phase-separated ridge shows geometrically similar growth. This kind of growth can be exploited to calculate the separation height from the volume of the ridge without having a detailed shape for the ridge. The similarity assumption, combined with the fact that the radius of the contact line ($\sim$ mm) is much larger than the size of the ridge ($\sim \mu m$), implies that the volume scales quadratically with the height of the ridge $V(t) \propto \Delta h^2(t)$. As time progresses, the height of the ridge scales up by a factor of $\alpha(t) = \frac{\Delta h(t)}{\Delta h_0}$, where Δh_0 is a reference height at a time t_0. We then have for the scaling factor $\alpha(t) = \sqrt{V(t)/V_0}$, where V_0 is the volume at time t_0. This finally allows us to relate the separation height to the volume of the liquid ridge

$$\Delta h(t) = \Delta h_0 \sqrt{\frac{V(t)}{V_0}}. \tag{5.10}$$

Using Eqs. (5.9) and (5.10) we can calculate the separation height $\Delta h(t)$ from $\lambda(t)$ as shown in Figure 5.6b.

With the goal of comparing our experimental data to this simplified theory, we solve the diffusion equation for a given set of fixed parameters (e.g. modulus of the material and the drop size, details in the Appendix) and vary the molecular weights and swelling ratios; these are chosen based on the molecular weight and swelling ratios from experiments. The parameter that appears in the theory (i.e., in the translational entropy) is the degree of polymerization of the oil N_o. For the 14, 28, and 49 $\mathrm{kg \cdot mol^{-1}}$ oils, N_o values are set to 184, 378, and 667 respectively, assuming a repeat unit (monomer) molar mass of 74 g/mol. The mobility in the theory is taken as $M = \frac{M_0}{N_o}$, such that it scales inversely with the molecular weight and M_0 is the mobility of an individual monomer. This assumes that there is no effect of entanglements. In the diffusion regime, the only effect of entanglements is that the mobility M varies more strongly with molecular weight M_w [255]. When it comes to inter-chain entanglements, an estimation of the entanglement molecular weight M_c for PDMS yields $M_c = 33 \pm 7\,\mathrm{kg \cdot mol^{-1}}$ [256]. A study of the transition between the two regimes shows that it can be smooth [257]. The $14\,\mathrm{kg \cdot mol^{-1}}$ is below M_c while the $28\,\mathrm{kg \cdot mol^{-1}}$ falls is within the confidence interval from below, and we will consider both to not have entanglements. The mobility of the $49\,\mathrm{kg \cdot mol^{-1}}$ oil might include

effects from entanglements. However, given the smoothness of the transition and that the molecular weight is not too far above the $M_c$value confidence obtained by Valles and Macosko [256], we assume that inter-chain entanglement plays a small role and will be neglected. Moreover, for elastomers prepared from commercial kits as we do here, it is difficult to estimate the density of crosslinks and strand lengths, which are relevant for determining the properties of the swollen elastomer [258]. Previous studies on the diffusion of unreactive PDMS chains in PDMS networks found that up to weight average molecular weights of $30\,\mathrm{kg}\cdot\mathrm{mol}^{-1}$, Rouse dynamics still govern the diffusion [259, 260]. Taking this into consideration, we use the scaling $M \propto \frac{1}{M_w}$ for our mobility.

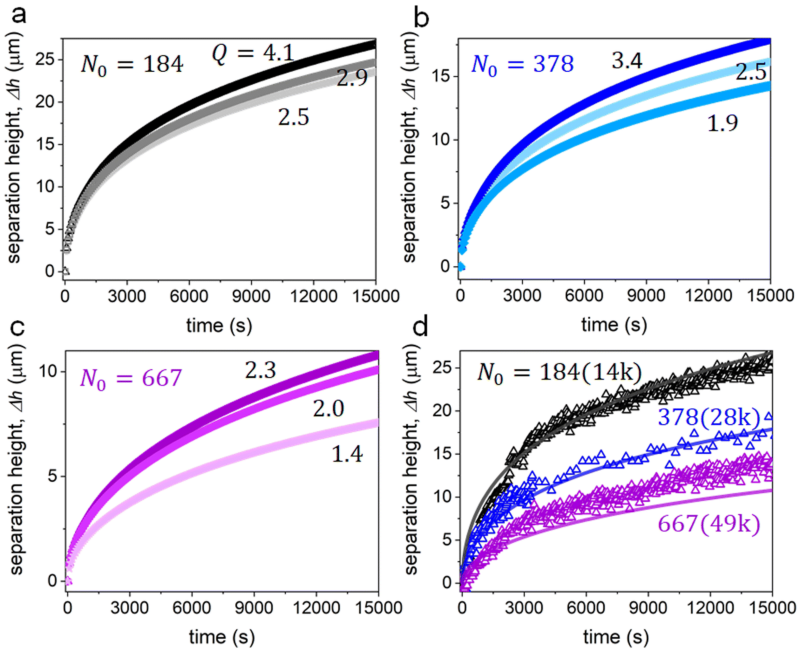

Figure 5.7.: Theoretical separation height $\Delta h_{th}(t)$ vs. time at different swelling ratios for (a) $N_o = 184$, (b) $N_o = 378$, (c) $N_o = 667$. (d) Same as (a)–(c) but for the highest swollen elastomers with oils of different molecular weights. The theoretical results are shown in solid lines, while the experimental results in triangles.

The results for the theoretical separation heights Δh_{th} are shown in Figure 5.7, which is designed to be analogous to Figure 5.5. Figs. 5.7a-c show the evolution of the separation height for $N_o = 184,\ 378,\ 667$ respectively, at different swelling ratios. One difference is apparent between the theory (Figs. 7a-c) and the experiments (Figs. 5a-c) for lower swelling ratios. In the experiments, we have little and quickly saturating growth for low swelling ratios, while in the theory the growth is significant and slow for all swelling ratios. Since the ridge heights reached for low swelling are much smaller than for high swelling, it is possible that all of the necessary oil is supplied from the immediate surrounding of the ridge, and equilibrium is reached before the diffusive regime sets in. One possible explanation for the discrepancy is our choice of parameters in the free energy for the ridge Eq. (5.2). We

choose the same value for the proportionality constant κ and for the saturation line density λ_0 while both could depend on the swelling ratio. For $Q_{\max}$ in particular, the theoretical curves are in good qualitative agreement with the experiments. This is illustrated in Figure 5.7d, showing the evolution of the separation height for different molecular weights at the highest swelling ratios for both theory (lines) and experiment (triangles). Above we made the choice for the scaling law of the mobility as $M \propto 1/M_w$, based on observations from the literature [259, 260]. The agreement of the theory with the experiment in Figure 5.7d supports the validity of this scaling.

To better quantify the similarities and differences we plot the data in a logarithmic scale and extract power law exponents of the form $\Delta h \propto t^{\beta}$. Figs. 8a and 8b show the data on a logarithmic scale for the experimental results and the theoretical results respectively, for different molecular weights at high swelling. The grey dotted lines in the plots are power law fits for the data at $t \geq 7500$s. It is clear in both the experiment and theory that different regimes exist at early and late stages, as evident from the deviation of the fit from the curves. The experimental exponents with standard errors are $\beta_{ex} = 0.296 \pm 0.005$ ($14\,\mathrm{kg \cdot mol^{-1}}$), 0.338 ± 0.029 ($28\,\mathrm{kg \cdot mol^{-1}}$), and 0.489 ± 0.016 ($49\,\mathrm{kg \cdot mol^{-1}}$), while the theoretical exponents are $\beta_{th} = 0.335$ ($N_0 = 184$), 0.356 ($N_0 = 378$), and 0.412 ($N_0 = 667$). The experimental and theoretical exponents are in reasonably good agreement, suggesting that the mechanisms governing the long-term growth of the ridge are most likely simple diffusion and geometry.

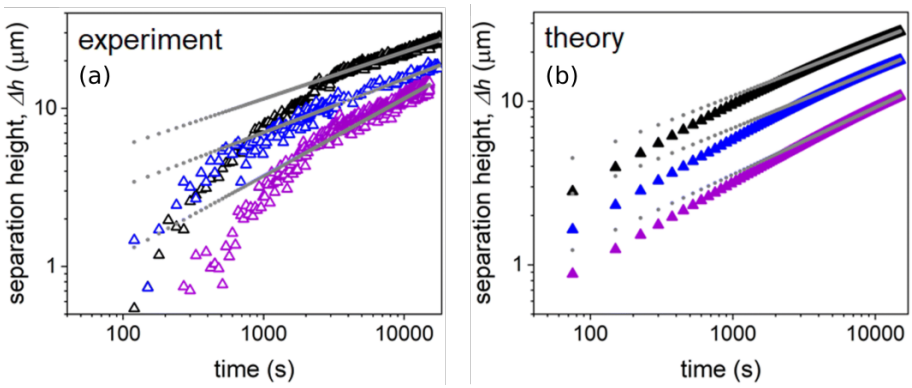

Figure 5.8.: (a) Logarithmic plot of the experimental height vs. time for saturated elastomers with different oil molecular weights. The grey dots are power law fits with $\Delta h \propto t^{\beta_{ex}}$ for $t \geq 7500\,\mathrm{s}$. $\beta_{ex} = 0.30, 0.34, 0.49$ for the 14 $\left[\mathrm{kg \cdot mol^{-1}}\right]$, 28 $\left[\mathrm{kg \cdot mol^{-1}}\right]$, 49 $\left[\mathrm{kg \cdot mol^{-1}}\right]$ molecular weight oils, respectively. (b) The same plots as part (a) but for the theoretical results. The grey dots are power law fits $\Delta h \propto t^{\beta_{th}}$ for $t \geq 7500\,\mathrm{s}$. $\beta_{th} = 0.34, 0.36, 0.41$ for the monomer numbers of $N_o = 184, 378, 667$, respectively.

It is interesting to note that in the early-stage of phase separation growth, the rates are in the order 14k > 28k > 49k; this is observed in initial slopes of Figure 5.5d, prior to reaching the second regime. On the other hand, the power law fits in Figure 5.8 show the scaling exponents in the order of 49k > 28k > 14k. Evidently, the late-stage phase

separation height grows faster with higher viscosity oils (e.g. 49k) compared to lower viscosity (e.g. 14k). This can be rationalized by considering the initial phase separation rate to be governed by two main two factors: (a) the swelling ratio is higher for lower molecular weight oils, meaning there is more oil available in the local vicinity and (b) a low viscosity permits faster oil flow. Hence, the 14k oil separates more and faster initially. For the the late-stage separation, the slower rates for lower molecular weight oil would then be due to the phase-separated ridge being closer to equilibrium, such that the chemical potential difference is lower.

5.3. Conclusions

In this study, we employ confocal microscopy to separately visualize the crosslinked network and the mobile oil of a swollen elastomer during wetting. When a drop is placed on the surface, we show that phase separation occurs near the contact line, where the phase separation dynamics is related to the molecular weight of the swelling oil and the degree of swelling. The ridge formation starts with a deformation of both components, followed by a quick separation of the liquid and subsequent relaxation of the polymer network. The liquid part of the phase separated ridge grows in a geometrically similar fashion. The ridge outlines collapse at different times after rescaling. For low swelling ratios, the ridge reaches the plateau height relatively fast, while at the highest swelling ratios, complete equilibrium is not reached even after long times (i.e., $\sim 15000 - 18000\,\mathrm{s}$). Higher degrees of swelling and lower molecular weight oils lead to larger phase separation sizes and rates in the early-stage wetting while, the separation rate appears to be faster for high viscosity oil at later stages of wetting, likely because less oil has separated compared to the lower viscosity counterpart, leading to a lower chemical potential. We confirm this by employing a model based on diffusion and by considering the geometrically similar growth of the phase separated ridge. The results of the model fit the experiments well for the highest swelling ratio. The theory fails, however, to predict the low equilibrium heights and the ensuing fast equilibration at lower swelling ratios. This shortcoming is most likely due to simplicity of the theoretical considerations, where the two free parameters κ and λ_0 are chosen to be independent of the swelling ratio or oil molecular weight. A detailed molecular theory may be needed to capture the complex physics in the ridge. The physics in the ridge and the details of what governs early-stage phase separation dynamics are still open questions for future consideration.

5.4. Experimental section

The details of the preparation of thin, swollen PDMS films for confocal imaging is described in our previous work [38]. Briefly, Sylgard 184 (Dow) is used as our model polydimethylsiloxane (PDMS) elastomer with base/crosslinker of 60:1. Fluorescein O,O'-diacrylate (Sigma-Aldrich) with concentration of $\sim 400\,\mu g$ per gram of PDMS is used to dye the crosslinked PDMS network. The samples are cured in a 65°C oven for 48 hours, followed

by extracting uncrosslinked chains with hexane. After extraction, silicone oil that is mixed with a red-shifted perylene monoimide (PMI) dye is used to reswell the PDMS. In this work, silicone oil (polydimethylsiloxane, trimethylsiloxy terminated, Gelest) with viscosities of 350, 1000, or 5000 cSt are used. During reswelling, a minor amount of hexane can be used to help increase the swelling rate of viscous silicone oil into PDMS network. The silicone oil is mixed with hexane with a volume ratio of 1:8, and the oil-hexane mixture is added directly onto the extracted PDMS film. The oil-hexane mixture spontaneously swells into the PDMS network, and the degree of swelling is controlled by the volume of oil-hexane mixture added. The container with samples is sealed with aluminum foil for 1 week, followed by unsealing the container and leaving the samples in the open environment for 1 hour to allow any residual hexane to evaporate.

Confocal images are captured on an inverted confocal microscope (Leica SP8) equipped with a 40x objective with a correction ring. Two lasers with wavelengths of 488 nm and 638 nm are utilized to excite the fluorescein and PMI dyes separately, and two high-sensitivity (HyD) detectors are used to collect emission wavelength ranges of 500-600 nm and $670-750\,\mathrm{nm}$. A $2\,\mu$L glycerol drop is placed on the sample and cross-sectional images of the surface deformation are taken every 30 s or 10 mins, depending on the wetting time of the experiment. The heights of oil and network are measured by the vertical distance between the flat surface and the highest tip of the oil and network through MATLAB and image analysis.

5.5. Acknowledgements

The authors appreciate discussion with Doris Vollmer. This research is funded by the US National Science Foundation through CBET 2326933 and 2043732. Part of this research was funded by the German Science Foundation (DFG) within the priority program SPP 2171 (Grant No. 422796905, projects Schm 985/22), and the DFG Emmy Noether Programme No. 460056461. Further support is acknowledged from the DFG-funded Graduate School RTG 2516 (Grant No. 405552959): RGMB is an associated member, FS is a member.

5.6. Theoretical details

5.6.1. Ridge model

List of symbols:

- F_r: total free energy in the ridge
- f_r: line free energy density of the ridge
- $\partial\Omega$: contact line between the drop and the gel

- κ: prefactor controlling the "rigidtity" of the free energy (implicitly holds information over the combined effect of elasticity of the gel, interfacial effects, osmotic pressure...)
- λ: line number density in the ridge
- λ_0: saturation line number density in the ridge.
- n_r: number of polymer chains in the ridge
- N_o: number of repeat units per chain
- n_0: saturation number of polymer chains in the ridge

Since the ridge is located at the three-phase contact line we write the free energy $\mathcal{F}_r$ as an integral over a line free energy density f_r

$$\mathcal{F}_r(\lambda) = \oint_{\partial\Omega} f_r \, \mathrm{d}l \tag{5.11}$$

where the integral is executed over the three-phase contact line of the drop with the gel. We assume that the state of the ridge is not too far away from the equilibrium, so that it is quadratic in the line number density in the ridge λ

$$f_r(\lambda) = \frac{1}{2}\kappa(\lambda - \lambda_0)^2 \tag{5.12}$$

with λ_0 the line density at saturation. The total number of polymer chains in the ridge is

$$n_r = \frac{1}{N_o} \oint_{\partial\Omega} \lambda \, \mathrm{d}l \tag{5.13}$$

with N_o the number of repeat units per chain. With this, the total free energy of the ridge can also be written in terms of the number of chains, up to a numerical prefactor that depends on the radius of the drop and N_o

$$\mathcal{F}_r \propto (n_r - n_0)^2 \tag{5.14}$$

with n_0 the number of chains at saturation.

5.6.2. Gel model

List of symbols:

- $\varphi(r, z)$: local lubricant fraction in gel
- $h_0(r)$: local height of the gel

- φ_b: initial fraction of lubricant in gel
- H_0: height of collapsed gel (no lubricant)
- K: gel elastic constant
- $\mathcal{F}[\varphi, \lambda]$: total free energy functional
- N_o: number of repeat units per chain
- Ω: the spatial domain of the gel

We consider a situation where the lubricant swells the brush or gel layer, and the elasticity of the gel layer contributes to the dynamic equation. We formulate the theory in terms of the bulk density $\varphi(r, z)$ inside the gel, where z is the coordinate perpendicular to the gel layer, and r the radial coordinate. We will assume that the layer is thin enough that the perpendicular lubricant diffusion is very fast, hence $\varphi(r, z) = \varphi(r)$ only depends on r. For given gel thickness H we have the relations:

$$\Phi(r) = \int_0^H \mathrm{d}z\, \varphi(r, z) = h_0(r)\, \varphi(r), \qquad h_0(r) = H_0/(1 - \varphi(r)). \tag{5.15}$$

The total free energy of the system has an elastic contribution due to the swelling of the gel. The elastic distortion is described in terms of a strain tensor ε, which is derived from the displacement $\vec{u}(\vec{r}_0) = \vec{r} - \vec{r}_0$ of a point in the swollen gel with respect to its position $\vec{r}_0$ in the unswollen reference gel. Here we only account for swelling in the z direction, therefore the strain tensor only has one nonzero component $\varepsilon_{zz} = \partial u_z/\partial r_{0,z} \approx \partial z/\partial z_0 = 1/(1 - \varphi)$. In coordinates z_0 of the unswollen gel, the elastic energy can then be written as $\mathcal{F}_{el} = \frac{K}{2} \int_0^{H_0} \mathrm{d}z_0\, \varepsilon_{zz}^2$. In coordinates of the swollen gel, this can be written as $\mathcal{F}_{el} = \frac{K}{2} \int_0^H \mathrm{d}z\, \varepsilon_{zz}$. The integral gives $\mathcal{F}_{el} = \frac{K}{2} H^2/H_0 \propto H^2$ as expected. Hence, we obtain the total free energy

$$\mathcal{F}[\varphi, \lambda] = \iint_\Omega \mathrm{d}A\, \mathrm{d}z \left\{ \frac{\varphi}{N_o} (\ln \varphi - 1) + \frac{K}{2} \frac{1}{1 - \varphi} \right\} + \oint_{\partial\Omega} \mathrm{d}l\, f(\lambda) \tag{5.16}$$

where the first term in the first integral is the mixing contribution, and the second integral is the contribution of the ridge from the previous section.

5.6.3. Dynamic equations

- $\vec{j}_r$: lateral diffusive current
- M: Mobility of the lubricant chains
- B: fill rate at the ridge
- R: Radius of the drop

- μ_G^{eff}: effective chemical potential in the gel
- μ_G^{eq}: equilibrium chemical potential in the gel

The lubricant density φ obeys the continuity equation $\partial_t\varphi + \nabla\vec{j} = 0$, but the current $\vec{j}$ has a diffusive and a convective component. The convective component is perpendicular to the substrate and describes the lubricant transport with the gel as it expands. Given our assumption that $\varphi(r, z)$ does not depend on z due to the joint effect of convection and fast perpendicular diffusion, we do not need to calculate it explicitly. The diffusive current in the lateral direction is given by

$$\vec{j}_r = -M\varphi\nabla_r\frac{\delta\mathcal{F}}{\delta\varphi} = -M\left\{\frac{1}{N_o} + \frac{K\varphi}{(1-\varphi)^3}\right\}\nabla_r\varphi. \tag{5.17}$$

The flux into the ridge is driven by a difference in effective chemical potentials at the boundary $\partial\Omega \equiv r = R$. In addition, it will be proportional to the fraction of lubricant present at the boundary $\Phi(R)$. Since material accumulates in the ridge, we have the following equation

$$\partial_t\lambda = -B\,\Phi(R)\left[f'(\lambda) - \mu_G^{eff}\right] \tag{5.18}$$

with B a filling rate at the ridge. We make the approximation that the effective chemical potential in the gel near the ridge stays close to the equilibrium value and set $\mu_G^{eff} = \mu_G^{eq}$. At equilibrium the free energy of the gel is

$$\mathcal{F}_G^{eq} = n_o(\ln\varphi - 1) + \frac{K}{2}\frac{n_o N_o}{\varphi(1-\varphi)} \tag{5.19}$$

and the chemical potential is

$$\mu_G^{eq} = \frac{\partial\mathcal{F}_G^{eq}}{\partial n_o} = \ln\varphi - \varphi + \frac{KN_o}{1-\varphi} \tag{5.20}$$

Hence, we have the set of equations

$$\partial_t\varphi = M\nabla_r\cdot\left\{\left[\frac{1}{N_o} + \frac{K\varphi}{(1-\varphi)^3}\right]\nabla_r\varphi\right\} \tag{5.21}$$

$$\partial_t\lambda = -B\,\Phi(R)\left[\kappa(\lambda - \lambda_0) - \mu_G^{eq}\right]. \tag{5.22}$$

We can define the equilibrium line density in the ridge $\lambda_e \equiv \lambda_0 + \frac{\mu_G^{eq}}{\kappa}$ and rewrite Eq. (5.22) as

$$\partial_t \lambda = -B\,\Phi(R)\,\kappa(\lambda - \lambda_e). \tag{5.23}$$

For the boundary conditions, we choose at the contact line an equal flux boundary condition, while at the outer boundary we choose constant volume fraction

$$\begin{aligned} -H(\varphi(R))\,j_r(R) &\stackrel{!}{=} \partial_t \lambda & (5.24)\\ \varphi(\infty) &= \varphi_b. & (5.25) \end{aligned}$$

The initial conditions are chosen as

$$\begin{aligned} \varphi(r, t=0) &= \varphi_b \qquad \text{inside } \Omega & (5.26)\\ \lambda(t=0) &= 0. & (5.27) \end{aligned}$$

Using eqs. (5.15), (5.17), and (5.22), the boundary condition Eq. (5.24) can be written as

$$\left[\frac{H_0\,M}{1-\varphi}\left\{\frac{1}{N_o} + \frac{K\varphi}{(1-\varphi)^3}\right\}\nabla_r\varphi\right]_{r=R} = -B\,\Phi(R)\,\kappa(\lambda - \lambda_e). \tag{5.28}$$

5.6.4. Numerical integration

In order to solve the equation numerically, we split the domain radially into bins with width Δr, and label the separate bins as r_i with $r_0 = R$. For any function $g(r)$ we call $g_i \equiv g(r_i)$. We use the discretization scheme :

$$\begin{aligned} \frac{\partial g_i}{\partial r} &= \frac{1}{2\Delta r}(g_{i+1} - g_{i-1}) & (5.29)\\ \frac{\partial^2 g_i}{\partial r^2} &= \frac{1}{\Delta r^2}(g_{i+1} + g_{i-1} - 2g_i) & (5.30) \end{aligned}$$

and the forward steps in time are executed as a forward Euler scheme.

The inner boundary condition is imposed by rewriting Eq. (5.28) in the following way and solving for $\varphi(R) \equiv \varphi_0$

$$\Big(\varphi_1 - \varphi_0\Big)\left[\frac{(1-\varphi_0)^3}{N_o} + K\varphi_0\right] - \frac{B}{M}\kappa(\lambda - \lambda_e)\varphi_0(1-\varphi_0)^3\Delta r = 0 \tag{5.31}$$

where we used a forward derivative definition instead of central derivative for the concentration at the ridge.

5.6.5. Height of the ridge by shape scaling

List of symbols:

- $h(r,t)$: shape function of the ridge at time t
- $\Delta h(t)$: separation height at time t
- $\alpha(t)$: scaling factor $\alpha(t) = \frac{\Delta h(t)}{\Delta h_0}$
- R: radius of the drop and position of the ridge tip
- $V(t)$: volume of the ridge at time t

Due to the symmetry of the system, the total ridge is a solid of revolution traced by rotating a curve $h(r-R,t)$ around the z-axis. The volume of the ridge is then

$$V(t) = 2\pi \int_0^\infty h(r-R,t) r \mathrm{d}r. \tag{5.32}$$

Assuming the drop is large enough, the position of the peak of the ridge R is constant. This is supported by the confocal microscopy images in Figure 3, where it seems that the ridge tip is moving vertically upwards. The position of the ridge $R \sim$ mm, while the size of the ridge is on the order of 10μm. That means that the shape function must decay very quickly as one moves away from $r = R$. Due to this, most of the contribution to the volume is coming from the region close to the tip, and the volume of the ridge is very well approximated by

$$V(t) = 2\pi R \int_0^\infty h(r-R,t) \mathrm{d}r. \tag{5.33}$$

Executing a change of variables $r' = r - R$ the expression for the volume becomes

$$V(t) = 2\pi R \int_{-\infty}^\infty h(r',t) \mathrm{d}r' \tag{5.34}$$

where we extend the lower bound to $-\infty$ since the radius R is much larger than the size of the ridge. From the confocal microscopy images, the shape of the ridge shows self-similar growth. We therefore choose a scaling form for the shape function $h(r',t)$

$$h(r',t) = \alpha(t) h\left(\frac{r'}{\alpha(t)}\right) \tag{5.35}$$

where $\alpha(t)$ is a time-dependent scaling factor. Following another change of variable $r' \to \alpha(t)r'$ in Eq. (5.34) the expression for the volume becomes

$$\begin{aligned} V(t) &= \alpha^2(t) 2\pi R \int_{-\infty}^{\infty} h(r')\mathrm{d}r' \\ &= \alpha^2(t) V_0 \end{aligned} \tag{5.36}$$

where V_0 is a constant with units of volume. We then see that the volume scales quadratically with the scaling factor. The scaling factor at time t is related to the height of the phase separated ridge $\Delta h(t)$ through

$$\alpha(t) = \frac{\Delta h(t)}{\Delta h_0} \tag{5.37}$$

where Δh_0 is the height of the ridge when the volume is equal to V_0. Putting all this together we finally get

$$\Delta h(t) = \Delta h_0 \sqrt{\frac{V(t)}{V_0}}. \tag{5.38}$$

The total volume can be obtained from the solution of the diffusion equation as

$$V(t) = \frac{N(t)}{\rho} = \frac{2\pi R \lambda(t)}{\rho} \tag{5.39}$$

where ρ is the density of the fluid. Having the volume $V(t)$ and choosing for V_0 and Δh_0, we use Eq. (5.38) to obtain the time evolution of the height.

5.6.6. Parameters and units

The diffusion equation was solved for the following fixed parameters:

- $R = 1$
- $K = 0.00004$
- $\kappa = 2.5$
- $\lambda_0 = 1$
- $B = 12 \times 10^{-5}$
- $H_0 = 1$

The mobility was chosen depending on the molecular weight of the fluid as $M = \frac{M_0}{N_o}$ with $M_0 = 10^{-3}$. We chose $N_o = 184,378,667$ which correspond to to the molecular weights of the oils in the experiment using 74 g/mol as the molecular weight of a monomer. For each

N_o we chose three values for φ_b that would correspond to the experimental swelling ratios using $\varphi_b = 1-1/Q$. We choose discretized time and spatial steps $\Delta t = 10^{-6}; \Delta r = 2\times 10^{-4}$. For the values of V_0 and Δh_0 we choose the shape of the ridge to be an isosceles triangle with side length $\approx 2R \times 10^{-4}$. We choose $\rho = 1$ in Eq. (5.39). A possible mapping of units is to identify the radius of the drop to $R = 1$mm and the mobility $M_0 = 10^{-12}\mathrm{m}^2/\mathrm{s}/k_BT$, which sets the unit of time in the theory to $[t] = 10^3$s.

5.U. Unpublished Results: Cloaking Kinetics on Lubricated Gels and Polymer Brushes

Note: The results of the experiments in section 5.U.1 were obtained under a tandem project as part of the GRK 2516 training program. The experiments were conducted in collaboration with Lukas Hauer, Azadeh Sharifi-Aghili, and Doris Vollmer. The simulation results related to the kinetics of cloak development in section 5.U.2 were generated mostly by Antonio Torregrosa Abellán in the context of his Master thesis under the supervision of R.G.M. Badr, the author of the current doctoral thesis.

Contributions to section 5.U:

- **Experiment:** The experiment was designed by the experimental collaborators. R.G.M. Badr and A. Sharifi-Aghili synthesized the samples. Surface tension measurements and analysis performed by R.G.M. Badr.

- **Simulation setup:** R.G.M. Badr designed the simulation initialization and execution scripts which rely on the HOOMD-Blue version 2.9.7 [160, 161]. A. Torregrosa Abellán translated the simulation codes into HOOMD-Blue version 4.5.0 and ran the simulations.

- **Analysis and figures in simulation work:** Simulation analysis schemes and codes were developed jointly by R.G.M. Badr and A. Torregrosa Abellán. A. Torregrosa Abellán executed the analysis codes and visualized the data. Interpretation of the results was performed by R.G.M. Badr, A. Torregrosa Abellán, and F. Schmid.

As described in Chapter 4, the water on PDMS system can exhibit cloaking of the drop by the lubricant in the brush. In addition, cloaking was observed for water droplets on PDMS gels [194]. The experiments described in the earlier sections of this chapter do not show sign of cloaking. This is likely due to the spacial and temporal resolutions in those particular experiments; therefore, we focused only on the growth of the phase separated ridge instead of the cloak. In order to get some insight into the cloaking kinetics, we perform experiments where we follow the cloaking kinetics on PDMS gels and simulations where we follow the kinetics on polymer brushes.

5.U.1. Cloaking kinetics on swollen polymer gels in experiment

PhD students who are part of the research training group GRK-2516 were required to take part in a tandem project with a research partner. The aim is to exchange knowledge and foster collaboration between theory/modeling and experiment. The results in this section were obtained under this context. Lukas Hauer provided the initial training in the experimental laboratory, supplemented by Doris Vollmer and Azadeh Sharifi-Aghili. Samples were synthesized by R.G.M. Badr and Azadeh Sharifi-Aghili. The experiments and analysis were performed by R.G.M. Badr. The experiment was designed by the experimental collaborators [261].

The time scales for cloaking make direct visualization methods such as fluorescent confocal microscopy unsuitable. Instead, the cloak development can be inferred by measuring the surface tension of a drop in contact with a PDMS gel [248, 261]. To that end, we perform experiments where we place a pendant drop in contact with a swollen PDMS gel and calculate the surface tension from the shape of the pendant drop.

5.U.1.1. Experimental details

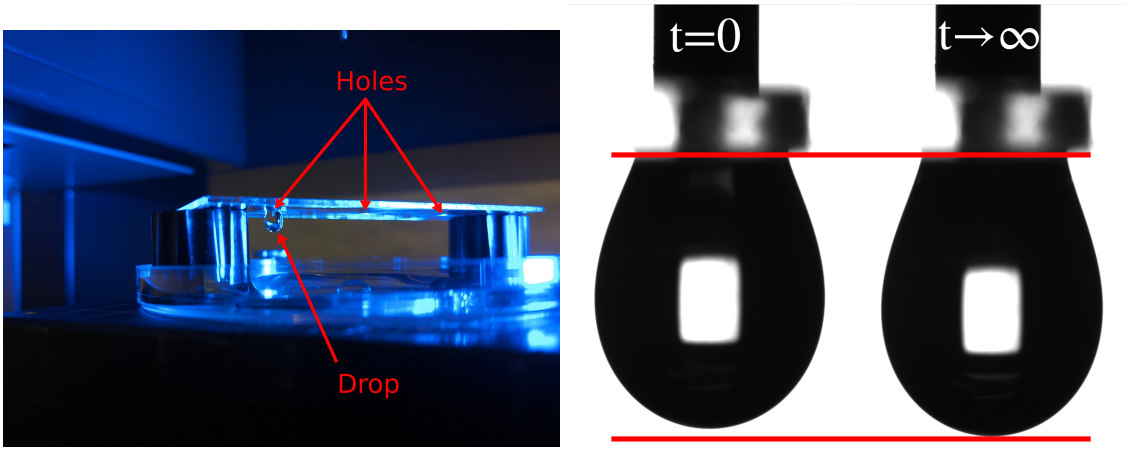

Figure 5.U.1.: A picture of the experimental setup and the resulting drop images. The drop pends over a water bath that provides humidity to slow down evaporation. The gel is at the bottom side of the glass slide so that the drop is in contact with the gel. The drop images correspond to the beginning and end of the experiment, where we can see the elongation of the drop due to the reduction in surface tension after cloaking.

To synthesize the swollen PDMS gels, we use commercially available kit Sylgard 184 (from Dow Chemical Company). The kit is composed of a base of functionalized PDMS and a crosslinker. We mix 10-1 ratio by weight of the base to crosslinker. To the mixture, we add unfunctionalized silicone oil which is composed of PDMS chains that will not react with the crosslinker. This will provide us with part of our uncrosslinked chains, and allows

us to control the degree of swelling by controlling the ratio of unfunctionalized silicone oil to the gel mixture. The added silicone oil does not account for all the uncrosslinked chains at the end of the synthesis, since it is expected that some of the chains from the base will also remain uncrosslinked [194]. The components are mixed vigorously for 5 minutes, then placed in vacuum to remove any air bubbles.

Glass slides were rinsed with acetone and ethanol then dried with a flow of nitrogen gas. The glass slides we used were modified to have three 2mm holes drilled into them. The purpose is to deposit drops through the holes so that they are pending under the slide. The purpose of having three holes is to reduce the variability due to synthesis between different slides, and to avoid having to use the same hole for repeated measurements. The dried glass slides were placed in a plasma oven at 300 W for 10 minutes. Afterwards, the gel mixture was placed on the slide and spin-coated at 1000 rpm for 60s. The spin-coated slides are then cured in an oven at 60° for 24h.

To measure the surface tension of pendant drops we use the Krüss Drop Shape Analyzer (DSA100). The glass slide is held by its edges at an elevated with the coated side facing down above a water bath. The purpose of the water bath is to reduce the evaporation of the drop after deposition. The setup is composed of a light shining into a camera with the drop in between. The drop then casts a shadow on the camera, which can then be used to analyze the shape of the drop (see Figure 5.U.1). In addition, the setup includes a syringe with a mechanism that can be controlled through a software on the computer. The mechanism allows us to control the volume of liquid to be deposited as well as the rates, position of the syringe, etc ... The software, in addition, has a built in shape analyzer which fits the shape to the Young-Laplace equation and extracts the corresponding surface tension (see section A.3). To set the units of length in the image, we calibrate to the width of the syringe we used, which was 1.637 mm. To deposit the drop, we follow the procedure described in Ref. [261] and we use the mechanism of the Krüss Drop Shape Analyzer to automate the procedure as much as possible (steps 3 onward):

1. lower the syringe through one of the holes until the tip is well below the slide, but still within the view of the camera
2. deposit 24 μL of water and measure the surface tension. If the surface tension corresponds to that of pure water 72 mN/m we proceed. Otherwise, the syringe is contaminated with oil and needs cleaning before repeating from step 1
3. raise the syringe until the drop is in contact with the coated side of the slide
4. dose an additional 11 μL of water at 5 μL/s
5. begin the measurement of the surface tension with time.

The result is a surface tension versus time graph that should correspond to the water surface tension at early times, and decrease with time until it reaches the equilibrium value for a cloaked drop. We repeated the experiment for different degrees of swelling of the gel and for different viscosities of the silicone oil.

5.U.1.2. Results

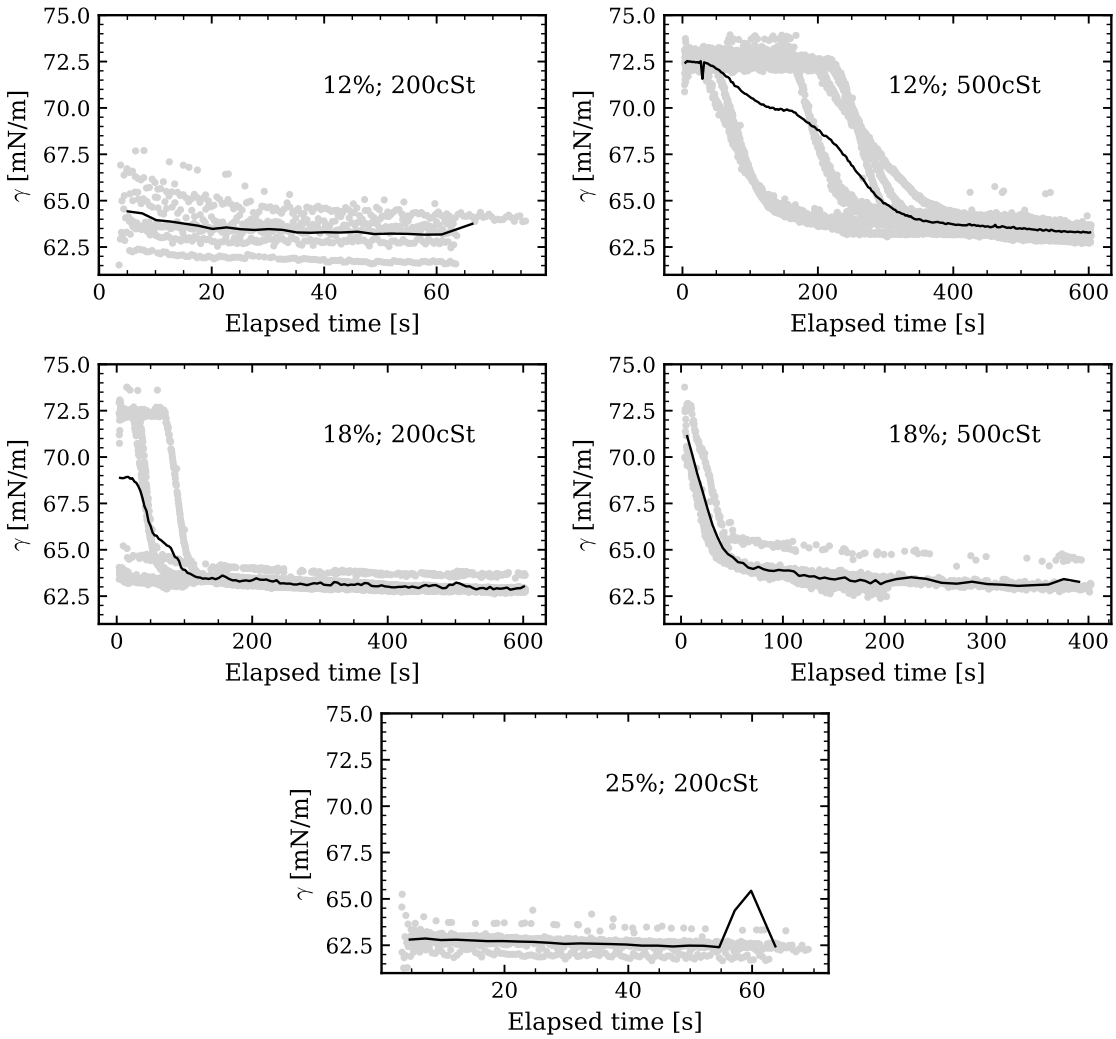

Figure 5.U.2.: Surface tension versus time for gels of different degrees of swelling swollen with oils of different viscosities. The percentage refers to the weight percentage of added oil to gel. The viscosity is also indicated in cSt. Grey dots are the data from different replicates, and the solid black line is an average over the replicates.

The experimental procedure described in the previous section results in values for the surface tension of the pendant drop versus time. We begin by measuring the evolution of the surface tension with time across different holes in different slides. We vary the degree of swelling by varying the percent by weight of the silicone oil added to the gel mixture. Figure 5.U.2 shows the results for different degrees of swelling and different oil viscosities. For the same parameters, the results from replicates are shown as gray dots. The black line is an average over the replicates. A problem is immediately apparent: either the

surface tension reaches its final value too quickly (12%;200cSt and 25%;200cSt), or the trends are not reproducible (12%;500cSt and 18%;200cSt). This makes it hard to draw any conclusions from the experiments. A possible reason for the quick variation in some cases might be the accumulation of oil at the rim of the hole. As for the problem with reproducibility, it might be due to inherent differences between the different hole that might arise during drilling, spin coating, or some other stage of the preparation of the samples.

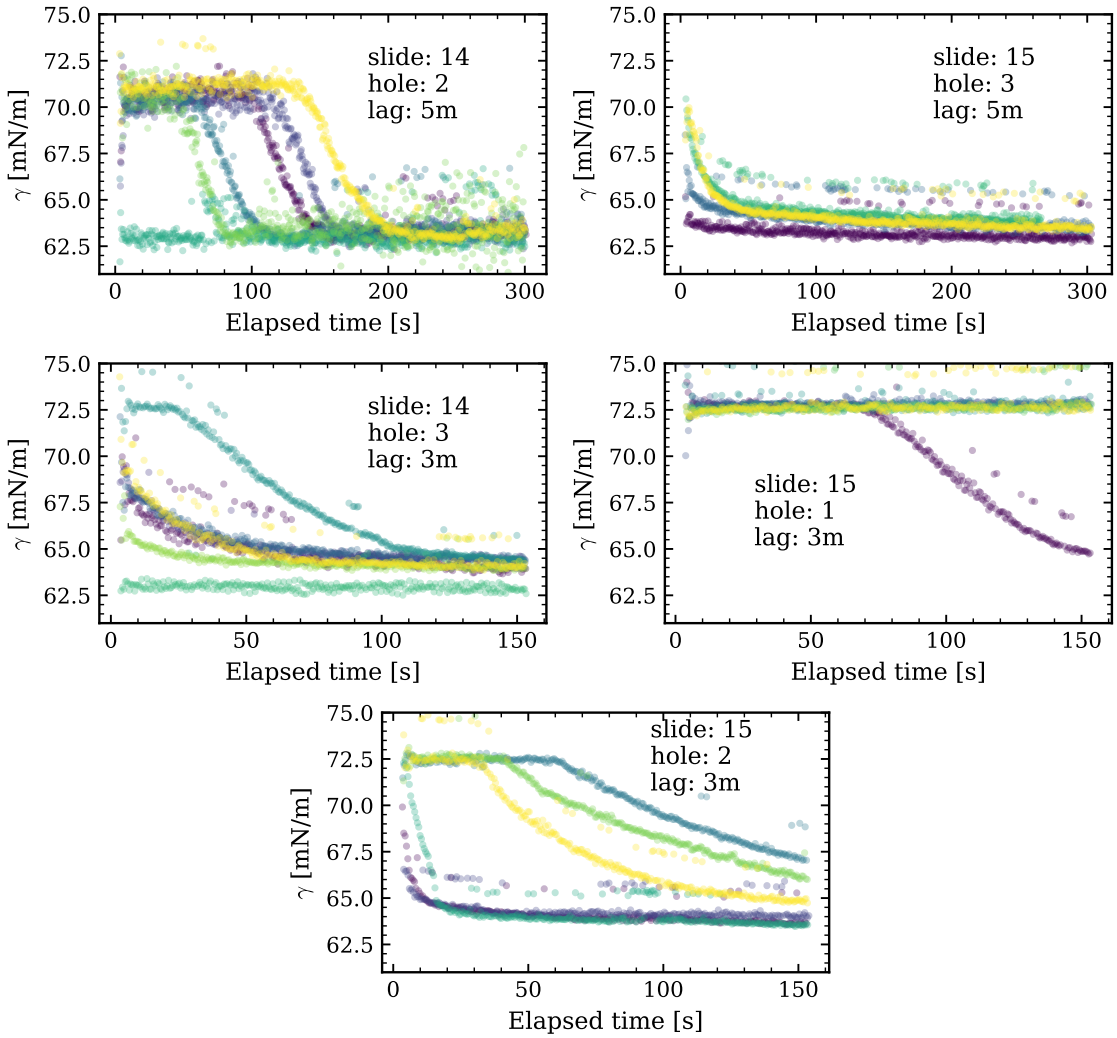

Figure 5.U.3.: Surface tension versus time for gels swollen with 12% weight of oil with viscosity 200 cSt. Each figure corresponds to repeated measurements in the same hole. The text indicates the slide, the hole in that slide, and the approximate lag time between the beginning of consecutive measurements.

In an attempt to circumvent such problems, we take a different approach to the mea-

surements. Although the original motivation behind having multiple holes on one sample was to avoid using one hole multiple times, it appears that the intrinsic variability between holes is leading to large variations. Therefore, instead of doing measurements on different holes, we repeat the measurement on only one, with a constant time interval between measurements. The motivation behind this approach is that any excess oil will be gradually removed with repeated measurements. In addition, as we are using the same hole, we exclude any aberrations due to the differences between holes. To perform those measurements, we perform steps as described in section 5.U.1.1. The surface tension is measured for a fixed period of time which we call the lag time. After the measurement is finished, the drop is removed with a tissue paper, and the steps are repeated without any further modification of the sample. We choose lag times of 5 minutes and 3 minutes. Figure 5.U.3 shows the results for 12% weight of oil with viscosity 200 cSt. The colors of the repeated measurement indicate the order of the measurement from blue for the earliest to yellow for the latest. The results across all samples and lag times do not show any sign of reproducibility or systematic change. Despite the problems with reproducibility in both approaches, the value for the surface tension at the end of each measurement is $\gamma \approx 63$ mN/m as expected for a cloaked drop. This means that the observed changes are indeed due to cloaking. However, the reasons behind the seemingly random cloaking times remain a mystery. A possible improvement on our method could be to use Reflection Interference Contrast Microscopy (RICM) as described in Ref. [29]. This method has the advantage of measuring the thickness of the film directly at an impressive temporal resolution. Applying this method also circumvents the need for drilling holes into the glass slides, as that might be a major source of inconsistency.

5.U.2. Cloaking kinetics on lubricated polymer brushes in simulation

What follows are results obtained by A. Torregrosa Abellán while working on his Master thesis under the supervision of R.G.M. Badr. The results already appeared in his written thesis. They are included in this thesis to provide a well rounded description of the kinetic properties of systems that exhibit cloaking. As the experiments cannot provide a detailed description of the cloaking process through time, simulations might provide valuable insights.

To follow the cloaking kinetics in simulation, we set up simulations analogous to those in Chapter 4. One difference is that we use larger brushes with $n_B = 120 \times 120$ chains. We choose lubricant fractions beyond the cloaking transition $\Phi^* \approx 0.44$, in particular we simulate brushes with $\Phi \in \{0.61, 0.73, 0.77\}$. To simulate the droplet we place a spherical cap of radius $R = 40\,[r_c]$ in contact with the swollen brushes, as described in section 3.2.5. Since we are dealing with an out of equilibrium and non-steady state process, we are limited in our statistical sample. To get reasonable results, we average the density map (see section 3.3.1) at every frame over 5 independent simulations before extracting quantities of interest. The downside of this approach is that we are not able to obtain

uncertainties for many of our results.

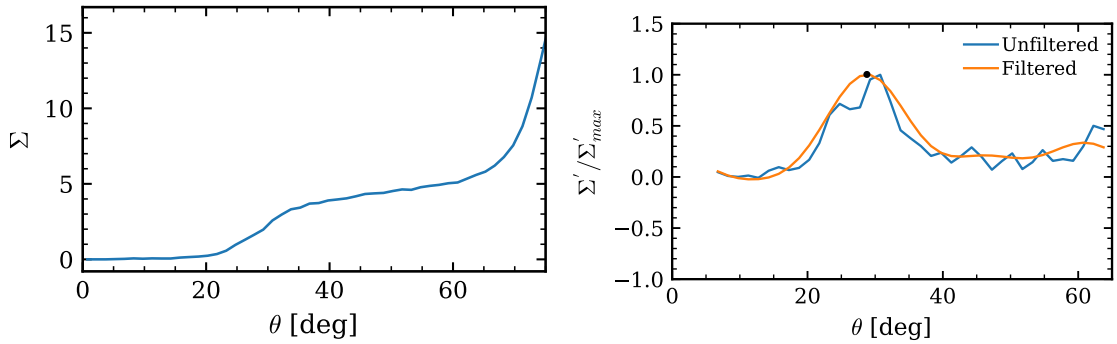

Figure 5.U.4.: (a) An example $\Sigma(\theta)$ from Eq. (5.U.1). We choose the first inflection point as the position of the cloak front. The large increase near $\theta \approx 65°$ is due to the wetting ridge. (b) The derivative of $\Sigma(\theta)$ normalized by its maximum value. The orange line shows the same data after applying a low pass filter. The filtered data shows a clearer peak at the inflection point. Graphs by Antonio Torregrosa Abellán.

5.U.2.1. Cloak front kinetics

The first quantity we look at is the progression of the cloak front. To find the position of the cloak front, we calculate the azimuthally symmetric local density of oil $\varrho_o(r, \theta)$ in spherical coordinates as described in section 3.3.1 (see Figure 3.4 d). From that, we calculate the quantity

$$\Sigma(\theta) = \int \varrho_o(r, \theta) dr. \tag{5.U.1}$$

Figure 5.U.4 (a) shows $\Sigma(\theta)$ at a particular time point in the simulations. The line is an average over 5 independent simulations. We define the position of the cloak front as the position of the first inflection point in $\Sigma(\theta)$

$$\frac{\mathrm{d}^2\Sigma}{\mathrm{d}\theta^2} = 0. \tag{5.U.2}$$

To find the inflection point, we first calculate the first derivative using the two point formula

$$\frac{\mathrm{d}\Sigma}{\mathrm{d}\theta} = \frac{\Sigma(\theta + \Delta\theta) - \Sigma(\theta - \Delta\theta)}{2\Delta\theta}. \tag{5.U.3}$$

Afterwards, we apply a low pass filter on the result to eliminate high frequency noise, and calculate the position of the highest peak as the position of the inflection point in $\Sigma(\theta)$

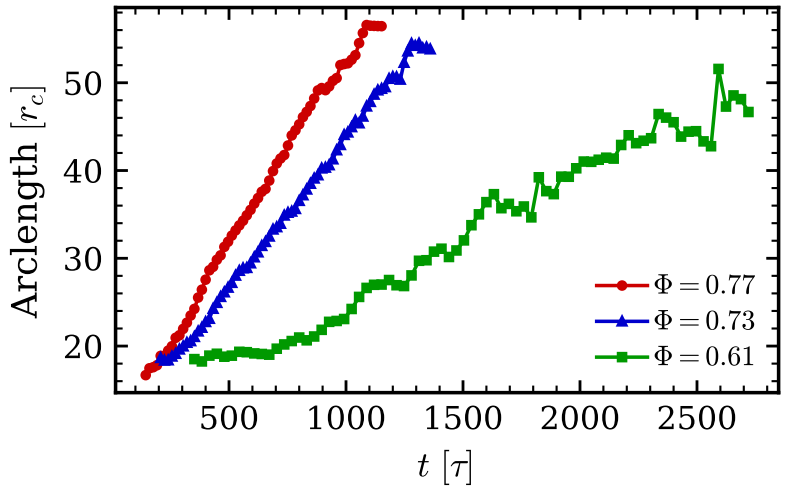

Figure 5.U.5.: Cloak front position versus time for three different lubricant fractions Φ, all beyond the cloaking transition. As expected the higher the lubricant fraction, the faster the cloaking progresses. Graph by Antonio Torregrosa Abellán.

(see Figure 5.U.4 b). The results for the progression of the cloak front are shown in Figure 5.U.5. The lines begin when the cloak has crossed a certain point ($\theta \approx 65°$) and terminate when the cloak closes at the top of the drop ($\theta = 0$). As expected, the cloak progresses faster for higher lubricant fractions. Interestingly, the arc length covered by the cloak on the drop grows linearly with time.

5.U.2.2. Cloak thickening regime

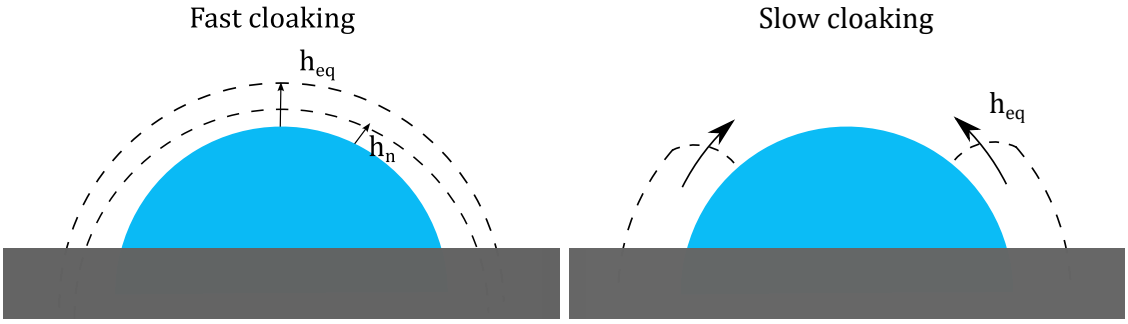

Figure 5.U.6.: Cartoons illustrating two extreme regimes of cloak thickening. In the fast cloaking regime the cloak covers the entire droplet quickly, then thickens homogeneously. In the slow cloaking regime, the cloak progresses onto the droplet with a thickness that is constant in time. Figure by Antonio Torregrosa Abellán.

One interesting aspect of the kinetics is the regime in which the cloak develops Two possible extreme cases are possible. If the material transport on the droplet is faster than in the brush, the cloak will cover the entire droplet rapidly before increasing in thickness homogeneously across the surface of the drop. We term this as the "fast cloaking" regime. On the other extreme, if the material transport is slow on the droplet, the cloak will reach its equilibrium thickness locally, before progressing on the droplet. We label this as the "slow cloaking" regime. Both regimes are illustrated in Figure 5.U.6. To quantify the thickness of the cloak with time, we begin with the relation

$$N = \int \varrho_o r^2 \sin\theta \, \mathrm{d}r \, \mathrm{d}\theta \, \mathrm{d}\varphi \tag{5.U.4}$$

where N is the number of oil monomers in the integration volume and $\varrho_o(r, \theta, \varphi)$ is the local density of oil in spherical coordinates centered at the center of curvature of the droplet. Since the cloak thickness is much smaller than the drop radius of curvature we set $r = R$, and since we have azimuthal symmetry, we rewrite Eq. (5.U.4) as

$$N(t) = 2\pi R^2 \int_{\theta_{\mathrm{ridge}}}^{\theta_{\mathrm{tip}}(t)} \int \varrho_o \sin\theta \, \mathrm{d}r \, \mathrm{d}\theta = 2\pi R^2 \int_{\theta_{\mathrm{ridge}}}^{\theta_{\mathrm{tip}}(t)} \Sigma \sin\theta \, \mathrm{d}\theta. \tag{5.U.5}$$

where θ_{tip} is the angular position of the cloak front and θ_{ridge} is the angular position of the wetting ridge. The ridge remains more or less unchanged as the cloaking progresses; therefore, we determine θ_{ridge} manually at $\theta_{\mathrm{ridge}} = 65°$ from the $\Sigma(\theta)$ curve at the highest lubrication, and use this value for all lower lubricant fractions. Given the number of oil monomers, the thickness of the cloak can be written as [65]

$$h = \frac{N}{\rho_o A} \tag{5.U.6}$$

with ρ_o and A the bulk density of oil and the area covered by the cloak respectively. The area can be calculated through

$$A(t) = 2\pi R^2 (\cos\theta_{\mathrm{tip}}(t) - \cos\theta_{\mathrm{ridge}}) \tag{5.U.7}$$

Finally, using Eqs. (5.U.5), (5.U.6), and (5.U.7), we can calculate the thickness of the cloak from $\Sigma(\theta, t)$ as

$$h(t) = \frac{\int_{\theta_{\mathrm{ridge}}}^{\theta_{\mathrm{tip}}(t)} \Sigma \sin\theta \, \mathrm{d}\theta}{\rho_o \left[\cos\theta_{tip}(t) - \cos\theta_{ridge}\right]}. \tag{5.U.8}$$

Figure 5.U.7 shows the thickness of the cloak versus time as calculated from Eq. (5.U.8). The results indicate that our simulations are in an intermediate regime between fast and

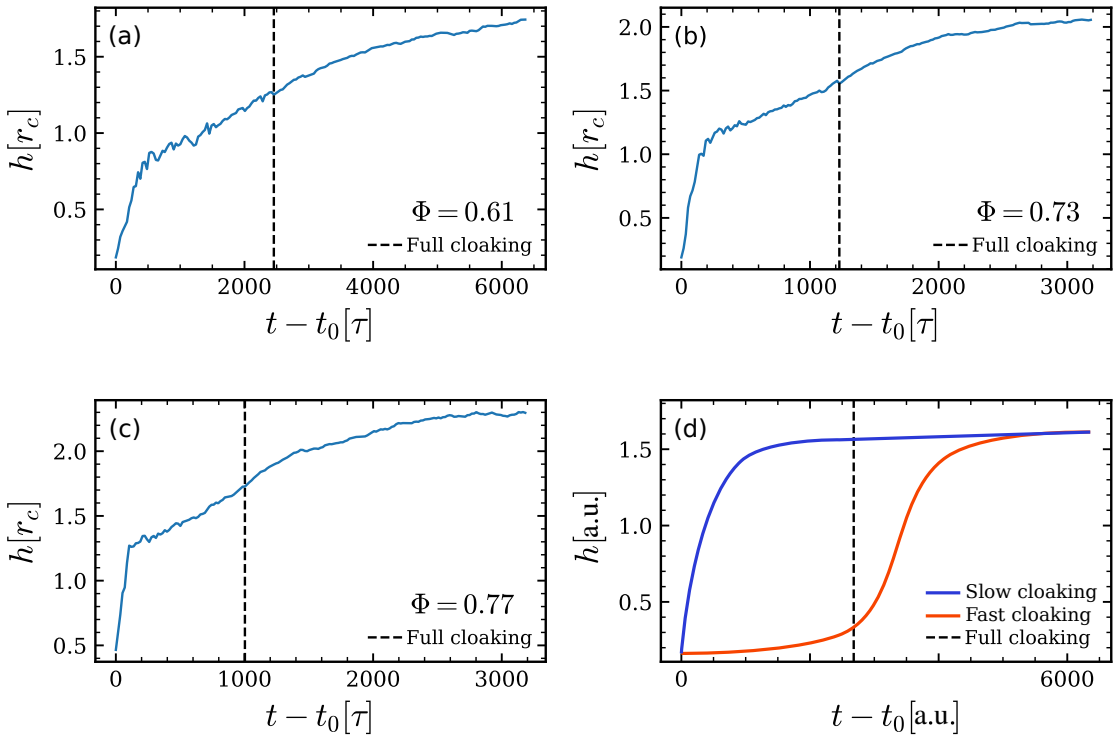

Figure 5.U.7.: Thickness of the cloak versus time for (a) $\Phi = 0.61$, (b) $\Phi = 0.73$, and (c) $\Phi = 0.77$. (d) Expected curves for the cases of fast and slow cloaking. The dashed lines indicate the time when the cloak reaches the top of the droplet. (a), (b), and (c) graphs by Antonio Torregrosa Abellán.

---

slow cloaking. In the case of fast cloaking, we expect the thickness to be low and constant then start increasing only after the cloak reaches the top of the drop; for slow cloaking, the thickness should increase rapidly then remain constant for the entirety of the simulation (see Figure 5.U.7 d).

5.U.2.3. Oil depletion

Another aspect of interest is the distribution of material in the brush as the cloak develops. To track this distribution, we calculate the quantity

$$\Lambda(\rho) = \int \varrho_o(\rho, z) dz \tag{5.U.9}$$

where $\varrho_p(\rho, z)$ is the local density of polymers in cylindrical coordinates with the axis aligned along the z-axis and passing through the center of curvature of the drop (see

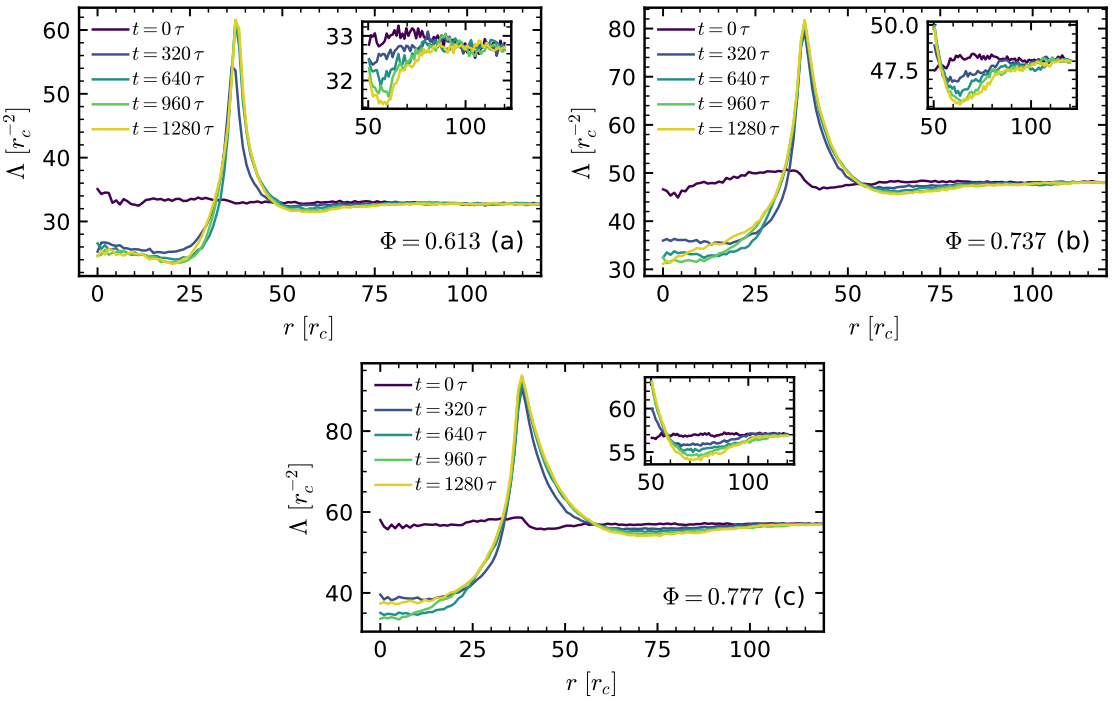

Figure 5.U.8.: $\Lambda(\rho)$ at different time points during cloaking for (a) $\Phi = 0.613$, (b) $\Phi = 0.737$, and (c) $\Phi = 0.777$. Insets are close ups near the three phase contact line. There is a clear depletion zone of material outside of the drop. The amount of material also drops from under the droplet.

---

section 3.3.1). $\Lambda(\rho)$ is akin to a local effective surface density of polymers and provides information of the quantity of material at a distance ρ from the center of the drop. The evolution of $\Lambda(\rho)$ is shown in Figure 5.U.8. A clear depletion zone is present outside the droplet. The radial extent of the depletion zone increases with the lubricant fraction Φ. Material is also depleted from under the droplet. The presence of the depletion zone is an indicator that the time scale is controlled by the diffusion of oil in the brush, which supports our motivation behind the model in section 5.2.3.

5.U.3. Conclusion

To investigate the kinetics of cloak development, we perform both experimental and numerical investigations. At the level of the experiments, we perform pendant drop experiments with the drop in contact with a swollen PDMS gel. A problem that appears immediately is the lack of reproducibility of the results with our experimental approach. The drops were pending through holes drilled in glass slides, which might have introduced inconsistencies between different measurements in different holes. However, even repeating measurements

in the same hole at regular intervals resulted in seemingly random results. Despite the lack of reproducibility, the initial and final values for the surface tension correspond to the values expected for a pure and cloaked drop respectively, which means that the observed changes are indeed due to cloaking.

At the numerical level, we use the local density distribution of oil to track the position of the cloak front with time. The cloak front progresses on the drop linearly with time, with the rate increasing with the fraction of oil. The cloak progresses towards the top of the droplet while thickening at the same time, reaching the top before reaching the equilibrium thickness. During cloak development a depletion zone emerges in the vicinity of the wetting ridge outside the droplet. This is indicative of a diffusive timescale set through the speed of diffusion of oil chains in the brush and supports the motivation behind our theoretical model.

6. Dynamics of Droplets Moving on Lubricated Polymer Brushes

Note: This chapter reproduces the results from the publication in Ref. 119. Additions and changes from the original publication are marked with a violet text color, while omissions are marked through the symbol [...].

Contributions to the publication:

- **Simulation setup:** R.G.M. Badr designed and wrote the simulation initialization and execution scripts which rely on the HOOMD-Blue version 2.9.7 [160, 161].
- **Analysis and figures:** R.G.M. Badr developed the analysis schemes with input from F. Schmid. R.G.M. Badr wrote and executed the analysis codes, visualized the data, and contributed to the interpretation of the results. Experiments were performed by L. Hauer and D. Vollmer.
- **Writing:** R.G.M. Badr in collaboration with F. Schmid wrote the bulk of the simulation results sections and parts of the introduction of the original article (omitted in this chapter). Other parts of the introduction were mainly written by D. Vollmer. Experiment section was written by L. Hauer and D. Vollmer. Conclusion was mainly written by F. Schmid.

6.1. Introduction

Droplets are ubiquitous in nature and technology. Understanding the wetting dynamics of liquid droplets enables improved use of droplets for various applications [262–265] such as self-cleaning [164–166], spray coating [266], efficient application of pesticides [168, 169], microfluidics [267], heat transfer [268], or drag reduction [269–271].

Coating a solid substrate by polymer brushes or gels provides a versatile way to tune the static and dynamic properties of deposited drops [40, 98, 243, 272–274]. In particular, the softness, type, and thickness of the coating govern the friction a drop experiences when sliding or rolling over a surface. The dynamic wetting properties of drops on soft surfaces result from the interplay between interfacial tension, contact line tension, substrate elasticity, and dissipation within the substrate and drop [38, 195, 211, 219, 275–279]. This intricate puzzle of coexisting effects makes understanding, predicting, and tuning the friction of drops on soft surfaces challenging.

Polydimethylsiloxane brushes form a class of promising soft coatings for applications [181, 280]. A PDMS brush is composed of PDMS chains grafted by one end to a surface. The resulting viscoelastic layer has a thickness of a few nm. PDMS chains are very flexible, having a persistence length of a few monomers [281]. In the brush, the chains keep their flexibility as opposed to PDMS gels where the chains are crosslinked, resulting in an elastic solid. Owing to the flexibility of the brush chains, water drops on PDMS can show a contact angle hysteresis of less than 10°[180]. Often PDMS brushes are swollen by PDMS chains which are not grafted-to the surface. These mobile chains may provide additional lubrication [32].

One characteristic of wetting on soft surfaces is the deformation of the surface surrounding a deposited drop. The vertical component of the interfacial tension pulls the substrate up. A wetting ridge forms [244, 282, 283]. The shape and height of the ridge result from the competition between the surface tension of the droplet applying a vertical stress on the substrate and the substrate elasticity [284]. The wetting ridge plays a crucial role in the dynamics of sliding droplets, with the main effect being viscoelastic energy dissipation inside the ridge[98, 216, 278, 279, 285]. This so-termed contact line friction contributes to the energy dissipation during the motion of the droplet.

In addition, mobile chains can remain in the PDMS film. The poor solubility of silicone oil in most solvents requires severe rinsing of the film to remove all mobile chains. Since the amount of remaining mobile chains is hard to quantify experimentally, its contribution to dynamic wetting is still unclear [32, 175, 226]. This is further complicated by the fact that mobile chains can cloak a drop, if the fraction of lubricant in the brush exceeds a certain critical amount (cloaking transition [163]). The cloaking of water by silicone oil on lubricated surfaces influences both static and dynamic experiments [29, 84]. It has the effect of dynamically reducing the surface tension of the drop [194, 248], and contributes to the depletion of lubricant for drops rolling off on surfaces as the cloaking material leaves the surface with the drop.

Despite the interesting physics and applications of wetting on PDMS brushes, recent experimental work on dynamic wetting on PDMS has largely focused on gels [219, 229]. This is partly due to the fact that polymer brushes typically have thicknesses in the order of nanometers, which makes it challenging to probe the microscopic details of the phenomena in question. Numerical and simulation methods can provide valuable insights. In particular, such methods allow us to look into details such as the flow [118] and dissipation within the droplet [117], the structure of the wetting ridge on polymer brushes [99, 163, 183, 286] and the structure of the cloaking layer [163].

To date and to our best knowledge, simulations of droplets on polymer brushes have been limited to the study of static properties [163, 183–185, 287], or dynamic properties for brushes that are swollen by the drop [288–291] or serve as coatings in nanochannels [292–294]. Molecular simulations of the properties and dynamics of droplets rolling on polymer brushes under the influence of body forces such as gravitational forces are still missing. Such studies can shed light on the molecular mechanisms underlying the friction between droplets and brushes, in particular in the presence of lubricants and, possibly, a cloaking layer.

In the present study, we use coarse-grained molecular dynamics simulations to address this problem. One question of integral importance is the dependence of drop dynamics on degree of lubrication. In order to study this, we first investigate the relation between friction forces and velocity, which provides a global measure of energy dissipation. This is mostly done by simulations, but we also present corresponding experimental studies. The dissipation stems from multiple sources, such as the slip between the droplet and the brush, viscoelastic dissipation in the ridge, or the flow within the droplet. To better understand these active players, we then use simulations to quantify the response of the brush and lubricant, and the flow within the droplet. Another standing question is that of the transport and depletion of lubricant. The cloak is expected to enhance the lubricant transport. However, it is not clear whether the cloak remains stable for moving droplets, and if so, how the velocity of the droplet affects the cloak. To better understand this, we characterize the cloaking layer for droplets moving with different velocities.

6.2. System preparation

The brush is composed of n_B chains of length $N_B = 50$ with the first monomer of each chain fixed on the grafting surface following a regular square lattice pattern. We choose the lattice constant $d = 2\,r_c$, corresponding to a grafting density $\sigma = 0.25\,r_c^{-2}$. We use $n_B = 100 \times 100$ chains resulting in typical box sizes of $200 \times 200 \times 300\,r_c^3$. The grafting density is such that the grafted polymer layer is in the brush regime and not the so-called mushroom regime [142]. The dry brush is in a collapsed state and is rough.

In addition, the system may contain n_o lubricant polymers of length $N_o = 5$. We characterize the amount of lubricant present in terms of the number fraction of lubricant

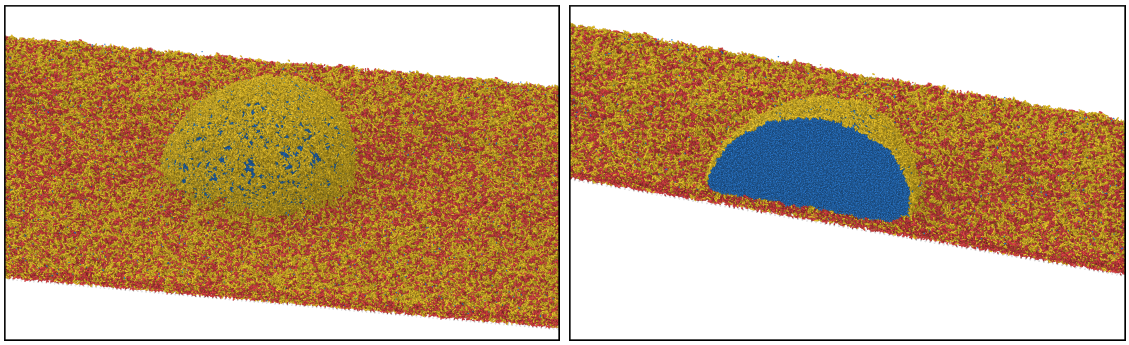

Figure 6.1.: Snapshots from simulations at lubricant fraction $\Phi = 0.444$ and applied force $F = 0.0002$. The top panel shows the full system, the bottom panel a cut across the droplet.

monomers to brush monomers,

$$\Phi = \frac{n_o N_o}{n_o N_o + n_B N_B}. \tag{6.1}$$

The brush is first equilibrated without any lubricant for 8×10^5 simulation steps. We separately prepare a film of lubricant of length $N_o = 5$ at the equilibrium melt density $\rho_o \approx 2.9\, r_c^{-3}$. The lubricant is then added to the system by placing the film in contact with the brush and letting the lubricant infuse the brush. Equilibrium is reached after a maximum of 64×10^5 steps. The swollen brush is in the strong stretching regime, as can be inferred from the monomer concentration profiles reported in our previous work [163].

To prepare the spherical droplets we take a pendant droplet and place it in contact with the brush, and let it equilibrate in the absence of gravity. The number of liquid particles was $n_w = 766 \times 10^3$ in all simulations. The systems are then left to equilibrate until no more conformational changes are observed. The systems with the droplet need at least 10^7 steps to reach equilibrium. This results in the equilibrium configurations described in our previous publication [163], where we observed a cloaking transition at a lubricant fraction of $\Phi \approx 0.4$. Therefore, droplets on brushes containing a higher amount of lubricant will be fully cloaked at equilibrium.

Finally, to induce the motion of the droplet, we apply a constant force of magnitude F in the positive x-direction. The force is applied to every individual liquid particle and only to the liquid particles i.e. the droplet experiences a total force $F_{tot} \approx N_w F$. This mimics the experimental situation where the force is transmitted to the droplet by a cantilever (see below). The simulations with the force are then run for at least 24×10^5 steps until a steady state with constant droplet velocity is reached. All measurements are made during a consequent run of 48×10^5 steps where 150 simulation snapshots are obtained. Simulation snapshots can be seen in Figure 6.1.

For each set of parameters, 5 independent simulations are performed. The independent

simulations are obtained by equilibrating 5 different polymer brushes from the same initial condition, but with different initial seeds for the random number generator. Following that, every stage of the system preparation is again conducted with fresh set of seeds for the random number generator, resulting in minimally correlated simulations. The results from those simulations are averaged to obtain mean values $\bar{x}$ and the error bars in the plots correspond to standard errors $\alpha_x = \sqrt{\frac{\sum_{i=1}^{N}(x_i-\bar{x})^2}{N(N-1)}}$ with $N = 5$ is the number of independent values.

To characterize regimes of the droplet motion we can calculate various dimensionless hydrodynamic numbers, using the values calculated above for the density of the liquid ρ_w, its surface tension with vapor γ_w, its dynamic viscosity μ, the droplet radius $R \sim 40r_c$, and typical droplet velocities in the simulations ($v \sim 0.001 - 0.1$), see section "Results and Discussion". The Reynolds number showing the ratio of inertial to viscous forces is in the range $\mathrm{Re} = \frac{\rho v R}{\mu} \in [0.01, 1.5]$, the Weber number showing the ratio of inertial to interfacial forces is in the range $\mathrm{We} = \frac{\rho v^2 R}{\gamma} \in [8 \times 10^{-6}, 1.8 \times 10^{-1}]$, the Ohnesorge number showing the ratio of viscous to inertia and interfacial tensions is around $\mathrm{Oh} = \frac{\sqrt{\mathrm{We}}}{\mathrm{Re}} \approx 0.28$. Another important dimensionless quantity is the Bond number, which gives the ratio of gravitation to interfacial forces. Our simulations are run in the absence of gravitational forces. However, we can calculate an analogue to the Bond number using our driving force instead of gravity: $\mathrm{Bo} = \frac{\rho_w F_{tot} R^2}{m_w \gamma_w}$, where $m_w = N_w m$ is the mass of the droplet. As mentioned above the total force is $F_{tot} = N_w F$, and using $m = 1$ this gives values in the range $\mathrm{Bo} \in [0.04, 0.8]$.

6.3. Experimental setup

The present work mainly focuses on simulations of droplet rolling/sliding dynamics on lubricated brushes. To complement the simulation study, we have also carried out experiments to investigate the friction forces between water droplets moving at constant velocity on lubricated PDMS brushes. Unfortunately, a direct quantitative comparison between simulations and experiments is not possible, mainly due to the size differences: Matching the surface tension at the liquid/vapor interface and the dynamic viscosity of the liquid with that of water ($\gamma_w = 3.2 k_B T / r_c^2$ and $\mu = 6.4 k_B T \tau / r_c^3$ in the simulation versus $\gamma_w = 0.072$ N/m and $\mu = 0.001$ Pa s in water), we find that our length unit should roughly correspond to $r_c \sim 4$ Å and our time unit to $\tau \sim 3 \cdot 10^{-12}$ ps. Even though our simulations include 1.2-2 million particles, the droplet radii are only $R \sim 40 r_c$, corresponding to $R \sim 16$ nm, whereas the droplet in the experiments have a radius of 1.5 mm. Nevertheless, we can still compare general trends regarding the relation between friction forces and droplet velocities, and the influence of free lubricant polymers.

Glass slides (24×60 mm^2, 170 ± 5 μm thickness, Menzel-Gläser) were coated with PDMS pseudo brushes, using the "grafting-from" [295] and the "grafting-to" [32] approaches. In short, "grafting-from" implies the polymerization of vaporous monomers from grafting

sites on the surface while prepolymerized chains are "grafted-to" grafting sites. For grafting sites, hydroxyl groups are formed by O_2-plasma activation (300 W, 10 min) of the glass surfaces. For "grafting-from", we placed the plasma-activated glass slides in a desiccator (20°C, 40% humidity) together with 1 ml dichlorotetramethyl-disiloxane (Sigma-Aldrich). After 10 min the samples were removed from the desiccator. The number or percentage of free PDMS chains can not be quantified experimentally because the amount is insufficient even for state of the art analytical techniques. For "grafting-to", tetramethyl-terminated PDMS oil (6 kDa and $N_b \approx 80$, Alfa Aesar) was drop cast on the activated glass slides. Atmospheric or surface-bound water can break Si-O bonds, allowing PDMS chains to bind to the surface hydroxyl groups. The samples were equilibrated overnight. Excess oil was removed by sonicating the samples for 30 min in toluene.

Sliding forces were measured with a cantilever set-up, mounted on a confocal microscope (Leica, SP8) [194]. The coated glass slides are mounted on a motorized stage, above the microscope lens. An approx. 100 mm long metal blade is vertically placed over the coated glass slides so that the upper end is fixed while the lower end hangs freely several microns above the surface. 10 μl large drops are placed on the coated glass slide and moved at constant speeds against the metal blade. This results in a displacement of the blade that we track with the microscope. The blade displacement is linearly related to a force by the spring constant. We determine the spring constant with a natural frequency analysis [261] to be around 214 mN/m, yielding a measurable force resolution of approx. 5 μN. In steady-state, the sliding forces of the droplet balance with the spring force of the displaced blade.

To characterize regimes of the droplet motion we again calculate the various dimensionless hydrodynamic numbers, using the density of water, $\rho = 1000\,\mathrm{kg/m^3}$, its surface tension with vapor, $\gamma = 0.072\,\mathrm{N/m}$, its dynamic viscosity $\mu = 0.001\,\mathrm{Pa\,s}$, droplet mass $m_w = 10^{-5}\,\mathrm{Kg}$, and the droplet radius $R \sim 1.5\,\mathrm{mm}$. In the experiments, the Reynolds number is in the range $\mathrm{Re} = \frac{\rho v R}{\mu} \in [0.015, 1.5]$, the Weber number in the range $\mathrm{We} = \frac{\rho v^2 R}{\gamma} \in [2 \times 10^{-6}, 2 \times 10^{-1}]$, the Ohnesorge number in the range $\mathrm{Oh} = \frac{\sqrt{\mathrm{We}}}{\mathrm{Re}} \approx 0.094$, and the Bond number in the range $\mathrm{Bo} = \frac{\rho_w F R^2}{m_w \gamma_w} \in [0.06, 0.3]$, where we consider the friction force instead of the gravitational force. For the most part, the dimensionless numbers in the simulations are comparable to those in the experiments.

6.4. Results and discussion

6.4.1. Friction force and dissipation

We first investigate the relation between the energy dissipation and the velocity of the droplet relative to the substrate. Experimentally, this is measured by imposing a constant substrate velocity while keeping the droplet in place by a cantilever, and measuring the force on the cantilever [194] (see Section "Experimental Setup" above). The measured force corresponds to the friction force felt by the droplet. Once the force is measured, the power dissipated is calculated as $P_{\mathrm{diss}} = \mathbf{F} \cdot \mathbf{v}$. In the experiments, the force was measured

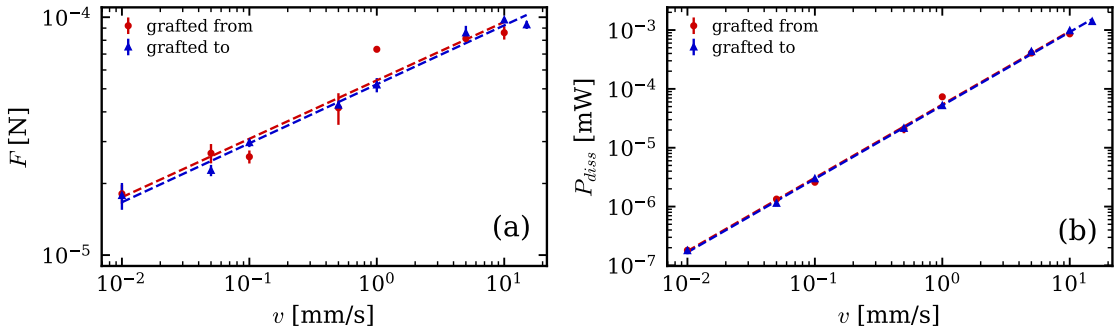

Figure 6.2.: Experimental measurements for two methods for synthesizing PDMS brushes, chemical vapor deposition (grafting from) and drop casting (grafting to). (a) Steady-state force exerted on the cantilever versus velocity v of the stage, on logarithmic axes. The dashed lines are power-law fits $F \propto v^{\alpha}$ with $\alpha_{\text{from}} \approx 0.246 \pm 0.028$ and $\alpha_{\text{to}} \approx 0.248 \pm 0.011$. (b) Steady-state power dissipation defined as $P_{\text{diss}} = Fv$ versus the velocity v of the stage, on logarithmic axes. The dashed lines are power-law fits $P_{\text{diss}} \propto v^{\beta}$, with $\beta_{\text{from}} \approx 1.246 \pm 0.028$ and $\beta_{\text{to}} \approx 1.248 \pm 0.011$.

for different velocities for droplets deposited on PDMS brushes synthesized using two different methods as described earlier: "grafting from" and "grafting to". The "grafting to" samples were washed after synthesis to remove free chains, while the "grafting from" samples were not washed. The results from the experiments are shown in Figure 6.2.

Figure 6.2 (a) shows the friction force versus velocity, while (b) shows the dissipated power versus velocity. The results show a power law dependence between the friction forces and velocity. Such a relation is expected, and was observed in previous work on the friction of moving droplets [117, 217, 296]. The force measurements on both samples seem to coincide and show very little effect of the synthesis method. One factor that would influence the friction force is the presence of free chains which would act as lubricant. Since the "grafting to" samples were washed, no lubricant should be present [32]. The experimental measurements then imply: either the "grafting from" method does not leave residual free chains, the amount of free chains in PDMS polymer brushes was insufficient to reduce drop friction, or free chains hardly lower friction. The latter would mean that the addition of a small amount of free chains will only swell the brush and not make the interface more liquid-like, hence not lowering drop friction. On the other hand, it has been demonstrated in Ref. 32 that free chains in a brush reduce the contact angle hysteresis, which is directly proportional to the friction force. Since it is difficult to control the amount of free chains in PDMS brushes experimentally, we turn to the simulations to investigate the effect of free chains on drop friction in a controlled fashion.

In the simulations, we apply a constant force F to each individual liquid particle and measure the ensuing steady-state velocity v_x. The velocity v_x is taken as the mean x-component of the velocity of all liquid particles. The simulations were performed at

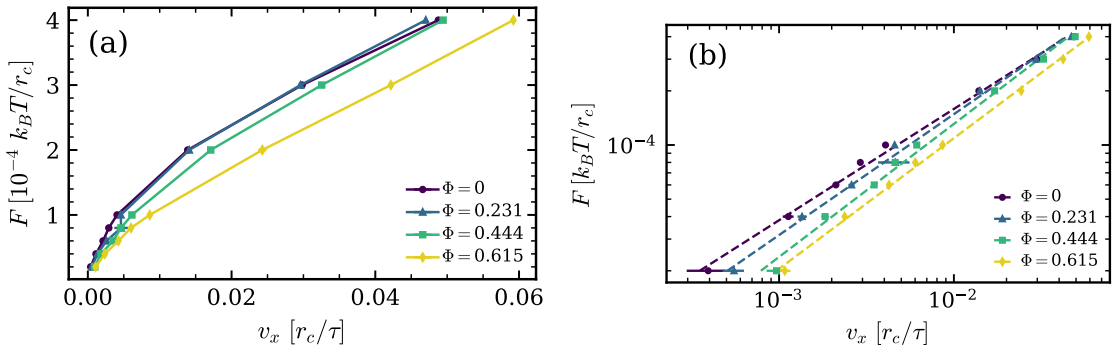

Figure 6.3.: Applied force F per particle versus the resulting steady-state velocity v_x (a) on linear axes, (b) on logarithmic axes. The dashed lines in (b) show a fit to a power-law behavior $F \propto v_x^{\alpha_{\text{sim}}}$, with $\alpha_{\text{sim}} = 0.618 \pm 0.015;\ 0.672 \pm 0.020; 0.739 \pm 0.025;\ 0.726 \pm 0.013$ for $\Phi = 0; 0.231; 0.444; 0.615$ respectively. $\Phi \geq 0.444$ corresponds to cloaked droplets.

varying fractions of free chains $\Phi = 0;\ 0.231;\ 0.444;\ 0.615$, giving brushes that are partly swollen by free chains, but not yet fully saturated (the saturation point is $\Phi \approx 0.77$)[163]. For each fraction Φ, forces ranging from $F = 2 \times 10^{-5} k_BT/r_c$ to $F = 4 \times 10^{-4} k_BT/r_c$ are applied on the liquid particles. For forces lower than $F = 2 \times 10^{-5} k_BT/r_c$ the droplet does not seem to move. For forces higher than $F = 4 \times 10^{-4} k_BT/r_c$ the droplet smears on the brush and forms a "rivulet" across the periodic boundary. Figure 6.3 shows the force F per particle versus the steady-state velocity v_x in linear (a) and logarithmic (b) representation. Looking at the trend lines, the velocity measurements for the lower free chain fractions $\Phi = 0;\ 0.231$ essentially coincide, whereas the velocity at the same force increases for $\Phi = 0.444$ and again for $\Phi = 0.615$, implying that the free chains indeed reduce the friction between the droplet and the substrate. Interestingly, this qualitative change of behavior coincides with the cloaking transition, which was located at $\Phi \sim 0.4$ in this system [163]: $\Phi = 0.444$ is just above the cloaking transition, and the droplets are not cloaked for the lower fractions. The trends in Figure 6.3 b) suggest a power law $v_x \propto F^{\alpha_{\text{sim}}}$ with exponents ranging between $\alpha_{\text{sim}} \sim 0.6$ for bare droplets on dry brushes to $\alpha_{\text{sim}} \sim 0.7$ for cloaked droplets on lubricated brushes.

Another way of looking at the data is to calculate the power dissipated by the droplet. This can be done like in the experiments using $P_{\text{diss}} = N_w \mathbf{F} \cdot \mathbf{v}$, where we multiply by the number of liquid particle N_w because our force $\mathbf{F}$ acts on each particle individually. Figure 6.4 shows the steady-state power dissipation P_{diss} versus the steady-state velocity v_x with linear axes in (a) and logarithmic in (b). This graph demonstrates again that the dissipated power is lower for higher lubrication (beyond the cloaking transition). The logarithmic plot also suggests a power law relation $P_{\text{diss}} \propto v_x^{\beta_{\text{sim}}}$ with exponents $\beta_{\text{sim}} = 1 + \alpha_{\text{sim}}$ in the range of $\beta \sim 1.6$ for droplets on dry brushes to $\beta \sim 1.7$ for cloaked droplets.

The power law exponents in experiment and simulation are not the same. We will discuss this further below. One interesting aspect is that the presence of a small amount of

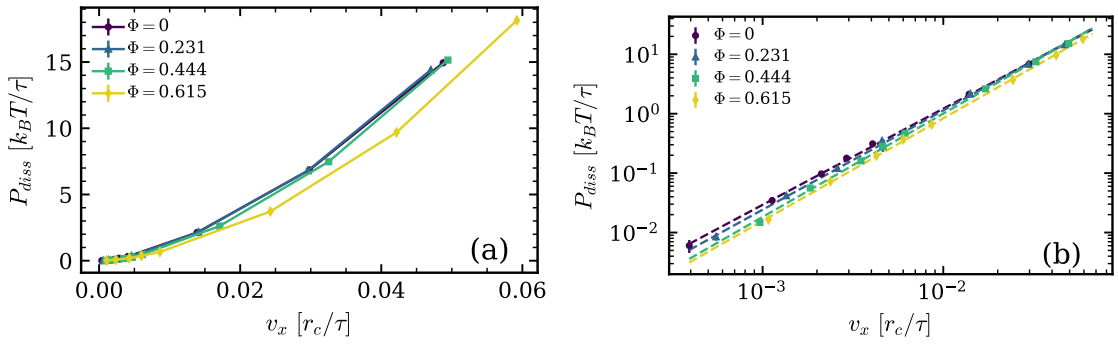

Figure 6.4.: Steady-state power dissipation defined as $P_{\text{diss}} = N_w F v_x$ versus the steady-state velocity v_x (a) on linear axes, (b) on logarithmic axes. The dashed lines in (b) show fits to a power-law behavior $P_{\text{diss}} \propto v_x^{\beta_{\text{sim}}}$, with exponents $\beta_{\text{sim}} = 1 + \alpha_{\text{sim}} = 1.618 \pm 0.015$; 1.672 ± 0.020; 1.739 ± 0.025; 1.726 ± 0.013 for $\Phi = 0; 0.231; 0.444; 0.615$ respectively. $\Phi \geq 0.444$ corresponds to cloaked droplets.

---

free chains has no significant effect on the friction force acting on the droplet. This suggests that the quantity of free chains in the "grafting from" method may not be large enough to lubricate the motion of the droplet. Beyond the cloaking transition, the friction between the droplets and the substrate is somewhat reduced. However, even this effect is comparatively small. As mentioned in the introduction, the total friction has contributions from multiple sources.

As discussed in section 2.4, the exponent β can take on a particular value depending on what source of dissipation dominates the friction force. When an exact exponent can be calculated, multiple approaches result in either $\beta = 2$ or $\beta = 5/3 \approx 1.67$. The exponent in our simulations is close to the value $\beta = 5/3 \approx 1.67$ which was also observed in Ref. 85 on LIS. This suggests that the dominant source of dissipation could be the dissipation in the contact line following the Cox-Voinov wedge dissipation theory of section 2.4.1.1 (see Eq. 2.37). However, since our contact angles are large, it is unlikely that the Cox-Voinov dissipation law is valid for our contact line. Another possibility is that the friction is dominated by the dissipation in the liquid wetting ridge as described in section 2.4.4 (see Eq. 2.47). Although difficult to rule out, an argument can be made against this since our wetting ridge is not composed of pure liquid, but likely include some stretched grafted chains. This brings us to another important component of our system: the polymer brush. The value of the exponent may be due to the viscoelastic properties of the brush, with the exponent β being set by the loss modulus as described in section 2.4.5.2. This offers a possible explanation on the variation of the exponent as the lubricant fraction is varied, since that may lead to changes in the rheology of the brush. In addition, this could explain the discrepancy between the simulations and experiments: the rheology of the brush is different, leading to different exponents. This is to be contrasted with the other sources of dissipation where the exponents are independent of the details of the system. One final

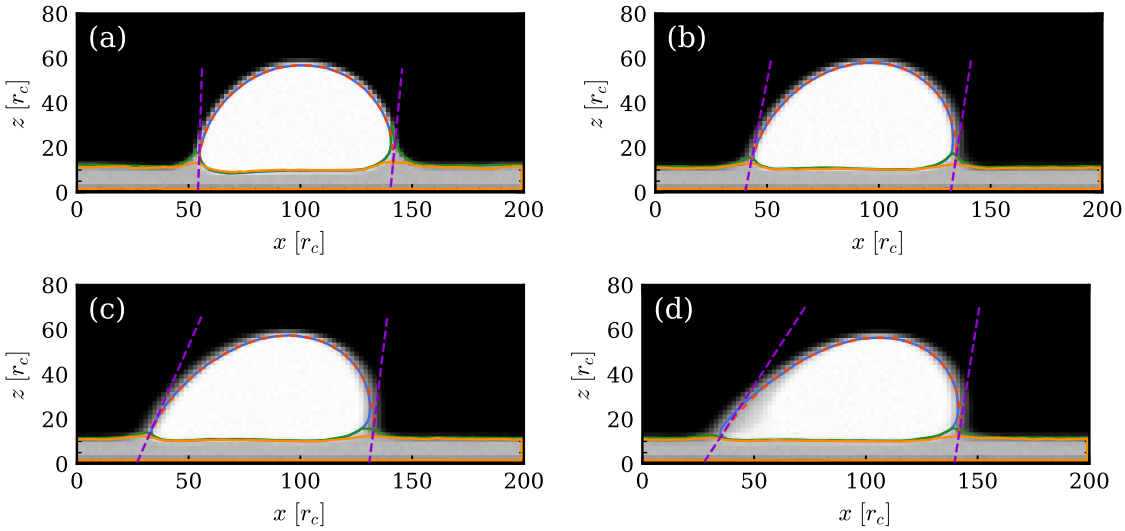

Figure 6.5.: Density map showing contours of the brush (orange), the free chains (green), the droplet (blue), along with a fit to an ellipse for the droplet (red dashed line). The fit was then used to find the tangents to the droplet where it intersects the unperturbed height of the brush (purple dashed lines). (a) $F = 8 \times 10^{-5}$, (b) $F = 20 \times 10^{-5}$, (c) $F = 30 \times 10^{-5}$, (d) $F = 40 \times 10^{-5}$. For all figures $\Phi = 0.615$. $\Phi \geq 0.444$ corresponds to cloaked droplets.

---

possibility is the dominance of the viscous dissipation in the bulk of the drop. Certain approximations result in an exponent $\beta = 2$ (see section 2.4.2); however, the flow can be complex and the shear rate could depend non-linearly on the center of mass velocity, leading to deviations from the value $\beta = 2$ for the exponent. While this could explain the discrepancy between simulation and experiment, it is not clear whether it can explain the small variation in the exponent as the lubricant fraction changes.

To try and address these questions, we quantify below the response of the substrate to the motion of the droplet, as well as the flow within the droplet to better understand the small dependence of the friction force on lubrication and the relevance of the different sources of dissipation.

6.4.2. Droplet shape and contact angles

As the droplet slides, the forces acting on it cause it to deform, and at steady-state the shape of the droplet can be approximated by an ellipse. In addition, the advancing and receding contact angles differ from each other due to the adhesion of the droplet to the substrate. In order to characterize these effects, we take a section of the droplet of thickness $2r_c$ along a plane parallel to the direction of motion and analyze the density map in that plane. Examples of such density maps are shown in Figure 6.5. From the density

maps we delimit the different interfaces as density isosurfaces. The droplet surface (blue lines in Figure 6.5) corresponds to the water density isosurface $\rho_w^{\text{iso}} \equiv 2r_c^{-3}$, and the full substrate surface (green lines) to the polymer density isosurface $\rho_o^{\text{iso}} \equiv 1.5r_c^{-3}$ (brush and free chains). These isosurfaces (or density contours) were set at densities corresponding to roughly half the bulk density of water and polymer. The brush surface (orange lines) is taken to be the brush monomer isosurface $\rho_b^{\text{iso}} \equiv \rho_b^{\text{mean}}/2$, where ρ_b^{mean} is the mean brush density and depends on the level of lubrication. Having determined the droplet surface, we can now fit the droplet-vapor part to a tilted ellipse. This is achieved by optimizing the coordinates of the foci F_1 and F_2 such that they best obey the relation $PF_1 + PF_2 = 2A$, with P a point on the droplet-vapor part of the contour, and A the semi-major axis of the ellipse. The parameters F_1, F_2, and A fully define the ellipse, and we can calculate contact angles at the advancing and receding ends. For this, we find the intersection of the ellipse with the horizontal line at the level of the unperturbed substrate and calculate the angle between the tangent to the ellipse at that point and the horizontal line. With this approach, we measure apparent, macroscopic, contact angles. In Figure 6.5, the ellipse and both the receding and advancing tangents are shown in red and purple dashed lines respectively. The ellipse fits the droplet quite well for all velocities at the receding end. However, right at the advancing front, the fit deviates significantly from the contour of the droplet. Thus the values of macroscopic advancing contact angles differ from the microscopic values. Unfortunately, it is difficult to unambiguously define microscopic contact angles in the presence of a wetting ridge, especially if the free chains spread on the droplet. Therefore, we limit our analysis to macroscopic contact angles.

Figure 6.6 a) shows the apparent advancing contact angle θ_{adv}^{app} versus velocity for different fractions of free chains. The shape of the curves is similar to that found in earlier experiments on expanding water drops on PDMS surfaces [297]: After an initial increase, the advancing contact angle quickly saturates, and it overall varies by less than ten degrees. In contrast, the receding contact angle θ_{adv}^{rec}, shown in Figure 6.6 b), decreases seemingly linearly as the velocity increases and drops to roughly 2/3 of the force-free value at the highest force. Along with this decrease of θ_{adv}^{rec}, the eccentricity of the ellipse strongly increases with velocity (Figure 6.6 c). However, all three quantities, i.e., the advancing and receding contact angles and the eccentricity, are not significantly affected by the presence of lubricant. This is already observed in equilibrium droplets: The equilibrium contact angles for different lubricant fractions are shown in Figure 4.10 (a) in the Supporting Information. For all lubricant fractions Φ we find an apparent angle $\theta_{app} \sim 92° - 95°$, which is roughly 5° below the value expected for macroscopic droplets [163].

6.4.3. The wetting ridge

Next we study the influence of the moving droplet on the brush. The droplet pulls up on the brush at the three-phase contact line, due to the interfacial tension. Beyond the cloaking transition, the wetting ridge separates into two "phases". One phase still includes the brush chains, and the other is purely composed of free chains. A similar phase separation has also been observed for swollen PDMS gels [38, 219, 228]. The formation and relaxation

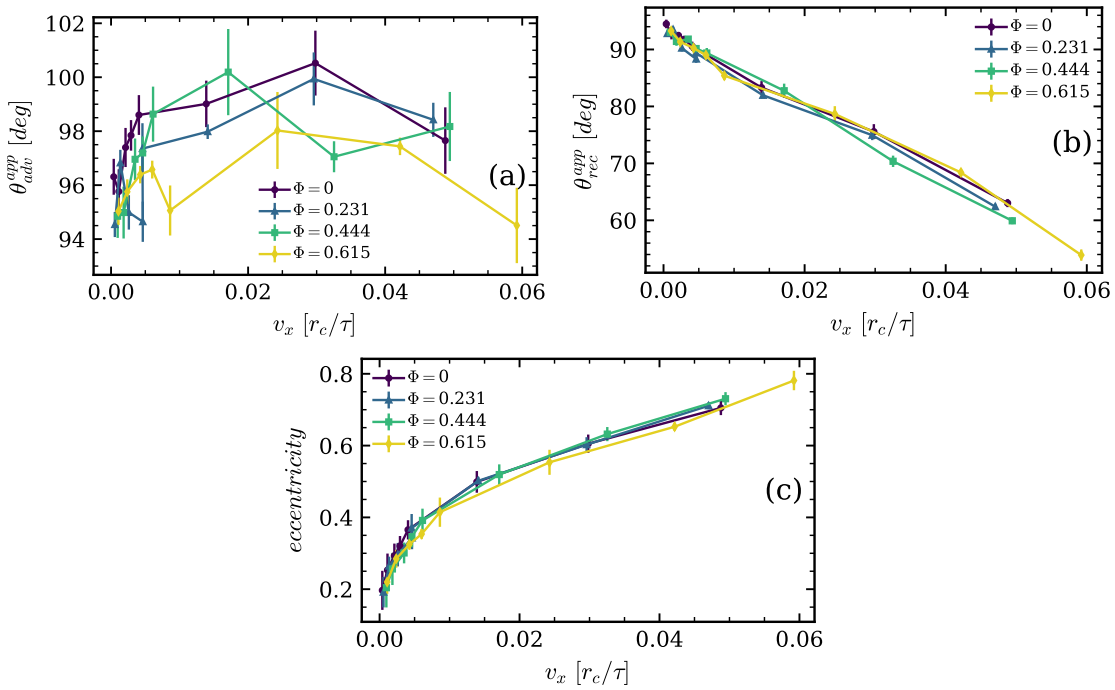

Figure 6.6.: (a) Advancing contact angle θ_{adv} versus droplet velocity. (b) Receding contact angle θ_{rec} versus droplet velocity showing a roughly linear decrease. (c) Eccentricity of the ellipse that best fits the droplet shape versus the droplet velocity.

---

of the wetting ridge at the contact line contributes to the total friction through viscoelastic and poroelastic dissipation [236, 283]. To quantify the effect of the moving droplet on the brush, we measure how the heights of the brush and the full ridge (brush and free chains) at the three-phase contact line vary with the velocity of the moving droplet. The heights are calculated as the highest points in the contours shown in Figure 6.5, measured from the grafting surface, both for the brush and the full substrate, and both for the receding end and the advancing front. In addition, a quantity of interest that has been studied in experiments is the separation height between the two phases [219]. It is calculated as the difference between the brush height and the height reached by the free chains. Since no separation is observed below the cloaking transition, we can only calculate the separation height for the two densities $\Phi = 0.444$ and $\Phi = 0.615$.

Figure 6.7 a) shows the height of the brush at the advancing front h_B^{adv} versus the steady state velocity v_x of the droplet. The brush height at the advancing front always decreases with increasing velocity. The decrease is less pronounced for high swelling. This is due to the fact that the more the brush is swollen by lubricant, the less it is affected by the presence of the droplet, as can be seen in Figure 4.10 b) [...]. This observation has implications for the contribution of the brush to the total friction force on the droplet: as the droplet moves, it pulls the brush at the advancing front. The further out the brush is

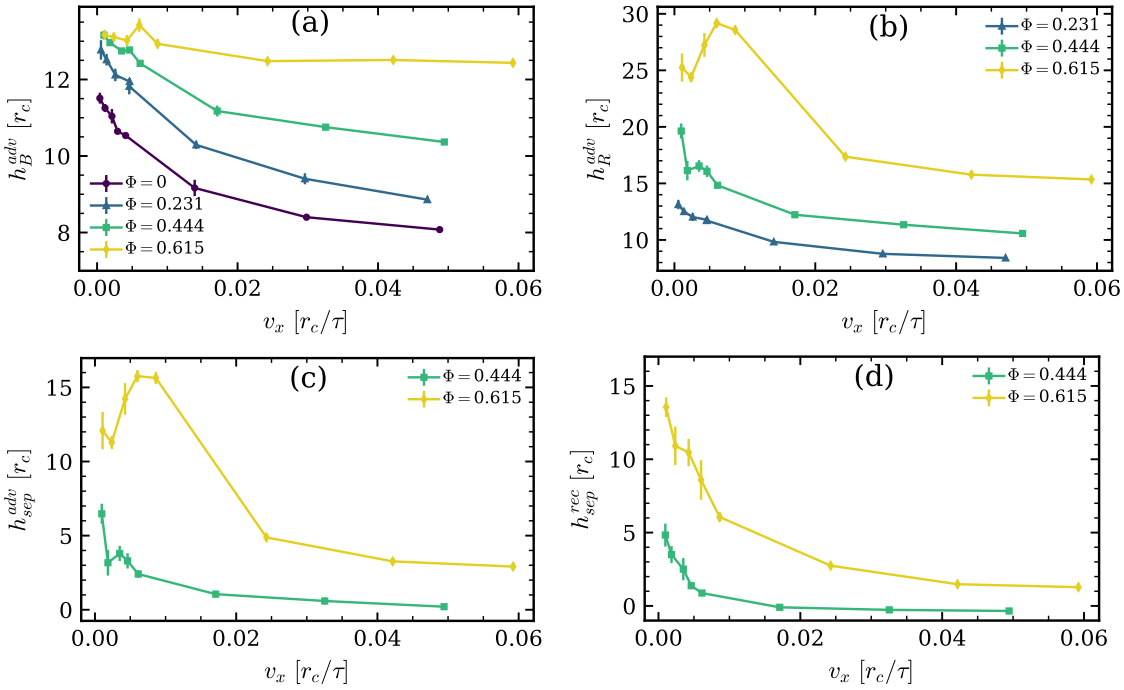

Figure 6.7.: (a) Height of the brush at the advancing front h_B^{adv} versus droplet velocity. (b) Height of the full ridge at the advancing front h_R^{adv} versus droplet velocity. (c) Separation height between the liquid part of the ridge and the brush part at the advancing front h_{sep}^{adv} versus droplet velocity, featuring non-monotonic behavior at high swelling. (d) Separation height between the liquid part of the ridge and the brush part at the receding end h_{sep}^{rec} versus droplet velocity. In (c) and (d) only data for cloaked droplets are shown ($\Phi \geq 0.444$) since only those exhibit a separation between the liquid part and the brush part in the ridge.

---

pulled, the larger the viscoelastic dissipation within the brush. Our results then suggest that at higher velocities the contribution of viscoelastic dissipation in the ridge could be reduced.

Figure 6.7 b) shows the height of the full ridge at the advancing front h_R^{adv} versus the steady state velocity v_x of the droplet. For low lubrication, the ridge height decreases as the speed of the droplet increases. However, for $\Phi = 0.615$ something interesting happens: With increasing droplet velocity, the ridge height first increases up to a maximum at $v_x \approx 0.01$, then it starts decreasing again. Figure 6.7 c) shows the separation height at the advancing front h_{sep}^{adv} versus the steady state velocity v_x of the droplet. For $\Phi = 0.444$ and within the confidence intervals, the trend follows the expected decrease with velocity, while for $\Phi = 0.615$ the trend mirrors that of the ridge height h_R^{adv}. Finally, Figure 6.7 d) shows the separation height at the receding end h_{sep}^{rec} versus the steady state velocity v_x of the droplet. The separation between the brush and the liquid ridge at the receding end

gradually decreases as the velocity of the droplet increases. The peculiar behavior at the advancing front could be explained as follows. As the droplet rolls, it drags material from the receding end onto the advancing front. The material is transported as part of the cloak. For all velocities, material is depleted from the receding end, hence the separation height decreases. At the advancing front, however, material will be deposited. At low velocities, the material is deposited there and the ridge grows, leading to an increase in the separation height. This is the case until a threshold velocity is reached. Then the droplet starts rolling over the advancing ridge leading to a decrease in the separation height.

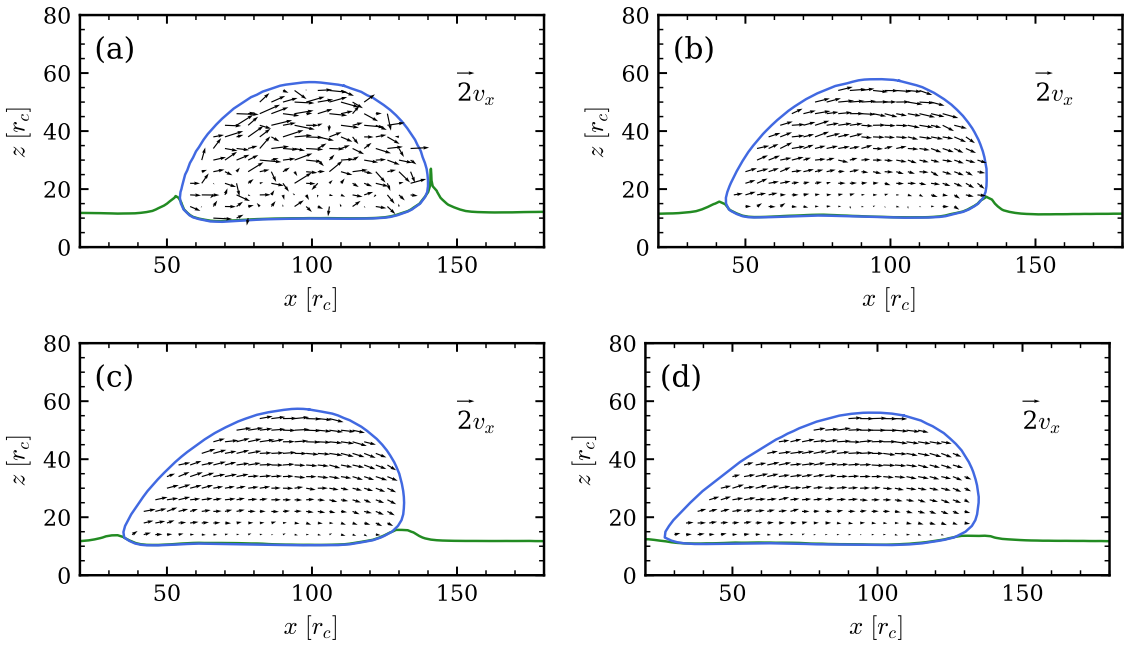

Figure 6.8.: Flow field inside the droplet in the xz-plane in the laboratory frame for different applied bulk forces and lubricant fraction $\Phi = 0.615$. Green contour represents the substrate, blue contour the droplet. (a) $F = 8{\times}10^{-5} k_B T/r_c$, (b) $F = 20{\times}10^{-5} k_B T/r_c$, (c) $F = 30 \times 10^{-5} k_B T/r_c$, (d) $F = 40 \times 10^{-5} k_B T/r_c$. The low flow velocity near the substrate indicates little to no slipping. The arrow outside the droplet sets the scale for twice the steady state velocity $2v_x$.

Summed up, the behavior of the wetting ridge does not allow us to conclude whether the dissipation is dominated by either the liquid wetting ridge or the viscoelastic braking in the brush. Above, we mention that the contribution of the dissipation in the wetting ridge is reduced at larger velocities. However, as will be shown in section 6.U.2, that contribution does not vanish. First, the height of the wetting ridge still extends higher than the unperturbed brush for lubricated brushes even at large velocities. In addition, the height of the wetting ridge in the middle of the drop (between the advancing and receding sides) is not affected by velocity in the same way; in particular, at the position

of the center of mass the wetting ridge is not affected by velocity (see Figure 6.U.4).

6.4.4. Flow field

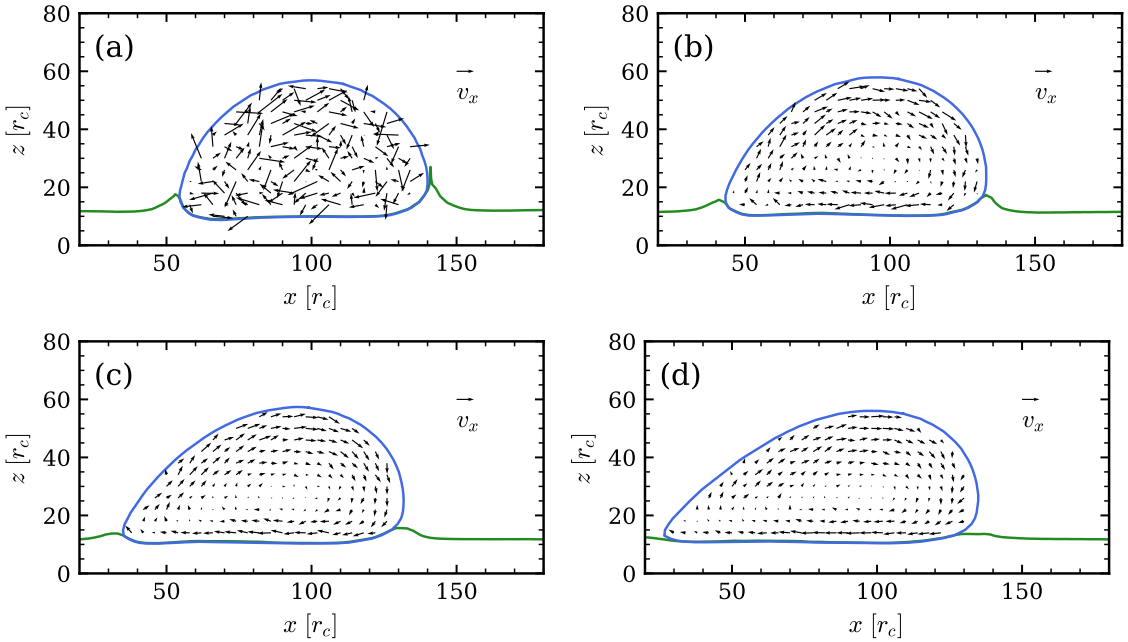

Figure 6.9.: Same as Figure 6.8 in the co-moving frame of the center of mass of the droplet. (a) $F = 8 \times 10^{-5} k_B T/r_c$, (b) $F = 20 \times 10^{-5} k_B T/r_c$, (c) $F = 30 \times 10^{-5} k_B T/r_c$, (d) $F = 40 \times 10^{-5} k_B T/r_c$. The flow field shows clear signs of rolling motion. The arrow outside the droplet sets the scale for the steady state velocity v_x.

To understand the contribution of the droplet motion to the total friction, we need to know whether the drop is rolling, sliding, or a combination of both. To answer this we calculate the flow field within the droplet. We select a slab of the droplet of thickness $2r_c$ along different planes and analyze the flow in this slab. To obtain the final flow fields we calculate a flow field from each simulation by taking an average over 150 snapshots, and subsequently average the flow fields of 5 independent simulations. Figure 6.8 shows the flow field in the xz-plane near the center of mass of the droplet in the laboratory frame. For $F = 8 \times 10^{-5} k_B T/r_c$ (Figure 6.8 a), the average local flow is on the order of the statistical error due to thermal motion within the droplet, hence flow profile is strongly affected by noise, but a net flow to the right can be discerned. For the other forces $F = 20 \times 10^{-5} k_B T/r_c$; $F = 30 \times 10^{-5} k_B T/r_c$; $F = 40 \times 10^{-5} k_B T/r_c$ in (b), (c), and (d) respectively, there is a clear net flow toward the right. At the interface between the droplet and the brush, the velocity is small indicating that the droplet rolls with little to no sliding even in the presence of lubricant. This is different from previous simulations of polymer droplets on hard corrugated substrates [117, 298], where significant slip was observed at

the surface. This safely eliminates the possibility of the dominance of dissipation due to slip.

Figure 6.9 shows the flow field in the co-moving frame of the center of mass of the droplet. Again, extracting a flow field is difficult at the lowest force due to the random thermal motion. For stronger forces, the flow field profiles clearly feature a rolling motion. Interestingly, the flow field inside the droplet seems to feature two vortices, one close to the center of the droplet and one towards the back end. Similar two-vortex structures have been visualized experimentally in flow profiles inside adhering droplets in shear flow [299]. Numerical Lattice Boltzmann simulations [300] and continuum simulations [118] of rolling droplets on flat and structured hydrophobic surfaces have also revealed complex flow patterns inside the droplets. The flow looks similar along different slices on the y-axis, except at the absolute edge of the droplet (see Figure 6.13). The complexity of the flow means that the exponent could deviate from the value $\beta = 2$ expected for the case of constant shear rate in the droplet (see section 2.4.2).

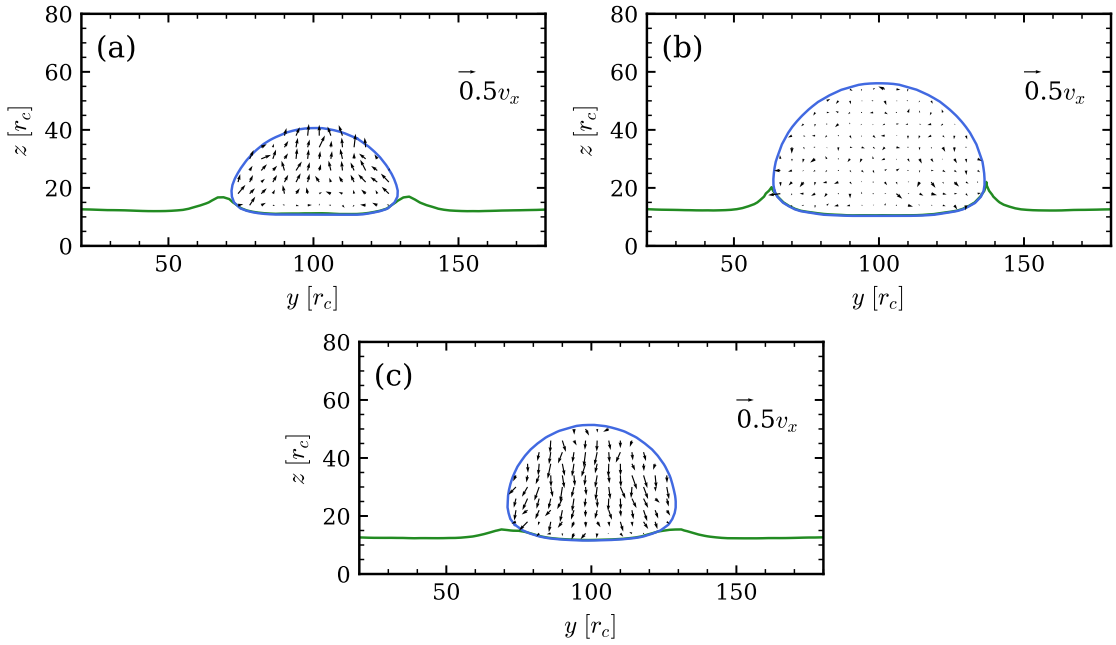

Figure 6.10.: Flow field inside the droplet in the yz-plane in the laboratory frame for $F = 40 \times 10^{-5} k_B T/r_c$ and lubricant fraction $\Phi = 0.615$. The different figures correspond to different slices along the x-axis: (a) near the receding end, (b) at the center, (c) near the advancing front. The arrow outside the droplet sets the scale for half the steady state velocity $0.5v_x$.

Figure 6.10 shows the flow field in the yz-plane in the laboratory frame for $F = 40 \times 10^{-5} k_B T/r_c$ and lubricant fraction $\Phi = 0.615$. The different sub-figures correspond to different slices along the x-axis: (a) near the receding end, (b) at the center, (c) near the

advancing front. Moving from the receding end to the advancing front, we see what is expected in the case of rolling motion, in addition to a lateral flow that brings material towards the center at the receding end, and away from the center at the advancing front.

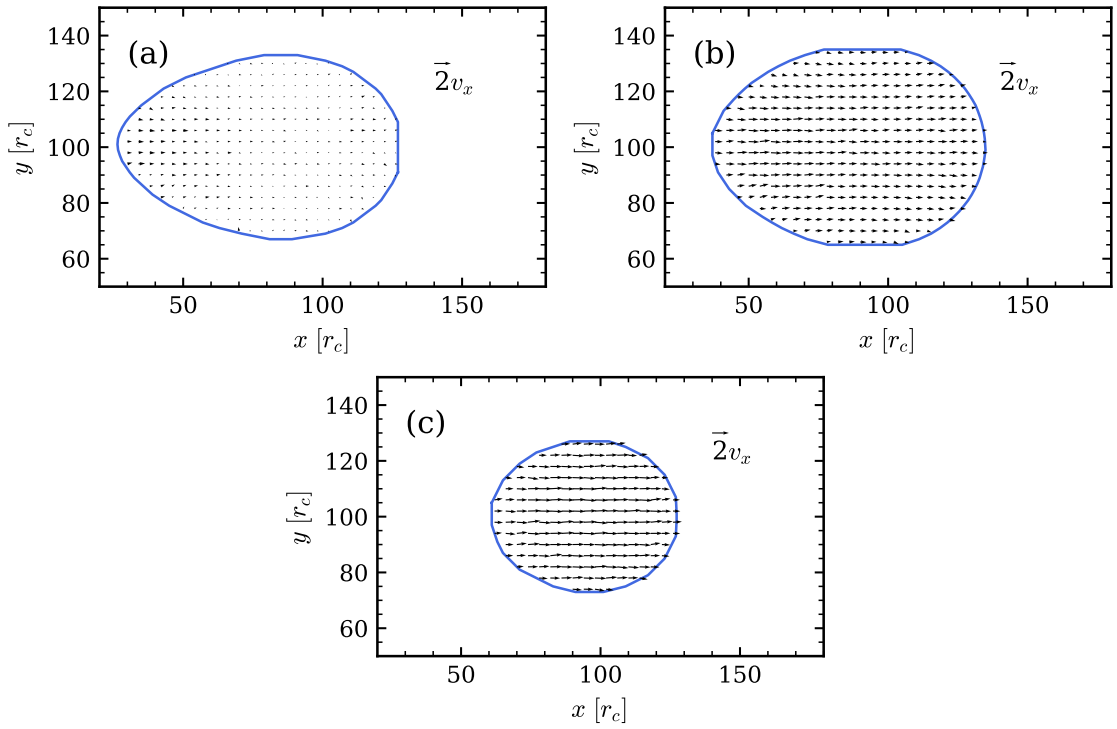

Figure 6.11.: Flow field inside the droplet in the xy-plane in the laboratory frame for $F = 40 \times 10^{-5} k_B T/r_c$ and lubricant fraction $\Phi = 0.615$. The different figures correspond to different slices along the z-axis: (a) near surface of the brush, (b) at the center, (c) near the top of the droplet. The arrow outside the droplet sets the scale for twice the steady state velocity $2v_x$.

Figure 6.11 shows the flow field in the xy-plane in the laboratory frame for $F = 40 \times 10^{-5} k_B T/r_c$ and lubricant fraction $\Phi = 0.615$. The different sub-figures correspond to different slices along the z-axis: (a) near surface of the brush, (b) at the center, (c) near the top of the droplet. We see the expected increase in velocity as we move away from the brush, and the flow is quite uniform throughout.

6.4.5. Cloak structure and oil transport

As real cloaked droplets move on PDMS substrates, they carry the lubricant with them, thus depleting the lubricant and reducing the associated favorable qualities of the substrate. To investigate the effect of the droplet motion on its cloak, we study how the cloak thickness is affected by the droplet velocity. We now section the droplet along a plane

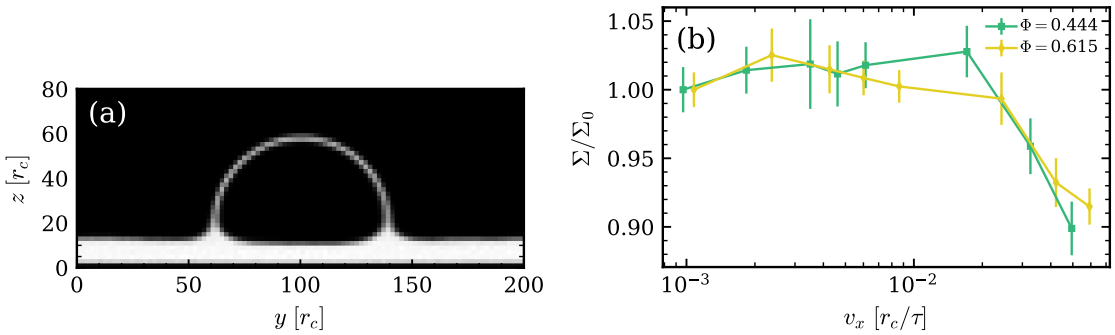

Figure 6.12.: (a) Example of a polymer density map in a cross-section perpendicular to the droplet velocity at $\Phi = 0.615$. (b) Normalized Surface density of free chains at the top of the droplet Σ/Σ_0 versus droplet velocity ($\Sigma_0 = 4.0/r_c^2$ at $\Phi = 0.444$, $\Sigma_0 = 4.4/r_c^2$ at $\Phi = 0.615$).

perpendicular to the direction of motion. We choose a section centered at the center of mass of the droplet and of thickness $2r_c$ and calculate the local density of polymers $\rho(y, z)$ within that section. Such a density map is shown in Figure 6.12 a). To measure the variation in the cloak we calculate an effective surface density at the top of the droplet

$$\Sigma = \int_{z_1}^{z_2} dz \rho(y = 0, z) \tag{6.2}$$

with z_1 corresponding to a point within the droplet, and $z_2 > z_1$ a point above the cloak. Figure 6.12 b) shows Σ versus the droplet velocity normalized by the value at the lowest velocity Σ_0. For low velocities the cloak is not affected, but for the highest two velocities the value slightly decreases by about 10%.

The fact that the cloaking layer is not strongly affected by the motion, combined with the fact that the area of the droplet increases at larger velocities due to shape deformations, implies that the transport of lubricant is expected to be enhanced at higher velocities.

6.5. Conclusion

In sum, we have studied the effect of adding lubricant on the motion of droplets on polymer brush coated surfaces under the influence of an external, e.g., gravitational, body force. The simulation model is adapted to describe water droplets on surfaces with PDMS brushes and free PDMS chains acting as lubricant. One characteristic feature of this system is the existence of a cloaking transition [163]: beyond a critical lubricant content, the water droplet is fully covered by a thin layer of free PDMS chains. Hence our study also addresses the question how such a cloaking layer affects the droplet motion.

In general, we find that the droplet velocity v increases with the applied force F following a power law, $v \propto F^{1/\alpha}$. With increasing velocity, the droplet deforms and elongates. The receding contact angle decreases roughly linearly as a function of v, while the advancing angle remains roughly constant at a value close to the equilibrium angle. In previous molecular dynamics simulations of rolling droplets on hydrophobic surfaces [301] or patterned superhydrophobic surfaces [302], and also of oil droplets that slide on polymer brush surfaces driven by shear flow [294], both the advancing and the receding angle were found to deviate strongly from the equilibrium value. In these examples, the surfaces were either hard, or soft but with negative spreading parameter S, i.e., a Neumann construction is possible. Assuming $S < 0$, linear vicoelastocapillary theory [98] predicts that the advancing contact angle should deviate from the static angle. However, recent experiments have suggested that this theory is no longer generally valid if the spreading parameter is positive [229]. Our simulation results support this hypothesis.

For the investigated fractions of lubricant in the brush, we find that lubrication has a surprisingly small effect on this behavior. Adding a limited amount of lubricant chains only slightly reduces the friction force between the droplet and the surface. This is also suggested indirectly by the experiments, where it was found that the friction does not depend on the method used to prepare the polymer brushes. In particular, whether or not free polymers have been washed out from the brushes after synthesis did not seem to make any difference. However, the degree of swelling could not be determined in the experiments. In the simulations, the velocity of droplets subject to a given driving force does not change at all (within the statistical error) if one adds lubricant amounts below the cloaking transition. Above the cloaking transition, the velocity somewhat increases, i.e., the friction is somewhat reduced, but by less than a factor 3/4 at the highest lubricant content. The power law exponent α increases slightly for cloaked droplets, but by less than 20%.

The value of the exponent $\beta = 1 + \alpha$ in simulation is close to the value $\beta = 5/3$ predicted by certain theoretical approaches for the dissipation in the three phase contact line and the liquid wetting ridge. However, it is not clear whether the value is due to those sources of dissipation dominating the friction, or it is coincidental, especially given that the experimental exponent deviates from that value.

Lubricants also have no discernible effect on the macroscopic properties of the droplet, i.e., its shape as a function of velocity, and the advancing and receding contact angles. They do, however, affect the local structure at the contact line, i.e., the wetting ridge. In particular, the ridge height of strongly cloaked droplets exhibits a maximum as a function of droplet velocity, suggesting a transition between a low-velocity regime where the droplet pushes the wetting ridge in front of it, to a regime where it partially rolls over it. At higher velocities, the height of the ridge is reduced. Regardless of the geometry of the ridge, our ridges are composed of both liquid lubricant and stretched grafted chains; although the exponent in the simulation is close in value to the prediction in section 2.4.4, the fact that the ridge is not a pure liquid could invalidate the arguments presented there.

To understand the reason for the unexpected low lubricating effect of free chains in the

brush, we analyzed the pattern of the flow field inside the droplet. The friction results from an interplay of energy dissipation at the adhesive surface (contact area dissipation), at the contact line, i.e., the wetting ridge (contact line dissipation), and inside the droplet (bulk dissipation). In previous molecular simulation studies of droplets driven by external forces move on flat or patterned forces, it was found that droplets may both roll and slide (slip) at the surface [117, 298, 303]. In such cases, it has been argued that the friction between the droplet and the surface is dominated by contact area dissipation for small droplet sizes [117, 298], and by contact line friction [298] or bulk dissipation [117] for larger droplets. In our system, we find that the flow velocity is very small at the interface between droplet and substrate, thus the droplet does not slide, and the dissipation due to slip at the adhesive surface can be neglected. The dissipation at the wetting ridge does contribute - as can be inferred from the fact that the friction force is affected by the cloaking transition [...] Given that the ridge is smaller at high velocities, the dissipation in the wetting ridge could play a smaller role at high velocities. However, the ridge does not fully vanish, and the dissipation in it might still be significant. Based on this, we argue that the dominating contribution to dissipation is either the shear flow inside the droplet, which is not affected by the lubricant (see Figures 6.14 and 6.15) or the viscoelastic dissipation in the brush. In the case where the viscous dissipation in the droplet dominates, for droplets of fixed shape with fixed flow patterns, one would expect the resulting friction force to scale linearly with the droplet velocity [117]. However, the droplets can partly reduce the dissipation at high velocities by changing their shape, which affects the flow profiles as discussed in Section 6.4.4. As a result, the increase of the friction force with droplet velocity is only sublinear, and could explain the discrepancy between experiment and simulation. In the experiment, the drop is fixed in place by a cantilever that is used to measure the force of friction and could affect the flow dramatically. In the other case, where the viscoelastic dissipation in the brush dominates, the exponent would be set by the rheology of the brush. This can also explain the different exponents between experiment and simulation as the two brushes likely have different rheologies. On top of that, the rheology in simulation is likely affected by the degree of lubrication, which might be the reason for the small variation in the exponent as the lubricant fraction is varied.

Ultimately, the question remains why the power exponent α measured in the simulations ($\alpha \sim 0.6 - 0.7$) differs from the one measured in the experiments ($\alpha \sim 0.25$). Although we have studied large droplets containing almost a million particles, they are still microscopic compared to the droplets considered in the experiments, which have sizes of the orders of millimeters. Nevertheless, the Reynolds numbers in the simulations and experiments are comparable (see section "Model and Methods"), suggesting that the flow fields may also be comparable. On the other hand, the experimental drop sizes are comparable to the capillary length (radius $\approx$ 1.5mm, capillary length $\approx$ 2.7mm) such that gravity may become important. The influence of droplet size and gravity on the friction force will be an interesting subject of future studies.

We should also note that, in the present study, we have only studied lubricant fractions where the brush is not yet fully saturated. If we had much more lubricant, it will form a thick film above the brush, and the situation will change. The droplet will then be

immersed in the lubricant film and the shear flow inside the film will significantly contribute to the dissipation.

6.6. Data availability

All codes used for simulation are available on the github repository `https://github.com/rodbadr/dropletOnLubricatedBrush`.

Data used for all figures except flow fields and density maps are available at `https://github.com/rodbadr/DataDynamicsOfMovingDroplets`. Simulation trajectories and flow field data can be provided upon reasonable request.

[...]

6.7. Acknowledgments

This work was funded by the German Science Foundation (DFG) within the priority program SPP 2171 (Grant No. 422796905, projects Schm 985/22 and VO 639/16). Further support is acknowledged from the DFG-funded Graduate School RTG 2516 (Grant No. 405552959): RGMB and LH are associated members, FS is a member. The simulations were partly carried out on the supercomputer system Mogon NHR Süd-West at Johannes Gutenberg University Mainz. RGMB thanks Leonid Klushin for useful discussions.

6.8. Supporting information to the published article in Chapter 6

Note: With the exception of Figure 6.13 (f), the figures in this section already appear as supporting info on the online page of the published article Ref. [119].

[...]

6.8.1. Additional flow fields

Below are some additional flow fields from the simulations. Figure 6.13 shows the flow field inside the droplet in the xz-plane in the co-moving frame at different positions across the droplet. Comparing the different slices indicates that the components of velocity along the x and z directions depend only weakly on the y-coordinate. This is made more clear by overlaying the flow fields at different positions of the xz-plane as shown in Figure 6.13 (f). The flow fields from the different slices overlap well in both magnitude and orientation excepts for small variations.

Figure 6.14 shows the flow field inside the droplet in the xz-plane in the co-moving frame with varying lubricant fraction for a driving force $F = 20 \times 10^{-5} k_B T / r_c$. The flow fields for lubricant fractions $\Phi < 0.615$ are more noisy than for $\Phi = 0.615$. This is likely due to

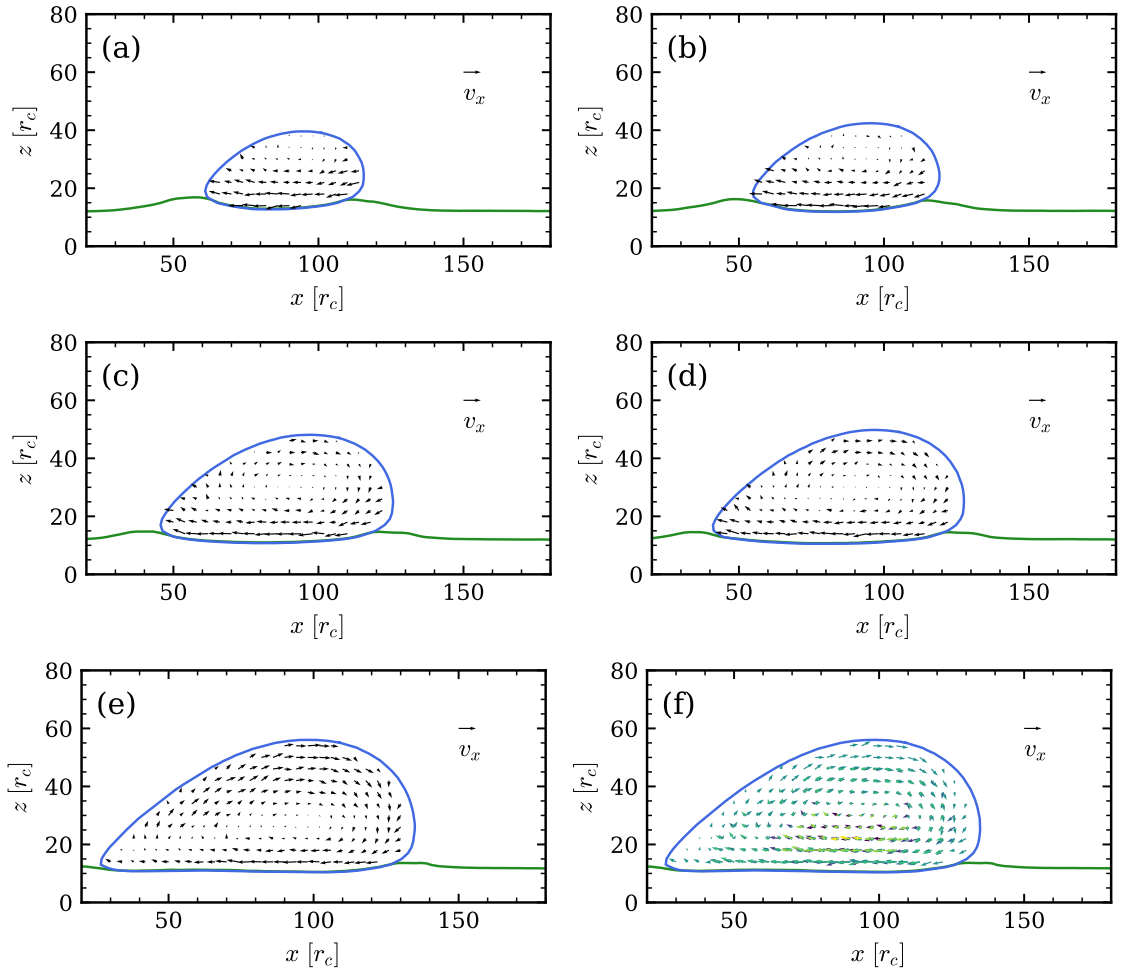

Figure 6.13.: Flow field inside the droplet in the xz-plane in the co-moving frame for $F = 40 \times 10^{-5} k_B T/r_c$ and lubricant fraction $\Phi = 0.615$. The different figures correspond to different slices along the y-axis: (a), (b) near the edge of the droplet, (c), (d) closer to the center, (e) at the center. The arrow outside the droplet sets the scale for twice the steady state velocity v_x. (f) Overlay of the flow field from different slices across the droplet; the color of the arrows relate to the position of the slice going from blue on one edge to yellow on the other.

---

the larger steady state velocity at $\Phi = 0.615$ which is almost twice as large as the velocity in the absence of lubricant. However, once the velocity is large enough, the lubricant has little effect on the flow field, as can be seen in Figure 6.15 which shows the flow fields for a force $F = 40 \times 10^{-5} k_B T/r_c$ at different lubricant fractions.

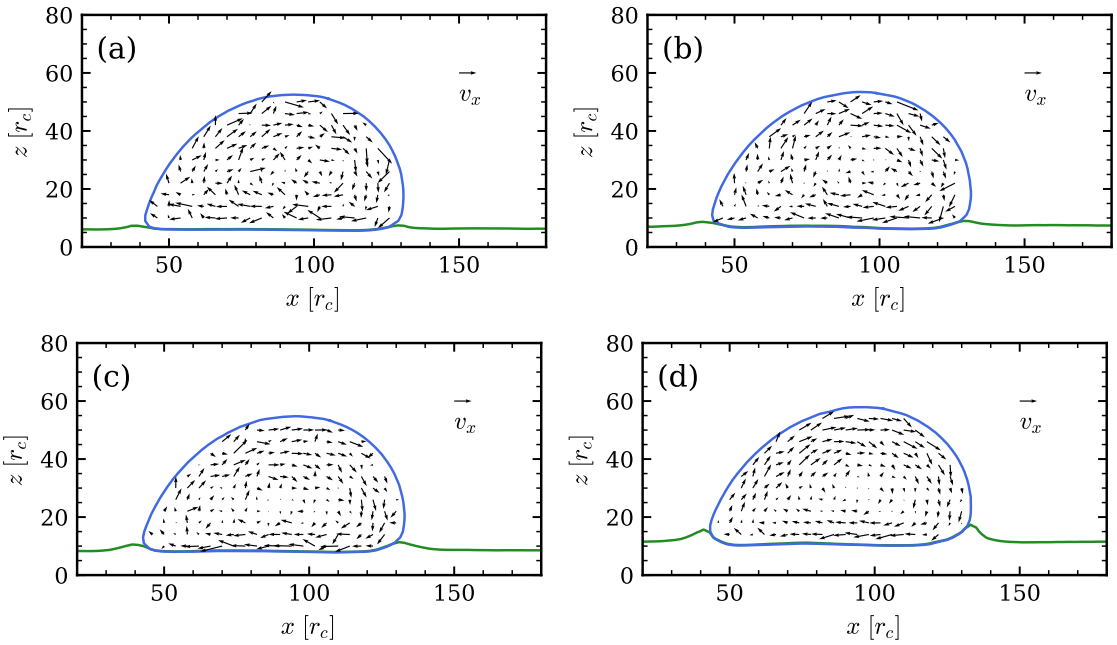

Figure 6.14.: Flow field inside the droplet in the xz-plane in the co-moving frame for $F = 20 \times 10^{-5} k_B T / r_c$ and varying lubricant fractions. (a) $\Phi = 0$, (b) $\Phi = 0.231$, (c) $\Phi = 0.444$, (d) $\Phi = 0.615$. The arrow outside the droplet sets the scale for twice the steady state velocity v_x.

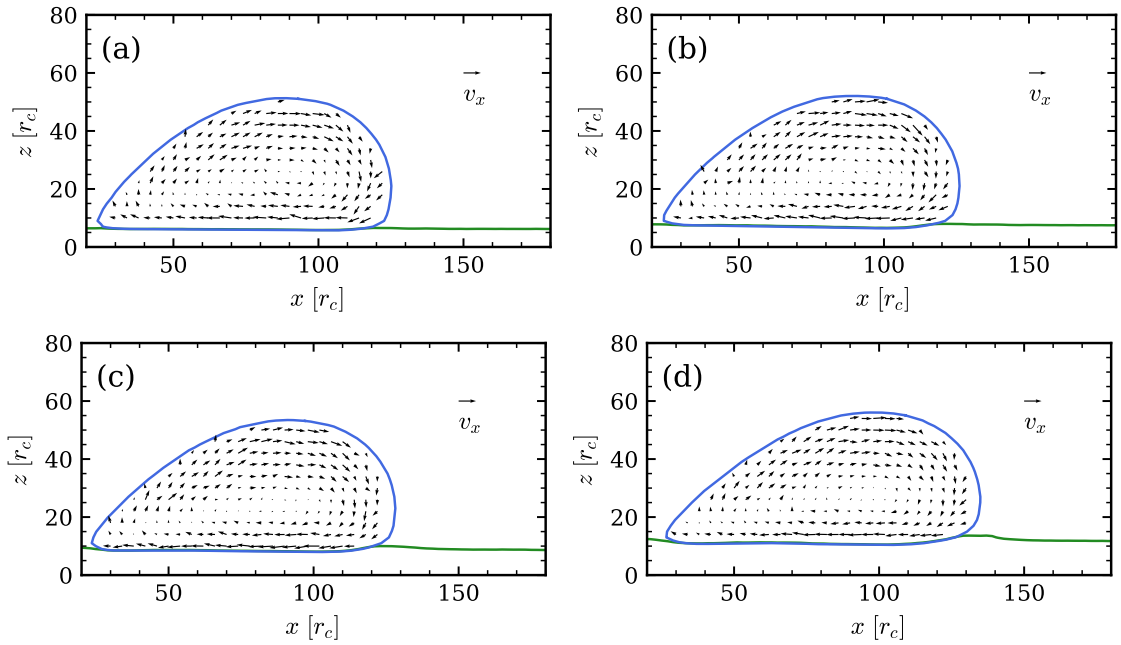

Figure 6.15.: Flow field inside the droplet in the xz-plane in the co-moving frame for $F = 40 \times 10^{-5} k_B T / r_c$ and varying lubricant fractions. (a) $\Phi = 0$, (b) $\Phi = 0.231$, (c) $\Phi = 0.444$, (d) $\Phi = 0.615$. The arrow outside the droplet sets the scale for twice the steady state velocity v_x.

6.U. Unpublished results: Dynamics of Droplets Moving on Lubricated Polymer Brushes

The following sections include unpublished results obtained in preparation or after the conclusion of the published article in Chapter 6.

6.U.1. Effect of MDPD model parameters on viscosity

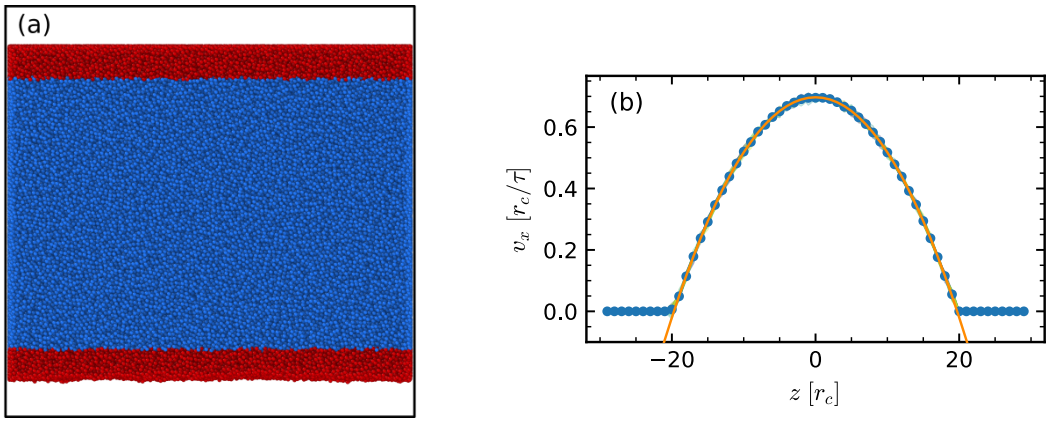

Figure 6.U.1.: (a) Snapshot from a Poiseuille flow simulation of a simple liquid. The red particles are frozen in place, while the blue particles are allowed to move. (b) The resulting flow field for the liquid shown in (a) with the corresponding fit to a parabola.

For the question of the dynamics of moving droplets, the viscosity plays an important role as viscous dissipation can be a major contributor to energy loss. To quantify the viscosity of our liquids, we run Poiseuille flow simulations. Liquid slabs are prepared as described in section 3.2.2 with the z-direction normal to the liquid-vapor interface. Afterwards, chains within $10r_c$ from either interface are frozen in place, and a force F in the x-direction is applied on each particle to create a flow. For a planar Poiseuille flow, the expected velocity profile has the form

$$v_x(z) = -\frac{F\rho_l}{2\mu}(z^2 - z_0^2) \tag{6.U.1}$$

where μ is the dynamic viscosity, ρ_l the number density and $v_x(\pm z_0) = 0$. An example simulation snapshot and the resulting flow field are shown in Figure 6.U.1. We perform simulations for both simple liquids ($N_o = 1$) and polymer liquids ($N_o = 5$), and we vary the drag coefficient and cohesion strength for each. The force per particle for the case of a simple liquid is $F = 0.01\,[k_bT/r_c]$, while for the polymer liquid we choose $F = 0.001\,[k_bT/r_c]$. Though the results are robust with changes in the force, occasionally an instability would kick in, where a bubble would spontaneously appear in the bulk of the liquid. The instability was not investigated systematically; however, it appears to be a static instability akin to a liquid-vapor phase separation. The liquid in the slab is at the coexistence density which is very close to the metastable region of the phase diagram; therefore, occasionally a nucleus of low density vapor would appear in the bulk and grow into a vapor bubble. The likelihood of the instability kicking in is reduced for thicker slabs, and every individual simulation was checked for bubbles before calculating the viscosity.

The results for the viscosity are shown in Figure 6.U.2. Interestingly, the drag coefficient seems to have very little effect on the viscosity: upon doubling the value of the drag coefficient the resulting change in the viscosity is about 10% for both the simple and polymer liquid (see Figure 6.U.2 a and b). On the other hand, the viscosity is more sensitive to changes in the strength of cohesion. For the simple liquid (Figure 6.U.2 c) the viscosity increases threefold upon doubling the strength of cohesion. For the polymer liquid, the sensitivity to the cohesion strength is stronger, with the viscosity increasing more than threefold upon an increase of 30% in the strength of cohesion. The results from the Poiseuille flow simulations provide a valuable insight into the MDPD model: the majority of the momentum transport is carried by the conservative force.

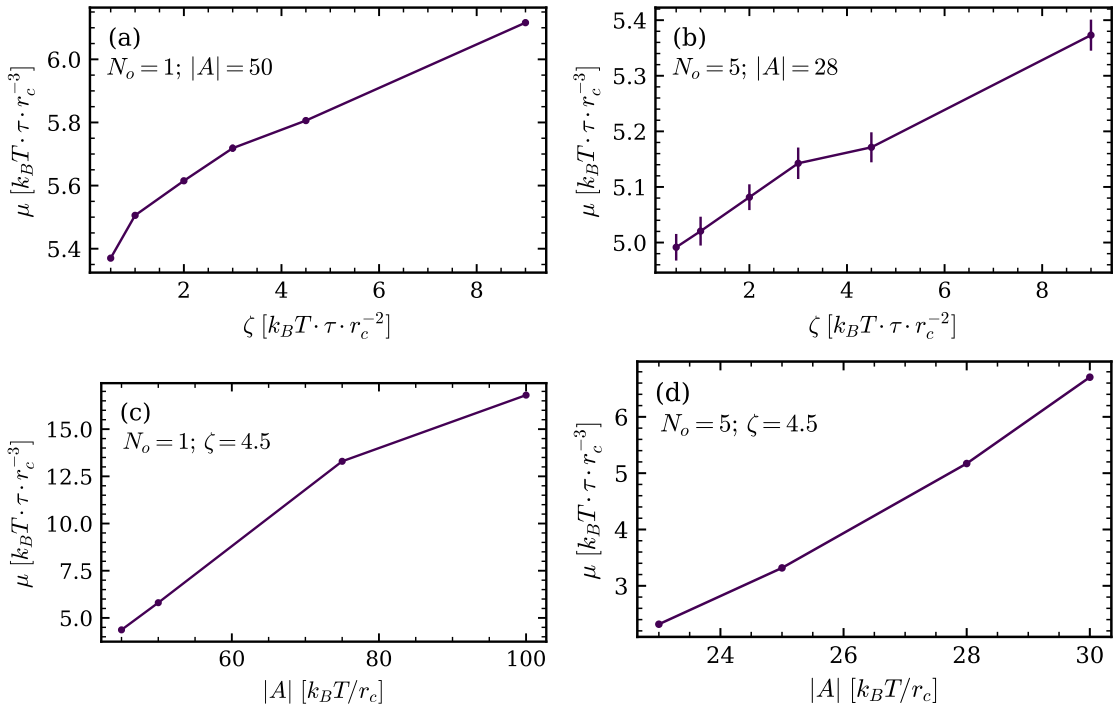

Figure 6.U.2.: Dynamic viscosity μ of (a) a simple liquid and (b) a polymer liquid versus the drag coefficient ζ. The value of the drag coefficient does not have a strong effect on the viscosity. Dynamic viscosity μ of (c) a simple liquid and (d) a polymer liquid versus the cohesion strength $|A|$. The viscosity increases significantly as the cohesion increases.

6.U.2. Dynamics at higher lubricant fractions

In the published part of this chapter we focused on polymer brushes with intermediate lubricant fractions and observed that the lubricant plays only a minor role in the dynamics. However, the situation might differ at higher lubrications. To investigate this we performed similar analysis as above with two additional lubricant fractions $\Phi = 0.737$ and $\Phi = 0.778$; the latter corresponds to the saturation limit, i.e. if more lubricant is added, the brush will not swell any further and the additional lubricant will form a film on top of the swollen brush.

We begin by looking at the power dissipated in terms of lubrication and velocity. Figure 6.U.3 (a) show the power dissipated $P_{\text{diss}} = N_w F v_x$ versus velocity on linear axes. For $\Phi \in [0, 0.444]$ the data is clustered and separated from the results for $\Phi > 0.444$. This indicates a possible change in behavior due to the cloaking transition at $\Phi \approx 0.444$ (see section 4.2.3). Figure 6.U.3 (b) shows P_{diss} versus velocity on logarithmic axes, where the dashed lines are linear fits to the data. The relevance of the cloaking transition can also be observed in the value of the exponent β_{sim} which captures the dependence of

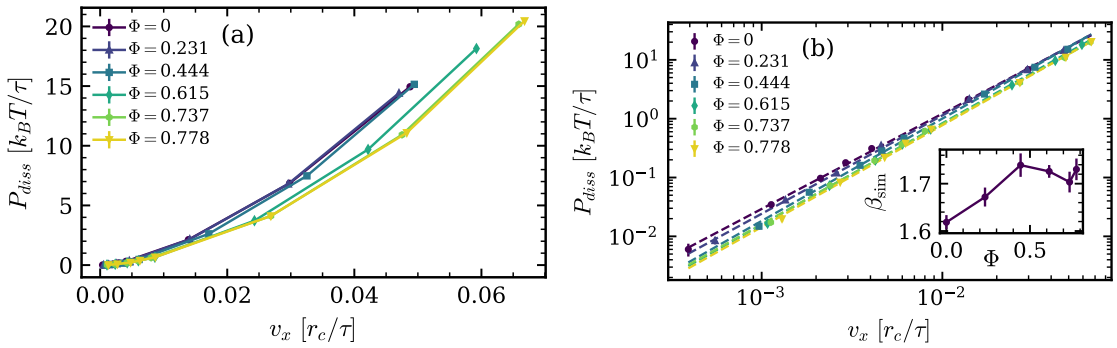

Figure 6.U.3.: Steady-state power dissipation defined as $P_{\mathrm{diss}} = N_w F v_x$ versus the steady-state velocity v_x (a) on linear axes, (b) on logarithmic axes. The dashed lines in (b) show fits to a power-law behavior $P_{\mathrm{diss}} \propto v_x^{\beta_{\mathrm{sim}}}$. $\Phi \geq 0.444$ corresponds to cloaked droplets.

---

the power dissipated on velocity $P_{\mathrm{diss}} \sim v^{\beta_{sim}}$. The dependence of the exponent on the lubricant fraction is shown in the inset of Figure 6.U.3 (b); the data points indicate a slight increase in the exponent until the cloaking transition, after which the value of the exponent saturates.

As mentioned above, the dissipation in the wetting ridge could constitute a significant contribution to the friction experienced by the droplet. We showed that an increase in the velocity of the drop is accompanied by a reduction in the height of the wetting ridge. Figure 6.U.4 (a) and (b) show the height of the wetting ridge at the receding and advancing ends of the droplet. We see a similar trend at the receding end for the high lubricant fractions as we did for the lower ones, namely that the height of the ridge decreases with velocity. When it comes to the advancing front, one feature was the accumulation of lubricant there for low velocities at certain lubricant fractions, resulting in an increase in the height of the wetting ridge, before it decreases at high velocities. This feature is maintained at $\Phi = 0.737$ but disappears when the brush is saturated at $\Phi = 0.778$. Despite the reduction in height at both the receding and advancing ends, the wetting ridge does not vanish even at the highest velocities. The open symbols in Figure 6.U.4 (a) and (b) show the height of the unperturbed brush; the vertical dashed lines indicate the difference between that height and the height of the wetting ridge at the fastest simulated velocity. For all lubricant fractions the height of the ridge exceeds the unperturbed height for all droplet velocities. In addition, the height of the wetting ridge between the two ends is affected differently by velocity. Figure 6.U.4 shows the height of the ridge h_R^{mid} at a plane that contains the center of mass of the droplet; there, the effect of the motion of the droplet on the height of the wetting ridge is minimal. Overall, the results for the height of the dynamic wetting ridge indicate that the contribution of the dissipation in the wetting ridge does not vanish at high velocities, and depending on its magnitude, might constitute a significant part of the total dissipation.

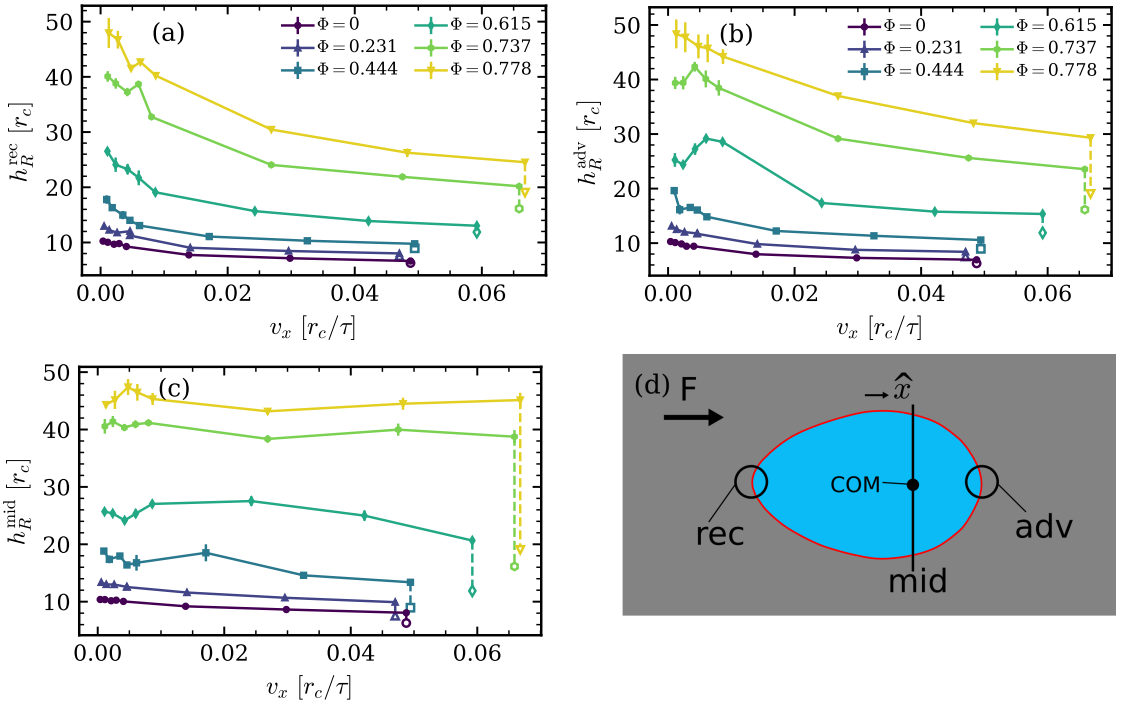

Figure 6.U.4.: (a) Height of the wetting ridge at the receding end h_R^{rec} versus droplet velocity. (b) Height of the wetting ridge at the advancing front h_R^{adv} versus droplet velocity. (c) Height of the wetting ridge in the middle of the droplet h_R^{mid} versus droplet velocity. The open symbols and dashed lines serve to compare the height of the wetting ridge to the height of the unperturbed brush. (d) Cartoon illustrating the positions of the receding end, the advancing front, and the middle position we chose with COM referring to the position of the center of mass.

Figure 6.U.5 shows the flow field in the co-moving plane of the droplet in the xz-plane passing through the center of mass of the droplet for a force per particle $F = 40 \times 10^{-5}$ $[k_BT/r_c]$ and varying lubricant fractions. Comparing the flow fields to those shown in Figure 6.15 we see that the effect of lubrication on the flow field is minimal even at high lubricant fractions. However, the shape of the wetting ridge changes significantly for $\Phi = 0.737$, and $\Phi = 0.778$ compared to the lower lubricant fractions. Since the flow field is not strongly affected, the viscous dissipation in the droplet is likely not the source of the change in the exponent β_{sim}; however, more detailed investigation is still needed to rule it out completely.

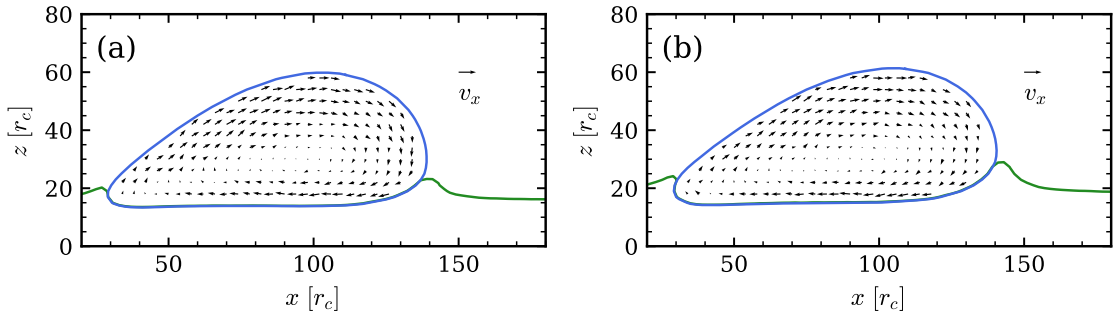

Figure 6.U.5.: Flow field inside the droplet in the xz-plane in the co-moving frame for $F = 40 \times 10^{-5}\ [k_BT/r_c]$ and varying lubricant fractions. (a) $\Phi = 0.737$, (b) $\Phi = 0.778$. The arrow outside the droplet sets the scale for the steady state velocity v_x.

6.U.3. Conclusion

In this section, we presented results for the viscosity of simple and polymer liquids in the MDPD model as well as results pertaining to the dynamics of rolling droplet at high lubricant fractions in the brush.

The results for the viscosity with varying MDPD model parameters showed an interesting behavior: the majority of the contribution to viscosity stems from the conservative forces. This is indicated by the small effect of varying the drag coefficient in the thermostat of our model, and by the more pronounced change in viscosity upon a change in the strength of cohesion.

Concerning the role of lubrication on the dynamics of rolling droplets, we find the the value of the exponent β_{sim} which relates the power dissipated to velocity through $P_{diss} \sim v^{\beta_{\text{sim}}}$ varies slightly with lubrication, but its value appears to remain constant after the cloaking transition sets in at lubricant fraction $\Phi = 0.444$ in our system.

The behavior of the wetting ridge at the receding end is similar at all lubrications. At the advancing front, the accumulation of lubricant for small velocities is still present for $\Phi = 0.737$, but does not occur at the saturation fraction $\Phi = 0.778$. Between the advancing and receding ends, the wetting ridge is affected differently by the motion of the droplet, and at a particular position is not affected at all by the motion. At all positions around the three phase contact line, the ridge is higher that the unperturbed brush for all velocities. Taken together, this indicates that if the dissipation in the wetting ridge is significant, it will remains so at all velocities. We also find that the flow field does not strongly depend on the lubricant fraction. Therefore, the viscous dissipation in the droplet does not explain the variation in the exponent β_{sim}. However, this does not mean that the viscous dissipation in the drop is not significant. The contributions from both the dissipation in the ridge and the viscous dissipation may be equally significant; the exponent β_{sim} could be set through a self-consistent interplay between the different dissipation sources. Quantifying

the separate contributions to dissipation and its localization in space is an interesting subject for future study.

7. Summary and outlook

The interaction of liquid drops, in particular water drops, with elastic substrates swollen with PDMS is an interesting problem, rich with challenging physics and yet to be answered questions. To address some of these questions, we perform numerical, theoretical, and experimental studies, focusing on the phenomenon of cloaking.

In our first study, we investigate the cloaking of a droplet on a lubricated polymer brush in MD simulations. The parameters of the simulation are tweaked so the surface tension ratios reflect those in experiments of water on PDMS. We show the existence of a cloaking transition in simulation, supported by theoretical thermodynamic considerations. The transition sets in when the brush is swollen with a particular fraction of lubricant. The effect of cloaking on the wetting properties is studied for both spherical and cylindrical droplets. For spherical droplets, we show that the dependence of the contact angle on a dry brush is consistent with the presence of a negative line tension that promotes the spreading of the drop, while on lubricated brushes the size dependence, though significant, cannot be simply attributed to line tension alone. For cylindrical droplets, the cloaking transition is still present and sets in at the expected lubricant fractions. As expected, the contact angle on dry brushes does not show a size dependence since the straight contact lines of cylindrical brushes eliminate the influence of line tension. The dependence of the contact angle on the lubricant fraction for spherical and cylindrical droplets shows some interesting features. For cylindrical droplets the contact angle increases slightly with lubrication, as expected from a cloaked drop with a contact angle larger than 90°. As for spherical drops, the contact angle is smaller than that for cylindrical drops, owing to the line tension; in addition, the contact angle for spherical drops decreases slightly with lubrication, suggesting a possible dependence of the line tension on the degree of lubrication of the brush.

The investigation of the static properties is followed by a probe into the kinetics of ridge and cloak development of the lubricant on both PDMS gels and brushes. Fluorescent confocal microscopy was used to probe the wetting ridges of drops on PDMS gels swollen with high viscosity oils. The oil was previously shown to separate from the gel and form a liquid phase of the wetting ridge [38]. In our work we followed the time evolution of this phase separated ridge. We first show that the ridge grows with a geometrically similar shape. In addition, we show that both the swelling ratio and oil viscosity play a role in the growth rate and size of the ridge. The higher the swelling ratio, the larger the resulting ridge, and the later the equilibrium size is reached. Higher viscosity oils exhibit slower ridge growth; however, at the same swelling ratio, the equilibrium size is larger for higher viscosities. Some of the conclusions of the experiments are consistent with a

theoretical analysis based on a diffusion model. The theoretical growth curves for heavily swollen gels overlay nicely with the theoretical data. However, the theoretical model does not capture well the curves for gels with low swelling ratio, neither in equilibrium size nor in saturation speed. This is likely due to the simplicity of the model. In addition to the experiments on the growth of the wetting ridge, we were interested in the kinetics of cloaking. We investigated cloaking on the experimental level indirectly by measuring the surface tension of pendant drops in contact with a swollen PDMS gel. The experiments exhibit very little reproducibility, likely due to the design of the experiment which utilizes holes drilled into glass slides. During the drilling process, defects appear around the holes which could have a significant effect on the behavior of the system. On the numerical level, we setup MD simulation similar to those used to study the static case, but follow the cloak development as it evolves towards equilibrium. We found that the cloak crawls onto the droplet while thickening simultaneously, and thickens further even after reaching the top of the droplet. The arc length covered on the drop grows linearly with time, and it grows faster for higher lubricant fractions in the brush. Looking at the distribution of lubricant in the brush during cloak development shows a depletion zone in the vicinity of the contact line, which indicates that the process is limited by the speed of lubricant diffusion in the brush.

Finally, we study the dynamics of droplets moving on lubricated polymer brushes. The experiments show that the dissipated power is a power law function of the velocity, with the same exponent regardless of the manner of preparation of the brush. In simulation, we find a similar power law dependence, albeit with a different exponent than that in experiments, and that varies slightly with lubrication. The exponent in simulation is close in value to the exponent $\beta = 5/3$ predicted by certain theories of dissipation. One situation where this exponent could arise is for moving contact lines at low contact angle, which is not the case in our system. Another situation is that of a droplet moving along with a purely liquid wetting ridge, which again is not the case for us due to the brush. The proximity in the value of the exponent might therefore be coincidental as it is unlikely for our system to be dominated by either of those sources. A deeper investigation into the possible sources of dissipation reveals that while the drop does not slip on the brush, is exhibits non-trivial flow patters, with the possible presence of multiple vortices in the bulk. In addition, the wetting ridge is present at all velocities and lubricant fractions, despite the reduction in its size at the advancing and receding ends of the droplet. Neither of those observations immediately explains the value of the exponent. However, either can explain the discrepancy between simulation of experiment, as the flow field of the drop and the rheology of the brush might differ dramatically between the two. Finally, a measurement of the cloak density near the apex of the droplet shows that it is not affected by the speed of the droplet, so that any effect that is present due to cloaking remains at all velocities.

While our study reveals many interesting results, many questions remain. The details of cloak development are still a mystery at the experimental level. A possible way of investigating the out of equilibrium cloak might be through Reflection Interference Contrast Microscopy (RICM) which can reveal the local thickness of the cloak at high temporal resolution. Another hanging question is that of the sources of dissipation for moving drops,

and whether any source dominates over others. While difficult to investigate in a detailed manner at the experimental level, the local contribution of the different dissipation sources can be quantified in simulations and will be an interesting avenue for future work.

A. Derivations

A.1. Line tension modification to the contact angle

Consider a drop on a solid as illustrated in Figure 2.4. We assume the presence of a line tension which results in a contribution $\mathcal{F}_{cl}$ to the free energy proportional to the length of the three phase contact line l_{cl}

$$\mathcal{F}_{cl} = \mathcal{T} l_{cl} \tag{A.1}$$

where $\mathcal{T}$ is the line tension and l_{cl} is the length of the contact line. The total area of the solid is labeled $\mathcal{A}$. We label the interfacial areas in the system as $\mathcal{A}_{sl}$ for the solid-liquid interface, $\mathcal{A}_{lv}$ for the liquid-vapor interface, and $\mathcal{A}_{sv} = \mathcal{A} - \mathcal{A}_{sl}$ for the solid-vapor interface, each with its corresponding surface tension. When a drop is deposited on the solid, the free energy is

$$\mathcal{F} = \gamma_{sl}\mathcal{A}_{sl} + \gamma_{lv}\mathcal{A}_{lv} + \gamma_{sv}(\mathcal{A} - \mathcal{A}_{sl}) + \mathcal{T} l_{cl}. \tag{A.2}$$

The total area of the solid $\mathcal{A}$ is constant meaning that the $\gamma_{sv}\mathcal{A}$ term is a constant shift in the free energy that can be ignored. We rewrite the free energy as

$$\mathcal{F} = (\gamma_{sl} - \gamma_{sv})\mathcal{A}_{sl} + \gamma_{lv}\mathcal{A}_{lv} + \mathcal{T} l_{cl}. \tag{A.3}$$

Assuming the drop has a radius of curvature R and contact angle θ, the surface areas and length of the contact line are

$$\mathcal{A}_{sl} = \pi R^2 \sin^2\theta \tag{A.4}$$
$$\mathcal{A}_{lv} = 2\pi R^2(1 - \cos\theta) \tag{A.5}$$
$$l_{cl} \quad = 2\pi R \sin\theta \tag{A.6}$$

which allows us to rewrite the free energy as

$$\mathcal{F} = \pi\big[(\gamma_{sl} - \gamma_{sv})R^2 \sin^2\theta + 2\gamma_{lv}R^2(1-\cos\theta) + 2\mathcal{T}R\sin\theta\big]. \tag{A.7}$$

To obtain the equilibrium contact angle for the system, we minimize the free energy in Eq. (A.7) with the constrain of constant volume V

$$V = \frac{\pi}{3}R^3(2+\cos\theta)(1-\cos\theta)^2 \tag{A.8}$$

which means that at a given volume of the drop, its radius of curvature is a function of the contact angle

$$R(\theta) = \left[\frac{3}{\pi}\frac{V}{(2+\cos\theta)(1-\cos\theta)}\right]^{1/3} \tag{A.9}$$

$$\frac{\partial R}{\partial\theta} = -R\frac{\sin^2\theta}{(2+\cos\theta)(1-\cos\theta)^2} \tag{A.10}$$

where we also write the derivative of R with respect to θ. Minimizing the free energy with respect to θ

$$\frac{\partial\mathcal{F}}{\partial\theta} = 0 \tag{A.11}$$

$$(\gamma_{sl} - \gamma_{sv})\frac{\partial}{\partial\theta}[R^2\sin^2\theta] + 2\gamma_{lv}\frac{\partial}{\partial\theta}[R^2(1-\cos\theta)] + 2\mathcal{T}\frac{\partial}{\partial\theta}[R\sin\theta] = 0 \tag{A.12}$$

$$R\sin\theta(\gamma_{sl} - \gamma_{sv}) + R\sin\theta\cos\theta\gamma_{lv} + \mathcal{T} = 0. \tag{A.13}$$

Identifying $r_{cl} \equiv R\sin\theta$ as the radius of the three phase contact line, and rearranging Eq. (A.13) we obtain

$$\cos\theta = \frac{\gamma_{sv} - \gamma_{sl}}{\gamma_{lv}} - \frac{\mathcal{T}/\gamma_{lv}}{r_{cl}}. \tag{A.14}$$

A.2. Young-Laplace equation from force balance

We consider an arbitrary interface between two fluids, shown in Figure A.1, with hydrostatic pressure P_1 and P_2 in the bulk of each fluid, and with interfacial tension γ. We seek to derive the condition for mechanical equilibrium, i.e. the balance of forces. For this purpose we consider an arbitrary section Ω and take a counter-clockwise orientation on the boundary $\partial\Omega$. Ω is considered as an open set of points, i.e. the boundary $\partial\Omega$ is not

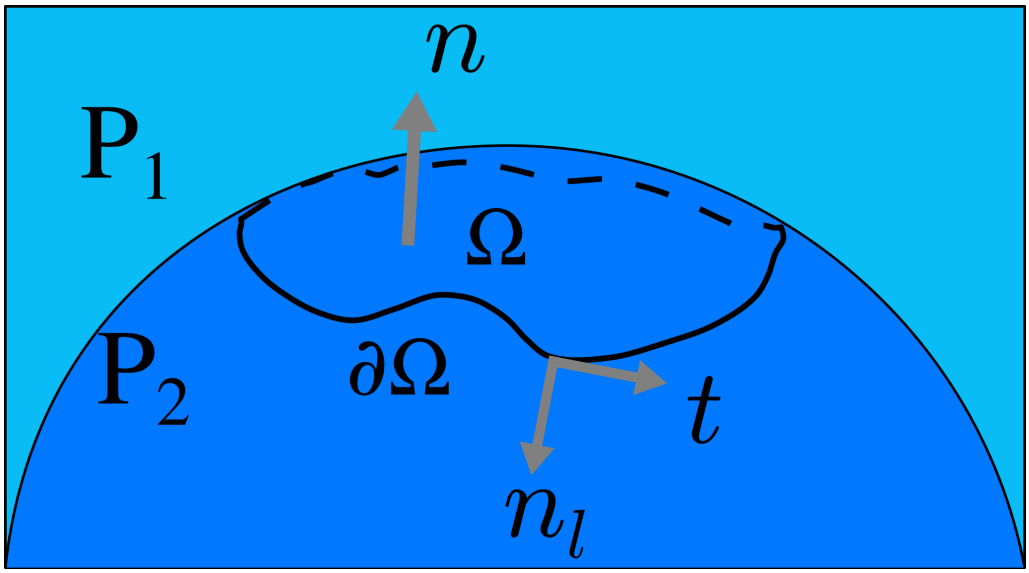

Figure A.1.: Sketch of an arbitrary section on an arbitrary interface between two fluids. P_1 and P_2 are the hydrostatic pressures in the bulk of each fluid, Ω is the domain of the section with boundary $\partial\Omega$, $\mathbf{n}$ is a unit normal to the interface, $\mathbf{t}$ is a unit tangent to the boundary $\partial\Omega$, $\mathbf{n}_l$ is a unit normal to the boundary $\partial\Omega$ that is at the same time tangent to the interface. On the boundary $\partial\Omega$ we have $\mathbf{n}_l = \mathbf{t} \times \mathbf{n}$.

---

included in Ω: $\partial\Omega \not\subset \Omega$. With this choice, all the internal forces on Ω vanish, and we only need to account for external forces, namely the force $\mathbf{F}_P$ due to the pressure difference acting on Ω, and the surface tension force $\mathbf{F}_\gamma$ acting on the boundary $\partial\Omega$. In case of a pressure difference $\Delta P = P_2 - P_1$ across the interface, the force on an area element $\mathrm{d}A$ is normal to the area element and equals $\Delta P\,\mathrm{d}\mathbf{A}$, and the force on Ω due to pressure is

$$\mathbf{F}_P = \int_\Omega \Delta P\,\mathrm{d}\mathbf{A} = \int_\Omega \Delta P\,\mathbf{n}\,\mathrm{d}A \tag{A.15}$$

where $\mathbf{n}$ is a unit vector normal to the interface. On the boundary, the parts of the interface exterior to Ω exert a local force $\gamma \mathrm{d}l$ on $\partial\Omega$ due to surface tension, where $\mathrm{d}l$ is a length element on $\partial\Omega$. This force is directed along a unit vector $\mathbf{n}_l$ that is tangent to the interface, but normal to $\partial\Omega$. The total force is then

$$\mathbf{F}_\gamma = \int_{\partial\Omega} \gamma\,\mathbf{n}_l\,\mathrm{d}l = \int_{\partial\Omega} \gamma\,\mathbf{t} \times \mathbf{n}\,\mathrm{d}l \tag{A.16}$$

where $\mathbf{t}$ is a unit vector tangent to $\partial\Omega$ in the counter-clockwise direction and $\mathbf{n}_l = \mathbf{t} \times \mathbf{n}$.

At equilibrium, the net force should vanish and we have

$$\mathbf{F}_P + \mathbf{F}_\gamma = \mathbf{0}$$
$$\int_\Omega \Delta P\, \mathbf{n}\, \mathrm{d}A + \int_{\partial\Omega} \gamma\, \mathbf{t} \times \mathbf{n}\, \mathrm{d}l = \mathbf{0}. \tag{A.17}$$

The second term in eq. (A.17) can be rewritten using the vector calculus identities

$$\int_{\partial\Omega} \mathbf{t} \times \mathbf{v}\, \mathrm{d}l = \int_\Omega (\nabla \mathbf{v}) \cdot \mathbf{n} - (\nabla \cdot \mathbf{v})\, \mathbf{n}\, \mathrm{d}A \tag{A.18}$$
$$\frac{1}{2}\nabla (\mathbf{v} \cdot \mathbf{v}) = (\nabla \mathbf{v}) \cdot \mathbf{v}. \tag{A.19}$$

Replacing $\mathbf{v}$ with $\mathbf{n}$ in eqs. (A.18) and (A.19) we get

$$\begin{aligned}\int_{\partial\Omega} \mathbf{t} \times \mathbf{n}\, \mathrm{d}l &= \int_\Omega (\nabla \mathbf{n}) \cdot \mathbf{n} - (\nabla \cdot \mathbf{n})\, \mathbf{n}\, \mathrm{d}A \\ &= \int_\Omega \frac{1}{2}\nabla (\mathbf{n} \cdot \mathbf{n}) - (\nabla \cdot \mathbf{n})\, \mathbf{n}\, \mathrm{d}A \\ &= -\int_\Omega (\nabla \cdot \mathbf{n})\, \mathbf{n}\, \mathrm{d}A \end{aligned} \tag{A.20}$$

where between the second and third lines we used $\nabla(\mathbf{n} \cdot \mathbf{n}) = \nabla(1) = 0$. Using the result from eq. (A.20) in eq. (A.17) we get

$$\int_\Omega [\Delta P - \gamma (\nabla \cdot \mathbf{n})]\, \mathbf{n}\, \mathrm{d}A = \mathbf{0}. \tag{A.21}$$

Since the domain Ω was arbitrary, the integrand must vanish; we finally get

$$\Delta P = \gamma (\nabla \cdot \mathbf{n}). \tag{A.22}$$

Eq. (A.22) is known as the Young-Laplace equation. It is a statement on the balance of forces at equilibrium due to pressure and surface tension. The $\nabla \cdot \mathbf{n}$ term is a measure of the local curvature of the interface.

A.3. Young-Laplace equation from variational principle

A.3.1. Free energy functional

Given a drop under the influence of gravity, the free energy will have interfacial contributions, and a contribution from the gravitational potential energy. The free energy can then be written as:

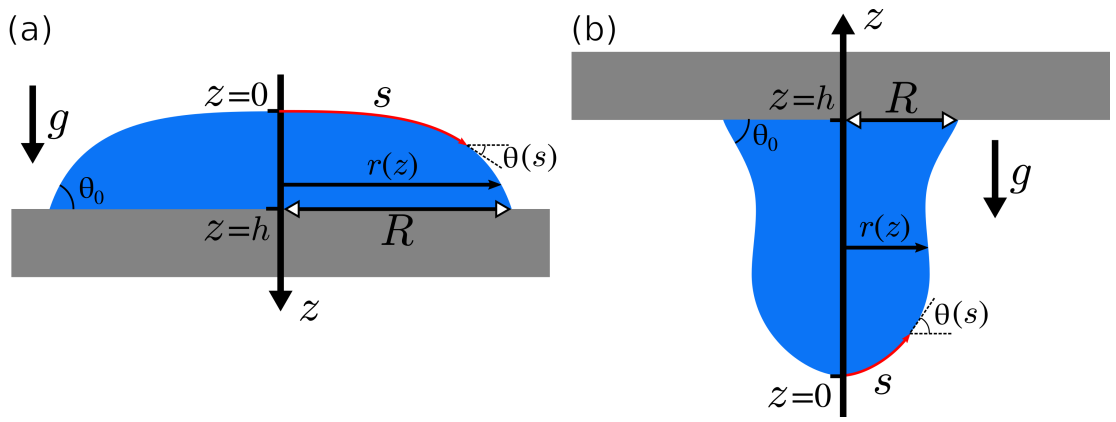

Figure A.2.: Illustration of (a) a sessile and (b) a pendant drop under the influence of gravity

---

$$\mathcal{F} = \gamma \mathcal{A}_{lv} + \gamma_{sl} \mathcal{A}_{sl} + \gamma_{sv}(\mathcal{A} - \mathcal{A}_{sv}) \pm \rho g h_{cm} V \tag{A.23}$$

where $\mathcal{A}_{lv}$, $\mathcal{A}_{sl}$, and $\mathcal{A}$ are the area of the drop, the area of the substrate-drop contact region, and the total area of the substrate respectively, ρ is the mass density of the drop, g is the gravitational acceleration, h_{cm} is the distance of the center of mass from a reference plane, and V is the volume of the drop. The sign in front of the gravitational contribution depends on the choice of orientation of the coordinate system. The total area of the substrate $\mathcal{A}$ is fixed, and assuming the substrate is not adaptive, γ_{sv} is constant. Therefore, the $\gamma_{sv}\mathcal{A}$ term is only an added constant and does not affect the physics. We therefore ignore it and rewrite the free energy as

$$\mathcal{F} = \gamma \mathcal{A}_{lv} + (\gamma_{sl} - \gamma_{sv}) \mathcal{A}_{sl} \pm \rho g h_{cm} V. \tag{A.24}$$

We would like to find the equilibrium shape of a sessile or pendant drop. Therefore, we write the free energy as a functional of the shape of the drop. We assume that the system has azimuthal symmetry, and define the shape of the drop through the cylindrical radius of the drop $r(z)$ at a distance z away from the tip of the drop (see Figure A.2). We choose the positive z-direction to be pointing from the tip of the drop towards the substrate. In addition, since we are interested in drops getting cloaked with time, it is possible that the surface of the drop is not homogeneous, and the surface tension varies with position; we therefore define a spatially varying surface tension $\gamma(z)$. Finally, assuming the evaporation is slow, and that we do not add material to the drop, the volume is constant and the free energy must also have a volume constraint term. For a sessile drop the positive z-direction points in the direction of gravity which results in the following form of the free energy functional

$$\mathcal{F}_s[r(z), r'(z)] = (\gamma_{sl} - \gamma_{sv})\ \pi R^2 + 2\pi \int_0^h \gamma(z) r(z) \sqrt{1 + r'^2(z)}\, \mathrm{d}z$$
$$- \ \pi \rho g \int_0^h r^2(z) z\, \mathrm{d}z + \pi \lambda \int_0^h r^2(z)\, \mathrm{d}z \tag{A.25}$$

where $R \equiv r(h)$ the radius of the three phase contact line, $r'(z)$ is the first derivative of $r(z)$, h the distance from the tip to the substrate, ρ is the mass density of the drop, and g the gravitational acceleration. The first two terms are the contributions from interfacial energy, the third term the contribution from gravitational energy, and the last term is a constraint on the total volume of the drop with a Lagrange multiplier λ.

In the case of a pendant drop, we choose the positive z-direction to point in the opposite direction of gravity (see Figure A.2). This results in the same form of the free energy functional, except that the sign of the gravitational term must be flipped

$$\mathcal{F}_p[r(z), r'(z)] = (\gamma_{sl} - \gamma_{sv})\ \pi R^2 + 2\pi \int_0^h \gamma(z) r(z) \sqrt{1 + r'^2(z)}\, \mathrm{d}z$$
$$+ \ \pi \rho g \int_0^h r^2(z) z\, \mathrm{d}z + \pi \lambda \int_0^h r^2(z)\, \mathrm{d}z. \tag{A.26}$$

In what follows we will derive the shape equations for a pendant drop. The equations for a sessile drop can be easily obtained by flipping the sign of the gravitational acceleration g in the equations.

A.3.2. Variation and shape equations

To find the equilibrium shape of the drop we vary the free energy functional and find its extremum

$$\delta \mathcal{F}[r(z), r'(z)] = 0. \tag{A.27}$$

One needs to be careful here to account for possible changes in the contact line and the height of the drop. We will perform the derivation for pendant drops, while the result for sessile drops can be obtained by changing $g \to -g$. The full variation of the functional in Eq. (A.26) is

$$\begin{aligned}\delta\mathcal{F}_p = 2(\gamma_{sl}-\gamma_{sv})\ \pi R\delta R + \pi\left[2\gamma r\sqrt{1+r'^2}+\rho g r^2 z+\lambda r^2\right]_{z\to h}\delta h \\ +\ 2\pi\int_0^h\left[\gamma(z)\sqrt{1+r'^2}+\rho g r z+\lambda r\right]\delta r\,\mathrm{d}z \\ +\ 2\pi\int_0^h\gamma(z)\frac{rr'}{\sqrt{1+r'^2}}\delta r'\,\mathrm{d}z.\end{aligned} \tag{A.28}$$

The first term is the variation in the radius of the contact line, while the second term is the variation in the height of the drop, i.e. the variation in the upper bound of the integrals. We require the drop to "close" at the tip or in other words $r(0)=0$; in addition, we require the drop profile to be smooth at $z=0$. We integrate the last term by parts resulting in

$$\int_0^h\gamma(z)\frac{rr'}{\sqrt{1+r'^2}}\delta r'\,\mathrm{d}z=\left[\gamma\frac{rr'}{\sqrt{1+r'^2}}\delta r\right]_0^h-\int_0^h\frac{\mathrm{d}}{\mathrm{d}z}\left[\gamma(z)\frac{rr'}{\sqrt{1+r'^2}}\right]\delta r\,\mathrm{d}z. \tag{A.29}$$

As stated above, we require that $r(0)=0$, getting rid of the lower bound of the first term in eq. (A.29).[1] Developing the derivative in the second term of eq. (A.29) and inserting the result into eq. (A.28) we obtain

$$\begin{aligned}\delta\mathcal{F}_p = 2\pi\int_0^h\left[\rho g r z+\lambda r+\gamma\left[\frac{1}{\sqrt{1+r'^2}}-\frac{rr''}{(1+r'^2)^{3/2}}\right]-\gamma'\frac{rr'}{\sqrt{1+r'^2}}\right]\delta r\,\mathrm{d}z \\ +\ 2\pi\left(\gamma(h)\frac{r'}{\sqrt{1+r'^2}}\bigg|_{z=h}+\gamma_{sl}-\gamma_{sv}\right)\ R\delta R+\pi\left[2\gamma r\sqrt{1+r'^2}+\rho g r^2 z+\lambda r^2\right]_{z=h}\delta h.\end{aligned} \tag{A.30}$$

where $\gamma'(z)$ is the first derivative of $\gamma(z)$. At equilibrium $\delta\mathcal{F}_p=0$ for any arbitrary variation $\delta r(z)$. Therefore, the integrand in the first term, the factor multiplying δR, and the factor multiplying δh must each vanish independently, giving us our final equations

$$\rho g z+\lambda+\gamma\left[\frac{1}{r\sqrt{1+r'^2}}-\frac{r''}{(1+r'^2)^{3/2}}\right]-\gamma'\frac{r'}{\sqrt{1+r'^2}}=0 \tag{A.31}$$

$$R\left(\gamma(h)\frac{r'}{\sqrt{1+r'^2}}\bigg|_{z=h}+\gamma_{sl}-\gamma_{sv}\right)=0 \tag{A.32}$$

$$2\gamma(h)R\sqrt{1+r'^2(h)}+\rho g R^2 h+\lambda R^2=0 \tag{A.33}$$

[1] Note: $\lim_{z\to 0}r'(z)=\infty$ due to the smoothness condition. However, the singularities in the numerator and denominator cancel each other in this situation.

A.3.3. Young-Laplace equation

Eq. (A.31) is nothing but the Young-Laplace equation with variable surface tension. To show that, we consider the case where the surface tension is uniform. In this case the last term vanishes and eq. (A.31) can be rewritten as

$$\rho g z + \lambda + \gamma \left[\frac{1}{r\sqrt{1+r'^2}} - \frac{r''}{(1+r'^2)^{3/2}} \right] = 0. \tag{A.34}$$

The terms in the square brackets are the principal curvatures for a surface of revolution [304, ch. 2], which can be used to rewrite

$$\frac{1}{R_1} \equiv \frac{1}{r\sqrt{1+r'^2}} \tag{A.35}$$

$$\frac{1}{R_2} \equiv -\frac{r''}{(1+r'^2)^{3/2}} \tag{A.36}$$

$$\rho g z + \lambda + \gamma \left[\frac{1}{R_1} + \frac{1}{R_2} \right] = 0 \tag{A.37}$$

where $R_1(z)$ and $R_2(z)$ are the principal radii of curvature of the surface at height z. From this we see that the Lagrange parameter $\lambda \equiv -\Delta P$ where ΔP is the Laplace pressure at the tip of the drop ($z = 0$). Not surprisingly, the additional term due to gravity takes the form a typical hydrostatic pressure. Eq. (A.37) can finally be written in the usual form of the Young-Laplace equation

$$\Delta P - \rho g z = \gamma \left[\frac{1}{R_1} + \frac{1}{R_2} \right]. \tag{A.38}$$

A.3.4. Reparametrization of the shape equation

An alternate form of the shape equation (A.31) can be obtained by expressing r and z in terms of the length element s along the shape

$$ds^2 = dr^2 + dz^2. \tag{A.39}$$

Defining the angle $\theta(s)$ as the angle between the horizontal and the tangent to the drop we find

$$\frac{\mathrm{d}z}{\mathrm{d}s} = \sin\theta \tag{A.40}$$
$$\frac{\mathrm{d}r}{\mathrm{d}s} = \cos\theta \tag{A.41}$$
$$\frac{\mathrm{d}f}{\mathrm{d}z} = \frac{1}{\sin\theta}\frac{\mathrm{d}f}{\mathrm{d}s} \tag{A.42}$$

where f is an arbitrary function of $z(s)$. Using the above equations we then obtain the following identities

$$r'(z(s)) = \cot\theta(s) \tag{A.43}$$
$$r''(z(s)) = -\frac{1}{\sin^3\theta(s)}\frac{\mathrm{d}\theta}{\mathrm{d}s} \tag{A.44}$$
$$\sqrt{1+r'^2} = \frac{1}{\sin\theta(s)}. \tag{A.45}$$

Using the above relations in Eq. (A.31) we can rewrite it into

$$\begin{aligned} &\rho g z + \lambda + \gamma\frac{\sin\theta}{r} + \gamma\frac{\mathrm{d}\theta}{\mathrm{d}s} - \frac{\mathrm{d}\gamma}{\mathrm{d}s}\cot\theta = 0 \\ &\frac{\mathrm{d}\theta}{\mathrm{d}s} = -\frac{\rho g z}{\gamma} - \frac{\lambda}{\gamma} - \frac{\sin\theta}{r} + \frac{\cot\theta}{\gamma}\frac{\mathrm{d}\gamma}{\mathrm{d}s}. \end{aligned} \tag{A.46}$$

The above equation is a linear ordinary differential equation in the angle $\theta(s)$, which along with eqs. (A.40) and (A.41) provides a system of equations that can be solved for the shape with the requirement that $\theta(0) = 0$ since we require the drop to be smooth at the tip of the drop, in addition to the initial conditions $r(0) = 0$ and $z(0) = 0$. The Lagrange multiplier λ can again be identified with the Laplace pressure $\lambda \equiv -\Delta P$. In addition, the Laplace pressure ΔP can be related to the curvature of the tip of the drop

$$\Delta P = \frac{2\gamma}{R_0} \tag{A.47}$$

which allows us to write the final form of the equation

$$\frac{\mathrm{d}\theta}{\mathrm{d}s} = -\frac{\rho g z}{\gamma} + \frac{2}{R_0} - \frac{\sin\theta}{r} + \frac{\cot\theta}{\gamma}\frac{\mathrm{d}\gamma}{\mathrm{d}s}. \tag{A.48}$$

A.3.5. Boundary equations

It is worth noting that when applying the Young-Laplace equation to fit the shape of a drop, the boundary terms Eqs. (A.32) and (A.33) do not play a role in the fitting procedure. The drop shape is typically fit away from the contact line.

A.3.5.1. Boundary equation 1: Young-Dupré equation

Eq. (A.32) can be rewritten by first requiring that $R \neq 0$ and identifying

$$r'(z) = \cot\theta(z) \tag{A.49}$$

$$\frac{r'}{\sqrt{1+r'^2}} = \cos\theta. \tag{A.50}$$

where $\theta(z)$ the angle that the tangent to the curve makes with the horizontal (see Figure A.2). Then Eq. (A.32) becomes

$$\gamma(h)\cos\theta_0 + \gamma_{sl} - \gamma_{sv} = 0 \tag{A.51}$$

which is the Young-Dupré equation with $\theta_0 \equiv \theta(h)$ the contact angle.

A.3.5.2. Boundary equation 2

Eq. (A.33) can be rewritten by again requiring that $R \neq 0$ and identifying

$$\sqrt{1+r'^2} = \sin\theta. \tag{A.52}$$

where $\theta(z)$ the angle that the tangent to the curve makes with the horizontal (see Figure A.2). Then Eq. (A.33) becomes

$$2\frac{\gamma(h)}{\sin\theta_0} + R\left(\rho g h + \lambda\right) = 0 \tag{A.53}$$

$$\rho g h + \lambda = -2\frac{\gamma(h)}{R\sin\theta_0} \tag{A.54}$$

A.4. Diffusion equation from free energy functional

A.4.1. The flow of matter

The dynamic evolution of a system, given a free energy functional $\mathcal{F}[\varphi]$, is perfectly captured and very well described in the context of Dynamic Density Functional Theory (DDFT). A review of the method is found in Ref. 305 where multiple mathematical derivations of the evolution equations are provided. The aim of this section, however, is not to provide a mathematically rigorous derivation, but instead to arrive at similar equations based on physical intuitions/interpretations. The key aspect is an interpretation of the relation between the local material current $j(x)$ and the functional derivative of the free energy functional $\frac{\delta\mathcal{F}}{\delta\varphi}$ eq. (A.61).

We seek a dynamic equation to model the evolution of the concentration profile and flow of matter given a thermodynamic framework. We specialize to one spatial dimension where in general we may start with a local free energy density that depends on position, the concentration $\varphi(x)$, and possibly its derivatives. For simplicity we focus on free energies which only depend on the first derivative: $f\left(\varphi(x), \varphi'(x)\right)$. The total free energy will then be in the form of a functional of the concentration profile:

$$\mathcal{F}[\varphi(x)] = \int_0^L f\left(\varphi(x), \varphi'(x), x\right) \mathrm{d}x. \tag{A.55}$$

The equilibrium is obtained by extremizing (minimizing) the total free energy, i.e. by setting the the variation of the functional to 0 (possibly under certain constraints)

$$\delta\mathcal{F} = 0. \tag{A.56}$$

Starting from a configuration $\varphi_0(x)$ and modifying by $\varphi_0(x) \to \varphi_0(x)+\delta\varphi(x)$, the variation in the total free energy is

$$\delta\mathcal{F}[\varphi(x)] \equiv \int_0^L \frac{\delta\mathcal{F}}{\delta\varphi}(x)\delta\varphi(x)\mathrm{d}x \tag{A.57}$$

$$= \int_0^L \left(\frac{\partial f}{\partial\varphi} - \frac{\mathrm{d}}{\mathrm{d}x}\frac{\partial f}{\partial\varphi'}\right)\delta\varphi(x)\mathrm{d}x. \tag{A.58}$$

which defines the variational derivative of the functional $\mathcal{F}[\varphi(x)]$ [306]. Another way to define the variational derivative is as the limit of a finite difference

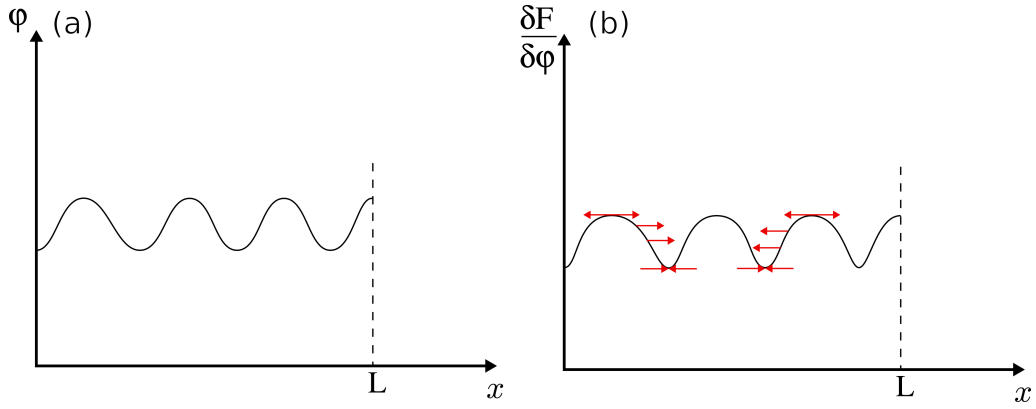

Figure A.3.: (a) The original concentration profile $\varphi(x)$. (b) The variational derivative of the free energy, assuming the free energy density increase monotonically and quickly with concentration. Red arrows indicate the direction of the flow of matter.

$$\mathcal{F}[\varphi + \varepsilon\delta](x') = \int_0^L f(\varphi(x) + \varepsilon\delta(x - x'), \varphi'(x) + \varepsilon\delta'(x - x'), x)\mathrm{d}x \tag{A.59}$$

$$\frac{\delta\mathcal{F}}{\delta\varphi}(x') \equiv \lim_{\varepsilon\to 0} \frac{\mathcal{F}[\varphi + \varepsilon\delta] - \mathcal{F}[\varphi]}{\varepsilon} \tag{A.60}$$

where $\delta(x)$ is the Dirac delta function. The result from the definition in eqs. (A.59) and (A.60) coincides with the result in eq. (A.58) [147, Appendix]. We can see then from eqs. (A.57) and (A.60) that $\frac{\delta\mathcal{F}}{\delta\varphi}(x')$ is a measure of the change in the total free energy upon an **increase** in the local value of the function $\varphi(x)$ at the point x'. Therefore, in a system that is out of equilibrium, matter will flow from regions where the variational derivative is large to regions where the value is smaller.

To illustrate this with an example we consider a system with specific properties. For simplicity, we consider a free energy density that only depends on the local concentration $f(\varphi, \varphi', x) = f(\varphi(x))$ and grows monotonically faster than $f(\varphi) \propto \varphi$. The resulting variational derivative is positive and the peaks in concentration $\varphi(x)$ correspond to peaks in $\frac{\delta\mathcal{F}}{\delta\varphi}(x)$.[2] Figure A.3 (a) shows a certain out of equilibrium concentration profile and A.3 (b) illustrates qualitatively the corresponding variational derivative based on our assumptions. The total change in free energy is related to the variational derivative through Eq. (A.57), which tells us that the total variation is a sum over the product of the variational derivative and the variation in concentration $\delta\varphi$ at every point; matter will flow in a manner that reduces the total free energy. Removing matter from a point x corresponds to a negative $\delta\varphi(x)$ while adding matter there corresponds to a positive $\delta\varphi(x)$. Removing matter from a point where the variational derivative is large corresponds to a large negative value of

[2] Those conditions are satisfied for example in the case of free diffusion.

the product $\frac{\delta\mathcal{F}}{\delta\varphi}(x)\delta\varphi(x)$, contributing to a reduction in the total free energy. Dumping this matter at an adjacent point $x + \mathrm{d}x$ where the variational derivative has a smaller value leads to a smaller positive value of the product $\frac{\delta\mathcal{F}}{\delta\varphi}(x+\mathrm{d}x)\delta\varphi(x+\mathrm{d}x)$, contributing to an increase in the total free energy. The net effect is a reduction in the total free energy upon a flow of matter from regions of high to low $\frac{\delta\mathcal{F}}{\delta\varphi}(x)$. The flow, therefore, is in the opposite direction to the gradient in $\frac{\delta\mathcal{F}}{\delta\varphi}(x)$, which results in a current (flux) $j(x)$

$$j(x) \sim -\frac{\mathrm{d}}{\mathrm{d}x}\frac{\delta\mathcal{F}}{\delta\varphi}(x). \tag{A.61}$$

The above equation can be generalized to three dimensional space by replacing the current $j(x)$ with a vector $\mathbf{j}(\mathbf{x})$ where each component corresponds to a spatial direction, and the derivative $\frac{\mathrm{d}}{\mathrm{d}x}$ replaced by a gradient

$$\mathbf{j}(\mathbf{x}) \sim -\nabla\frac{\delta\mathcal{F}}{\delta\varphi}(\mathbf{x}). \tag{A.62}$$

A.4.2. Continuity equation

To obtain the final form of the dynamic equations, we invoke the concept of conservation of matter, captured through a continuity equation. Consider a volume Ω enclosed by a boundary $\partial\Omega$. The total amount of matter M in Ω is

$$M = \int_\Omega \varphi \,\mathrm{d}V. \tag{A.63}$$

In the absence of sources and sinks of matter, any change in M must be due to the current $\mathbf{j}(\mathbf{x})$; the latter is a flux through the boundary $\partial\Omega$, i.e. it is the amount of matter flowing through a unit area per unit time. Therefore, we can write

$$\frac{\partial M}{\partial t} = \int_\Omega \frac{\partial\varphi}{\partial t}\,\mathrm{d}V = -\int_{\partial\Omega}\mathbf{j}(\mathbf{x})\cdot\mathrm{d}\mathbf{A} \tag{A.64}$$

where $\mathrm{d}\mathbf{A}$ is an area element on the boundary $\partial\Omega$ pointing outside of the volume Ω. Eq. (A.64) is the integral from of the continuity equation. Using the divergence theorem we can rewrite

$$\int_{\partial\Omega}\mathbf{j}(\mathbf{x})\cdot\mathrm{d}\mathbf{A} = \int_\Omega \nabla\cdot\mathbf{j}(\mathbf{x})\,\mathrm{d}V \tag{A.65}$$

and Eq. (A.64) becomes

$$\int_\Omega\left[\frac{\partial\varphi}{\partial t} + \nabla\cdot\mathbf{j}(\mathbf{x})\right]\mathrm{d}V = 0. \tag{A.66}$$

Since this equation must be valid for any choice of the volume Ω, the integrand must vanish at every point, which results in the differential form of the continuity equation

$$\frac{\partial \varphi}{\partial t} + \nabla \cdot \mathbf{j}(\mathbf{x}) = 0. \tag{A.67}$$

The current $\mathbf{j}(\mathbf{x})$ can be obtained from Eq. (A.62) and inserted into Eq. (A.67) to obtain the final form of the dynamical equations.

A.4.3. Pressure and virial theorem

The virial theorem in classical mechanics is derived in the following way (based on Landau mechanics and statistical mechanics §10 and §31 problem 2 respectively)

$$\begin{aligned}
\frac{\mathrm{d}}{\mathrm{d}t} \sum_i \mathbf{r}_i \cdot \mathbf{p}_i &= \sum_i \dot{\mathbf{r}}_i \cdot \mathbf{p}_i + \sum_i \mathbf{r}_i \cdot \dot{\mathbf{p}}_i && \text{(A.68)} \\
&= \sum_i \frac{\dot{\mathbf{p}}_i \cdot \dot{\mathbf{p}}_i}{m_i} + \sum_i \mathbf{r}_i \cdot \dot{\mathbf{p}}_i && \text{(A.69)} \\
&= 2K + \sum_i \mathbf{r}_i \cdot \dot{\mathbf{p}}_i && \text{(A.70)}
\end{aligned}$$

where $\mathbf{r}_i$ is the position of a particle, $\mathbf{p}_i$ its momentum, m_i its mass, i is an index that goes over all particles in the system, and K is the total kinetic energy. For any bounded function of time $f(t)$ we have for the time average of its derivative

$$\begin{aligned}
\left\langle \frac{\mathrm{d}f(t)}{\mathrm{d}t} \right\rangle_t &\equiv \lim_{\tau \to \infty} \frac{1}{\tau} \int_0^\tau \frac{\mathrm{d}f(t)}{\mathrm{d}t} \, \mathrm{d}t && \text{(A.71)} \\
&= \lim_{\tau \to \infty} \frac{f(\tau) - f(0)}{\tau} && \text{(A.72)} \\
(\text{since } f(\tau) - f(0) \text{ is finite}) &= 0. && \text{(A.73)}
\end{aligned}$$

For most cases of interest, the quantity $\mathbf{r}_i \cdot \mathbf{p}_i$ is bounded and so the average of the LHS in Eq. (A.68) vanishes, and we are left with the virial theorem in classical mechanics

$$2 \langle K \rangle_t + \left\langle \sum_i \mathbf{r}_i \cdot \dot{\mathbf{p}}_i \right\rangle_t = 0. \tag{A.74}$$

The derivative of momentum in the second term can be related to the forces acting on the particle i, which, in the case of particles in a box, are the interaction forces with other

particles $\mathbf{F}_i$, and the forces from the walls. For the latter, assuming an isotropic pressure P, the force acting on a particle i near the wall is $-P\mathrm{d}\mathbf{A}_i$ ($\mathrm{d}\mathbf{A}_i$ is taken to be pointing outwards) and the contribution to the virial is

$$-\sum_i P\mathbf{r}_i \cdot \mathrm{d}\mathbf{A}_i = -P \oint \mathbf{r} \cdot \mathrm{d}\mathbf{A} \tag{A.75}$$

where the sum includes only particles near the surface of the box, and the intergral is executed over that surface. The divergence theorem can be used to change the surface integral to a volume one, and we use $\nabla \cdot \mathbf{r} = 3$ to obtain

$$P \oint \mathbf{r} \cdot \mathrm{d}\mathbf{A} = P \int \nabla \cdot \mathbf{r}\, \mathrm{d}V = 3PV. \tag{A.76}$$

Finally, the virial theorem gives:

$$3PV = 2\left\langle K \right\rangle_t + \left\langle \sum_i \mathbf{r}_i \cdot \mathbf{F}_i \right\rangle_t. \tag{A.77}$$

Now we consider the product of two different components of the velocity and the momentum, instead of the dot product:

$$\left\langle \frac{\mathrm{d}}{\mathrm{d}t} \sum_i r_i^\alpha p_i^\beta \right\rangle_t = \left\langle \sum_i \dot{r}_i^\alpha p_i^\beta \right\rangle_t + \left\langle \sum_i r_i^\alpha \dot{p}_i^\beta \right\rangle_t \tag{A.78}$$

$$0 = \left\langle \sum_i m_i v_i^\alpha v_i^\beta \right\rangle_t + \left\langle \sum_i r_i^\alpha \dot{p}_i^\beta \right\rangle_t \tag{A.79}$$

where the LHS was set to 0 following similar arguments as above, and $\mathbf{v}_i \equiv \dot{\mathbf{r}}_i \equiv \frac{\dot{\mathbf{p}}_i}{m_i}$ was used. The change in the β component in momentum is on average due to intermolecular forces $\mathbf{F}_i$, as well as the stresses acting on the boundary of the box. The total force due to the latter is $-P^{\lambda\beta}\,\mathrm{d}A_i^\lambda$, where we sum over repeated indices, and we only consider particles near the walls. As we did above, we can change the sum to an integral and we obtain

$$\left\langle \sum_i m_i v_i^\alpha v_i^\beta \right\rangle_t + \left\langle \sum_i r_i^\alpha \mathcal{F}_i^\beta \right\rangle_t - P^{\lambda\beta} \oint r^\alpha\, \mathrm{d}A^\lambda = 0 \tag{A.80}$$

where again the integral is executed over the whole box. Considering a cubic box, $\mathrm{d}A^\lambda$ is non-zero for only 2 of the 6 faces, and on the faces where it is non-zero, it is equal but opposite in sign, namely $\mathrm{d}A_1^\lambda = -\mathrm{d}A_2^\lambda$. For a given λ, we differentiate between 2 cases.

The first is when $\lambda \neq \alpha$. In that case, r^α will vary in the same way on both faces when the integral is evaluated, and we have

$$\oint r^\alpha \, \mathrm{d}A^\lambda = \int_1 r^\alpha \, \mathrm{d}A_1^\lambda + \int_2 r^\alpha \, \mathrm{d}A_2^\lambda \tag{A.81}$$

$$= \int_1 r^\alpha \, \mathrm{d}A_1^\lambda 1 - \int_2 r^\alpha \, \mathrm{d}A_1^\lambda \tag{A.82}$$

$$= 0. \tag{A.83}$$

The other possibility is that $\lambda = \alpha$. In this case, r^α is constant on each of the two faces, and we have

$$\oint r^\alpha \, \mathrm{d}A^\alpha = \int_1 r^\alpha \, \mathrm{d}A_1^\alpha + \int_2 r^\alpha \, \mathrm{d}A_2^\alpha \tag{A.84}$$

$$= \int_1 r_1^\alpha \, \mathrm{d}A_1^\alpha - \int_2 r_2^\alpha \, \mathrm{d}A_1^\alpha \tag{A.85}$$

$$= (r_1^\alpha - r_2^\alpha) L^2 \tag{A.86}$$

$$= L^3 \tag{A.87}$$

where in the last step we used the fact that the distance between faces is equal to the length of the box. Finally we obtain for the virial theorem with mixed components

$$\left\langle \sum_i m_i v_i^\alpha v_i^\beta \right\rangle_t + \left\langle \sum_i r_i^\alpha \mathcal{F}_i^\beta \right\rangle_t - P^{\lambda\beta} V = 0. \tag{A.88}$$

When the forces are pair forces, we can rewrite the second term as

$$\sum_i r_i^\alpha \mathcal{F}_i^\beta = \sum_{<ij>} r_i^\alpha \mathcal{F}_{ij}^\beta \tag{A.89}$$

$$\text{(symmetric form)} = \sum_{<ij>} \frac{1}{2} \left(r_i^\alpha \mathcal{F}_{ij}^\beta + r_j^\alpha \mathcal{F}_{ji}^\beta \right) \tag{A.90}$$

$$(\mathbf{F}_{ji} = -\mathbf{F}_{ij}) = \sum_{<ij>} \frac{1}{2} \left(r_i^\alpha - r_j^\alpha \right) \mathcal{F}_{ij}^\beta \tag{A.91}$$

where the sum is over all pairs of particles $< ij >$.

A.5. Useful relations

A.5.1. The volume of a section of a cylinder

The volume of a section of a cylinder with $\rho_1 \leq \rho \leq \rho_2$; $\varphi_1 \leq \varphi \leq \varphi_2$; $z_1 \leq z \leq z_2$:

$$V = \int_{z_1}^{z_2} \int_{\varphi}^{\varphi} \int_{\rho_1}^{\rho_2} \rho \, \mathrm{d}\rho \, \mathrm{d}\varphi \, \mathrm{d}z = \frac{1}{2}(\varphi_1 - \varphi_2)(z_2 - z_1)(\rho_2^2 - \rho_1^2) \tag{A.92}$$

If the space is divided into radial bins of size $\Delta\rho$ with $\rho_i = i \times \Delta\rho$, angular bins $\varphi_j = j \times \Delta\varphi$, and axial bins $z_k = k \times \Delta z$ then

$$V_{ijk} = \frac{1}{2}\Delta z \Delta\varphi \Delta\rho^2 (2i + 1) \tag{A.93}$$

A.5.2. The volume of a section of a sphere

The volume of a section of a sphere with $r_1 \leq r \leq r_2$; $\theta_1 \leq \theta \leq \theta_2$; $\varphi_1 \leq \varphi \leq \varphi_2$:

$$V = \int_{\varphi_1}^{\varphi_2} \int_{\theta_1}^{\theta_2} \int_{r_1}^{r_2} r^2 \sin\theta \, \mathrm{d}r \, \mathrm{d}\theta \, \mathrm{d}\varphi = \frac{1}{3}(\varphi_2 - \varphi_1)(\cos\theta_1 - \cos\theta_2)(r_2^3 - r_1^3) \tag{A.94}$$

If the space is divided into radial bins of size Δr with $r_i = i \times \Delta r$, polar bins $\theta_j = j \times \Delta\theta$, and azimuthal bins $\varphi_k = k \times \Delta\varphi$

$$V_{ijk} = \frac{1}{3}\Delta\varphi \Delta r^3 (\cos\theta_j - \cos\theta_{j+1})[(i+1)^3 - i^3] \tag{A.95}$$

A.5.3. Angles at the intersection of an ellipse and a horizontal line

A rotated ellipse centered at the origin as shown in Figure A.4 can be parametrized as

$$x(\varphi) = a\cos\alpha\cos\varphi - b\sin\alpha\sin\varphi \tag{A.96}$$
$$y(\varphi) = a\sin\alpha\cos\varphi + b\cos\alpha\sin\varphi \tag{A.97}$$

where a is the semi-major axis, b the semi-minor axis, α is the rotation angle of the ellipse, φ is an angle measured from the major axis of the ellipse, and x_c and y_c are the coordinates of the center of the ellipse. At every point (x, y) on the ellipse, the tangent vector can be written as

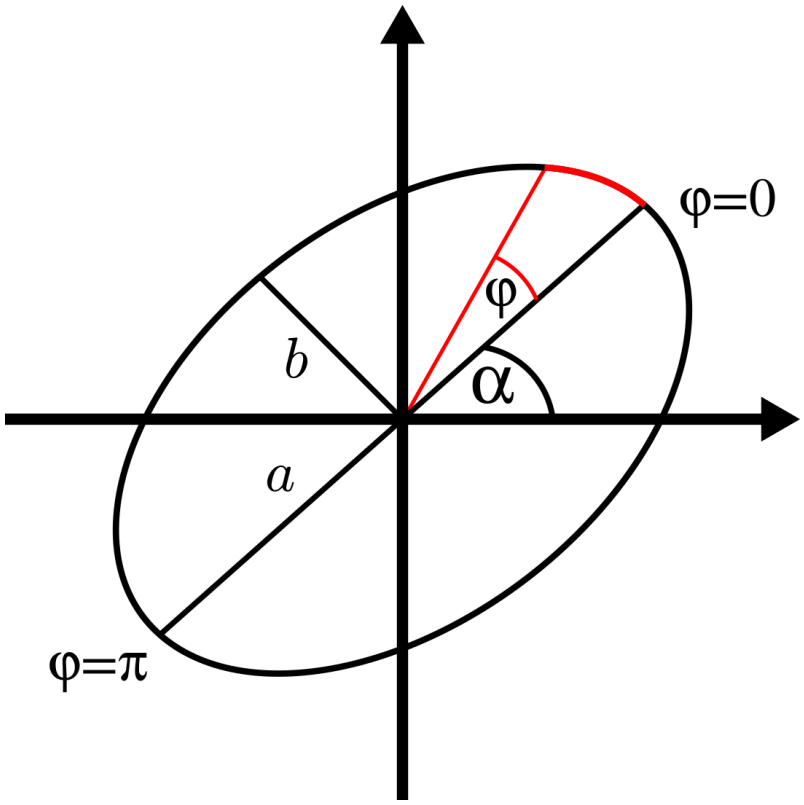

Figure A.4.: Rotated ellipse with the relevant angles and axes.

$$x_t(\varphi) = \frac{\partial x}{\partial \varphi} = -a\cos\alpha\sin\varphi - b\sin\alpha\cos\varphi \tag{A.98}$$

$$y_t(\varphi) = \frac{\partial y}{\partial \varphi} = -a\sin\alpha\sin\varphi + b\cos\alpha\cos\varphi. \tag{A.99}$$

Given a horizontal line at level y_0 that intersects the ellipse at two points with parameter values φ_1 and φ_2, the internal angle at each point can be calculated as

$$\theta(\varphi) = \cos^{-1}\left[-\frac{x_t}{\sqrt{x_t^2 + y_t^2}}\right]. \tag{A.100}$$

A.5.3.1. Finding the intersection points

To find the intersection points of the ellipse with a horizontal line at y_0 we need to solve the equation

$$y(\varphi) = y_0. \tag{A.101}$$

Using the parametrization in Eq. (A.97) we have

$$a\sin\alpha\cos\varphi + b\cos\alpha\sin\varphi = y_0 \tag{A.102}$$
$$a\sin\alpha\cos\varphi - y_0 = -b\cos\alpha\sin\varphi \tag{A.103}$$
$$(a\sin\alpha\cos\varphi - y_0)^2 = (-b\cos\alpha\sin\varphi)^2 \tag{A.104}$$
$$(a\sin\alpha)^2\cos^2\varphi - 2a\sin\alpha y_0\cos\varphi + y_0^2 = (b\cos\alpha)^2\sin^2\varphi \tag{A.105}$$

$$[(a\sin\alpha)^2 + (b\cos\alpha)^2]\cos^2\varphi - [2a\sin\alpha y_0]\cos\varphi + [y_0^2 - (b\cos\alpha)^2] = 0 \tag{A.106}$$

where in the last step we used $\sin^2\varphi = 1-\cos^2\varphi$ and rearranged the equation. Eq. (A.106) is a quadratic equation in $\cos\varphi$ with two solutions $\cos\varphi_1$ and $\cos\varphi_2$. Using similar steps one can write an equation for $\sin\varphi$

$$[(a\sin\alpha)^2 + (b\cos\alpha)^2]\sin^2\varphi - [2b\sin\alpha y_0]\sin\varphi + [y_0^2 - (a\cos\alpha)^2] = 0 \tag{A.107}$$

whose solution provides $\sin\varphi_1$ and $\sin\varphi_2$. The solutions to Eqs. (A.106) and (A.107) can then be used in equations Eq. (A.100) to obtain the required angles.

A.5.4. Miscellaneous

Having

$$\mathrm{d}f = a\frac{\mathrm{d}x_1}{b_1} = a\frac{\mathrm{d}x_2}{b_2} \tag{A.108}$$

it can be rewritten as

$$\mathrm{d}f = \frac{a}{b_1 - b_2}\mathrm{d}(x_1 - x_2) \tag{A.109}$$

B. Additional Data

B.1. MDPD Phase Diagrams

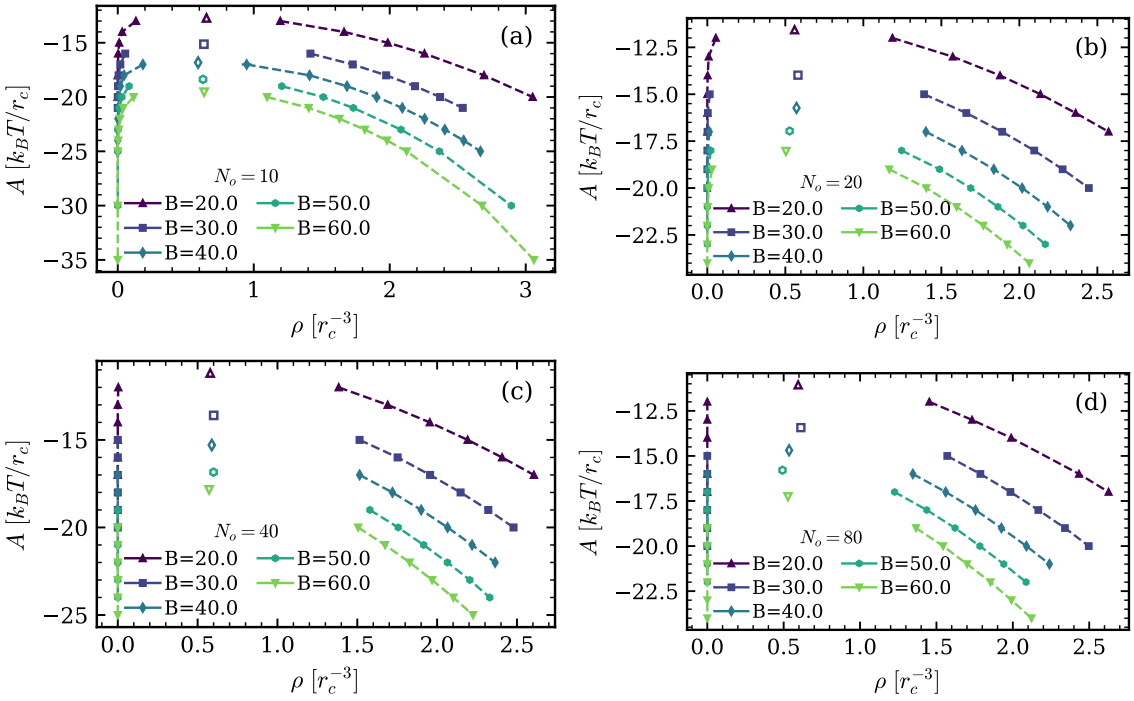

Figure B.1.: Phase Diagrams for the MDPD model for oligomers of length (a) $N_o = 10$, (b) $N_o = 20$, (c) $N_o = 40$, (d) $N_o = 80$. A_{mm} is the strength of monomer-monomer cohesion, ρ is the number density, and B is the strength of many-body repulsion. Dashed lines connect the data points to guide the eye. Open symbols are the critical points.

Bibliography

[1] Xiaoyi Liu, Daniel Beysens, and Tarik Bourouina. Water harvesting from air: Current passive approaches and outlook. *ACS Materials Letters*, 4(5):1003–1024, 2022.

[2] Wilhelm Barthlott and Christoph Neinhuis. Purity of the sacred lotus, or escape from contamination in biological surfaces. *Planta*, 202:1–8, 1997.

[3] Huawei Chen, Pengfei Zhang, Liwen Zhang, Hongliang Liu, Ying Jiang, Deyuan Zhang, Zhiwu Han, and Lei Jiang. Continuous directional water transport on the peristome surface of nepenthes alata. *Nature*, 532(7597):85–89, 2016.

[4] Hao Chen, Xiaoping Li, and Dachao Li. Superhydrophilic–superhydrophobic patterned surfaces: From simplified fabrication to emerging applications. *Nanotechnology and Precision Engineering (NPE)*, 5(3):035002, 2022.

[5] Weihao Pan, Qiulin Wang, Jun Ma, Wen Xu, Jing Sun, Xin Liu, and Jinlong Song. Solid-like slippery coating with highly comprehensive performance. *Advanced Functional Materials*, 33(31):2302311, 2023.

[6] H Steinfink, B Post, and I Fankuchen. The crystal structure of octamethyl cyclotetrasiloxane. *Acta Crystallographica*, 8(7):420–424, 1955.

[7] Frank Weinhold and Robert West. The nature of the silicon–oxygen bond. *Organometallics*, 30(21):5815–5824, 2011.

[8] Wikimedia Commons. Condensation smiley face, 2021. URL `https://commons.wikimedia.org/wiki/File:Condensation_Smiley_Face.jpg`.

[9] Wikimedia Commons. Windshield rain on freret st, 2009. URL `https://commons.wikimedia.org/wiki/File:Windshield_Rain_on_Freret_St.jpg`.

[10] Wikimedia Commons. Water droplets in a lotus leaf, 2014. URL `https://commons.wikimedia.org/wiki/File:Water_droplets_in_a_lotus_leaf.JPG`.

[11] Wikimedia Commons. Water drops on taro plant leaf, 2020. URL `https://commons.wikimedia.org/wiki/File:Water_drops_on_taro_plant_leaf.jpg`.

[12] Wikimedia Commons. Nepenthes rafflesiana ant, 2005. URL `https://commons.wikimedia.org/wiki/File:Nepenthes_rafflesiana_ant.jpg`.

[13] M Mayhoub. Cleaning innovative daylighting systems: Review and suggested methods. *Lighting Research & Technology*, 49(8):1015–1033, 2017.

[14] Robert N Wenzel. Resistance of solid surfaces to wetting by water. *Industrial & engineering chemistry*, 28(8):988–994, 1936.

[15] Kuan-Yu Yeh, Li-Jen Chen, and Jeng-Yang Chang. Contact angle hysteresis on regular pillar-like hydrophobic surfaces. *Langmuir*, 24(1):245–251, 2008.

[16] Christian Dorrer and Jürgen Rühe. Some thoughts on superhydrophobic wetting. *Soft Matter*, 5(1):51–61, 2009.

[17] Shuaijun Pan, Arun K Kota, Joseph M Mabry, and Anish Tuteja. Superomniphobic surfaces for effective chemical shielding. *Journal of the American Chemical Society*, 135(2):578–581, 2013.

[18] Arun K Kota, Gibum Kwon, and Anish Tuteja. The design and applications of superomniphobic surfaces. *NPG Asia Materials*, 6(7):e109–e109, 2014.

[19] Junping Zhang and Stefan Seeger. Superoleophobic coatings with ultralow sliding angles based on silicone nanofilaments. *Angewandte Chemie-International Edition*, 50(29):6652, 2011.

[20] Hongxia Wang, Yuhua Xue, Jie Ding, Lianfang Feng, Xungai Wang, and Tong Lin. Durable, self-healing superhydrophobic and superoleophobic surfaces from fluorinated-decyl polyhedral oligomeric silsesquioxane and hydrolyzed fluorinated alkyl silane. *Angewandte Chemie-International Edition*, 50(48):11433, 2011.

[21] Qian Feng Xu, Yang Liu, Fang-Ju Lin, Bikash Mondal, and Alan M Lyons. Superhydrophobic tio2–polymer nanocomposite surface with uv-induced reversible wettability and self-cleaning properties. *ACS applied materials & interfaces*, 5(18): 8915–8924, 2013.

[22] Denis Bartolo, Farid Bouamrirene, Emilie Verneuil, Axel Buguin, Pascal Silberzan, and Sébastien Moulinet. Bouncing or sticky droplets: Impalement transitions on superhydrophobic micropatterned surfaces. *Europhysics Letters*, 74(2):299, 2006.

[23] Choongyeop Lee and Chang-Jin Kim. Underwater restoration and retention of gases on superhydrophobic surfaces for drag reduction. *Physical review letters*, 106(1): 014502, 2011.

[24] Neelesh A Patankar. Vapor stabilizing substrates for superhydrophobicity and superslip. *Langmuir*, 26(11):8783–8786, 2010.

[25] Kripa K Varanasi, Tao Deng, J David Smith, Ming Hsu, and Nitin Bhate. Frost formation and ice adhesion on superhydrophobic surfaces. *Applied Physics Letters*, 97(23), 2010.

[26] Aurélie Lafuma and David Quéré. Slippery pre-suffused surfaces. *Europhysics Letters*, 96(5):56001, 2011.

[27] Jacopo Seiwert, Christophe Clanet, and David Quéré. Coating of a textured solid. *Journal of Fluid Mechanics*, 669:55–63, 2011.

[28] Philseok Kim, Michael J Kreder, Jack Alvarenga, and Joanna Aizenberg. Hierarchical or not? effect of the length scale and hierarchy of the surface roughness on omniphobicity of lubricant-infused substrates. *Nano letters*, 13(4):1793–1799, 2013.

[29] Michael J Kreder, Dan Daniel, Adam Tetreault, Zhenle Cao, Baptiste Lemaire, Jaakko VI Timonen, and Joanna Aizenberg. Film dynamics and lubricant depletion by droplets moving on lubricated surfaces. *Physical Review X*, 8(3):031053, 2018.

[30] Philipp Baumli, Maria D'Acunzi, Katharina I Hegner, Abhinav Naga, William SY Wong, Hans-Juergen Butt, and Doris Vollmer. The challenge of lubricant-replenishment on lubricant-impregnated surfaces. *Advances in Colloid and Interface Science*, 287:102329, 2021.

[31] Wikimedia Commons. Contact angle microstates, 2014. URL `https://commons.wikimedia.org/wiki/File:Contact_angle_microstates.svg`.

[32] Hannu Teisala, Philipp Baumli, Stefan AL Weber, Doris Vollmer, and Hans-Jürgen Butt. Grafting silicone at room temperature—a transparent, scratch-resistant nonstick molecular coating. *Langmuir*, 36(16):4416–4431, 2020.

[33] Brandon Barajas, Irene S Kurtz, Abraham J Waldman, and Jessica D Schiffman. Stiffness and oligomer content affect the initial adhesion of staphylococcus aureus to polydimethylsiloxane gels. *ACS Applied Materials & Interfaces*, 15(45):52197–52206, 2023.

[34] Jessamine Ng Lee, Cheolmin Park, and George M Whitesides. Solvent compatibility of poly (dimethylsiloxane)-based microfluidic devices. *Analytical chemistry*, 75(23): 6544–6554, 2003.

[35] Chander Shekhar Sharma, Athanasios Milionis, Abhinav Naga, Cheuk Wing Edmond Lam, Gabriel Rodriguez, Marco Francesco Del Ponte, Valentina Negri, Hopf Raoul, Maria D'Acunzi, Hans-Jürgen Butt, et al. Enhanced condensation on soft materials through bulk lubricant infusion. *Advanced Functional Materials*, 32(17): 2109633, 2022.

[36] Xiaotong Wu, Wufang Yang, Ying Liu, Xingwei Wang, Yunlei Zhang, Shuanhong Ma, Bin Li, Xiaowei Pei, Bo Yu, Daoai Wang, et al. Silicon gels with sustainable self-replenishment: Fluid drag reduction through viscosity dependency. *Tribology International*, page 109460, 2024.

[37] Mees M Flapper, Anupam Pandey, MH Essink, EH Van Brummelen, S Karpitschka, and JH Snoeijer. Reversal of solvent migration in poroelastic folds. *Physical review letters*, 130(22):228201, 2023.

[38] Zhuoyun Cai, Artem Skabeev, Svetlana Morozova, and Jonathan T Pham. Fluid separation and network deformation in wetting of soft and swollen surfaces. *Communications Materials*, 2(1):21, 2021.

[39] Xiao Gong and Shuang He. Highly durable superhydrophobic polydimethylsiloxane/silica nanocomposite surfaces with good self-cleaning ability. *ACS omega*, 5(8): 4100–4108, 2020.

[40] Behrooz Khatir, Zahra Azimi Dijvejin, Peter Serles, Tobin Filleter, and Kevin Golovin. Molecularly capped omniphobic polydimethylsiloxane brushes with ultrafast contact line dynamics. *Small*, 19(38):2301142, 2023.

[41] Jie Liu, Yuling Sun, Xiaoteng Zhou, Xiaomei Li, Michael Kappl, Werner Steffen, and Hans-Jürgen Butt. One-step synthesis of a durable and liquid-repellent poly (dimethylsiloxane) coating. *Advanced Materials*, 33(23):2100237, 2021.

[42] Xiaoxiao Zhao, Md Arifur Rahman Khandoker, and Kevin Golovin. Non-fluorinated omniphobic paper with ultralow contact angle hysteresis. *ACS applied materials & interfaces*, 12(13):15748–15756, 2020.

[43] G Tovar, S Paul, W Knoll, O Prucker, and J Rühe. Patterning molecularly thin films of polymers—new methods for photolithographic structuring of surfaces. *Supramolecular Science*, 2(2):89–98, 1995.

[44] Shuai Li, Cheuk Wing Edmond Lam, Matteo Donati, Kartik Regulagadda, Emre Yavuz, Till Pfeiffer, Panagiotis Sarkiris, Evangelos Gogolides, Athanasios Milionis, Dimos Poulikakos, et al. Durable, ultrathin, and antifouling polymer brush coating for efficient condensation heat transfer. *ACS Applied Materials & Interfaces*, 16(1): 1941–1949, 2023.

[45] Youtube The Slow Down Show. Bubbles bursting in slow motion, 2013. URL `https://www.youtube.com/watch?v=blNe2Ae5a2c&ab_channel=TheSlowDownShow,`.

[46] Ro Shuttleworth. The surface tension of solids. *Proceedings of the physical society. Section A*, 63(5):444, 1950.

[47] Thomas Young. Iii. an essay on the cohesion of fluids. *Philosophical transactions of the royal society of London*, 95:65–87, 1805.

[48] Athanase Dupré and Paul Dupré. *Théorie mécanique de la chaleur*. Gauthier-Villars, 1869.

[49] Josiah Willard Gibbs. *The Collected Works of J. Willard Gibbs...: Thermodynamics*, volume 1. Longmans, Green and Company, 1928.

[50] Pierre-Gilles de Gennes, Françoise Brochard-Wyart, David Quéré, et al. *Capillarity and wetting phenomena: drops, bubbles, pearls, waves*. Springer, 2004.

[51] JS Rowlinson. A drop of liquid. *Journal of Physics: Condensed Matter*, 6(23A):A1, 1994.

[52] Yongan Gu, Dongqing Li, and P Cheng. Determination of line tension from the shape of axisymmetric liquid–vapor interfaces around a conic cylinder. *Journal of colloid and interface science*, 180(1):212–217, 1996.

[53] P Chen, SS Susnar, A Amirfazli, C Mak, and AW Neumann. Line tension measurements: an application of the quadrilateral relation to a liquid lens system. *Langmuir*, 13(11):3035–3042, 1997.

[54] John Shipley Rowlinson and Benjamin Widom. *Molecular theory of capillarity*. Courier Corporation, 2013.

[55] Robert Aveyard and John H Clint. Particle wettability and line tension. *Journal of the Chemical Society, Faraday Transactions*, 92(1):85–89, 1996.

[56] Jaroslaw Drelich, Jan D Miller, and Jan Hupka. The effect of drop size on contact angle over a wide range of drop volumes. *Journal of colloid and interface science*, 155(2):379–385, 1993.

[57] Philip Ofori, Bruce Firth, Graham O'Brien, Clint McNally, and Anh V Nguyen. Assessing the hydrophobicity of petrographically heterogeneous coal surfaces. *Energy & Fuels*, 24(11):5965–5971, 2010.

[58] Hans-Jürgen Butt, Jie Liu, Kaloian Koynov, Benedikt Straub, Chirag Hinduja, Ilia Roismann, Rüdiger Berger, Xiaomei Li, Doris Vollmer, Werner Steffen, et al. Contact angle hysteresis. *Current Opinion in Colloid & Interface Science*, 59:101574, 2022.

[59] Ciro Semprebon and Martin Brinkmann. On the onset of motion of sliding drops. *Soft Matter*, 10(18):3325–3334, 2014.

[60] CGL Furmidge. Studies at phase interfaces. i. the sliding of liquid drops on solid surfaces and a theory for spray retention. *Journal of colloid science*, 17(4):309–324, 1962.

[61] Charles W Extrand and Y Kumagai. Liquid drops on an inclined plane: the relation between contact angles, drop shape, and retentive force. *Journal of colloid and interface science*, 170(2):515–521, 1995.

[62] NV Churaev and VD Sobolev. Prediction of contact angles on the basis of the frumkin-derjaguin approach. *Advances in colloid and interface science*, 61:1–16, 1995.

[63] V. M. Muller B. V. Derjaguin, N. V. Churaev. *Surface Forces*. Springer New York, NY, 1 edition, 2013.

[64] Hugo C Hamaker. The london—van der waals attraction between spherical particles. *physica*, 4(10):1058–1072, 1937.

[65] Dimo Platikanov and Dotchi Exerowa. Chapter 6 - thin liquid flms. In J. Lyklema, editor, *Soft Colloids*, volume 5 of *Fundamentals of Interface and Colloid Science*, pages 6.1–6.91. Academic Press, 2005.

[66] BV Derjaguin and NV Churaev. Structural component of disjoining pressure. *Journal of Colloid and Interface Science*, 49(2):249–255, 1974.

[67] NV Churaev and BV Derjaguin. Inclusion of structural forces in the theory of stability of colloids and films. *Journal of colloid and interface science*, 103(2):542–553, 1985.

[68] Nikolai Kubochkin and Tatiana Gambaryan-Roisman. Wetting at nanoscale: Effect of surface forces and droplet size. *Physical Review Fluids*, 6(9):093603, 2021.

[69] Uwe Thiele, Michael Mertig, and Wolfgang Pompe. Dewetting of an evaporating thin liquid film: Heterogeneous nucleation and surface instability. *Physical review letters*, 80(13):2869, 1998.

[70] Günter Reiter, Ashutosh Sharma, Alain Casoli, Marie-Odile David, Rajesh Khanna, and Philippe Auroy. Thin film instability induced by long-range forces. *Langmuir*, 15(7):2551–2558, 1999.

[71] Vitaly B Svetovoy, Ivan Dević, Jacco H Snoeijer, and Detlef Lohse. Effect of disjoining pressure on surface nanobubbles. *Langmuir*, 32(43):11188–11196, 2016.

[72] Taeil Yi and Harris Wong. Theory of slope-dependent disjoining pressure with application to lennard–jones liquid films. *Journal of colloid and interface science*, 313 (2):579–591, 2007.

[73] Luuk A Lubbers, Joost H Weijs, Lorenzo Botto, Siddhartha Das, Bruno Andreotti, and Jacco H Snoeijer. Drops on soft solids: free energy and double transition of contact angles. *Journal of fluid mechanics*, 747:R1, 2014.

[74] Lev Davidovich Landau, LP Pitaevskii, Arnol'd Markovich Kosevich, and Evgenii Mikhailovich Lifshitz. *Course of theoretical physics: Theory of elasticity*, volume 7. Elsevier, 2012.

[75] MER Shanahan. The influence of solid micro-deformation on contact angle equilibrium. *Journal of Physics D: Applied Physics*, 20(7):945, 1987.

[76] Kenneth Langstreth Johnson. *Contact mechanics*. Cambridge university press, 1987.

[77] Mathijs van Gorcum, Stefan Karpitschka, Bruno Andreotti, and Jacco H Snoeijer. Spreading on viscoelastic solids: are contact angles selected by neumann's law? *Soft Matter*, 16(5):1306–1322, 2020.

[78] Francois Chambon and H Henning Winter. Stopping of crosslinking reaction in a pdms polymer at the gel point. *Polymer Bulletin*, 13:499–503, 1985.

[79] Ian D Johnston, Daniel K McCluskey, Christabel KL Tan, and Monica C Tracey. Mechanical characterization of bulk sylgard 184 for microfluidics and microengineering. *Journal of Micromechanics and Microengineering*, 24(3):035017, 2014.

[80] Lukas Hauer, Abhinav Naga, Rodrique GM Badr, Jonathan T Pham, William SY Wong, and Doris Vollmer. Wetting on silicone surfaces. *Soft Matter*, 20(27):5273–5295, 2024.

[81] S Alexander. Adsorption of chain molecules with a polar head a scaling description. *Journal De Physique*, 38(8):983–987, 1977.

[82] Pierre-Gilles de Gennes. Conformations of polymers attached to an interface. *Macromolecules*, 13(5):1069–1075, 1980.

[83] Armelle Keiser, Philipp Baumli, Doris Vollmer, and David Quéré. Universality of friction laws on liquid-infused materials. *Physical Review Fluids*, 5(1):014005, 2020.

[84] Dan Daniel, Jaakko VI Timonen, Ruoping Li, Seneca J Velling, and Joanna Aizenberg. Oleoplaning droplets on lubricated surfaces. *Nature Physics*, 13(10):1020–1025, 2017.

[85] Armelle Keiser, Ludovic Keiser, Christophe Clanet, and David Quéré. Drop friction on liquid-infused materials. *Soft Matter*, 13(39):6981–6987, 2017.

[86] Göran Ström, Monica Fredriksson, Per Stenius, and Bovjan Radoev. Kinetics of steady-state wetting. *Journal of colloid and interface science*, 134(1):107–116, 1990.

[87] Dohyung Kim, Minki Lee, Jeong-Hyun Kim, and Jinkee Lee. Dynamic contact angle measurements on lubricant infused surfaces. *Journal of Colloid and Interface Science*, 586:647–654, 2021.

[88] Nathalie Fraysse and George M Homsy. An experimental study of rivulet instabilities in centrifugal spin coating of viscous newtonian and non-newtonian fluids. *Physics of fluids*, 6(4):1491–1504, 1994.

[89] Yuming Pan, Zhibei Wang, Xinyan Zhao, Weiwei Deng, and Huihui Xia. On axisymmetric dynamic spin coating with a single drop of ethanol. *Journal of Fluid Mechanics*, 951:A30, 2022.

[90] Jürgen Becker, Günther Grün, Ralf Seemann, Hubert Mantz, Karin Jacobs, Klaus R Mecke, and Ralf Blossey. Complex dewetting scenarios captured by thin-film models. *Nature materials*, 2(1):59–63, 2003.

[91] Muhammad Rizwanur Rahman, Li Shen, James P Ewen, David M Heyes, Daniele Dini, and Edward R Smith. Life and death of a thin liquid film. *Communications Physics*, 7(1):242, 2024.

[92] LH Tanner. The spreading of silicone oil drops on horizontal surfaces. *Journal of Physics D: Applied Physics*, 12(9):1473, 1979.

[93] H Pirouz Kavehpour, Ben Ovryn, and Gareth H McKinley. Microscopic and macroscopic structure of the precursor layer in spreading viscous drops. *Physical review letters*, 91(19):196104, 2003.

[94] Naoya Yoshida, Yuu Abe, Hiroaki Shigeta, Akira Nakajima, Hisashi Ohsaki, Kazuhito Hashimoto, and Toshiya Watanabe. Sliding behavior of water droplets on flat polymer surface. *Journal of the American Chemical Society*, 128(3):743–747, 2006.

[95] Xiaomei Li, Francisco Bodziony, Mariana Yin, Holger Marschall, Rüdiger Berger, and Hans-Jürgen Butt. Kinetic drop friction. *Nature Communications*, 14(1):4571, 2023.

[96] Gang Pu and Steven J Severtson. Characterization of dynamic stick-and-break wetting behavior for various liquids on the surface of a highly viscoelastic polymer. *Langmuir*, 24(9):4685–4692, 2008.

[97] Tadashi Kajiya, Adrian Daerr, Tetsuharu Narita, Laurent Royon, François Lequeux, and Laurent Limat. Advancing liquid contact line on visco-elastic gel substrates: stick-slip vs. continuous motions. *Soft Matter*, 9(2):454–461, 2013.

[98] Stefan Karpitschka, Siddhartha Das, Mathijs van Gorcum, Hugo Perrin, Bruno Andreotti, and Jacco H Snoeijer. Droplets move over viscoelastic substrates by surfing a ridge. *Nature communications*, 6(1):7891, 2015.

[99] Dominic Mokbel, Sebastian Aland, and Stefan Karpitschka. Stick-slip contact line motion on kelvin-voigt model substrates. *Europhysics letters*, 139(3):33002, 2022.

[100] TD Blake and JM Haynes. Kinetics of liquid/liquid rg cox. *The dynamics of the Spreading of Liquids displacement", J. Colloid Interface Sci*, 30(3):421–423, 1969.

[101] Pierre-Gilles de Gennes. Wetting: statics and dynamics. *Reviews of modern physics*, 57(3):827, 1985.

[102] Yulii D Shikhmurzaev. Mathematical modeling of wetting hydrodynamics. *Fluid Dynamics Research*, 13(1):45, 1994.

[103] Oleg V Voinov. Hydrodynamics of wetting. *Fluid dynamics*, 11(5):714–721, 1976.

[104] AM Cazabat, S Gerdes, MP Valignat, and S Villette. Dynamics of wetting: From theory to experiment. *Interface Science*, 5:129–139, 1997.

[105] Terence D Blake. The physics of moving wetting lines. *Journal of colloid and interface science*, 299(1):1–13, 2006.

[106] Chun Huh and Laurence E Scriven. Hydrodynamic model of steady movement of a solid/liquid/fluid contact line. *Journal of colloid and interface science*, 35(1):85–101, 1971.

[107] William SY Wong, Lukas Hauer, Abhinav Naga, Anke Kaltbeitzel, Philipp Baumli, Rüdiger Berger, Maria D 'Acunzi, Doris Vollmer, and Hans-Jürgen Butt. Adaptive wetting of polydimethylsiloxane. *Langmuir*, 36(26):7236–7245, 2020.

[108] Daniel Bonn, Jens Eggers, Joseph Indekeu, Jacques Meunier, and Etienne Rolley. Wetting and spreading. *Reviews of modern physics*, 81(2):739–805, 2009.

[109] RG Cox. The dynamics of the spreading of liquids on a solid surface. part 1. viscous flow. *Journal of fluid mechanics*, 168:169–194, 1986.

[110] LM Hocking. A moving fluid interface. part 2. the removal of the force singularity by a slip flow. *Journal of Fluid Mechanics*, 79(2):209–229, 1977.

[111] C Huh and SG Mason. The steady movement of a liquid meniscus in a capillary tube. *Journal of fluid mechanics*, 81(3):401–419, 1977.

[112] Tak Shing Chan, Catherine Kamal, Jacco H Snoeijer, James E Sprittles, and Jens Eggers. Cox–voinov theory with slip. *Journal of fluid mechanics*, 900:A8, 2020.

[113] Richard L Hoffman. A study of the advancing interface. i. interface shape in liquid—gas systems. *Journal of colloid and interface science*, 50(2):228–241, 1975.

[114] Michel J de Ruijter, TD Blake, and Joël De Coninck. Dynamic wetting studied by molecular modeling simulations of droplet spreading. *Langmuir*, 15(22):7836–7847, 1999.

[115] Robert Francis Allen and Philip Roy Benson. Rolling drops on an inclined plane. *Journal of Colloid and Interface Science*, 50(2):250–253, 1975.

[116] Lev Davidovich Landau and Evgenii Mikhailovich Lifshitz. *Fluid Mechanics: Volume 6*, volume 6. Elsevier, 1987.

[117] James Servantie and Marcus Müller. Statics and dynamics of a cylindrical droplet under an external body force. *The Journal of chemical physics*, 128(1), 2008.

[118] Sumesh P Thampi, Ronojoy Adhikari, and Rama Govindarajan. Do liquid drops roll or slide on inclined surfaces? *Langmuir*, 29(10):3339–3346, 2013.

[119] Rodrique GM Badr, Lukas Hauer, Doris Vollmer, and Friederike Schmid. Dynamics of droplets moving on lubricated polymer brushes. *Langmuir*, 40(24):12368–12380, 2024.

[120] Claude Navier. *Mémoire sur les lois du mouvement des fluides*. Gauthier-Villars, Paris, 1827, 1822.

[121] SC Hendy and NJ Lund. Effective slip boundary conditions for flows over nanoscale chemical heterogeneities. *Physical Review E—Statistical, Nonlinear, and Soft Matter Physics*, 76(6):066313, 2007.

[122] Lydéric Bocquet and Jean-Louis Barrat. Hydrodynamic boundary conditions, correlation functions, and kubo relations for confined fluids. *Physical review E*, 49(4): 3079, 1994.

[123] Dan Daniel, Jaakko VI Timonen, Ruoping Li, Seneca J Velling, Michael J Kreder, Adam Tetreault, and Joanna Aizenberg. Origins of extreme liquid repellency on structured, flat, and lubricated hydrophobic surfaces. *Physical review letters*, 120 (24):244503, 2018.

[124] Lev Davidovich Landau and Veniamin Grigorievich Levich. Dragging of a liquid by a moving plate. In *Dynamics of curved fronts*, pages 141–153. Elsevier, 1988.

[125] Boris Vladimirovich Derjaguin. On the thickness of the liquid film adhering to the walls of a vessel after emptying. *Progress in Surface Science*, 43(1-4):134–137, 1993.

[126] Davide Bottone and Stefan Seeger. Droplet memory on liquid-infused surfaces. *Langmuir*, 39(17):6160–6168, 2023.

[127] Abhinav Naga, Michael Rennick, Lukas Hauer, William SY Wong, Azadeh Sharifi-Aghili, Doris Vollmer, and Halim Kusumaatmaja. Direct visualization of viscous dissipation and wetting ridge geometry on lubricant-infused surfaces. *Communications Physics*, 7(1):306, 2024.

[128] Kun Li, Cunjing Lv, and Xi-Qiao Feng. Rapid droplet leads the liquid-infused slippery surfaces more slippery. *arXiv preprint arXiv:2309.02038*, 2023.

[129] John D. Ferry. *Viscoelastic properties of polymers*. Wiley, 3rd edition, 1980.

[130] Nicholas W. Tschoegl. *The Phenomenological Theory of Linear Viscoelastic Behavior*. Springer Berlin Heidelberg, 1989.

[131] Bernard D Coleman and Walter Noll. Foundations of linear viscoelasticity. *Reviews of modern physics*, 33(2):239, 1961.

[132] John S Toll. Causality and the dispersion relation: logical foundations. *Physical review*, 104(6):1760, 1956.

[133] H Henning Winter and Francois Chambon. Analysis of linear viscoelasticity of a crosslinking polymer at the gel point. *Journal of rheology*, 30(2):367–382, 1986.

[134] Francois Chambon and H Henning Winter. Linear viscoelasticity at the gel point of a crosslinking pdms with imbalanced stoichiometry. *Journal of Rheology*, 31(8): 683–697, 1987.

[135] James C Scanlan and H Henning Winter. Composition dependence of the viscoelasticity of end-linked poly (dimethylsiloxane) at the gel point. *Macromolecules*, 24(1): 47–54, 1991.

[136] Pierre-Gilles de Gennes. Soft adhesives. *Langmuir*, 12(19):4497–4500, 1996.

[137] Michael Rubinstein and Ralph H Colby. *Polymer physics*. Oxford university press, 2003.

[138] Hsiao-Ping Hsu and Peter Grassberger. Polymers confined between two parallel plane walls. *The Journal of chemical physics*, 120(4):2034–2041, 2004.

[139] Pierre-Gilles de Gennes. *Scaling Concepts in Polymer Physics*. Cornell University Press, 1979.

[140] JPl Wittmer, P Beckrich, A Johner, AN Semenov, SP Obukhov, H Meyer, and J Baschnagel. Why polymer chains in a melt are not random walks. *Europhysics Letters*, 77(5):56003, 2007.

[141] Hendrik Meyer, Eric Horwath, and Peter Virnau. Mapping onto ideal chains overestimates self-entanglements in polymer melts. *ACS Macro Letters*, 7(6):757–761, 2018.

[142] K. Binder and A. Milchev. Polymer brushes on flat and curved surfaces: How computer simulations can help to test theories and to interpret experiments. *J. Pol. Sci. Part B - Polymer Physics*, 50(22):1515–1555, NOV 15 2012. doi: 10.1002/polb.23168.

[143] DRM Williams. Grafted polymers in bad solvents: octopus surface micelles. *Journal de physique II*, 3(9):1313–1318, 1993.

[144] Christoph Jentzsch and Jens-Uwe Sommer. Polymer brushes in explicit poor solvents studied using a new variant of the bond fluctuation model. *The Journal of Chemical Physics*, 141(10), 2014.

[145] TM Birshtein and Yu V Lyatskaya. Theory of the collapse-stretching transition of a polymer brush in a mixed solvent. *Macromolecules*, 27(5):1256–1266, 1994.

[146] Alexander N Semenov. Contribution to the theory of microphase layering in block-copolymer melts. *Zh. Eksp. Teor. Fiz*, 88(4):1242–1256, 1985.

[147] Mark W. Matsen. Self-Consistent Field Theory and Its Applications. In *Soft Matter: Polymer Melts and Mixtures*, volume 1, chapter 2, pages 87–178. John Wiley & Sons, Ltd, 2005.

[148] Scott T Milner, Thomas A Witten, and Michael E Cates. Theory of the grafted polymer brush. *Macromolecules*, 21(8):2610–2619, 1988.

[149] Daan Frenkel and Berend Smit. *Understanding molecular simulation: from algorithms to applications*. Elsevier, 2023.

[150] Michael P Allen and Dominic J Tildesley. *Computer simulation of liquids*. Oxford university press, 2017.

[151] Robert D Groot and Patrick B Warren. Dissipative particle dynamics: Bridging the gap between atomistic and mesoscopic simulation. *The Journal of chemical physics*, 107(11):4423–4435, 1997.

[152] I. Pagonabarraga and D. Frenkel. Dissipative particle dynamics for interacting systems. *J. Chem. Phys.*, 115(11):5015–5026, 2001.

[153] S. Trovimov, E. Nies, and M. Michels. Thermodynamic consistency in dissipative particle dynamics simulations of strongly nonideal liquids and liquid mixtures. *J. Chem. Phys.*, 117(20):9383–9394, 2002.

[154] PB Warren. Vapor-liquid coexistence in many-body dissipative particle dynamics. *Phys. Rev. E*, 68(6):066702, 2003.

[155] Patrick B Warren. No-go theorem in many-body dissipative particle dynamics. *Phys. Rev. E*, 87(4):045303, 2013.

[156] CA Marsh, G Backx, and MH Ernst. Static and dynamic properties of dissipative particle dynamics. *Phys. Rev. E*, 56(2):1676, 1997.

[157] PJ Hoogerbrugge and JMVA Koelman. Simulating microscopic hydrodynamic phenomena with dissipative particle dynamics. *Europhys. Lett.*, 19(3):155, 1992.

[158] Pep Espanol. Hydrodynamics from dissipative particle dynamics. *Phys. Rev. E*, 52 (2):1734, 1995.

[159] John D Weeks, David Chandler, and Hans C Andersen. Role of repulsive forces in determining the equilibrium structure of simple liquids. *J. Chem. Phys.*, 54(12): 5237–5247, 1971.

[160] Joshua A Anderson, Jens Glaser, and Sharon C Glotzer. Hoomd-blue: A python package for high-performance molecular dynamics and hard particle monte carlo simulations. *Comput. Mater. Sci.*, 173:109363, 2020.

[161] Carolyn L Phillips, Joshua A Anderson, and Sharon C Glotzer. Pseudo-random number generation for brownian dynamics and dissipative particle dynamics simulations on gpu devices. *J. Comput. Phys.*, 230(19):7191–7201, 2011.

[162] Alexander Stukowski. Visualization and analysis of atomistic simulation data with ovito–the open visualization tool. *Model. Simul. Mater. Sci. Eng.*, 18(1):015012, 2009.

[163] Rodrique GM Badr, Lukas Hauer, Doris Vollmer, and Friederike Schmid. Cloaking transition of droplets on lubricated brushes. *The Journal of Physical Chemistry B*, 126(36):7047–7058, 2022.

[164] Ralf Blossey. Self-cleaning surfaces—virtual realities. *Nature materials*, 2(5):301–306, 2003.

[165] Akira Nakajima, Kazuhito Hashimoto, Toshiya Watanabe, Kennichi Takai, Goro Yamauchi, and Akira Fujishima. Transparent superhydrophobic thin films with self-cleaning properties. *Langmuir*, 16(17):7044–7047, 2000.

[166] Ivan P Parkin and Robert G Palgrave. Self-cleaning coatings. *Journal of materials chemistry*, 15(17):1689–1695, 2005.

[167] Alexander K Epstein, Tak-Sing Wong, Rebecca A Belisle, Emily Marie Boggs, and Joanna Aizenberg. Liquid-infused structured surfaces with exceptional anti-biofouling performance. *Proceedings of the National Academy of Sciences*, 109(33): 13182–13187, 2012.

[168] Vance Bergeron, Daniel Bonn, Jean Yves Martin, and Louis Vovelle. Controlling droplet deposition with polymer additives. *Nature*, 405(6788):772–775, 2000.

[169] Laurence Gaume, Stanislav Gorb, and Nick Rowe. Function of epidermal surfaces in the trapping efficiency of nepenthes alata pitchers. *New Phytologist*, 156(3):479–489, 2002.

[170] Helen Yang, Haijin Zhu, Marco MRM Hendrix, Niek JHGM Lousberg, Gijsbertus de With, A Catarina C Esteves, and John H Xin. Temperature-triggered collection and release of water from fogs by a sponge-like cotton fabric. *Advanced Materials*, 25(8):1150–1154, 2013.

[171] John A Howarter and Jeffrey P Youngblood. Self-cleaning and anti-fog surfaces via stimuli-responsive polymer brushes. *Advanced materials*, 19(22):3838–3843, 2007.

[172] Guido C Ritsema van Eck, Leonardo Chiappisi, and Sissi de Beer. Fundamentals and applications of polymer brushes in air. *ACS Applied Polymer Materials*, 4(5): 3062–3087, 2022.

[173] Hans-Jürgen Butt, Rüdiger Berger, Werner Steffen, Doris Vollmer, and Stefan AL Weber. Adaptive wetting—adaptation in wetting. *Langmuir*, 34(38):11292–11304, 2018.

[174] Amy Z Stetten, Dmytro S Golovko, Stefan AL Weber, and Hans-Jürgen Butt. Slide electrification: charging of surfaces by moving water drops. *Soft Matter*, 15(43): 8667–8679, 2019.

[175] J David Smith, Rajeev Dhiman, Sushant Anand, Ernesto Reza-Garduno, Robert E Cohen, Gareth H McKinley, and Kripa K Varanasi. Droplet mobility on lubricant-impregnated surfaces. *Soft Matter*, 9(6):1772–1780, 2013.

[176] Tak-Sing Wong, Sung Hoon Kang, Sindy KY Tang, Elizabeth J Smythe, Benjamin D Hatton, Alison Grinthal, and Joanna Aizenberg. Bioinspired self-repairing slippery surfaces with pressure-stable omniphobicity. *Nature*, 477(7365):443–447, 2011.

[177] David Quéré. Non-sticking drops. *Reports on Progress in Physics*, 68(11):2495, 2005.

[178] Antonin Marchand, Siddhartha Das, Jacco H Snoeijer, and Bruno Andreotti. Contact angles on a soft solid: From young's law to neumann's law. *Physical review letters*, 109(23):236101, 2012.

[179] Joseph W Krumpfer and Thomas J McCarthy. Rediscovering silicones:"unreactive" silicones react with inorganic surfaces. *Langmuir*, 27(18):11514–11519, 2011.

[180] Sanghyuk Wooh and Doris Vollmer. Silicone brushes: omniphobic surfaces with low sliding angles. *Angewandte Chemie International Edition*, 55(24):6822–6824, 2016.

[181] Liming Wang and Thomas J McCarthy. Covalently attached liquids: instant omniphobic surfaces with unprecedented repellency. *Angewandte Chemie International Edition*, 55(1):244–248, 2016.

[182] André Colas. Silicones: preparation, properties and performance. *Dow corning, life sciences*, 2005.

[183] Fabien Léonforte and Marcus Müller. Statics of polymer droplets on deformable surfaces. *The Journal of chemical physics*, 135(21):214703, 2011.

[184] Liz IS Mensink, Jacco H Snoeijer, and Sissi De Beer. Wetting of polymer brushes by polymeric nanodroplets. *Macromolecules*, 52(5):2015–2020, 2019.

[185] Liz IS Mensink, Sissi de Beer, and Jacco H Snoeijer. The role of entropy in wetting of polymer brushes. *Soft matter*, 17(5):1368–1375, 2021.

[186] Lin Guo, GH Tang, and Satish Kumar. Droplet morphology and mobility on lubricant-impregnated surfaces: a molecular dynamics study. *Langmuir*, 35(49): 16377–16387, 2019.

[187] Lin Guo, GH Tang, and Satish Kumar. Dynamic wettability on the lubricant-impregnated surface: From nucleation to growth and coalescence. *ACS Applied Materials & Interfaces*, 12(23):26555–26565, 2020.

[188] JH Maas, GJ Fleer, FAM Leermakers, and MA Cohen Stuart. Wetting of a polymer brush by a chemically identical polymer melt: Phase diagram and film stability. *Langmuir*, 18(23):8871–8880, 2002.

[189] Xueyun Zhang, Fuk Kay Lee, and Ophelia KC Tsui. Wettability of end-grafted polymer brush by chemically identical polymer films. *Macromolecules*, 41(21):8148–8151, 2008.

[190] HT Davis and LE Scriven. Stress and structure in fluid interfaces. *Advances in Chemical Physics*, 49:357–454, 1982.

[191] Carlos Braga, Edward R Smith, Andreas Nold, David N Sibley, and Serafim Kalliadasis. The pressure tensor across a liquid-vapour interface. *The Journal of chemical physics*, 149(4), 2018.

[192] J. Lyklema. 2 - interfacial tension: Molecular interpretation. In J. Lyklema, editor, *Liquid-Fluid Interfaces*, volume 3 of *Fundamentals of Interface and Colloid Science*, pages 2.1–2.78. Academic Press, 2000.

[193] Lars B Veldscholte, Jacco H Snoeijer, Wouter K den Otter, and Sissi de Beer. Pressure anisotropy in polymer brushes and its effects on wetting. *Langmuir*, 40(8): 4401–4409, 2024.

[194] Abhinav Naga, Anke Kaltbeitzel, William SY Wong, Lukas Hauer, Hans-Jürgen Butt, and Doris Vollmer. How a water drop removes a particle from a hydrophobic surface. *Soft Matter*, 17(7):1746–1755, 2021.

[195] Joost H Weijs, Antonin Marchand, Bruno Andreotti, Detlef Lohse, and Jacco H Snoeijer. Origin of line tension for a lennard-jones nanodroplet. *Physics of fluids*, 23(2):022001, 2011.

[196] Sai Ankit Etha, Parth Rakesh Desai, Harnoor Singh Sachar, and Siddhartha Das. Wetting dynamics on solvophilic, soft, porous, and responsive surfaces. *Macromolecules*, 54(2):584–596, 2021.

[197] Melissa C Brindise, Margaret M Busse, and Pavlos P Vlachos. Density-and viscosity-matched newtonian and non-newtonian blood-analog solutions with pdms refractive index. *Experiments in fluids*, 59(11):1–8, 2018.

[198] Koichi Takamura, Herbert Fischer, and Norman R Morrow. Physical properties of aqueous glycerol solutions. *Journal of Petroleum Science and Engineering*, 98:50–60, 2012.

[199] John W Cahn and John E Hilliard. Free energy of a nonuniform system. i. interfacial free energy. *The Journal of chemical physics*, 28(2):258–267, 1958.

[200] Jean-Pierre Hansen and Ian Ranald McDonald. *Theory of simple liquids: with applications to soft matter*. Academic press, 2013.

[201] Filip Kos, David Poland, David Simmons-Duffin, and Alessandro Vichi. Precision islands in the ising and o (n) models. *Journal of High Energy Physics*, 2016(8):1–16, 2016.

[202] Richard C Tolman. The effect of droplet size on surface tension. *The journal of chemical physics*, 17(3):333–337, 1949.

[203] JR Henderson and J Lekner. Surface oscillations and the surface thickness of classical and quantum droplets. *Molecular Physics*, 36(3):781–789, 1978.

[204] Zakarya Benayad, Soren von Bulow, Lukas S Stelzl, and Gerhard Hummer. Simulation of fus protein condensates with an adapted coarse-grained model. *Journal of chemical theory and computation*, 17(1):525–537, 2020.

[205] Zhuoyun Cai, Rodrique GM Badr, Lukas Hauer, Krishnaroop Chaudhuri, Artem Skabeev, Friederike Schmid, and Jonathan T Pham. Phase separation dynamics in wetting ridges of polymer surfaces swollen with oils of different viscosities. *Soft Matter*, 20(36):7300–7312, 2024.

[206] Daniela Rus and Michael T Tolley. Design, fabrication and control of soft robots. *Nature*, 521(7553):467–475, 2015.

[207] Irini Sotiri, Amanda Tajik, Yang Lai, Cathy T Zhang, Yevgen Kovalenko, Carine R Nemr, Haylea Ledoux, Jack Alvarenga, Edythe Johnson, Huseini S Patanwala, et al. Tunability of liquid-infused silicone materials for biointerfaces. *Biointerphases*, 13 (6), 2018.

[208] Chihiro Urata, Gary J Dunderdale, Matt W England, and Atsushi Hozumi. Self-lubricating organogels (slugs) with exceptional syneresis-induced anti-sticking properties against viscous emulsions and ices. *Journal of Materials Chemistry A*, 3(24): 12626–12630, 2015.

[209] Nicolas Lavielle, Dalal Asker, and Benjamin D Hatton. Lubrication dynamics of swollen silicones to limit long term fouling and microbial biofilms. *Soft Matter*, 17 (4):936–946, 2021.

[210] Longquan Chen, Elmar Bonaccurso, Tatiana Gambaryan-Roisman, Victor Starov, Nektaria Koursari, and Yapu Zhao. Static and dynamic wetting of soft substrates. *Current opinion in colloid & interface science*, 36:46–57, 2018.

[211] Bruno Andreotti and Jacco H Snoeijer. Statics and dynamics of soft wetting. *Annual review of fluid mechanics*, 52(1):285–308, 2020.

[212] Menghua Zhao, François Lequeux, Tetsuharu Narita, Matthieu Roché, Laurent Limat, and Julien Dervaux. Growth and relaxation of a ridge on a soft poroelastic substrate. *Soft matter*, 14(1):61–72, 2018.

[213] Krishnaroop Chaudhuri and Jonathan T Pham. Temperature-dependent soft wetting on amorphous, uncrosslinked polymer surfaces. *Soft Matter*, 18(19):3698–3704, 2022.

[214] Apurva Pandey, Bruno Andreotti, Stefan Karpitschka, GJ Van Zwieten, E Harald van Brummelen, and Jacco H Snoeijer. Singular nature of the elastocapillary ridge. *Physical review X*, 10(3):031067, 2020.

[215] Julia Gerber, Tobias Lendenmann, Hadi Eghlidi, Thomas M Schutzius, and Dimos Poulikakos. Wetting transitions in droplet drying on soft materials. *Nature communications*, 10(1):4776, 2019.

[216] Menghua Zhao, Julien Dervaux, Tetsuharu Narita, François Lequeux, Laurent Limat, and Matthieu Roché. Geometrical control of dissipation during the spreading of liquids on soft solids. *Proceedings of the National Academy of Sciences*, 115(8): 1748–1753, 2018.

[217] Hamza K Khattak, Stefan Karpitschka, Jacco H Snoeijer, and Kari Dalnoki-Veress. Direct force measurement of microscopic droplets pulled along soft surfaces. *Nat. Commun.*, 13(1):4436, 2022.

[218] Alain Carré, Jean-Claude Gastel, and Martin ER Shanahan. Viscoelastic effects in the spreading of liquids. *Nature*, 379(6564):432–434, 1996.

[219] Lukas Hauer, Zhuoyun Cai, Artem Skabeev, Doris Vollmer, and Jonathan T Pham. Phase separation in wetting ridges of sliding drops on soft and swollen surfaces. *Phys. Rev. Lett.*, 130(5):058205, 2023.

[220] Zhuoyun Cai and Jonathan T Pham. How swelling, cross-linking, and aging affect drop pinning on lubricant-infused, low modulus elastomers. *ACS Applied Polymer Materials*, 4(5):3013–3022, 2022.

[221] Martin H Essink, Stefan Karpitschka, Hamza K Khattak, Kari Dalnoki-Veress, Harald van Brummelen, and Jacco H Snoeijer. Wetting ridge dissipation at large deformations. *arXiv preprint arXiv:2402.06344*, 2024.

[222] Mathieu Oléron, Laurent Limat, Julien Dervaux, and Matthieu Roché. Morphology and stability of droplets sliding on soft viscoelastic substrates. *Soft Matter*, 20(4): 762–772, 2024.

[223] Hong-Huy Tran, Daeyeon Lee, and David Riassetto. Wetting ridges on slippery liquid-infused porous surfaces. *Reports on Progress in Physics*, 86(6):066601, 2023.

[224] Jianxing Sun and Patricia B Weisensee. Microdroplet self-propulsion during dropwise condensation on lubricant-infused surfaces. *Soft Matter*, 15(24):4808–4817, 2019.

[225] Ciro Semprebon, Glen McHale, and Halim Kusumaatmaja. Apparent contact angle and contact angle hysteresis on liquid infused surfaces. *Soft matter*, 13(1):101–110, 2017.

[226] Frank Schellenberger, Jing Xie, Noemí Encinas, Alexandre Hardy, Markus Klapper, Periklis Papadopoulos, Hans-Jürgen Butt, and Doris Vollmer. Direct observation of drops on slippery lubricant-infused surfaces. *Soft Matter*, 11(38):7617–7626, 2015.

[227] Qihan Liu and Zhigang Suo. Osmocapillary phase separation. *Extreme Mechanics Letters*, 7:27–33, 2016.

[228] Katharine E Jensen, Raphael Sarfati, Robert W Style, Rostislav Boltyanskiy, Aditi Chakrabarti, Manoj K Chaudhury, and Eric R Dufresne. Wetting and phase separation in soft adhesion. *Proc. Natl. Acad. Sci. U.S.A.*, 112(47):14490–14494, 2015.

[229] Hansol Jeon, Youchuang Chao, and Stefan Karpitschka. Moving wetting ridges on ultrasoft gels. *Physical Review E*, 108(2):024611, 2023.

[230] Matthieu Roché, Laurence Talini, and Emilie Verneuil. Complexity in wetting dynamics. *Langmuir*, 40(6):2830–2848, 2024.

[231] Sohei Kaneko, Chihiro Urata, Tomoya Sato, Roland Hönes, and Atsushi Hozumi. Smooth and transparent films showing paradoxical surface properties: the lower the static contact angle, the better the water sliding performance. *Langmuir*, 35(21): 6822–6829, 2019.

[232] Satoshi Nakamura, Hiroshi Kakiuchida, Masahisa Okada, and Atsushi Hozumi. Statically very hydrophilic but dynamically hydrophobic surfaces showing surprising water sliding performance. *Advanced Functional Materials*, 34(6):2310265, 2024.

[233] Jonathan T Pham, Frank Schellenberger, Michael Kappl, and Hans-Jürgen Butt. From elasticity to capillarity in soft materials indentation. *Physical Review Materials*, 1(1):015602, 2017.

[234] Yuhang Hu, Xuanhe Zhao, Joost J Vlassak, and Zhigang Suo. Using indentation to characterize the poroelasticity of gels. *Applied Physics Letters*, 96(12), 2010.

[235] A-Reum Kim, Sushanta K Mitra, and Boxin Zhao. Capillary pressure mediated long-term dynamics of thin soft films. *Journal of Colloid and Interface Science*, 628: 788–797, 2022.

[236] Qin Xu, Lawrence A Wilen, Katharine E Jensen, Robert W Style, and Eric R

Dufresne. Viscoelastic and poroelastic relaxations of soft solid surfaces. *Phys. Rev. Lett.*, 125(23):238002, 2020.

[237] Zefan Shao and Qihan Liu. Osmocapillary adhesion: Reversible and strong adhesion between any hydrogel. *Extreme Mechanics Letters*, 61:101996, 2023.

[238] Yang Lai and Yuhang Hu. The relation between adhesion properties and network properties of hydrogels: A study based on an indentation adhesion method. *Mechanics of Materials*, 159:103877, 2021.

[239] Jie Zhu and Qihan Liu. The osmocapillary effect on a rough gel surface. *Journal of the Mechanics and Physics of Solids*, 170:105124, 2023.

[240] Wenjie Qian, Weiwei Zhao, Tiezheng Qian, and Qin Xu. Emergence and growth dynamics of wetting-induced phase separation on soft solids. *Physical Review Research*, 6(3):033210, 2024.

[241] Robert W Style, Callen Hyland, Rostislav Boltyanskiy, John S Wettlaufer, and Eric R Dufresne. Surface tension and contact with soft elastic solids. *Nature communications*, 4(1):2728, 2013.

[242] Su Ji Park, Byung Mook Weon, Ji San Lee, Junho Lee, Jinkyung Kim, and Jung Ho Je. Visualization of asymmetric wetting ridges on soft solids with x-ray microscopy. *Nature communications*, 5(1):4369, 2014.

[243] Stefan Karpitschka, Anupam Pandey, Luuk A Lubbers, Joost H Weijs, Lorenzo Botto, Siddhartha Das, Bruno Andreotti, and Jacco H Snoeijer. Liquid drops attract or repel by the inverted cheerios effect. *Proceedings of the National Academy of Sciences*, 113(27):7403–7407, 2016.

[244] Rishav Roy, Robert L Seiler, Justin A Weibel, and Suresh V Garimella. Droplets on soft surfaces exhibit a reluctance to coalesce due to an intervening wetting ridge. *Advanced Materials Interfaces*, 7(17):2000731, 2020.

[245] Daniel R Darby, Zhuoyun Cai, Christopher R Mason, and Jonathan T Pham. Modulus and adhesion of sylgard 184, solaris, and ecoflex 00-30 silicone elastomers with varied mixing ratios. *Journal of Applied Polymer Science*, 139(25):e52412, 2022.

[246] Justin D Glover, Xingwei Yang, Rong Long, and Jonathan T Pham. Creasing in microscale, soft static friction. *Nature Communications*, 14(1):2362, 2023.

[247] Justin D Glover, Colbi E McLaughlin, Mary K McFarland, and Jonathan T Pham. Extracting uncrosslinked material from low modulus sylgard 184 and the effect on mechanical properties. *Journal of Polymer Science*, 58(2):343–351, 2020.

[248] Aurélie Hourlier-Fargette, Julien Dervaux, Arnaud Antkowiak, and Sébastien Neukirch. Extraction of silicone uncrosslinked chains at air–water–polydimethylsiloxane triple lines. *Langmuir*, 34(41):12244–12250, 2018.

[249] Alicia D Gruber, Chris W Widenhouse, Steven Mathes, and Ronald P Gruber. Exhaustive soxhlet extraction for the complete removal of residual compounds to provide a nonleaching silicone elastomer. *Journal of Biomedical Materials Research: An Official Journal of The Society for Biomaterials, The Japanese Society for Biomaterials, and The Australian Society for Biomaterials and the Korean Society for Biomaterials*, 53(5):445–448, 2000.

[250] Aurélie Hourlier-Fargette, Arnaud Antkowiak, Antoine Chateauminois, and Sébastien Neukirch. Role of uncrosslinked chains in droplets dynamics on silicone elastomers. *Soft Matter*, 13(19):3484–3491, 2017.

[251] Justin D Berman, Manjari Randeria, Robert W Style, Qin Xu, James R Nichols, Aidan J Duncan, Michael Loewenberg, Eric R Dufresne, and Katharine E Jensen. Singular dynamics in the failure of soft adhesive contacts. *Soft matter*, 15(6):1327–1334, 2019.

[252] Guido Bartalena, Reto Grieder, Ram I Sharma, Tomaso Zambelli, Roman Muff, and Jess G Snedeker. A novel method for assessing adherent single-cell stiffness in tension: design and testing of a substrate-based live cell functional imaging device. *Biomedical microdevices*, 13:291–301, 2011.

[253] Sazzadul A Rahat, Krishnaroop Chaudhuri, and Jonathan T Pham. Capillary detachment of a microparticle from a liquid–liquid interface. *Soft Matter*, 19(33): 6247–6254, 2023.

[254] Grigory Isaakovich Barenblatt. *Scaling, self-similarity, and intermediate asymptotics: dimensional analysis and intermediate asymptotics*. Number 14 in Cambridge Texts in Applied Mathematics. Cambridge University Press, 1996.

[255] Leoneio Garrido, Jerome L Ackerman, and James E Mark. Self-diffusion of poly (dimethylsiloxane) chains. *New Trends in Physics and Physucal Chemistry of Polymers*, pages 355–365, 1989.

[256] Enrique M Valles and Christopher W Macosko. Structure and viscosity of poly (dimethylsiloxanes) with random branches. *Macromolecules*, 12(3):521–526, 1979.

[257] Tadao Kataoka and Shigeyuki Ueda. Viscosity–molecular weight relationship for polydimethylsiloxane. *Journal of Polymer Science Part B: Polymer Letters*, 4(5): 317–322, 1966.

[258] Ying Li, Martin Kröger, and Wing Kam Liu. Primitive chain network study on uncrosslinked and crosslinked cis-polyisoprene polymers. *Polymer*, 52(25):5867–5878, 2011.

[259] AN Gent and RH Tobias. Diffusion and equilibrium swelling of macromolecular networks by their linear homologs. *Journal of Polymer Science: Polymer Physics Edition*, 20(12):2317–2327, 1982.

[260] J Mazan, B Leclerc, N Galandrin, and G Couarraze. Diffusion of free polydimethylsiloxane chains in polydimethylsiloxane elastomer networks. *European polymer journal*, 31(8):803–807, 1995.

[261] Abhinav Naga. *Capillary interactions in wetting: rotation of particles at interfaces and removal of particles by drops.* PhD thesis, Johannes Gutenberg-Universität Mainz, 2021.

[262] D. Brutin and V. Starov. Recent advances in droplet wetting and evaporation. *Chem. Soc. Rev.*, 47(2):558–585, JAN 21 2018. doi: 10.1039/c6cs00902f.

[263] Zhenying Wang, Daniel Orejon, Yasuyuki Takata, and Khellil Sefiane. Wetting and evaporation of multicomponent droplets. *Phys. Rep.*, 960:1–37, MAY 19 2022. doi: 10.1016/j.physrep.2022.02.005.

[264] Aurélie Lafuma and David Quéré. Superhydrophobic states. *Nat. Mater.*, 2(7): 457–460, 2003.

[265] Hong Wang, Xinhong Xiong, Li Yang, and Jiaxi Cui. Droplets in soft materials. *Droplet*, 1(2):110–138, 2022.

[266] D. Tejero-Martin, M. Rezvani Rad, A. McDonald, and T. Hussain. Beyond traditional coatings: A review on thermal-sprayed functional and smart coatings. *J. Therm. Spray Technol.*, 28(4):598–644, APR 2019. doi: 10.1007/s11666-019-00857-1.

[267] Kihwan Choi, Alphonsus HC Ng, Ryan Fobel, and Aaron R Wheeler. Digital microfluidics. *Annual review of analytical chemistry*, 5(1):413–440, 2012.

[268] H. Jeremy Cho, Daniel J. Preston, Yangying Zhu, and Evelyn N. Wang. Nanoengineered materials for liquid-vapour phase-change heat transfer. *Nat. Rev. Mater.*, 2 (2):16092, FEB 2017. doi: 10.1038/natrevmats.2016.92.

[269] Jonathan P. Rothstein. Slip on superhydrophobic surfaces. *Annu. Rev. Fluid Mech.*, 42:89–109, 2010. doi: 10.1146/annurev-fluid-121108-145558.

[270] Choongyeop Lee, Chang-Hwan Choi, and Chang-Jin Kim. Superhydrophobic drag reduction in laminar flows: a critical review. *Exp. Fluids*, 57(12):176, DEC 2016. doi: 10.1007/s00348-016-2264-z.

[271] Hyungmin Park, Chang-Hwan Choi, and Chang-Jin Kim. Superhydrophobic drag reduction in turbulent flows: a critical review. *Exp. Fluids*, 62(11):229, NOV 2021. doi: 10.1007/s00348-021-03322-4.

[272] Xinjie Liu, Qian Ye, Bo Yu, Yongmin Liang, Weimin Liu, and Feng Zhou. Switching water droplet adhesion using responsive polymer brushes. *Langmuir*, 26(14):12377–12382, JUL 20 2010. doi: 10.1021/la101909e.

[273] Xinjie Liu, Meirong Cai, Yongmin Liang, Feng Zhou, and Weimin Liu. Photo-

regulated stick-slip switch of water droplet mobility. *Soft Matter*, 7(7):3331–3336, 2011. doi: 10.1039/c0sm01144d.

[274] Kenji Okada, Yoko Miura, Tomoya Chiya, Yasuaki Tokudome, and Masahide Takahashi. Thermo-responsive wettability surface roughness change on polymer-coated titanate nanorod brushes toward fast and multi-directional droplet transport. *RSC Adv.*, 10(47):28032–28036, JUL 30 2020.

[275] Joost H. Weijs, Jacco H. Snoeijer, and Bruno Andreotti. Capillarity of soft amorphous solids: A microscopic model for surface stress. *Phys. Rev. E*, 89(4):042408, APR 28 2014. doi: 10.1103/PhysRevE.89.042408.

[276] Bruno Andreotti and Jacco H. Snoeijer. Soft wetting and the shuttleworth effect, at the crossroads between thermodynamics and mechanics. *EPL*, 113(6):66001, MAR 2016. doi: 10.1209/0295-5075/113/66001.

[277] Dan Daniel, Yunita Florida, Chee Leng Lay, Xue Qi Koh, Anqi Sng, and Nikodem Tomczak. Quantifying surface wetting properties using droplet probe atomic force microscopy. *ACS Appl. Mater. Interfaces*, 12(37):42386–42392, SEP 16 2020. doi: 10.1021/acsami.0c12123.

[278] Dirk Peschka. Variational approach to dynamic contact angles for thin films. *Phys. Fluids*, 30(8):082115, AUG 2018. doi: 10.1063/1.5040985.

[279] Lorenzo Giacomelli, Manuel V. Gnann, and Dirk Peschka. Droplet motion with contact-line friction: long-time asymptotics in complete wetting. *Proc. Royal Soc. A*, 479(2274):20230090, JUN 28 2023. doi: 10.1098/rspa.2023.0090.

[280] Liwei Chen, Shilin Huang, Robin HA Ras, and Xuelin Tian. Omniphobic liquid-like surfaces. *Nat. Rev. Chem.*, 7(2):123–137, 2023.

[281] Xiaoxiao Zhao, Behrooz Khatir, Kiana Mirshahidi, Kai Yu, Jayachandran N Kizhakkedathu, and Kevin Golovin. Macroscopic evidence of the liquidlike nature of nanoscale polydimethylsiloxane brushes. *ACS nano*, 15(8):13559–13567, 2021.

[282] Martin ER Shanahan and Alain Carre. Anomalous spreading of liquid drops on an elastomeric surface. *Langmuir*, 10(6):1647–1649, 1994.

[283] MER Shanahan and A Carre. Viscoelastic dissipation in wetting and adhesion phenomena. *Langmuir*, 11(4):1396–1402, 1995.

[284] José Bico, Étienne Reyssat, and Benoît Roman. Elastocapillarity: When surface tension deforms elastic solids. *Annu. Rev. Fluid Mech.*, 50:629–659, 2018.

[285] Muhammad S Sadullah, Ciro Semprebon, and Halim Kusumaatmaja. Drop dynamics on liquid-infused surfaces: The role of the lubricant ridge. *Langmuir*, 34(27): 8112–8118, 2018.

[286] Simon Hartmann, Jan Diekmann, Daniel Greve, and Uwe Thiele. Drops on polymer

brushes: Advances in thin-film modeling of adaptive substrates. *Langmuir*, 40(8): 4001–4021, 2024.

[287] Zhen Cao and Andrey V. Dobrynin. Polymeric droplets on soft surfaces: From neumann's triangle to young's law. *Macromolecules*, 48(2):443–451, JAN 27 2015. doi: 10.1021/ma501672p.

[288] Daniel Greve, Simon Hartmann, and Uwe Thiele. Stick-slip dynamics in the forced wetting of polymer brushes. *Soft Matter*, 19(22):4041–4061, 2023.

[289] Russell Kajouri, Panagiotis E. Theodorakis, Jan Židek, and Andrey Milchev. Antidurotaxis droplet motion onto gradient brush substrates. *Langmuir*, 39(43):15285–15296, SEP 6 2023. doi: 10.1021/acs.langmuir.3c01999.

[290] Russell Kajouri, Panagiotis E Theodorakis, Piotr Deuar, Rachid Bennacer, Jan Židek, Sergei A Egorov, and Andrey Milchev. Unidirectional droplet propulsion onto gradient brushes without external energy supply. *Langmuir*, 39(7):2818–2828, 2023.

[291] Oezlem Kap, Simon Hartmann, Harmen Hoek, Sissi de Beer, Igor Siretanu, Uwe Thiele, and Frieder Mugele. Nonequilibrium configurations of swelling polymer brush layers induced by spreading drops of weakly volatile oil. *J. Chem. Phys.*, 158(17): 174903, MAY 7 2023. doi: 10.1063/5.0146779.

[292] K. Speyer and C. Pastorino. Droplet transport in a nanochannel coated by hydrophobic semiflexible polymer brushes: The effect of chain stiffness. *Langmuir*, 33 (40):10753–10763, OCT 10 2017. doi: 10.1021/acs.langmuir.7b02640.

[293] C. Pastorino and M. Mueller. Liquid and droplet transport in brush-coated cylindrical nanochannels: Brush-assisted droplet formation. *J. Phys. Chem. B*, 125(1): 442–449, JAN 14 2021. doi: 10.1021/acs.jpcb.0c09189.

[294] Fong Yew Leong and Duc-Vinh Le. Dynamics of a droplet on a polymer brush in channel flow. *Phys. Fluids*, 33(4):043303, APR 2021. doi: 10.1063/5.0042161.

[295] Katharina I Hegner, Chirag Hinduja, Hans-Jürgen Butt, and Doris Vollmer. Fluorine-free super-liquid-repellent surfaces: Pushing the limits of pdms. *Nano Lett.*, 23(8):3116–3121, 2023.

[296] DW Pilat, P Papadopoulos, D Schaffel, Doris Vollmer, Rüdiger Berger, and H-J Butt. Dynamic measurement of the force required to move a liquid drop on a solid surface. *Langmuir*, 28(49):16812–16820, 2012.

[297] S. Y. Wong William, Lukas Hauer, Abhinav Naga, Anke Kaltbeitzel, Philipp Baumli, Rüdiger Berger, Maria D'Acunzi, Doris Vollmer, and Hans-Jürgen Butt. Adaptive wetting of polydimethylsiloxane. *Langmuir*, 36(26):7236–7245, 2020. doi: 10.1021/acs.langmuir.0c00538.

[298] Shuhang Lyu, Zhen Yang, and Yuanyuan Duan. The sliding mode and dissipative

force of moving nanodroplets on smooth and striped hydrophobic surfaces. *J. Mol. Liquids*, 346:118284, JAN 15 2022. doi: 10.1016/j.molliq.2021.118284.

[299] Sebastian Burgmann, Veronika Krämer, Martin Rohde, Michael Dues, and Uwe Janoske. Inner and outer flow of an adhering droplet in shear flow. *Int. J. Multiph. Flow*, 153:104140, 2022. doi: 10.1016/j.ijmultiphaseflow.2022.104140.

[300] Abba Abdulhamid Abubakar, Bekir Sami Yilbas, Hussain Al-Qahtani, and Anwaruddin Siddiqui Mohammed. Droplet rolling dynamics over a hydrophobic surface with a minute width channel. *Langmuir*, 37(25):7851–7861, JUN 29 2021. doi: 10.1021/acs.langmuir.1c01268.

[301] Wenchuan Liu and Dengwei Jing. Droplet rolling transport on hydrophobic surfaces under rotating electric fields: A molecular dynamics study. *Langmuir*, 39(41):14660–14669, OCT 6 2023. doi: 10.1021/acs.langmuir.3c01989.

[302] Hao Li, Tianyu Yan, Kristen A. Fichthorn, and Sirong Yu. Dynamic contact angles and mechanisms of motion of water droplets moving on nanopillared superhydrophobic surfaces: A molecular dynamics simulation study. *Langmuir*, 34(34):9917–9926, AUG 28 2018. doi: 10.1021/acs.langmuir.8b01324.

[303] A. F. W. Smith, K. Mahelona, and S. C. Hendy. Rolling and slipping of droplets on superhydrophobic surfaces. *Phys. Rev. E*, 98(3):033113, SEP 21 2018. doi: 10.1103/PhysRevE.98.033113.

[304] Sergey Nikolaevich Krivoshapko and Vyacheslav N Ivanov. *Encyclopedia of analytical surfaces*. Springer, 2015.

[305] Michael te Vrugt, Hartmut Löwen, and Raphael Wittkowski. Classical dynamical density functional theory: from fundamentals to applications. *Advances in Physics*, 69(2):121–247, 2020.

[306] Walter Greiner and Joachim Reinhardt. *Field quantization*. Springer Science & Business Media, 2013.